Implicit Large Eddy Simulation for Unsteady Multi-Component Compressible Turbulent Flows

Ben Thornber

Submitted for the Degree of Ph.D.

Fluid Mechanics and Computational Science Group
School of Engineering
Cranfield University
Cranfield, UK

2007

Abstract

Numerical methods for the simulation of shock-induced turbulent mixing have been investigated, focussing on Implicit Large Eddy Simulation. Shock-induced turbulent mixing is of particular importance for many astrophysical phenomena, inertial confinement fusion, and mixing in supersonic combustion. These disciplines are particularly reliant on numerical simulation, as the extreme nature of the flow in question makes gathering accurate experimental data difficult or impossible.

A detailed quantitative study of homogeneous decaying turbulence demonstrates that existing state of the art methods represent the growth of turbulent structures and the decay of turbulent kinetic energy to a reasonable degree of accuracy. However, a key observation is that the numerical methods are too dissipative at high wavenumbers (short wavelengths relative to the grid spacing). A theoretical analysis of the dissipation of kinetic energy in low Mach number flows shows that the leading order dissipation rate for Godunov-type schemes is proportional to the speed of sound and the velocity jump across the cell interface squared. This shows that the dissipation of Godunov-type schemes becomes large for low Mach flow features, hence impeding the development of fluid instabilities, and causing overly dissipative turbulent kinetic energy spectra.

It is shown that this leading order term can be removed by locally modifying the reconstruction of the velocity components. As the modification is local, it allows the accurate simulation of mixed compressible/incompressible flows without changing the formulation of the governing equations. In principle, the modification is applicable to any finite volume compressible method which includes a reconstruction stage. Extensive numerical tests show great improvements in performance at low Mach compared to the standard scheme, significantly improving turbulent kinetic energy spectra, and giving the correct Mach squared scaling of pressure and density variations down to Mach 10^{-4}. The proposed modification does not significantly affect the shock capturing ability of the numerical scheme.

The modified numerical method is validated through simulations of compressible, deep, open cavity flow where excellent results are gained with minimal modelling effort. Simulations of single and multimode Richtmyer-Meshkov instability show that the modification gives equivalent results to the standard scheme at twice the grid resolution in each direction. This is equivalent to sixteen times decrease in computational time for a given quality of results. Finally, simulations of a shock-induced turbulent mixing experiment show excellent qualitative agreement with available experimental data.

Acknowledgements

Completing this thesis has been a tough challenge, and there are many people who I wish to thank without whom the last three years would have been much less educational and entertaining.

Firstly I would like to thank Prof. Drikakis for his supervision and guidance, for his advice in choosing which direction to investigate, and for his boundless enthusiasm for the development and understanding of numerical methods for turbulence. I am extremely grateful to David Youngs and Robin Williams at AWE for sharing their considerable experience in numerical methods and understanding of flow physics with me, and for being an interested audience for my 'work in progress' once every three months.

After three years in working in the same office, I have to give considerable thanks to the people who I have shared my time at Cranfield with; Jason Bennett, Steve Carnduff, Ian Cowling, Simon Croucher, Marco Hahn, Marco Kalweit, Sunil Mistry, John Murphy, Sanjay Patel and Adam Ruggles. The days of golf and Quake III tournaments certainly helped keep the creative ideas coming, and the football tournaments were a great way to relieve the pain of a day spent debugging code. Within the FMACS group, I would like to especially thank Marco Hahn, Sanjay Patel, Evgeniy Shapiro, Marco Kalweit, Andrew Mosedale and Anthony Weatherhead for many, many discussions about numerical methods, flow physics and coding methods. Also, I want to thank Les Oswald at the High Performance Computing Centre at Cranfield University for (what appeared to be) 24/7 advice when running on the HPC.

On a more personal note, I would like to thank my girlfriend Colleen for sharing with me both the joys and pains of working on a PhD, for never once complaining if I had to spend the weekend at university to finish some work, and for being a continuous source of belief.

Finally, I would not have come this far without the support of my whole family. I would like to dedicate this thesis to my Mum and Dad, who have always encouraged me to do the best I can at whatever I choose to pursue, and have given me constant support and advice throughout my life.

Ben Thornber

Contents

List of Figures

List of Tables

Nomenclature

Acronyms

CFL	Courant-Friedrichs-Levy
dB	deciBel
DNS	Direct Numerical Simulation
DT	semi-implicit Dual Timestepping
ES	Extended Stability
FFT	Fast Fourier Transform
FV	Finite Volume
HLLC	Harten, Lax, and van Leer Riemann solver plus contact wave
ILES	Implicit Large Eddy Simulation
JC	Quasi-conservative scheme of Johnsen and Colonius [97]
KH	Kelvin-Helmholtz
LES	Large Eddy Simulation
M3	MUSCL third-order
M5	MUSCL fifth-order
M5+LM	MUSCL fifth-order with Low Mach correction
MF	Mass Fraction model
MM	Minmod
MUSCL	Monotone Upstream-centered Schemes for Conservation Laws
PDF	Probability Distribution Function
PVRS	Primitive Variable Riemann Solver
QCA	Quasi-conservative scheme of Allaire *et al.* [4]
RANS	Reynolds Averaged Navier Stokes
RK	Runge-Kutta
RM	Richtmyer-Meshkov
RT	Rayleigh-Taylor
SF_6	Sulphur Hexaflouride

SPL	Sound Pressure Level
ThCM	Total Enthalpy Conservation of the Mixture model
TVD	Total Variation Diminishing
VA	van Albada
VL	van Leer
W5	WENO fifth-order
W9	WENO ninth-order
WENO	Weighted Essentially Non-Oscillatory

Units

The units which are used in the nomenclature have the following meanings:

M	mass
L	length
T	time
θ	temperature
mol	mole

Operators and Frame Decorations

Symbol	Definition
Δ	increment or difference in the quantity
$\overline{(.)}$	ensemble average
$\lvert(.)\rvert$	absolute magnitude of the quantity
$(.)'$	fluctuating quantity
$\widetilde{(.)}$	reconstructed characteristic quantity
$\tilde{(.)}$	Favre weighted average
$\overline{(.)}$	average of left and right quantity
$(.)\lvert_{k=a}$	quantity evaluated at $k = a$

Latin letters

Symbol	Unit	Quantity
a	L/T	speed of sound
A	L	amplitude of the mode
At	-	Atwood number
$\mathbf{A}$	-	flux jacobian
$\mathcal{A}$	-	ratio of finite volume fluxes in spectral space to spectral fluxes
c_v	$L^2/T^2\theta$	specific heat at constant volume
C	-	Courant-Friedrichs-Levy number
e	M/LT^2	energy per unit volume
E	L^3/T^2	turbulent kinetic energy spectrum
$\mathbf{E}$, $\mathbf{F}$, $\mathbf{G}$	-	vector of convective fluxes in the ξ, η, and ζ directions
$\mathcal{E}$	L^2/T^3	z averaged kinetic energy dissipation rate
f	-	longitudinal correlation function
F	-	finite volume flux
g	L/T^2	acceleration
$\mathcal{G}$	-	curvature of the isotrope
h	L	measure of the width of the mixing zone
H	L^2/T^2	specific enthalphy $q^2/2 + i + p/\rho$
i	L^2/T^2	internal energy per unit mass
I	-	$\sqrt{-1}$
J	-	jacobian of the cell volume
k	$1/L$	total wave number, $k = \sqrt{k_x^2 + k_y^2 + k_z^2}$
$\mathbf{k}$	$1/L$	wave vector
$\mathbf{K}$	-	eigenvector array
$\mathbf{K}^{1-7}$	-	right eigenvectors of the quasi-conservative system
KE	L^2/T^2	kinetic energy per unit mass
k_p	$1/L$	wave number at peak energy
K_q	L^2/T	turbulent energy eddy diffusion coefficient
l	-	mode number in the x direction
ℓ	L	integral length scale
L	L	reference lengthscale
m	-	mode number in the y direction

M	-	Mach number
$\mathcal{M}$	M	molecular mass
n	-	mode number in the z direction
p	M/LT^2	pressure
$p_{(.)}$	-	derivative of pressure with respect to (.)
P	-	Power spectrum
$\mathcal{P}$	-	kinetic energy decay exponent
$\dot{\mathcal{P}}_s$	$M/LT^3\theta$	production rate of entropy
$\mathbf{P}$	-	vector of cell averaged primitive variables
q	-	growth exponent of the integral length scales
q_K	L^2/T^2	turbulent kinetic energy per unit mass
$\mathbf{q}$	M/T^3	heat diffusion flux
$\mathbf{Q}$	L^2/T^2	second order velocity correlation function
r	L	separation distance
r^{lim}	-	ratio of jumps in limiter function
R	$L^2/T^2\theta$	specific gas constant
Re	-	Reynolds number
R_u	$ML^2/T^2\theta mol$	universal gas constant
s	-	the pole of a system
S	$ML^2/T^2\theta$	entropy per unit mass
$\mathbf{S}$	L^2	surface area
$\mathcal{S}$	L	interface perturbation
sd	L	standard deviation of the interface perturbation
t	T	time
T	θ	temperature
u, v, w	L/T	velocity components in the x, y, or z cartesian directions respectively
U	L/T	reference velocity
$\mathbf{U}$	-	vector of conserved variables
V	L^3/M	specific volume
Vol	L^3	volume
W	L	integral mixing width
x, y, z	L	cartesian directions
Y	-	mass fraction

Greek letters

Symbol	Unit	Quantity
α	-	volume fraction
χ	-	quantity advected in the ThCM gas mixture model
δ_{1-7}	-	wave strengths in the Roe scheme
δ_{tz}	L	half thickness of the turbulent mixing zone
Δu_s	L/T	velocity jump across the shock wave
Δv^p	$(L/T)^p$	velocity structure function of order p
ϵ	L^2/T^3	turbulent kinetic energy dissipation rate per unit mass
η_K	L	Kolmogorov lengthscale
γ	-	ratio of specific heats
κ	L^3/M	derivative of internal energy per unit mass with pressure
κ_3	L^3/T^3	third order structure function
κ_θ	$ML/T^3\theta$	thermal conductivity
λ	L	perturbation wavelength
λ_{tay}	L	Taylor microscale
λ^{eig}	L/T	wavespeed (eigenvalue)
Λ	L/T	diagonal array of eigenvalues
μ	M/LT	dynamic viscosity
ν	T/L	$\Delta t/\Delta x$
ν_{vis}	L^2/T	kinematic viscosity, μ/ρ
ν_n^+	-	effective normalised numerical viscosity
ω	$1/LT$	vorticity
ϕ^{lim}	-	limiter function
ϕ_{ij}	L^2/T^2	spectrum tensor
Φ	L^2/T	velocity potential
ψ	-	dimensionless turbulent lengthscale
ρ	M/L^3	density
σ	M/T^2L	viscous stresses
τ	-	dimensionless scaled time
τ^ν	M/LT^2	shear stress tensor
θ	-	power law growth rate, i.e. t^θ
Θ	-	mix parameter (slow reaction)

ξ, η, ζ	L	curvilinear co-ordinates
Ξ	-	mix parameter (fast reaction)

Subscripts and Superscripts

Symbol	Definition
$(.)_{11}$	longitudinal quantity
$(.)_{1D}$	one dimensional quantity
$(.)_{22}$	lateral quantity
$(.)^{-}$, $(.)^{+}$	pre- and post-shocked quantities
$(.)^{*}$	solutions for the quantity in the ‘star’ region of the Riemann problem
$(.)_{d}$	dilational component
$(.)_{i}$, $(.)_{j}$, $(.)_{k}$	components in the i, j, and k direction respectively, or grid reference co-ordinate
$(.)_{L}$,$(.)_{R}$	left or right quantity
$(.)_{l,m,n}$	indicates a coefficient in the fourier transform of the vector potential
$(.)^{n}$	finite volume co-ordinate in time
$(.)_{max}$	maximum value of the quantity
$(.)_{rms}$	root mean square quantity
$(.)_{s}$	solenoidal component
$(.)_{SGS}$	sub-grid quantity
$(.)_{x}$, $(.)_{y}$, $(.)_{z}$	derivative in the x, y and z directions respectively

CHAPTER 1

Introduction

1.1 Problem Statement

When considering fluid flow the first question typically asked is: What is the Reynolds number of the flow? The Reynolds number is a means of determining approximately whether a flow is laminar or turbulent. A laminar flow is characterised by smooth motion with large scale, coherent structures. As the Reynolds number increases, the flow transitions from a stable, laminar configuration to a highly chaotic turbulent state. This occurs as inertial forces overcome the natural dampening due to viscous effects, allowing the growth of perturbations in the flow which are naturally unstable. Fully turbulent flow is characterised by extremely complex flow fields with motion at a huge range of scales, often behaving in a chaotic manner.

This process is illustrated in Figure 1.1, where a round jet is initially smooth and laminar, becomes unstable and transitions to a fully turbulent flow. The fine scales and sharp gradients present in the turbulent jet are typical of turbulent flows.

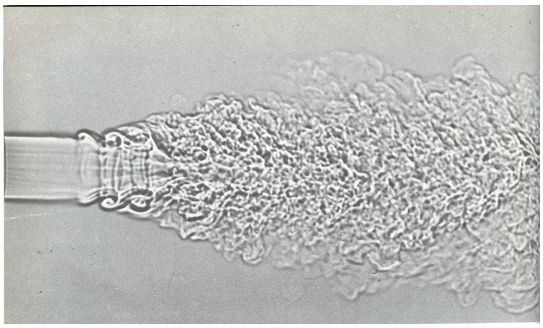

Figure 1.1: Transition from laminar to turbulent flow in a round jet at Reynolds number approximately $30,000$ shown via shadowgraph [186]

Classical examples of instabilities which trigger turbulence include Kelvin-Helmholtz (KH) and Rayleigh-Taylor (RT) instabilities, examples of which are shown in Figure 1.2. The KH instability occurs in shear layers, causing roll up of the shear layer into discrete vortices. Indeed, the primary instability in Figure 1.1 is a three dimensional

form of this. The RT instability is due to unstable stratification (i.e. a heavy gas on top of a light gas), and causes bubbles of light fluid to rise into the heavy fluid, and spikes of heavy fluid fall through the light fluid.

Figure 1.2: Kelvin-Helmholtz instability causing wave-like formations in clouds over Mount Shasta, California (left)[162], and Rayleigh-Taylor billowing in the plume of Mount Etna (right)[125]

As these instabilities grow exponentially, they can trigger the transition from laminar to turbulent flow if not suppressed by viscous forces. Once a perturbation has been amplified through growth of a certain instability, it seeds motion at many different length scales due to nonlinear interaction in the governing equations. The motion is passed from large to small scales until, finally, the motion is at a sufficiently small scale to be damped by viscosity. Through this process the motion of the large scales is typically governed by the instability mechanism (or mechanisms), whereas the small scales are usually assumed to be independent of the seeding instability.

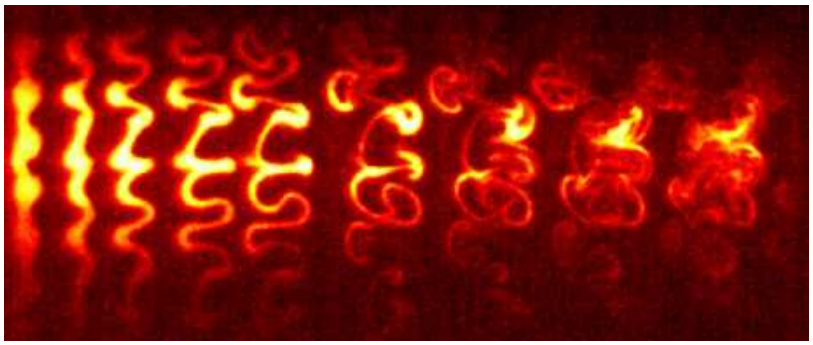

Figure 1.3: Transition from linear and nonlinear growth to a turbulent mixing layer for RM instability of a gas curtain [156]

This thesis is concerned with developing numerical methods for the simulation of the Richtmyer-Meshkov (RM) instability. This is related to the RT instability, in that it involves the motion of a heavy and light fluid, driven in this case by an impulsive instead of continuous acceleration. The impulsive acceleration typically arises due to a shock wave, which passes from one fluid into another. On the interface between the two fluids, there is usually a small perturbation, which could be surface roughness, a slightly non-planar shock, a machined perturbation, or an uneven fluid interface.

The interaction between this perturbation and the incident shock wave seeds the fluid instability. The development of RM instability of a gas curtain from seed perturbation to turbulent mixing layer is shown in the two-dimensional case in Figure 1.3. The instability initially grows in a laminar, ordered manner. At late time, further to the right of the image, the ordered structures become turbulent, enhancing greatly the mixing of the heavy and light gases.

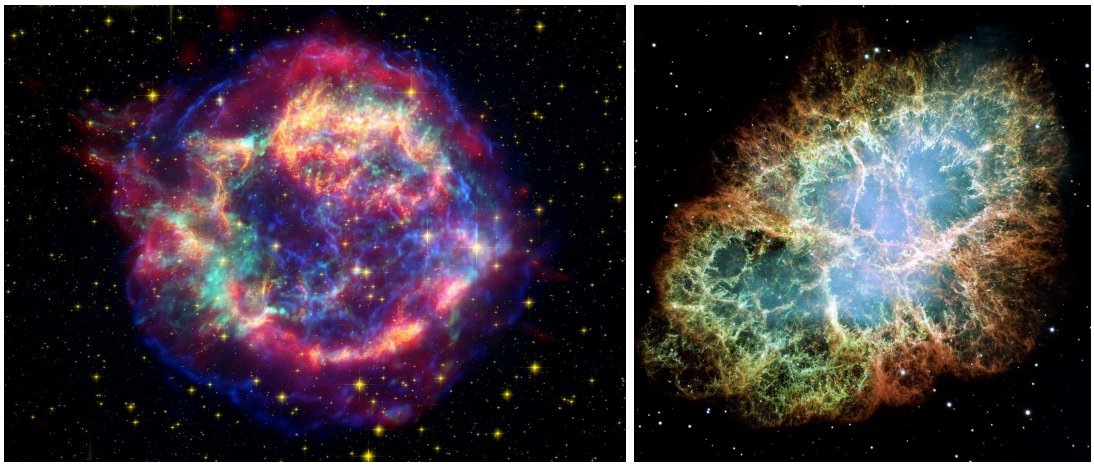

(a) Cassiopeia A (b) Crab Nebula

Figure 1.4: Remnants of the Cassiopeia A supernova (left) [141] , and the Crab Nebula (right) [57]

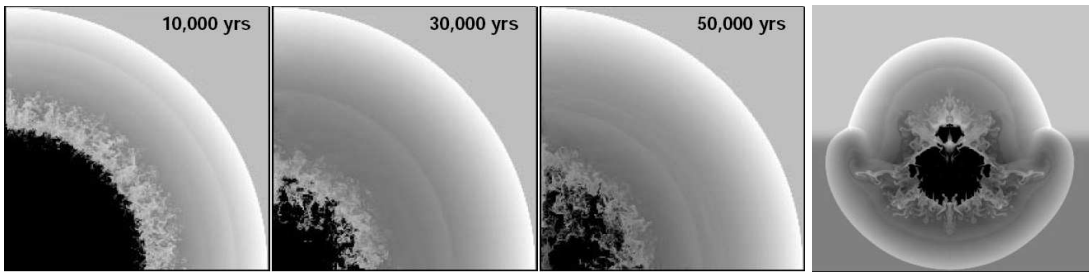

(a) Crushing of the pulsar nebula (one quarter) (b) Inhomogeneous supernova

Figure 1.5: Numerical simulation of the development of a spherical, homogeneous pulsar nebula (first three images from the left), and the same case but with inhomogeneous initial conditions (right). Images are coloured by density on a logarithmic scale [23]

This form of impulsive mixing is important in the understanding of many astrophysical phenomena, from supernovae to the dynamics of interstellar media. In the past few decades it has been realised that the assumption of spherical symmetry in the simulations of supernovae are inadequate due to the growth of RM instabilities. Figure 1.4 a) shows a false colour image of the Cassiopeia A supernova remnants, where the uneven shape of the remnants is due in part to the combined influence of RM and RT instabilities acting on perturbations within the star before the supernova. Figure 1.4b) shows

the Crab Nebula, whose development is linked to the expansion of shock-accelerated material after RM and RT induced mixing. Visualisations of density from two dimensional simulations of pulsar nebula and supernova remnants by Blondin *et al.* [23] are shown in Figure 1.5. The development of RM and RT instabilities can be seen clearly in the spherical, homogeneous case, however they have a greater influence in the inhomogeneous case where mixed material can extend well beyond the area expected from the homogeneous simulations.

Earth-bound phenomena include inertial confinement fusion, where a spherical capsule containing thermonuclear material is compressed using a powerful laser until temperatures sufficiently high for fusion reactions to occur is achieved [7]. This one of several proposed methods for generation of power from fusion, and is an extension of the methods employed within nuclear bombs.

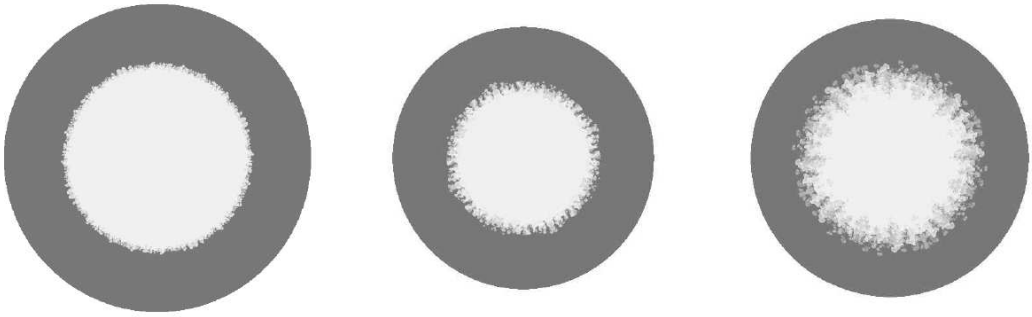

Early stages Near max. compression After max. compression

Figure 1.6: Simulation results demonstrating the influence of RM and RT instabilities during the implosion of a spherical capsule [200]

This process is illustrated using via results from three-dimensional numerical simulations in Figure 1.6 [200]. Very high pressures generated at the outside of the capsule cause it to be compressed. Once a critical level of compression has been reached, ignition is achieved and a burst of energy is released. In this case RM instability occurs at the interface between the light and heavy materials, triggering turbulent mixing. The qualitative similarities between these simulations and those of supernovae in Figure 1.5 are striking. In inertial confinement fusion, turbulent mixing has the dual effect of diluting and cooling the fuel, which reduces the efficiency of the reaction, hence it important that this phenomena is well understood. One further application of RM mixing is in the field of supersonic combustion, where weak shocks can be employed to improve the mix ratios and hence give more efficient combustion.

A key observation regarding all of these applications is that experimental data (especially quantitative data) is very difficult to measure, most notably in the cases of astrophysical flows and inertial confinement fusion. Thus understanding of the underlying flow physics relies to an unusual level on insights gained through modelling and numerical simulation.

A numerical method developed for simulating the RM and associated instabilities must be capable of capturing several simultaneous phenomena. Firstly, the instability grows from an initially small perturbation meaning that this growth must be simulated accu-

rately without unwanted dissipation. Secondly, the instability rapidly becomes turbulent due to the combined influence of RM and KH growth, meaning that the numerical scheme must be able to simulate a chaotic turbulent flow field, and dissipate turbulent kinetic energy appropriately. As the RM instability is triggered by a shock wave, the numerical method must be able to simulate compressibility effects, and capture shock waves with reasonable accuracy. It is essential that both shock waves and low Mach near-incompressible flow features can be captured accurately, at the same time, with the same numerical method. Finally, the mixing usually occurs between two different fluids, hence requiring the physically realistic simulation of two or more fluid species that have different thermodynamic properties.

The scope of this thesis is to implement, analyse, improve and validate numerical methods which satisfy all of the above criteria for compressible, turbulent, mixing flows seeded by the RM instability.

1.2 Structure of the Thesis

The thesis commences with an introduction to turbulent flows. It discusses the key elements from growth of an initially small instability, through to the behaviour of a fully developed turbulent flow field. It describes the key quantities of interest which will used later in the thesis to measure the performance of the numerical simulation. Chapter 3 details the numerical methods employed, including the validation and selection of the optimum gas mixture model to use for flows with more than one component. It also introduces the numerical approach for unsteady turbulent flows, and initialisation methods for turbulent flow fields.

Chapter 4 discusses in depth the performance of the standard Finite Volume methods when applied to the canonical problem of homogeneous decaying turbulence. Several quantitative metrics are employed to highlight the strengths and weaknesses of each numerical method. Chapter 5 analyses theoretically the source of dissipation of kinetic energy in Godunov methods, demonstrating that the dissipation of kinetic energy is proportional to the speed of sound. Chapter 6 proposes a simple modification to the standard Godunov type method which improves the resolution of turbulent flow fields, especially at low Mach which maintaining shock capturing capability. The modification is local in space, and does not require a change in the formulation of the governing equations.

Validation of the modified numerical scheme against experimental and theoretical results is conducted in Chapter 7. The numerical methods are applied to a compressible cavity flow, single and multiple mode Richtmyer-Meshkov instability, and simulations of a multicomponent, compressible turbulent shock tube experiment. In addition to validating the numerical methods, the flow physics are also discussed.

Chapter 8 concludes the thesis with a summary of key results and recommendations for future research.

1.3 Journal and Conference Publications

Whilst writing the thesis several papers have been written and submitted. At the date of writing, the following papers have been accepted for journal publication:

Thornber, B.,Mosedale, A., Drikakis, D., *'On the Implicit Large Eddy Simulation of Homogeneous Decaying Turbulence'*, J. Comput. Phys, 2007

Thornber, B., Drikakis, D. and Youngs, D., *'Large-eddy simulation of multi-component compressible turbulent flows using high resolution methods'*, Comput. Fluids, 2007

Thornber, B., Drikakis, D., *'Large Eddy Simulation of Shock-Wave-Induced Turbulent Mixing'*, J. Fluids Eng., 2007

Thornber, B., Drikakis, D., *'Numerical Dissipation of Godunov Schemes in Low Mach Flow'*, Int. J. Numer. Meth. Fl., 2007

The following papers have been submitted, and are currently under review:

Thornber, B., Drikakis, D., Williams, R. *'On Entropy Generation and Dissipation of Kinetic Energy in Godunov-type Schemes'*, submitted to J.Comput. Phys., 2007

Thornber, B., Mosedale, A., Drikakis, D., Youngs, D. *'An Improved Reconstruction Method for Compressible Flows with Low Mach Features'*, submitted to J. Comput. Phys, 2007

In addition to journal papers, a number of conference papers have been written and presented:

Thornber, B., Mosedale, A., Drikakis, D., *'Large-eddy simulation of Compressible Turbulent Mixing across Gas Interfaces'*, 5th International Symposium on Turbulence and Shear Flow Phenomena, Germany, 2007

Thornber, B., Drikakis, D., *'Numerical dissipation of Godunov Schemes in low Mach flows'*, Numerical Methods for Fluid Dynamics, UK, 2007

Thornber, B., Drikakis, D. and Youngs, D., *'Large-eddy simulation of multi-component compressible turbulent flows using high resolution methods'*, Conference on Turbulence and Interactions, France, 2006

Thornber, B., Drikakis, D. and Youngs, D., *'High Resolution Methods for Planar 3D Richtmyer Meshkov Instabilities*, 10th International Workshop on the Physics of Compressible Turbulent Mixing, Paris, 2006

Thornber, B., Drikakis, D., *'Large-eddy Simulation of Isotropic Homogeneous Decaying Turbulence'*, ECCOMAS, Netherlands, 2006

Thornber, B., Drikakis, D., *'ILES of shock waves and turbulent mixing using high-resolution Riemann solvers and TVD methods'*, ECCOMAS, Netherlands, 2006

Thornber, B., Drikakis, D., *'Approximate Riemann solvers for multi-component flows'*, Workshop on Numerical Methods of Multi-material flow problems, Oxford, 2005

CHAPTER 2

Fundamentals of Turbulent Flow

2.1 Linear Analysis of the Fundamental Instabilities

The understanding of fluid instabilities is critical in the understanding of transitional turbulent flows. This is where the flow field has an initially small perturbation, which grows to form a large feature. This large feature can then combine non-linearly with the flow field around it to generate a fully turbulent flow. In this subsection, fundamental theory regarding the early and late time growth for single and multimode perturbations in the Kelvin-Helmholtz and Richtmyer-Meshkov instabilities will be summarised. This gives an insight into the dominant flow mechanisms at early times, which can potentially persist for a considerable period of time after the transition to turbulent flow.

2.1.1 Kelvin Helmholtz and Rayleigh Taylor

The classical analysis of the Kelvin-Helmholtz (KH) instability considers an incompressible, inviscid shear layer [105]. As the linear analysis is the same, Rayleigh Taylor instabilities is also considered by including gravitational forces [50]. Figure 2.1 shows the schematic for the instability. Essentially, two parallel flows are given an infinitesimal perturbation which can be decomposed into separate modes. The stability of each mode is analysed to find out if it grows in amplitude, shrinks, or remains stable. The instabilities are centred around the points at the vortex sheet where the fluid is in compression, as indicated in Figure 2.1.

Consider initial conditions as shown in Figure 2.1, where gravity g is chosen to act in the z direction. By treating the fluid as irrotational, the analysis employs the concept of a velocity potential where $\nabla\Phi = u$ such that $\nabla^2\Phi_1 = \nabla^2\Phi_2 = 0$. The initial pressure is given as $p = p_0 - \rho_1 gz$ for $z \leq 0$ and $p = p_0 - \rho_2 gz$ for $z \geq 0$. A normal mode analysis consists of decomposing the perturbation into a series of linearly independent modes of the form

$$\mathcal{S} = \mathcal{S}^* \exp^{I(k_x x + k_y y) + st}, \tag{2.1.1}$$

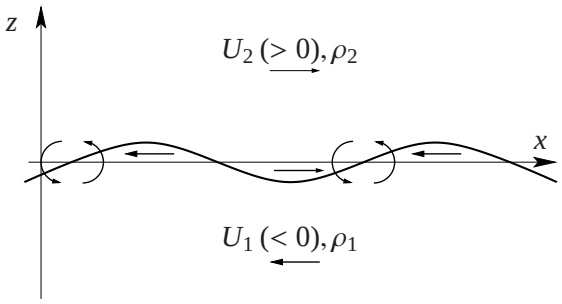

Figure 2.1: Schematic of the Kelvin-Helmholtz instability (after Drazin and Reid [50])

where $\mathcal{S}$ is the shape of the initial interface, $\mathcal{S}^*$ is the magnitude of the initial interface perturbation, k_x and k_y are wavenumbers of the perturbation in the x and y direction, and total wavenumber is $k = \sqrt{k_x^2 + k_y^2}$. If the mode is unstable (i.e. grows in time) then s will have a positive real component, if stable s will have a negative real component. The solution to this instability (see Drazin and Reid for full analysis [50]) is given by two modes:

$$s = -Ik_x \frac{\rho_1 U_1 + \rho_2 U_2}{\rho_1 + \rho_2} \pm \left(\frac{k_x^2 \rho_1 \rho_2 (U_1 - U_2)^2}{(\rho_1 + \rho_2)^2} - \frac{kg(\rho_1 - \rho_2)}{\rho_1 + \rho_2} \right)^{1/2} \tag{2.1.2}$$

Thus the interface is stable if $kg(\rho_1^2 - \rho_2^2) \geq k_x^2 \rho_1 \rho_2 (U_1 - U_2)^2$, and one mode is stable and the other unstable if $kg(\rho_1^2 - \rho_2^2) < k_x^2 \rho_1 \rho_2 (U_1 - U_2)^2$ Consider simple shear where $g = 0$

$$s = -Ik_x \frac{\rho_1 U_1 + \rho_2 U_2}{\rho_1 + \rho_2} \pm \frac{k_x \sqrt{\rho_1 \rho_2}(U_1 - U_2)}{(\rho_1 + \rho_2)}, \tag{2.1.3}$$

demonstrating that in KH the flow is unstable at all wavelengths, where the modes grow proportional to the wavenumber, i.e. small wavelengths grow much faster. A further simplification is gained by setting $\rho_1 = \rho_2, U_1 \neq U_2$,

$$s = -\frac{1}{2} Ik_x (U_1 + U_2) \pm \frac{1}{2} k_x (U_1 - U_2). \tag{2.1.4}$$

If waves of random orientation are within a mixing layer, the waves orientated to the direction of flow (wavenumber k_x) will grow most rapidly. The Rayleigh-Taylor (RT) instability is defined as $U_1 = U_2 = 0$, giving,

$$s = \pm \left(\frac{kg(\rho_2 - \rho_1)}{\rho_1 + \rho_2} \right)^{1/2}, \tag{2.1.5}$$

showing that the interface is unstable only if the acceleration g points from the lighter to the denser fluid. In reality, both the RT and KH instabilities occur over a range

of wavenumbers at the same time, each wavenumber growing at a different rate according to it's respective stability criterion. In addition, these modes travel at a phase velocity and hence will interact to produce additional modes which also grow, the flow becoming rapidly more and more complex.

As each mode reaches an amplitude comparable to it's wavelength, the perturbation no longer grows at an exponential rate, and saturates. It was proposed by Youngs [194] that the growth follows three stages. First there is exponential growth of the small wavelengths. As the amplitude reaches the wavelength of the mode, the short waves saturate, and the growth slows. These then get overtaken by the longer waves which are still growing exponentially (bubble competition). Finally, a self-similar mixing region is formed, where the late time growth can be described by scaling arguments which will be discussed further in Section 2.3.

2.1.2 Richtmyer Meshkov

Richtmyer-Meshkov instabilities [155, 134] can be understood as the impulsive limit of the Rayleigh-Taylor instability, where the interface acceleration occurs impulsively as a result of a shock wave or a very rapid acceleration. This is often referred to as baroclinic deposition of vorticity on the interface. The analysis considers the flow schematic in Figure 2.2 where the flow is at rest, with an initial sinusoidal perturbations between two fluids of density ρ_1 and ρ_2.

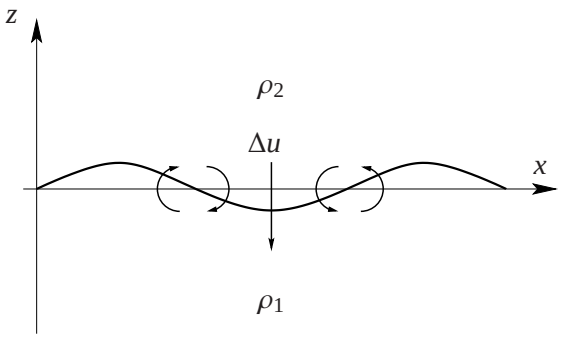

Figure 2.2: Schematic of the Richtmyer Meshkov instability

Beginning with the expression for the growth rate of the RT instability in Equation (2.1.5), it can be noted that the growth or decay of the interface amplitude A can be described by

$$\frac{d^2A(t)}{dt^2} = kg(t)A(t)\frac{\rho_2 - \rho_1}{\rho_1 + \rho_2} \tag{2.1.6}$$

If it is assumed that the acceleration $g(t)$ is very large and occurs over a very short period of time then the increment of velocity, Δu, imparted by this acceleration can be defined as $\Delta u = \int g(t)dt$. As the impulse occurs rapidly, Equation (2.1.6) can be integrated holding all parameters constant except for the acceleration, giving

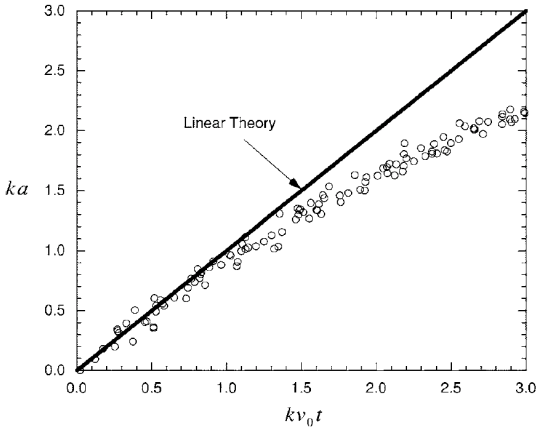

Figure 2.3: Experimentally measured early time growth rate compared to linear theory [30]

$$\frac{dA}{dt} = k\Delta u A_0 \frac{\rho_2 - \rho_1}{\rho_1 + \rho_2}, \tag{2.1.7}$$

thus giving the linear growth rate for an instability of wavenumber k. It is unstable for all impulses regardless of direction of the acceleration. This demonstrates that the amplitude of the mixing layer grows linearly in time (as opposed to RT and KH which are both exponential), proportional to the wavenumber k and the Atwood number At, defined as

$$At = \frac{\rho_2 - \rho_1}{\rho_1 + \rho_2}. \tag{2.1.8}$$

This relationship has been tested by Chapman and Jacobs [30] by measuring the growth of single mode three-dimensional bubbles at $At = 0.15$, and results in Figure 2.3 demonstrate good applicability of linear growth up to $kA \approx 1$. Similar results have been gained for shock-induced two dimensional perturbations by Collins and Jacobs [40], and for strong radiative driven shocks (shock Mach $M_S > 10$) by Holmes *et al.* [84]. When modelling the passage of a shock wave the densities change as compression occurs. Equation (2.1.7) is typically most accurate when the post-shock amplitude and densities are employed, where the post-shock amplitude can be computed by taking the initial amplitude and multiplying by the mean compression rate,

$$\frac{(\rho_1 + \rho_2)^-}{(\rho_1 + \rho_2)^+}. \tag{2.1.9}$$

Again, the growth of the initial instability is only valid until the amplitude of the wave reaches the same magnitude as the wavelength, after which a more complex non-linear or dimensional scaling analysis is required. At late time the interface is composed of ‘bubbles’, where the lighter fluid penetrates into the heavier fluid, and ‘spikes’, where the heavier fluid penetrates into the lighter fluid. The sinusoidal shape usually

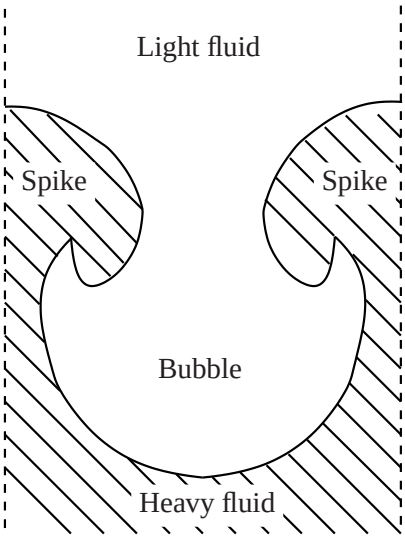

Figure 2.4: Non-linear RM development and terminology

becomes mushroom shaped due to Kelvin-Helmholtz instabilities along the interface. This configuration is illustrated in Figure 2.4.

2.2 Homogeneous Turbulence

Turbulence is an incredibly complex phenomena characterised by extremely chaotic motion, complex interactions between vastly different sized vortices, and intermittent viscous dissipation of kinetic energy at the small scales. This section describes qualitatively and quantitatively this phenomenology, summarising key theoretical and experimental results as regards turbulent length scales, dynamic behaviour, and extensions to anisotropic flows. The full derivations from first principles of material in this section can be found in any one of several well known texts and is summarised for the sake of brevity. An interested reader can consult any of [44, 82, 148, 178, 119, 14] for further details.

2.2.1 Turbulent Length Scales

Figure 2.5 shows a typical distribution of turbulent kinetic energy over the different scales in wave number space. Considering the case of high turbulent Reynolds numbers the energy spectrum can be split up into three main regimes. At the large scales (low wavenumbers) the eddies are typically problem dependent, usually formed by an external generating mechanism (a fundamental instability, or wing, for example), and are characterised by the integral length scale ℓ. At the very high end of the wavenumber scale there is the dissipative range. At this scale the turbulent kinetic energy passed from the large scales is dissipated by the action of viscosity. This occurs at the Kol-

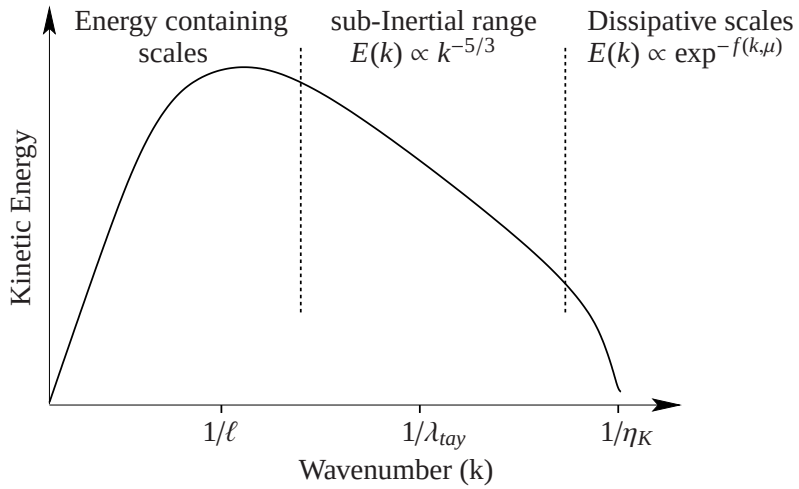

Figure 2.5: A schematic of a typical turbulent kinetic energy spectrum for homogeneous turbulence plotted with logarithmic scales

mogorov length scale, denoted by η_K [110, 111]. Given a large enough Reynolds number, there exists a range between the Integral and Kolmogorov length scale where the flow is independent of both viscous forces and the mechanism which is injecting energy at the large scales. This is called the sub-inertial range, in which the Taylor microscale [177], λ_{tay}, typically lies. The cascade of energy from the large scales through to the small scales was famously described in a short poem by L.F. Richardson,

> Big whirls have little whirls,
> which feed on their velocity.
> Little whirls have lesser whirls,
> and so on to viscosity.

The relative sizes of the various length scales are determined by consideration of the nature of the flow field. The integral length scale is chosen as the scale which reflects the averaged distance over which the turbulent motion is correlated, which is typically the size of the largest energy containing vortices. Define the velocity correlation function and the longitudinal correlation function as

$$\mathbf{Q}_{ij} = \overline{u_i(\mathbf{x})u_j(\mathbf{x}+\mathbf{r})}, \qquad \mathbf{f} = \frac{\overline{u_1(x_1)u_1(x_1+r)}}{u_{rms}^2} \tag{2.2.1}$$

where u_i is the turbulent velocity in the i direction, $\overline{(.)}$ indicates an ensemble average, and u_{rms} is the root mean square turbulent velocity. The integral length scale is defined as

$$\ell = \int_0^\infty f(r)dr, \tag{2.2.2}$$

alternatively with the assumption of isotropy the following relations can be employed in spectral space

$$\ell = \frac{\pi}{2u_{rms}^2}\int_0^{k_{max}} k^{-1}E(k)dk = \frac{\pi}{2u_{rms}^2}\,E_{1D}|_{k=0} = \frac{\pi}{u_{rms}^2}\,E_{11}|_{k=0} = \frac{2\pi}{u_{rms}^2}\,E_{22}|_{k=0}\,. \quad (2.2.3)$$

where E, E_{1D}, E_{11}, E_{22} are the three dimensional, one dimensional, longitudinal and transverse turbulent energy spectra respectively, which will be defined later in this section. The Taylor microscale λ_{tay} is the length scale typically used to define the Reynolds number of a turbulent flow. It is defined from the expansion of the longitudinal correlation function f about the $r = 0$ axis

$$f(r) = 1 - \frac{r^2}{2\lambda_{tay}^2} + ..., \quad (2.2.4)$$

however it is more commonly calculated from one of the following relations [44]

$$\lambda_{tay,i}^2 = \frac{\overline{u_i^2}}{\overline{(\partial u_i/\partial x_i)^2}} = \frac{15\nu_{vis}\overline{u_i^2}}{\epsilon} = \frac{15\overline{u_i^2}}{\overline{\omega^2}}, \quad (2.2.5)$$

where ω is the vorticity. The Kolmogorov microscale is defined as the length scale at which viscous forces become dominant, thus where the Reynolds number of the vortices is one, and where the form of the flow is dependent only on the transfer of energy from the large scales and viscosity ν_{vis}. If the smallest eddies are assumed to have $Re = u\eta_K/\nu_{vis} \approx 1$, and the velocity u is related to the dissipation rate ϵ via $u \propto (\nu_{vis}\epsilon)^{1/4}$, then

$$\eta_K = (\nu_{vis}^3/\epsilon)^{1/4}. \quad (2.2.6)$$

With the additional assumption of isotropy, this can be computed in several different ways depending on the definition of the dissipation rate ϵ which could be any of

$$\epsilon = 15\nu_{vis}\overline{(\partial u_i/\partial x_i)^2} = \nu_{vis}\overline{\omega^2} = 2\nu_{vis}\int_0^\infty k^2E(k)dk. \quad (2.2.7)$$

The length scales are connected to each other through the Reynolds number, which provide approximate relations of the form

$$\frac{\lambda_{tay}}{\ell} \approx \sqrt{15}Re^{-1/2}, \qquad \frac{\eta_K}{\ell} \approx Re^{-3/4}. \quad (2.2.8)$$

It is important to note that many of these relations rely on a relatively simple dimensional observation that

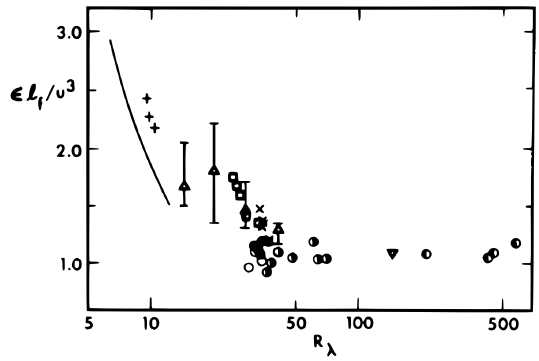

Figure 2.6: Scaling of the dissipation rate measured behind a square mesh grid [174]

$$\epsilon \approx \frac{C u_{rms}^3}{\ell}, \tag{2.2.9}$$

where C is a constant of order 1. This is similar to stating that the typical large scale eddies break down in a single eddy turnover time u_{rms}/ℓ. As the turbulence is assumed to be stationary, then the rate at which energy enters the turbulent spectrum equals the dissipation rate. Figure 2.6 shows a compilation of experimental results by Sreenivasan [174] demonstrating that this relationship holds well for $Re_{\lambda_{tay}} > 100$.

2.2.2 Kolmogorov Scaling

Given that $Re_{\lambda_{tay}} > 100$ there exists sufficient separation between the large and small scales that the vortices are independent of the mechanism generating energy, and the viscous forces dissipating it. The separation from the large scales is required such that it can be assumed that the eddies are homogeneous and isotropic. The physics of this range were first investigated in physical space by Kolmogorov [110, 111] employing the velocity structure function, defined as

$$\overline{\Delta v^p} = \overline{[u(x + \Delta x) - u(x)]^p}, \tag{2.2.10}$$

where p is a positive integer. Assuming that there is a homogeneous, isotropic turbulent field then the velocity structure function can only be a function of separation distance r and dissipation rate (=energy transfer rate) ϵ. The only possible relation dimensionally is [110]

$$\overline{\Delta v^p} = \beta_p \epsilon^{p/3} r^{p/3}, \tag{2.2.11}$$

where β_p is the Kolmogorov constant. Setting $p = 2$ gives the two-thirds law, and possibly more importantly setting $p = 3$ gives the four-fifths law which is believed to be exact even assuming turbulent intermittency, where $\beta_3 = -4/5$ [111]. Experimentally,

it has been shown to be valid for Taylor Reynolds numbers greater than 1000 and when the length scale r lies within the inertial range [139].

As much analysis of the turbulent flow field is conducted in Fourier space, it is useful to derive the turbulent kinetic energy spectrum. Firstly, the second order correlation $\mathbf{Q}_{ij}$ is used to give the spectrum tensor $\phi_{ij}(\mathbf{k})$

$$\phi_{ij}(\mathbf{k}) = \frac{1}{(2\pi)^3} \int_{-\infty}^{\infty} \mathbf{Q}_{ij}(\mathbf{r}) \exp^{-I\mathbf{kr}} d\mathbf{r}, \tag{2.2.12}$$

$$\mathbf{Q}_{ij}(\mathbf{r}) = \int_{-\infty}^{\infty} \phi_{ij}(\mathbf{k}) \exp^{I\mathbf{kr}} d\mathbf{k}. \tag{2.2.13}$$

Now if $r = 0$, Equation (2.2.13) simplifies to

$$\frac{1}{2}\overline{u_i u_i} = \frac{1}{2} \int_{-\infty}^{\infty} \phi_{ii}(\mathbf{k}) d\mathbf{k}. \tag{2.2.14}$$

This is essentially a volume integral. In isotropic homogeneous flows, spherical symmetry can be assumed. The integral over the vector $\mathbf{k}$ can be replaced by an integral in spherical co-ordinates using the magnitude of the wave vector $k = \sqrt{k_x^2 + k_y^2 + k_z^2}$

$$\frac{1}{2} \int_{-\infty}^{\infty} \phi_{ii}(\mathbf{k}) d\mathbf{k} = \frac{1}{2} \int_{-\infty}^{\infty} 4\pi k^2 \phi_{ii}(k) dk. \tag{2.2.15}$$

The definition of the three dimensional energy spectrum is

$$\int_0^{\infty} E(k) dk = \frac{1}{2}\overline{u_i u_i}, \tag{2.2.16}$$

giving,

$$E(k) = 2\pi k^2 \phi_{ii}(k). \tag{2.2.17}$$

Via dimensional analysis similar to that used to gain Equation (2.2.11) the form of the energy spectrum in the sub-inertial range under the given assumptions must be

$$E(k) = C_k \epsilon^{2/3} k^{-5/3}, \tag{2.2.18}$$

where C_k is the Kolmogorov constant in wavenumber space. A further implication of Kolmogorov scaling is that the scaled turbulent kinetic energy spectrum,

$$\frac{E_{11}(k)}{(\epsilon \nu_{vis}^5)^{1/4}}, \tag{2.2.19}$$

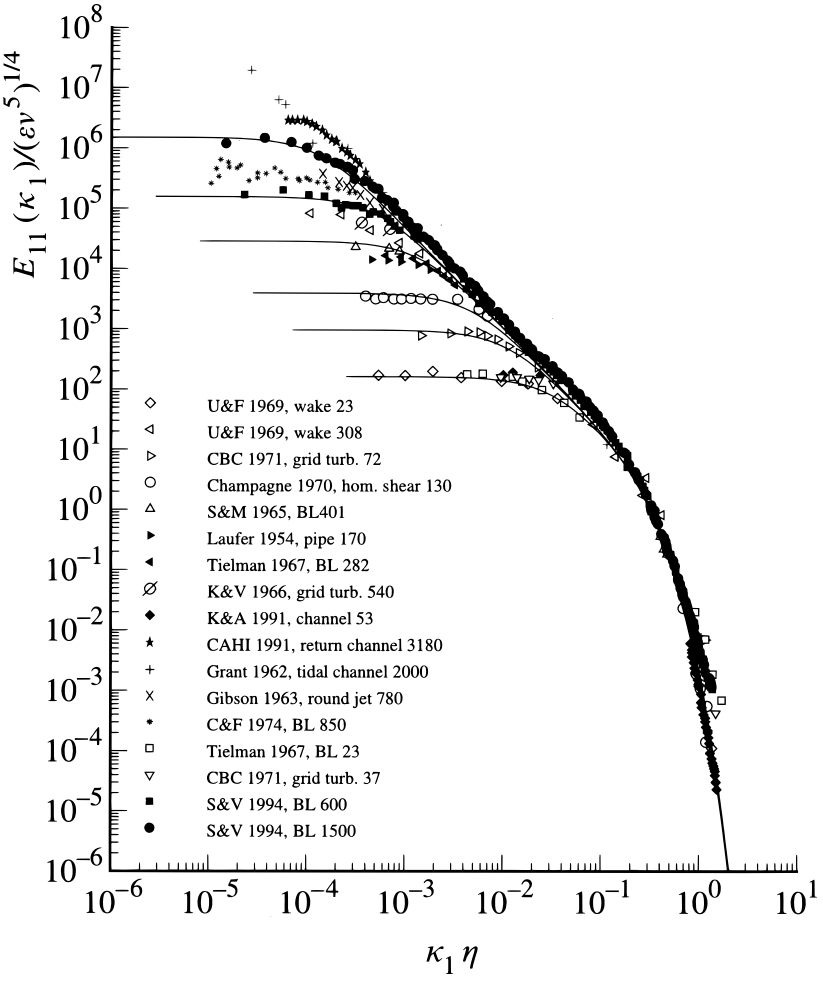

Figure 2.7: Experimental measurements of E_{11} (symbols). Experimental data is from [158], figure reproduced from [148].

should be universal when plotted against $k\eta_K$. E_{11} is the one-dimensional turbulent kinetic energy spectrum which is typically measured in experiments, defined as the square of the Fourier transform of the velocity component in the 1 direction [44, 178],

$$E_{11}(k_1) = \frac{1}{2\pi}\left|\int_{-\infty}^{\infty} u_1(x_1)\exp^{-Ik_1x_1}\,dx_1\right|^2. \tag{2.2.20}$$

Figure 2.7 summarises experimental data from [158] showing E_{1D} for various flow types and at various $Re_{\lambda_{tay}}$. It lends great encouragement that under-resolved simulations of turbulent flows with models for the unresolved components could be applied to many different flow regimes. The one dimensional turbulent kinetic energy spectrum allows experimental measurement of the one dimensional Kolmogorov constant $C_{k,11}$ which is related to Kolmogorov constant via

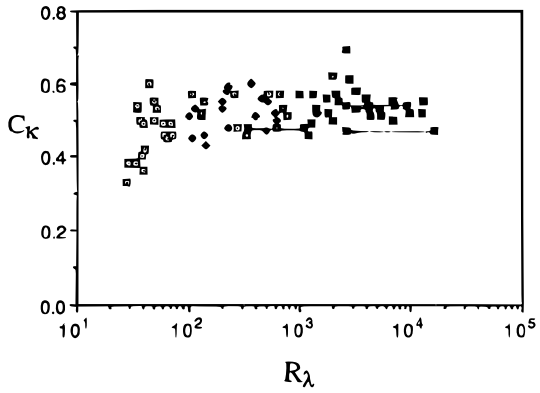

Figure 2.8: The one dimensional Kolmogorov constant $C_{k,11}$ (labelled C_k by [175]) plotted against $Re_{\lambda_{tay}}$ for a variety of flows

$$C_{k,11} = \frac{18}{55} C_k. \tag{2.2.21}$$

This has been measured in several experiments using grid generated turbulence, and the results were collated by Sreenivasan [175], reproduced in Figure 2.8. At present there is little evidence for a Reynolds number dependence of C_k, and the data gives a mean value of $C_{k,11} = 0.53 \pm 0.055$, or $C_k \approx 1.6$, if data for $Re_{\lambda_{tay}} < 50$ is discarded [175, 100, 158, 140, 29].

2.2.3 The Decay of Homogeneous Turbulence

The crucial component of a simulation of turbulence is that it can predict certain fundamental properties of the real turbulent flow. There are two principal properties which will be discussed extensively throughout this work; the rate of decay of turbulent kinetic energy, and related to this the rate of growth of the dominant length scales. It is through consideration of the dissipation rate of kinetic energy that many semi-empirical formulas define growth rates of turbulent mixing layers.

To examine the decay of homogeneous turbulence it is necessary to describe the Karman-Howarth equation, which governs the evolution of turbulent kinetic energy. It forms the basis of the theoretical analysis of isotropic, homogeneous turbulence. Next, there is a brief introduction to the Loitsyanskii and Birkhoff invariants, which are further assumptions used to close the resultant set of equations. These determine the behaviour of decaying homogeneous, isotropic turbulence governed by the Karman-Howarth equation. The work by Oberlack [144] is briefly summarised which uses group theory to determine the growth rate of the integral length scales, and the decay rate of turbulence kinetic energy under the two principle invariants. These results are discussed in relation to recent experimental and numerical simulations.

Together this forms a theoretical and experimental guide to the expected behaviour of

turbulence generated through numerical simulations.

The Karman-Howarth Equation

This brief derivation follows the methodology in [82] and [124]. The evolution in time of $\overline{(u_i)_A (u_j)_B}$, where A and B are two points separated in space, can be written as

$$\frac{\partial}{\partial t}\overline{(u_i)_A (u_j)_B} = \overline{(u_i)_A \frac{\partial}{\partial t}(u_j)_B} + \overline{(u_j)_B \frac{\partial}{\partial t}(u_i)_A}. \tag{2.2.22}$$

The equation for u_i at the point A reads:

$$\frac{\partial}{\partial t}(u_i) + \left(\overline{U_k} + u_k\right)\frac{\partial u_i}{\partial x_k} = -\frac{1}{\rho}\frac{\partial p}{\partial x_i} + \nu_{vis}\frac{\partial^2}{\partial x_k \partial x_k}(u_i). \tag{2.2.23}$$

where $\overline{U_k}$ is the mean flow velocity. Multiplying this equation by $(u_j)_B$, and the corresponding equation for $(u_j)_B$ by $(u_i)_A$ yields an evolution equation for the second order velocity correlation. In addition, a co-ordinate system is chosen where $\xi_k = (x_k)_B - (x_k)_A$ as the exact location of A and B does not matter. Taking the assumption that the flow is isotropic and incompressible then the pressure-velocity correlations are zero, this gives

$$\frac{\partial}{\partial t}\left(\mathbf{Q}_{i,j}\right)_{A,B} - \frac{\partial}{\partial \xi_k}\left[\left(\mathbf{S}*_{ik,j}\right)_{A,B} + \left(\mathbf{S}*_{i,kj}\right)_{A,B}\right] = 2\nu_{vis}\frac{\partial^2}{\partial \xi_k \partial \xi_k}\left(\mathbf{Q}_{i,j}\right)_{A,B}. \tag{2.2.24}$$

The second term on the left hand side is a second order tensor, which is labelled $\mathbf{S}_{i,j}$. Dropping the A,B notation

$$\frac{\partial}{\partial t}\mathbf{Q}_{i,j} - \mathbf{S}_{i,j} = 2\nu_{vis}\frac{\partial^2}{\partial \xi_k \partial \xi_k}\mathbf{Q}_{i,j}. \tag{2.2.25}$$

In the case of incompressible flow, an isotropic tensor of the third order can be expressed in terms of one scalar. As the diagonal terms are of prime interest, i.e. $\mathbf{S}_{i,i}$, then, after applying a contraction and noting that $\delta_{ii} = 3$, and $\xi_i \xi_i = r^2$, Equation (2.2.25) becomes

$$\frac{\partial}{\partial t}\mathbf{Q}_{i,i}(r,t) - \mathbf{S}_{i,i}(r,t) = 2\nu_{vis}\frac{1}{r^2}\frac{\partial}{\partial r}r^2\frac{\partial}{\partial r}\mathbf{Q}_{i,i}(r,t). \tag{2.2.26}$$

For isentropic, incompressible flows the velocity correlation functions can be simplified significantly, and the above equation can be written in terms of the second and third order correlation functions f and κ_3

$$\frac{\partial}{\partial t}\left(u_{rms}^2 f\right) - u_{rms}^3\frac{1}{r^4}\frac{\partial}{\partial r}\left(r^4\kappa_3\right) = 2\nu_{vis}u_{rms}^2\frac{1}{r^4}\frac{\partial}{\partial r}\left(r^4\frac{\partial f}{\partial r}\right), \tag{2.2.27}$$

$$\kappa_3(r,t) = \frac{\overline{\left(u_1^2\right)_A (u_1)_B}}{u_{rms}^3}. \tag{2.2.28}$$

This is the Karman-Howarth equation for homogeneous isotropic turbulence [101]. In Fourier space:

$$\frac{\partial}{\partial t}\int_0^k E(k,t)dk = \int_0^k F(k,t)dk - 2\upsilon\int_0^k k^2 E(k,t)dk + H_k(k,t), \tag{2.2.29}$$

$$F(k,t) = 2\pi k^2 F_{i,i}(k,t) = \frac{1}{\pi}\int_0^\infty kr\sin(kr)S_{i,i}(r,t)dr, \tag{2.2.30}$$

$$\mathbf{E}(k,t) = \frac{1}{\pi}\int_0^\infty kr\sin(kr)\mathbf{Q}_{i,i}(r,t)dr, \tag{2.2.31}$$

where S is the third order correlation tensor at locations A and B, $H(k,t)$ is the energy supplied to the turbulent flow as a function of wavenumber. $F(k,t)$ is often called the 'energy transfer spectrum function', as this gives the contribution from inertial transfer of energy from different wave numbers to the total energy.

Loitsyanskii and Birkhoff Invariants

These two invariants form the heart of two different descriptions of decay of a homogeneous isotropic turbulent field, giving additional conditions which constrain the solution to a certain form. They arise through consideration of the behaviour of the system as r tends to infinity, or as the wave number k tends to zero. By taking the second moment of the Karman-Howarth equation it can be shown by invoking continuity for an incompressible fluid that the rate of decay of $\mathbf{Q}_{i,i}$ must be at least faster then r^{-n} with $n > 1$. Taking the fourth moment gives:

$$\frac{\partial}{\partial t}\left(u_{rms}^2\int_0^\infty r^4 f\right)dr - \left(u_{rms}^3 r^4 k\right)\Big|_0^\infty = 2\nu_{vis}u_{rms}^2\left(r^4\frac{\partial f(r,t)}{\partial r}\right)\Big|_0^\infty. \tag{2.2.32}$$

It can be shown that under the assumption of isotropy and homogeneity, the second term on the left hand side, and the term on the right hand side equal zero. Integrating with respect to time gives the Loitsyanskii invariant:

$$u_{rms}^2\int_0^\infty r^4 f dr = I_1. \tag{2.2.33}$$

However, Proudman and Reid [152] showed by assuming a certain distribution of the turbulent field that the assumption regarding the decrease of the third order velocity correlations as r tends to infinity does not hold, implying that the Loitsyanskii invariant varies during the decay process. This was shown to be true in a later paper by Batchelor and Proudman [15]. In the final stage of decay the third order correlations

can be neglected as compared to the effects of the viscous forces, thus the Loitsyanskii invariant becomes constant.

Birkhoff [21] demonstrated that the energy spectrum need not be proportional to k^4 as k tends to zero, but that the leading order term can be of order k^2. He also pointed out that there is no reason for an initial energy spectrum to tend towards a k^4 structure unless it is initially designed to do so. He also noted that this implies the divergence of the Loitsyanskii invariant, but proposed that

$$\int_0^\infty r^2 \mathbf{Q}_{i,i}(r,t)dr = u_{rms}^2 \lim_{r\to\infty} r^3 f(r,t) = I_2, \tag{2.2.34}$$

is an invariant, thus called the Birkhoff invariant. It is also called the Saffman invariant, after Saffman who considered the production of homogeneous turbulence via a set of random impulsive forces with convergent integral moments of cumulants. Through this consideration he arrived at the same conclusion as Birkhoff, demonstrating that the energy spectrum is of the order k^2 if the force is solenoidal and not bounded with increase in volume.

Decay Rates

In this section the decay rates present in large Reynolds number turbulence is examined, i.e. where the viscous terms in Equation (2.2.27) can be neglected, and then the decay rates during the final period of decay when viscous effects are dominant. The traditional approach to determining decay rates is outlined in [82], where it is assumed that turbulence decays self-similarly. Utilising the Taylor microscale as defined in Equation (2.2.4), the behaviour of the Karman-Howarth equations as r tends to zero can now be examined. At $O(r^2)$ the equation reduces to:

$$\frac{\partial}{\partial t}\left[u_{rms}^2\left(1-\frac{1}{2}\frac{r^2}{\lambda_{tay}^2}\right)\right] = 2\nu_{vis}u_{rms}^2\frac{1}{r^4}\frac{\partial}{\partial r}\left(r^4\frac{\partial}{\partial r}\left(1-\frac{1}{2}\frac{r^2}{\lambda_{tay}^2}\right)\right) + O(r^2) + ... \tag{2.2.35}$$

Differentiating, and removing the second term in the time derivative as it is second order in r,

$$\frac{3}{2}\frac{\partial}{\partial t}\left(u_{rms}^2\right) = \frac{15\nu_{vis}u_{rms}^2}{\lambda_{tay}^2} + O(r^2) + ... \tag{2.2.36}$$

However, this equation cannot be solved analytically without further assumptions, as both u_{rms}^2 and λ_{tay} depend on t. It is clear from this equation that the turbulent kinetic energy dissipation rate ϵ is:

$$\epsilon = -\frac{3}{2}\frac{\partial}{\partial t}\left(u_{rms}^2\right) = \frac{15\nu_{vis}u_{rms}^2}{\lambda_{tay}^2}. \tag{2.2.37}$$

Now, assume that $f(r,t)$ and $\kappa_3(r,t)$ are functions of $\psi = r/L$ only, where L is some length scale which is a function of time only. Substituting this into the Karman-Howarth equation,and replacing $\frac{\partial}{\partial t}\left(u_{rms}^2\right)$ using Equation (2.2.36), gives an ordinary differential equation for $\mathbf{f}(\psi)$,

$$10f + \frac{\lambda_{tay}^2}{\nu_{vis}}\frac{1}{L}\frac{dL}{dt}\psi\frac{df}{d\psi} + \frac{u_{rms}}{\nu_{vis}}\frac{\lambda_{tay}^2}{L}\frac{1}{\psi^4}\frac{d}{d\psi}\left(\psi^4\kappa_3\right) + 2\frac{\lambda_{tay}^2}{L^2}\frac{1}{\psi^4}\frac{d}{d\psi}\left(\psi^4\frac{df}{d\psi}\right). \tag{2.2.38}$$

This can only be solved if the coefficients are proportional to each other - or if we can neglect one of the terms. For example as $Re \to \infty$ we can neglect the constraint $\frac{\lambda_{tay}}{L} = const.$. It is reasonable to assume that the decay is self-similar to the energy containing eddies, thus the integral length scale $\ell(t)$ is chosen for L, defined as:

$$\ell(t) = \int_0^\infty f(r,t)dr. \tag{2.2.39}$$

This, together with the assumption of $Re \to \infty$ leads to the following conditions:

$$\frac{u_{rms}}{\nu_{vis}}\frac{\lambda_{tay}^2}{\ell} = const., \quad \frac{\lambda_{tay}^2}{\nu_{vis}}\frac{1}{\ell}\frac{d\ell}{dt} = const. \tag{2.2.40}$$

In the case of invariance of Loitsyanskii's integral the following relation can be added:

$$u_{rms}^2\ell^5 = const. \tag{2.2.41}$$

Combining this constraints gives the following decay rates:

$$u_{rms}^2 \propto (At+B)^{-10/7}, \quad \ell \propto (At+B)^{2/7}, \quad \lambda_{tay}^2 \propto \frac{25\nu_{vis}}{3}\left(t + \frac{B}{A}\right). \tag{2.2.42}$$

This solution was already recognised by Kolmogorov [110]. Next, for Birkhoff's invariant:

$$u_{rms}^2\ell^3 = const. \tag{2.2.43}$$

Leading to:

$$u_{rms}^2 \propto (At+B)^{-6/5}, \quad \ell \propto (At+B)^{2/5}, \quad \lambda_{tay}^2 \propto 7\nu_{vis}(t + \frac{B}{A}). \tag{2.2.44}$$

Oberlack [144] approached this solution method in a new way using group theory. Given the following scaling invariants under a certain choice of scaling group:

$$\hat{r} = \frac{r}{t^{\frac{2}{\sigma+3}}}, \quad \hat{f} = \frac{u_{rms}^2 f}{t^{-2\frac{\sigma+1}{\sigma+3}}}, \quad \hat{\kappa_3} = \frac{u_{rms}^3\kappa_3}{t^{-3\frac{\sigma+1}{\sigma+3}}}. \tag{2.2.45}$$

For $Re \to \infty$ this gives:

$$\lim_{r\to\infty} f(r) \approx r^{-\sigma}, \quad \text{or} \quad \lim_{k\to 0} \mathbf{E}(k) \approx k^{\sigma}. \tag{2.2.46}$$

Returning to Equation (2.2.39) and substituting from Equations (2.2.45):

$$\ell(t) \propto t^{\frac{2}{\sigma+3}}, \quad u_{rms}^2 \propto t^{-2\frac{\sigma+1}{\sigma+3}}. \tag{2.2.47}$$

Invariance of Loitsyanskii's integral implies that $\sigma = 4$, and Birkhoff's integral implies that $\sigma = 2$, thus recovering the initial solutions in Equations (2.2.42) and (2.2.44). In addition, Oberlack considers the case where the integral length scale is constant, i.e. it is constrained. In this case $\ell = const.$ thus $\sigma = \infty$, yielding:

$$u_{rms}^2 \propto t^{-2}, \quad \lambda_{tay} \propto t^{1/2}. \tag{2.2.48}$$

This decay rate has already been determined by Taylor [177] by assuming that the work done by the large eddies corresponds to the dissipation rate, i.e. that $\epsilon = Au_{rms}^3/\ell = \partial u_{rms}^2/\partial t$. In addition, there is one case that is fully consistent with all of the constraints given in Equation (2.2.38) without neglecting viscous terms:

$$u_{rms}^2 \propto t^{-1}, \quad \lambda_{tay} \approx \ell \propto t^{1/2}. \tag{2.2.49}$$

This is the case of complete self preservation of the correlation functions with decay in time. Interestingly, Oberlack concludes that only the conservation of energy determines σ, and demonstrates that Birkhoff's integral in the limit of infinite Reynolds number is in agreement with this. In the final stages of decay the interactions between different sized eddies becomes negligible compared to the direct effects of viscosity. Note that in this regime the Loitsyanskii integral is an exact invariant with respect to time. Thus the Karman-Howarth equation is reduced to:

$$\frac{\partial}{\partial t}\mathbf{Q}_{i,i}(r,t) = 2\nu_{vis}\frac{1}{r^2}\frac{\partial}{\partial r}r^2\frac{\partial}{\partial r}\mathbf{Q}_{i,i}(r,t)\,. \tag{2.2.50}$$

The general solution after application of the invariance of Loitsyanskii's integral is:

$$\mathbf{Q}_{i,i}(r,t) = -4At^{-\frac{5}{2}}\left(3 - \frac{r^2}{4\nu_{vis}t}\right)\exp\left(\frac{-r^2}{8\nu_{vis}t}\right), \tag{2.2.51}$$

$$u_{rms}^2 \propto t^{-\frac{5}{2}}. \tag{2.2.52}$$

After application of Birkhoff's integral:

$$u_{rms}^2 \propto t^{-\frac{3}{2}}. \tag{2.2.53}$$

Table 2.1: Turbulence decay rates - Note that in addition to the listed assumptions, both models only apply to homogeneous, isotropic incompressible turbulence

Invariant	Loitsyanskii			Birkhoff		
Property	u_{rms}^2	ℓ	λ_{tay}	u_{rms}^2	ℓ	λ_{tay}
Decay $Re \to \infty$	-10/7	2/7	1/2	-6/5	2/5	1/2
Assumptions and Implications	f, $\kappa_3 = \text{func}(r/\ell(t))$ only					
	E(k=0,t) finite and analytic. $\lim_{r\to\infty} r^4\kappa_3 = 0$ $\lim_{k\to 0} E(k,t) \propto k^4$			$\lim_{k\to 0} E(k,t) \propto k^2$		
Decay $Re \to 0$	-5/2	-	-	-3/2	-	-
Assumption	$\lim_{k\to 0} E(k,t) \propto k^4$			$\lim_{k\to 0} E(k,t) \propto k^2$		
Decay $Re \to \infty$, constrained	-2	0	1/2	-2	0	1/2
Assumption	$\ell = const.$ $\epsilon = Au_{rms}^3/\ell$					

More recent analysis using renormalisation group analysis by Yakhot and Orszag [193] gave kinetic energy decay rates of -1.47. Finally, Yakhot [192] proposed a new time dependent integral scale and integral invariant, which only holds in the upper end of the inertial range. This gives the same decay rate as with the Loitsyanskii invariant but does not have the limitations of this invariant. Table 2.1 summarises the decay exponents, and the assumptions inherent in their derivation.

Finally the decay rate can also be 'reverse engineered' from a given energy spectrum. Assuming that for small wavenumbers the energy spectrum is of the form $E(k) = Ak^m$, and above this it follows a Kolmogorov scaling $E(k) = C\epsilon^{2/3}k^{-5/3}$, this can be substituted into the simplified dynamical equation $d(u_{rms}^2)/dt = -\epsilon$ to gain the decay rate as a function of time. This method was introduced by Comte-Bellot and Corrsin [41].

To date the experimental results are not conclusive, however they appear to be favouring Birkhoff's invariant. Conclusive results are extremely hard to gain as they should be at high Reynolds number, in a very large wind tunnel (to reduce wall effects) and for a very long period of decay so that the exponent can be determined accurately. The positioning of the virtual origin of the decay (B in Equation (2.2.42) and (2.2.44)) remains a key issue, as this effects dramatically the decay exponent gained. Examining the excellent summary papers of Comte-Bellot and Corrsin [41], Mohammed and LaRue [138] and Skrbek and Stalp [169] gives mixed results. Data summarised in [41] shows a wide range of scatter, decay exponents ranging from -1.0 to -1.37. More careful results reported in [41] with the level of isotropy improved by a secondary contraction gave decay rates of -1.25 with an error of 4%. Mohammed and LaRue [138] report results at higher $Re_{\lambda_{tay}}$ of -1.3 ± 0.02. To increase the maximum Reynolds number active grids have been developed to 'stir' the flow. This leads to higher anisotropy, where the mean turbulent velocities in the streamwise direction can be up to 20% greater than

those in the cross-stream direction. Results from Mydlarski and Warhaft [140] give decay rates of -1.21.

Skrbek and Stalp [169] examine the rate of decay assuming a model spectrum in a similar manner to [41], however truncating it at a large scale to model the effects of an enclosed experiment, and at a small scale to model the effects of viscosity. They show analytically that the rate of decay should increase slowly as the Reynolds number decreases. By analysing previous data sets and new experiments in superfluid Helium they propose that Birkhoff's invariant holds true. The most recent results at $Re_{\lambda_{tay}} = 720$ have been reported by Kang *et al.* [100] where the exponent was -1.25, however in this case the integral length scale was approximately one quarter the size of the wind tunnel.

2.3 Shock-Induced Turbulent Mixing Zones

The assumption that the turbulent flow is isotropic and homogeneous allows considerable simplification of the governing equations, as can be seen in the derivation of the Karman-Howarth equation. Without this simplification the analysis becomes intractable in the majority of cases. Headway is typically made by assuming that the flow develops in a self-similar manner, that is that the same flow field at two different instants can be made to fit the same function by good choice of scaling parameters.

This concept can be illustrated for a spatially developing mixing layer. Take a reference length L which is some measure of the mean width at a fixed point in space, and reference quantity ΔU then the non-dimensional mean longitudinal velocity profile $\tilde{U} = U/\Delta U$ at several points in the development of the mixing layer collapses to the same curve when plotted against $\tilde{x} = x/L$. Furthermore, these assumptions can be inserted into the mean continuity equation, yielding a linear increase of mixing layer width with respect to space [148],

$$\frac{dL}{dx} = \mathcal{G}_{\mathcal{R}} \frac{\Delta U}{U_{mean}} \tag{2.3.1}$$

where $\mathcal{G}_{\mathcal{R}}$ is the growth rate, and U_{mean} the average of the upper and lower velocities. Considering a temporally developing self similar mixing layer in a similar manner leads to a growth rate of $\mathcal{G}_{\mathcal{R}}\Delta U$, where in both spatial and temporal layers $\mathcal{G}_{\mathcal{R}}$ is reported from 0.06 to 0.11.

It is generally assumed that the width of the turbulent mixing zone generated by a fully developed Richtmyer-Meshkov instability grows proportionally to t^{θ}, where θ is a positive number typically less than 1. Several approaches have been developed based on; the development of an isolated slab of turbulence; self similarity arguments; 'bubble competition'; and momentum-drag formulations. It should be noted that only multi-mode initial perturbations are considered. Single mode perturbations are not representative of typical initial conditions as their late time behaviour tends to be dominated

by the appearance of large, coherent structures, usually in the form of parallel vortex pairs in two dimensions [91], or vortex rings in three dimensions [30, 183].

2.3.1 Growth of a Self-similar Turbulent Zone

Barenblatt [12] discussed the case of an isolated sheet of developing turbulence. This is equivalent to assuming that the perturbations present in the initial condition have gone past the initial linear stage of growth dictated by Richtmyer's formula (Equation (2.1.7)) and become a fully turbulent mixing layer. Assuming that the flow is not deformed by a mean shear, then the evolution of turbulent kinetic energy $q_K = \overline{(u^2 + v^2 + w^2)}/2$ is governed by a balance of turbulent diffusion and dissipation into heat,

$$\frac{\partial q_K}{\partial t} = -\frac{\partial(q'_K w' + p' w'/\rho)}{\partial z} - \epsilon, \tag{2.3.2}$$

where q'_K is the turbulent energy fluctuation, w' is the turbulent fluctuation in the direction of expansion of the mixing layer, and p' is the fluctuating pressure. Assuming a turbulent energy eddy diffusion coefficient, K_q, then dimensional analysis gives

$$K_q = L\sqrt{q}_K, \qquad \epsilon = \frac{b q_K^{3/2}}{L}, \tag{2.3.3}$$

where L is a reference length scale, which can be taken as $L = Ch(t)$, where h is a measure of the width of the mixing zone, and b is a positive coefficient. Inserting these into Equation (2.3.2) gives

$$\frac{\partial q_K}{\partial t} = \frac{\partial(Ch(t)\sqrt{q}_K)}{\partial z} - \frac{b q_K^{3/2}}{Ch(t)}. \tag{2.3.4}$$

In the case where viscosity equals zero ($b = 0$) then the solution can only depend on the initial magnitude of the kinetic energy $\mathcal{K}_0 = \int_{-\delta_{tz}}^{\delta_{tz}} q_K(z,0)dz$, t, z and C. Here z is the position within the mixing zone in the direction of the expansion, and it is assumed that the initial turbulent kinetic energy profile is given as a function of z. The initial distribution of the mixing zone extend from $-\delta_{tz} \le z \le \delta_{tz}$. Dimensional analysis then gives

$$q_K = \frac{\mathcal{K}_0^{2/3} t^{-2/3} \xi_0^2 (1-\zeta^2)^2}{36C}, \qquad h(t) = \xi_0 \mathcal{K}_0^{1/3} t^{2/3}, \tag{2.3.5}$$

where the positive constant $\xi_0 = (135C^2/4)^{1/3}$, is determined from energy conservation and $\zeta = z/h(t)$. This gives an upper limit on the growth of the mixing layer. If the dissipation is finite ($b \neq 0$) then the solution is now not completely self-similar, additionally dependent on b. The asymptotic late time form now becomes $h(t) \propto t^{1-\mu}$

where $\mu \geq 1/3$. Hence the influence of turbulent viscosity is to slow the development of the mixing layer. It should be emphasised that this is under the assumption of partial self-similarity, and additionally it is assumed that the turbulence is in free decay, i.e. any influence of the initial perturbations has been forgotten.

This argument was further developed by Youngs [196] who employed the following model equations,

$$\frac{d(Lq_K)}{dt} = -bu^3, \qquad \frac{dW}{dt} = u, \text{where} \quad L = cW + d\lambda_{min}, \tag{2.3.6}$$

where the reference length L is taken as the minimum perturbation length scale λ_{min}, and b, c and d are model constants. Taking initial conditions of $W = 0$ and $u = \Delta u$ then

$$\frac{W}{\lambda_{min}} = \frac{d}{c}\left[\left(1 + \frac{c\Delta u t}{\theta d \lambda_{min}}\right)^{\theta} - 1\right], \tag{2.3.7}$$

where $\theta = 2/(3 + bc)$ again recovering $\theta = 2/3$ for the case of zero viscosity, but now including some influence of the initial conditions. Ramshaw [154] also gained $\theta = 2/3$ when dissipation is zero via a Lagrangian description of the mixing layer width.

Gauthier and Bonnet [63] extended the established $k - \epsilon$ methodology to model shock tube experiments. By analysis of the the diffusion term in the turbulent kinetic energy equation, and assuming self-similar growth, leads to a growth of the mixing layer proportional to $t^{1/3}$. Huang and Leonard [86] proposed a new self-similar decay of homogeneous turbulence which was shown to give a growth rate of $t^{1/4}$ at late times where the Reynolds number is low [150]. Mikaelian [136] used the impulsive limit of the RT instability within a model for developing turbulent kinetic energy, predicting that the mixing layer grows as $0.14\Delta u(At)t$ at late times.

More recently, Zhou [202] has applied theory developed for turbulent flows with an external agent to the RM instability. It is assumed that the energy flux through the inertial range, and the dissipation rate ϵ are the same, and that the energy flux is proportional to the typical time scale of the low wavenumber features (according to turbulence theories). For homogeneous, isotropic turbulence $\tau_{HDT} = (kU(k))^{-1} = \left(k^3 E(k)\right)^{-1/2}$. From dimensional analysis the dissipation rate is determined by

$$\epsilon = C^2 \tau(k) k^4 E^2(k). \tag{2.3.8}$$

As RM turbulence is anisotropic in the z-direction (the direction of shock propagation) then the wavenumber is chosen as $k = \sqrt{k_x^2 + k_y^2}$, i.e. a two-dimensional spectra in the plane perpendicular to shock propagation. The time scale associated with the development of the large scales is estimated from Richtmyer's linear theory, Equation (2.1.7), giving $\tau_{RM} = (k(At)\Delta u)^{-1}$. Substituting this into Equation (2.3.8) gives

$$E(k) = C\,[(At)\Delta u\epsilon(z)]^{1/2}\,k^{-3/2}. \tag{2.3.9}$$

A key observation made by Zhou is that when $\tau_{RM} << \tau_{HDT}$ then the spectra should take the form above, else the turbulence will become fully developed and revert to a Kolmogorov form. Next the growth rate of the mixing layer is determined using a similar approach to that described by Comte-Bellot and Corrsin [41] for homogeneous isotropic turbulence. Consider the model spectrum

$$E(k,z) = \begin{cases} c_1(z)k^m & \text{if } k < k_L \\ c_2\,[(At)\Delta u\epsilon(z)]^{1/2}\,k^{-3/2} & \text{if } k > k_L \end{cases}, \tag{2.3.10}$$

where the two portions of the spectra are matched at $k = k_L$. The kinetic energy $q_K = \int_0^\infty E(k)dk$ can be computed from this. As the flow field is assumed to be incompressible and freely decaying then, similar to the approach by Youngs [196], the two-equation turbulence model reduces to

$$\frac{Dq_K}{Dt} = -\mathcal{E}, \tag{2.3.11}$$

$$\frac{D\mathcal{E}}{Dt} = C_\mathcal{E}\mathcal{E}^2/q_K, \tag{2.3.12}$$

where $\mathcal{E}$ is the z averaged dissipation rate. Taking the derivative of q_K computed from the assumed spectrum, and inserting this into Equation (2.3.11), then comparing with Equation (2.3.12) gives

$$q_K(t) = q_{K,0}\left[1 + \left(\frac{2m+3}{m+1} - 1\right)\mathcal{E}_0 t/q_{K,0}\right]^{\frac{2m+3}{m+1}}, \tag{2.3.13}$$

and the mixing layer width is implied from the approximation

$$W \approx \frac{q_K^{3/2}}{\mathcal{E}} = \frac{q_{K,0}^{3/2}}{\mathcal{E}_0}\left[1 + \left(\frac{2m+3}{m+1} - 1\right)\mathcal{E}_0 t/q_{K,0}\right]^{\frac{m+3}{2m+4}}, \tag{2.3.14}$$

hence the final growth rate depends crucially on the form of the energy spectrum at low wavenumbers, as is the case for homogeneous isotropic turbulence. With $m = 4$ this gains $\theta = 7/12$, for $m = 2$, $\theta = 5/8$. It is additionally noted that with specially chosen conditions m could equal 1, in which case $\theta = 2/3$. For freely decaying turbulence the above considerations can be applied to a Kolmogorov spectrum, using grid turbulence data to fix the coefficient $C_\mathcal{E}$, giving $\theta \approx 0.29 - 0.4$, as discussed further in Clark and Zhou [37].

Finally, Llor [123] has examined the behaviour of a freely decaying slab of turbulence with respect to the invariance of angular momentum at the large scales. The results additionally used the observations by Kolmogorov that given a low wavenumber range which scales k^c then there exists an invariant of the form $I = k\lambda^{c+1}$. From this it

can be shown that for self-similar decay the kinetic energy $q_K \propto t^{-n}$, and $\lambda \propto t^{1-n/2}$, where $n = (2c + 2)/(c + 3)$ (i.e. $\theta = 1 - n/2$). Assuming a Saffman impulse field as initial conditions for the turbulent slab, this gave $n = 4/3$ equal to $\theta = 1/3$. Llor also proposes a maximum decay rate of turbulent kinetic energy of $n = 10/7$, corresponding to $\theta = 2/7$.

It should be noted that these analysis are typically applicable to moderate Atwood numbers where the growth exponent of the bubble and spike can be assumed to be close [37]. As $At \to 1$ then there is little or no shear force applied to the spike side of the interaction. This means that the initial linear growth is not slowed by interaction with the second fluid, and hence does not form a vortex or turbulent mixing layer. This Atwood number dependence is not considered in the models presented within this section.

2.3.2 'Just-Saturated' Mode Analysis

The previous subsection details the behaviour of a slab of fully developed turbulence, making the essential assumption that either all modes present in the initial problem have become saturated (i.e. they are past the linear stage of growth characterised by Richtmyer's formula) or that the remaining long wavelength modes are at low levels and do not influence the growth rate of the mixing layer. The models outlined in this section investigate the growth of a mixing layer where the perturbations have not yet become linearly saturated. This means that the short wavelengths can be nonlinear (turbulent), but that these can be overtaken by longer wavelengths growing at a slower but more persistent rate.

An analysis by Dimonte *et al.* [46] showed that if the mixing layer width is governed by the width of the 'just saturated' bubble, then the total width (envelope described by the saturated modes) should grow with $\theta = 1/2$. This was derived by assuming that the 'just saturated' mode has amplitude $a \approx C_{RM}/k$, i.e. $ka \approx C_{RM}$, where C_{RM} should be of order one. Given linear growth of each mode to this amplitude, the governing equation is $da/dt = (At)k\Delta u a_0$. Substituting $k = C_{RM}/a$, $W = 2a$, and $W_0 = 2a_0$ then $d(W^2)/dt = 4C_{RM}(At)\Delta u W_0$. The solution of this equation is

$$W \approx \sqrt{W_0^2 + 4C_{RM}At\Delta u(t - t_0)} \tag{2.3.15}$$

Youngs [198] proposed a modification to the growth rate by including the effects of initial conditions. Assuming that the power spectrum of the initial perturbation is represented by $P(k) \propto Ck^m$ then the mean amplitude as a function of wavelength is $a(\lambda) \propto \sqrt{kP(k)} = C^{1/2}k^{(m+1)/2}$. The velocity corresponding to the each wavenumber is then $v(k) = C^{1/2}(At)\Delta u k^{(m+3)/2}$. A structure of size $1/k$ appears in time $t = 1/kv(k)$. Linking the width of the mixing layer W with the wavelength λ gives

$$W \approx \lambda \approx \left(C^{1/2}(At)\Delta u t\right)^{2/(m+5)}, \tag{2.3.16}$$

thus giving $\theta = 2/(m+5)$. Youngs argues that growth from mode coupling alone is approximately $\theta = 0.24$, hence if the linearised growth rate is faster than this ($m < 3.3$) then θ is dependent on initial conditions.

Inogamov [89] proposed another variant based upon the expansion of the mixing layer due to linearly saturated modes, considering a power spectrum of the initial perturbations which becomes constant at low wavenumbers (long wavelengths). He then examines the differences in velocity fluctuations at a given scale, denoted by λ, concluding that

$$u_{n,m} = (At^+)\sqrt{n^2+m^2}\Delta u a_{n,m}, \tag{2.3.17}$$

$$u_\lambda =< |u(x,t) - u(x-\lambda,t)| > \propto \sqrt{n^2+m^2}u_{n,m}, \tag{2.3.18}$$

where u_n is the linear velocity perturbation for each individual two-dimensional mode number n and m, and At^+ the post-shock Atwood number. It is argued that $u_\lambda \propto \lambda_{ini}^2 u_{\lambda_{ini}}/\lambda^2$ where λ_{ini} is the characteristic average perturbation wavelength. Assuming that the rate of increase of mixing layer width W is proportional to the mean velocity difference of the just saturated mode, ie. $dW/dt \propto u_\lambda|_{\lambda=W}$ gives the differential equation

$$\frac{dW}{dt} \propto u_{\lambda_{ini}}\lambda_{ini}^2/W^2, \tag{2.3.19}$$

with solution $W \propto t^{1/3}$. It should be noted that this solution is only valid for initial perturbations of a certain type. More specifically, the amplitude of the Fourier harmonics of the perturbation should not change significantly in the region $\pm n$ from the mode number n. Implicit in this assumption is that the range of the Fourier harmonics is sufficiently wide - narrow band solutions would not follow the proportionality argument in Equation (2.3.18).

2.3.3 Bubble Merger Models

The late time behaviour of the RM instability can be considered through the class of Bubble merger models. These assume a phenomenological approach, considering the dominant modes at the limit of linear growth, and the merging of these dominant modes to create larger structures.

It is usually assumed that the bubbles grow according to potential flow, following a method by Layzer [116]. Assuming that the velocity is inviscid, irrotational ($\mathbf{u} = -\nabla\Phi$), and incompressible ($\nabla^2\Phi = 0$) a solution is sought which matches the initial conditions and Bernoulli's equation

$$\Phi_t - \frac{1}{2}(\Phi_z^2 + \Phi_r^2) - gz = a(t). \tag{2.3.20}$$

The resulting asymptotic bubble velocity based on potential flow models is equal to $C_{b/s}/kt$, which implies that a possible solution for the width of the mixing layer could be logarithmic in time [26]. The subscripts $(.)_{b/s}$ indicate the coefficient for the (b)ubble or (s)pike respectively. Recently, $C_{b/s}$ has been derived as $2/3$ by Hecht *et al.* [79], $2/(1 \pm At.)$ by both Goncharov [66] and Oron [145] and 1 by Sohn[172].

Bubble merger models track the development of individual bubbles, which are allowed to grow and interact with neighbouring bubbles, such that a bubble of size λ_1 can interact with a bubble of size λ_2 over a period of time to generate a final bubble of size $\lambda_1 + \lambda_2$. Two dimensional results published by Alon *et al.* [6] (employing the multimode potential defined by Hecht *et al.*[79]) gave $\theta_b \approx 0.4$, and $\theta_s \approx \theta_b\,(1 + At)$, however later results gained by Oron *et al.* [145] extended the bubble merger model to three dimensions giving $\theta_b \approx 0.25$, caused by the reduced rate of bubble merger in three dimensions.

2.3.4 Momentum-Drag Models

Another phenomenological method of analysing RM mixing is adapted from the analysis of Rayleigh-Taylor (RT) instabilities. The late time behaviour of the RT instability was modelled by Youngs [195] as a balance between buoyancy and drag for bubbles and spikes. This gave two equations for the evolution of the interface

$$(\rho_1 + \kappa_1\rho_2)\,Vol_1\frac{dU_1}{dt} = B_1(\rho_1 - \rho_2)Vol_1 - C_1\rho_2U_1^2\mathbf{S}_1, \tag{2.3.21}$$

$$(\rho_2 + \kappa_2\rho_1)\,Vol_2\frac{dU_2}{dt} = B_2(\rho_2 - \rho_1)Vol_2 - C_2\rho_1U_2^2\mathbf{S}_2, \tag{2.3.22}$$

where $\rho_{1,2}$ are the densities of the light and heavy material, $U_{1,2}$ is the velocity of the tip of the light and heavy material, where $U_{1,2} = dH_{1,2}/dt$. The volume of the structure is denoted by Vol and the surface area $\mathbf{S}$. Equation (2.3.21) refers to the evolution of the upward moving bubble, and Equation (2.3.22) refers to the evolution of the downward moving spike. This is a balance of mass times acceleration on the left, and the forces of buoyancy and drag on the right. This requires the specification of three model constants, the added mass κ, buoyancy B and drag coefficient C. Setting $g = 0$, and dividing the equations by the volume of the structure gives

$$\frac{dU_1}{dt} = -C_1'\frac{U_1^2}{L_1}, \tag{2.3.23}$$

$$\frac{dU_2}{dt} = -C_2'\frac{U_2^2}{L_2}, \tag{2.3.24}$$

$$C_{1,2}' = \frac{C_{1,2}(1 - (-1)^{1,2}At)}{1 + \kappa_{1,2} + (-1)^{1,2}(1 - \kappa_{1,2})At}, \tag{2.3.25}$$

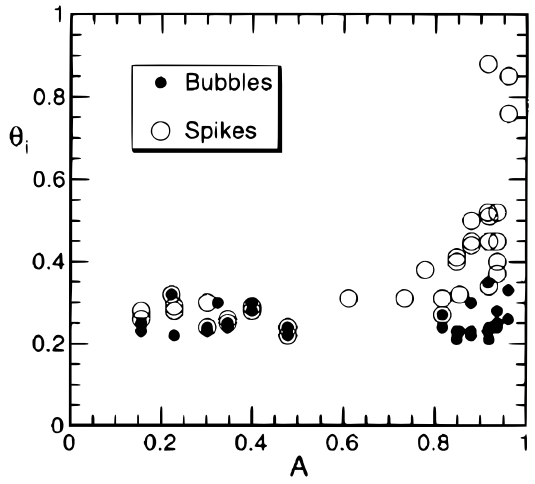

Figure 2.9: RM late time growth rate θ for the bubble and spike as a function of Atwood number At [48]

where $L = Vol/S$. As with the previous models, this gives asymptotic growth of $H_{1,2} \propto t^{\theta_{1,2}}$, where $\theta_{1,2}$ is typically derived from experimental and numerical data where $C'_{1,2} = 1/\theta_{1,2} - 1$ [47, 48]. Youngs' model assumes that $L_1 = L_2 = \mathrm{m}in(H_1, H_2) = H_2$. Taking $C'_{1,2} = C' = 3.67$ from experimental data [48] gives $\theta_1 = 0.21$ and $\theta_2 = 1/(1 + C'\sqrt{\rho_2/\rho_1})$, giving excellent results over a range of Atwood numbers [45].

2.3.5 Experimental Data

Experimental data has a wide scatter, primarily due to what appears to be a strong dependence on initial conditions. Dimonte and Schnieder [47] measure the growth rate at $At \approx 0.9$, for a Mach > 10 shock. They determined the value of $\theta = 0.5 \pm 0.1$, higher than previous investigations, suggesting an Atwood number dependence on the growth rate. The dependence of the growth rate θ on the Atwood number was investigated in a linear electric motor experiment [48]. The results are reproduced in Figure 2.9, where the relationship between the bubble and spike growth rate was found to be

$$\theta_S = \theta_B \left(\frac{1+At}{1-At}\right)^{0.21\pm0.05} = \theta_B \left(\frac{\rho_2}{\rho_1}\right)^{0.21\pm0.05}, \quad \text{for} \quad 0.15 \le At \le 0.96, \tag{2.3.26}$$

however in this case the issue of initial conditions was not investigated. In an assessment of the potential flow models, three dimensional single mode experiments at $At = 0.15$ conducted by Chapman and Jacobs [30] show the best agreement with the potential models of Goncharov [66] and Oron [145], who state $H_{b/s} = (2/(1 \pm At))/kt$.

Experiments in air and sulphur hexafluoride ($At \approx 0.67$) conducted by Prasad *et al.* [150] examined the influence of initial conditions on the late time growth of the turbulent mixing layer. The initial conditions were taken as a series of large scale sinusoidal perturbations, broken by a high wavenumber component introduced via a wire

mesh. There is a dependence of initial conditions, the largest wavelengths producing the thickest mixing layer, however it is a weak dependence as the growth exponent over all experiments is $0.26 \leq \theta \leq 0.33$.

CHAPTER 3

Numerical Methods

3.1 Governing Equations

The three dimensional compressible Euler equations for a generalised co-ordinate system can be written in conservative variables as

$$\frac{\partial \overline{\mathbf{U}}}{\partial t} + \frac{\partial \overline{\mathbf{E}}}{\partial \xi} + \frac{\partial \overline{\mathbf{F}}}{\partial \eta} + \frac{\partial \overline{\mathbf{G}}}{\partial \zeta} = 0, \tag{3.1.1}$$

where,

$$\mathbf{U} = [\rho,\ \rho u,\ \rho v,\ \rho w,\ e]^T, \tag{3.1.2}$$

$$\mathbf{E} = \left[\rho u,\ \rho u^2 + p,\ \rho uv,\ \rho uw,\ (e+p)u\right]^T, \tag{3.1.3}$$

$$\mathbf{F} = \left[\rho v,\ \rho uv,\ \rho v^2 + p,\ \rho vw,\ (e+p)v\right]^T, \tag{3.1.4}$$

$$\mathbf{G} = \left[\rho w,\ \rho uw,\ \rho vw,\ \rho w^2 + p,\ (e+p)w\right]^T, \tag{3.1.5}$$

$$\overline{\mathbf{U}} = J\mathbf{U}, \tag{3.1.6}$$

$$\overline{\mathbf{E}} = J(\mathbf{E}\xi_x + \mathbf{F}\xi_y + \mathbf{G}\xi_z), \tag{3.1.7}$$

$$\overline{\mathbf{F}} = J(\mathbf{E}\eta_x + \mathbf{F}\eta_y + \mathbf{G}\eta_z), \tag{3.1.8}$$

$$\overline{\mathbf{G}} = J(\mathbf{E}\zeta_x + \mathbf{F}\zeta_y + \mathbf{G}\zeta_z), \tag{3.1.9}$$

$$e = \rho i + 0.5\rho(u^2 + v^2 + w^2), \tag{3.1.10}$$

and J, ρ, i, u, v, w are the Jacobian of the cell volume under consideration, density, internal energy and Cartesian velocity components respectively. The subscripts $(.)_x$ indicate a partial derivative with respect to x. The system of equations is completed with the specification of an equation of state, which for an ideal gas is

$$p = \rho i\,(\gamma - 1)\,. \tag{3.1.11}$$

3.2 The Finite Volume Godunov Method

The governing equations are solved using the Godunov method [65]. The problem of interest is typically split into a number of finite volumes (or 'control volumes') where the initial values for the conserved variables are specified at the beginning of the simulation. The conserved variables are then evolved by computing the fluxes (**E**,**F**, and **G** above) across the interfaces of each control volume. The first order method proposed by Godunov can be summarised in one dimensional form as:

$$\mathbf{U}_j^{n+1} = \mathbf{U}_j^n + \frac{\Delta t}{\Delta x}\left(F_{j-1/2} - F_{j+1/2}\right), \tag{3.2.1}$$

where the inter-cell numerical flux $F_{j+1/2}$ is computed based on the solution to the Riemann problem using $\left(\mathbf{U}_j^n, \mathbf{U}_{j+1}^n\right)$, and similarly $F_{j-1/2}$ is computed from the Riemann problem using $\left(\mathbf{U}_j^n, \mathbf{U}_{j-1}^n\right)$.

3.3 Time Integration

Several time stepping methods are employed within this thesis, and are described in this subsection in order of increasing accuracy. The first is a second-order dual time stepping scheme proposed by Jameson [92]. The governing equations can be written as:

$$\frac{\partial \mathbf{U}}{\partial t}^{n+1} + \mathbf{F}(\mathbf{U}^{n+1}) = 0, \tag{3.3.1}$$

where $(.)^{n+1}$ indicates a quantity evaluated at the current time step. This is an implicit method, thus applying a second-order accurate expansion:

$$\frac{\partial \mathbf{U}}{\partial t}^{n+1} = -\left(\frac{3/2\mathbf{U}^{n+1} - 2\mathbf{U}^n + 1/2\mathbf{U}^{n-1}}{\Delta t}\right). \tag{3.3.2}$$

An explicit sub time step is utilised until the above flux has converged, using a first-order integration in the sub time step $\Delta\tau$, where the sub iterations are labelled with an m:

$$\frac{\mathbf{U}^{m+1} - \mathbf{U}^m}{\Delta\tau} + \frac{3/2\mathbf{U}^m - 2\mathbf{U}^n + 1/2\mathbf{U}^{n-1}}{\Delta t} + \mathbf{F}(\mathbf{U}^m) = 0. \tag{3.3.3}$$

Once the sub iterations have converged to a specified limit, the value at $m+1$ becomes the value at $n+1$ and the sub iterations are completed. Additionally, four fully explicit Runge-Kutta (RK) time stepping methods have been implemented as these methods

perform better in simulations with shock waves. The simplest version is the second-order method defined as:

$$\mathbf{U}_j^1 = \mathbf{U}_j^n + \frac{1}{2}\frac{\Delta t}{\Delta x}\mathbf{F}\left(\mathbf{U}_j^n\right), \tag{3.3.4}$$

$$\mathbf{U}_j^{n+1} = \mathbf{U}_j^n + \frac{\Delta t}{\Delta x}[\mathbf{F}\left(\mathbf{U}_j^1\right)], \tag{3.3.5}$$

Next a second-order TVD version [164]:

$$\mathbf{U}_j^1 = \mathbf{U}_j^n + \frac{\Delta t}{\Delta x}\mathbf{F}\left(\mathbf{U}_j^n\right), \tag{3.3.6}$$

$$\mathbf{U}_j^{n+1} = \mathbf{U}_j^n + \frac{1}{2}\frac{\Delta t}{\Delta x}[\mathbf{F}\left(\mathbf{U}_j^n\right) + \mathbf{F}\left(\mathbf{U}_j^1\right)], \tag{3.3.7}$$

and a third-order Total Variation Diminishing (TVD) Runge-Kutta method [69]:

$$\mathbf{U}_j^1 = \mathbf{U}_j^n + \frac{\Delta t}{\Delta x}\mathbf{F}\left(\mathbf{U}_j^n\right), \tag{3.3.8}$$

$$\mathbf{U}_j^2 = \mathbf{U}_j^n + \frac{1}{4}\frac{\Delta t}{\Delta x}[\mathbf{F}\left(\mathbf{U}_j^n\right) + \mathbf{F}\left(\mathbf{U}_j^1\right)], \tag{3.3.9}$$

$$\mathbf{U}_j^{n+1} = \mathbf{U}_j^n + \frac{1}{6}\frac{\Delta t}{\Delta x}[\mathbf{F}\left(\mathbf{U}_j^n\right) + \mathbf{F}\left(\mathbf{U}_j^1\right) + 4\mathbf{F}\left(\mathbf{U}_j^2\right)]. \tag{3.3.10}$$

Finally, a third order extended stability method is employed where the Courant-Friedrichs-Levy (CFL) number has a limit of 2 [173]:

$$\mathbf{U}_j^1 = \mathbf{U}_j^n + \frac{1}{2}\frac{\Delta t}{\Delta x}\mathbf{F}\left(\mathbf{U}_j^n\right), \tag{3.3.11}$$

$$\mathbf{U}_j^2 = \mathbf{U}_j^n + \frac{1}{2}\frac{\Delta t}{\Delta x}[\mathbf{F}\left(\mathbf{U}_j^1\right)], \tag{3.3.12}$$

$$\mathbf{U}_j^{n+1} = \frac{1}{3}\left(2\mathbf{U}_j^2 + \mathbf{U}_j^n + \frac{\Delta t}{\Delta x}[\mathbf{F}\left(\mathbf{U}_j^2\right) + \mathbf{F}\left(\mathbf{U}_j^1\right)]\right). \tag{3.3.13}$$

3.4 Higher-order Spatial Accuracy

Higher-order spatial accuracy is achieved in this thesis using van Leer's 'Monotone Upstream-centred Schemes for Conservation Laws' (MUSCL) technique [187], and 'Weighted Essentially Non-Oscillatory' (WENO) methods [11]. The base range of standard extrapolation methods used are

- Second-order: Minmod (MM), van Leer (VL) and van Albada (VA) ([184, 53] and references therein)

- Third-order (M3) [203]
- Fifth-order (M5) [107]
- WENO fifth- and ninth-order (W5 and W9)[11]

For MUSCL extrapolation, the left and right states of the conservative (or primitive) variables at the cell faces are computed as

$$\mathbf{U}^{L}_{i+1/2} = \mathbf{U}_i + \frac{1}{4}\left[(1-c)\,\phi^{lim}\left(r_i^{lim,L}\right)(\mathbf{U}_i - \mathbf{U}_{i-1}) + (1+c)\,\phi^{lim}\left(\frac{1}{r_i^{lim,L}}\right)(\mathbf{U}_{i+1} - \mathbf{U}_i)\right], \tag{3.4.1}$$

$$\mathbf{U}^{R}_{i+1/2} = \mathbf{U}_{i+1} - \frac{1}{4}\left[(1-c)\,\phi^{lim}\left(r_i^{lim,R}\right)(\mathbf{U}_{i+2} - \mathbf{U}_{i+1}) + (1+c)\,\phi^{lim}\left(\frac{1}{r_i^{lim,R}}\right)(\mathbf{U}_{i+1} - \mathbf{U}_i)\right], \tag{3.4.2}$$

$$r_i^{lim,L} = \frac{\mathbf{U}_{i+1} - \mathbf{U}_i}{\mathbf{U}_i - \mathbf{U}_{i-1}}, \qquad r_i^{lim,R} = \frac{\mathbf{U}_{i+1} - \mathbf{U}_i}{\mathbf{U}_{i+2} - \mathbf{U}_{i+1}}, \tag{3.4.3}$$

where $\mathbf{U}$ is the vector of cell averaged conserved (or primitive) variables, c is a free parameter which is set to $1/3$ for the third-order limiter, and the cells are labelled by the integer i. It should be noted that the parameter c does not influence the accuracy of the second-order limiters considered here as they are symmetric (See Appendix A for the definition of this criteria). For multicomponent flows primitive variables are usually extrapolated as this provides better resolution of contact surfaces. In this study the following limiters are considered

$$\phi^{lim}_{MM} = min\left(1, r_i^{lim}\right), \tag{3.4.4}$$

$$\phi^{lim}_{VA} = \frac{r_i^{lim}\left(1 + r_i^{lim}\right)}{1 + (r_i^{lim})^2}, \tag{3.4.5}$$

$$\phi^{lim}_{VL} = \frac{2r_i^{lim}}{1 + r_i^{lim}}, \tag{3.4.6}$$

$$\phi^{lim}_{M3} = 1 - \left(1 + \frac{2N r_i^{lim}}{1 + (r_i^{lim})^2}\right)\left(1 - \frac{2r_i^{lim}}{1 + (r_i^{lim})^2}\right)^{N}. \tag{3.4.7}$$

M3 includes a 'steepening' parameter N to improve the resolution of discontinuities, in this thesis $N = 2$. All of the above limiters are constrained in the normal fashion to first-order accuracy at local maxima and minima. The fifth order MUSCL scheme (M5) is slightly more complex [107]

$$\phi*^{lim}_{M5,L} = \frac{-2/r^{lim,L}_{i-1} + 11 + 24r^{lim,L}_{i} - 3r^{lim,L}_{i}r^{lim,L}_{i+1}}{30}, \tag{3.4.8}$$

$$\phi*^{lim}_{M5,R} = \frac{-2/r^{lim,R}_{i+2} + 11 + 24r^{lim,R}_{i+1} - 3r^{lim,R}_{i+1}r^{lim,R}_{i}}{30}, \tag{3.4.9}$$

where the ratio of the slopes is defined slightly differently:

$$r^{lim,L}_{i} = \frac{\mathbf{U}_{i+1} - \mathbf{U}_{i}}{\mathbf{U}_{i} - \mathbf{U}_{i-1}}, \qquad r^{lim,R}_{i} = \frac{\mathbf{U}_{i} - \mathbf{U}_{i-1}}{\mathbf{U}_{i+1} - \mathbf{U}_{i}}, \tag{3.4.10}$$

and monotonicity is maintained by limiting the above extrapolations using

$$\phi^{lim}_{M5,L} = max(0, min(2, 2r^{lim,L}_{i}, \phi*^{lim}_{M5,L})), \tag{3.4.11}$$

$$\phi^{lim}_{M5,R} = max(0, min(2, 2r^{lim,R}_{i}, \phi*^{lim}_{M5,R})). \tag{3.4.12}$$

The WENO methodology takes a weighted average of several possible stencils to choose the 'smoothest' option [11, 165, 166, 95]. This is an extension of the Essentially Non-Oscillatory (ENO) scheme presented by Harten *et al.* [76]. It is not strictly monotone (hence the 'essentially' label), however, close to an isolated discontinuity the weights for stencils which cross the discontinuity should become very small. By combining the stencils in this manner very high order accuracy can be achieved, in smooth regions of flow the order of accuracy is $2r-1$, where r is the number of points in each of the candidate stencils. Hence a ninth order method requires a stencil of five cells each side of the interface where the fluxes are computed.

To demonstrate the concept, the third order WENO reconstruction is outlined, for which $r = 2$. Given cell i the two polynomials are defined as,

$$\mathbf{p}_i(x) = \mathbf{U}_i + \frac{\mathbf{U}_i - \mathbf{U}_{i-1}}{\Delta x}(x - x_i), \tag{3.4.13}$$

$$\mathbf{p}_{i+1}(x) = \mathbf{U}_i + \frac{\mathbf{U}_{i+1} - \mathbf{U}_i}{\Delta x}(x - x_i). \tag{3.4.14}$$

The polynomials are then combined to give the reconstructed quantity for cell i,

$$\mathbf{P}_i = \frac{\mathbf{a}^i_0}{\mathbf{a}^i_0 + \mathbf{a}^i_1}\mathbf{p}_i(x) + \frac{\mathbf{a}^i_1}{\mathbf{a}^i_0 + \mathbf{a}^i_1}\mathbf{p}_{i+1}(x) \tag{3.4.15}$$

$$\mathbf{a}^i_0 = \frac{C_0}{(10^{-16} + (\mathbf{IS})_i)^2}, \qquad \mathbf{a}^i_1 = \frac{C_1}{(10^{-16} + (\mathbf{IS})_{i+1})^2}, \tag{3.4.16}$$

where the coefficients C_k are determined for optimal weighting and the smoothness indicators (**IS**) are calculated by $(\mathbf{IS})_i = (\mathbf{U}_i - \mathbf{U}_{i-1})^2$ and $(\mathbf{IS})_{i+1} = (\mathbf{U}_{i+1} - \mathbf{U}_i)^2$. Finally,

10^{-16} is a small number used to prevent divisions by zero in a perfectly smooth flow. The values for $\mathbf{U}_{i-1/2,R}$ and $\mathbf{U}_{i-1/2,L}$ are given by inserting $x = x_{i-1/2}$ and $x = x_{i+1/2}$ into Equation (3.4.15).

Regarding the time taken to complete the very high order accuracy simulations, the ratio of CPU times to that required to carry out the second-order van Leer simulations is 1.2 for M5 and W5, and 2.5 for W9. This does not include communication times for parallel computations as these depend on the hardware used and the number of parallel blocks utilised. This was not significant for the number of processors employed (maximum of 512 processors for the multimode RM simulations).

3.5 Multicomponent flows

3.5.1 Introduction

The complete approach to simulating multi-component flows is to have a different set of governing equations for each component. However, this thesis is concerned with the simulation of miscible, single phase fluids. With this in mind, several simplifying assumptions can be made. Firstly it is assumed that two gases in a single cell have the same velocity. This means that only one set of momentum equations are required. Secondly, the assumption of instantaneous temperature equilibrium between the gas species is made, so that only one energy and continuity equation is required (see [137]).

Thus the remaining task is to add an additional one or two governing equations which advect a quantity that can be used to compute the parameters required for the equation of state. There are several possible model equations, each based on different assumptions. A key issue with multicomponent models is conservation of pressure equilibrium. It has been shown that fully conservative models fail to preserve pressure equilibrium across a moving material interface when the temperature is different on each side [1, 31, 38, 85, 93, 103, 104, 114]. Note that these oscillations do not appear in the single gas case, and are not related to the order of accuracy of the scheme.

Following on from this apparent failure of fully conservative schemes, a number of quasi-conservative or non-conservative schemes were proposed. Quirk and Karni [153] built upon the earlier paper by Karni [102] to develop a scheme based on the non-conservative equations corrected at shock waves with good results. Jenny *et al.* [93] modified the energy equation to render the computation of the conservative variables a single fluid computation hence reducing the oscillations present in the basic scheme. Karni [103] added an additional non-conservative governing equation for the pressure, which successfully removed the oscillations present in the modified Sod shock tube problem. Abgrall [2] proposed a ‘quasi-conservative’ method, named so as it produces results with extremely small conservation errors. Abgrall and Karni [3] proposed a non-conservative numerical method in which two fluxes are computed at the cell face, which also removes the pressure oscillations, at a computational cost.

However, Wang *et al.* [191] derived a new model based on total enthalpy conservation of the mixture (henceforth labelled as 'ThCM') within a control volume. As the model is fully conservative it captures strong shock waves accurately, and due to the method of formulation the resulting numerical scheme showed no pressure oscillations in several test cases when using an exact Riemann solver.

Finally, Johnsen and Colonius [97] recently proposed an alternative method of solution of the model equations of Shyue [167] using the HLLC solver. This removes pressure oscillations completely from the resulting solution.

This section validates the multicomponent method used throughout the rest of the paper. It compares the mass fraction model, quasi-conservative models of Abgrall [2] and Johnsen [97], and the fully conservative model of Wang *et al.* [191]. First the model equations are described, then (if not presented in the original publications) approximate Riemann solvers are derived. These are validated at first order accuracy in space on several test cases, and extension to higher order is described. Finally, a higher order test case is used to illustrate the behaviour of the selected schemes using realistic methods.

3.5.2 Model Equations

Mass Fraction

In this model an additional equation is added to the Euler equations to track the mass fraction $Y = \rho_1/(\rho_1 + \rho_2) = \rho_1/\rho$, where $Y = 1$ indicates a cell containing only species 1, and $Y = 0$ is only species 2. A value between 0 and 1 indicates a mixture . Thus the mass conservation equation for a two species computation can be solved by adding a single equation to the Euler equations:

$$\frac{\partial \rho Y}{\partial t} + \frac{\partial \rho u Y}{\partial \xi} + \frac{\partial \rho v Y}{\partial \eta} + \frac{\partial \rho w Y}{\partial \zeta} = 0. \tag{3.5.1}$$

It is assumed that within each cell the two fluids have exactly the same temperature, pressure and velocities, thus from Dalton's law of partial pressures:

$$\gamma(Y) = \frac{c_{v1}\gamma_1 Y + c_{v2}\gamma_2 (1 - Y)}{c_{v1} Y + c_{v2} (1 - Y)}. \tag{3.5.2}$$

ThCM Model

The multi-component model proposed by Wang *et al.* [191] is based on the conservation of total enthalpy within the fluid mixture. The initial model derived requires two additional equations:

$$\frac{\partial}{\partial t}\left(\frac{\rho\chi}{\mathcal{M}}\right)+\frac{\partial}{\partial \xi}\left(\frac{\rho u\chi}{\mathcal{M}}\right)+\frac{\partial}{\partial \eta}\left(\frac{\rho v\chi}{\mathcal{M}}\right)+\frac{\partial}{\partial \zeta}\left(\frac{\rho w\chi}{\mathcal{M}}\right)=0, \tag{3.5.3}$$

$$\frac{\partial}{\partial t}\left(\frac{\rho}{\mathcal{M}}\right)+\frac{\partial}{\partial \xi}\left(\frac{\rho u}{\mathcal{M}}\right)+\frac{\partial}{\partial \eta}\left(\frac{\rho v}{\mathcal{M}}\right)+\frac{\partial}{\partial \zeta}\left(\frac{\rho w}{\mathcal{M}}\right)=0, \tag{3.5.4}$$

where $\mathcal{M}$ is the molecular mass of the mixture, and the variable χ is defined as,

$$\chi=\frac{\rho i}{p}+1, \tag{3.5.5}$$

for a perfect gas,

$$\chi_i=\frac{\gamma_i}{\gamma_i-1}, \qquad \chi=\sum_{i=1,N}\chi_i. \tag{3.5.6}$$

The mass fractions and volume fractions can be calculated from

$$Y_1=\frac{1/\mathcal{M}-1/\mathcal{M}_2}{1/\mathcal{M}_1-1/\mathcal{M}_2}, \tag{3.5.7}$$

$$\alpha_1=\frac{Y_1\mathcal{M}}{\mathcal{M}_1}=\frac{1-\mathcal{M}/\mathcal{M}_2}{1-\mathcal{M}_1/\mathcal{M}_2}. \tag{3.5.8}$$

If the volume fraction is used to initialise a simulation,

$$\mathcal{M}=\mathcal{M}_2\left(1-\alpha\left(1-\frac{\mathcal{M}_1}{\mathcal{M}_2}\right)\right), \tag{3.5.9}$$

$$\chi=\alpha_1\left(\chi_1-\chi_2\right)+\chi_2. \tag{3.5.10}$$

Quasi-conservative Approach

The model equations of Abgrall [2] and Shyue [167] are based on the advection of a thermodynamic quantity which does not allow pressure oscillations at a material interface. For an ideal gas it requires the addition of one equation,

$$\frac{\partial \kappa}{\partial t}+u\frac{\partial \kappa}{\partial \xi}+v\frac{\partial \kappa}{\partial \eta}+w\frac{\partial \kappa}{\partial \zeta}=0. \tag{3.5.11}$$

where $\kappa = 1/(\gamma - 1)$. It is clear that this equation is not in conservative form, as when cast in conservative form oscillations in the pressure field will occur. The clear advantage in this system is that a single equation can represent several gas components, as the advected quantity is the mixture γ. This is the ideal gas version of the model equations employed by Johnsen and Colonius [97].

Allaire *et al.* [4] use a different approach, removing the continuity equation and replacing it with the following,

$$\frac{\partial \alpha_1 \rho_1}{\partial t} + \frac{\partial \alpha_1 \rho_1 u}{\partial \xi} + \frac{\partial \alpha_1 \rho_1 v}{\partial \eta} + \frac{\partial \alpha_1 \rho_1 w}{\partial \zeta} = 0, \tag{3.5.12}$$

$$\frac{\partial \alpha_2 \rho_2}{\partial t} + \frac{\partial \alpha_2 \rho_2 u}{\partial \xi} + \frac{\partial \alpha_2 \rho_2 v}{\partial \eta} + \frac{\partial \alpha_2 \rho_2 w}{\partial \zeta} = 0, \tag{3.5.13}$$

$$\frac{\partial \alpha_1}{\partial t} + u\frac{\partial \alpha_1}{\partial \xi} + v\frac{\partial \alpha_1}{\partial \eta} + w\frac{\partial \alpha_1}{\partial \zeta} = 0, \tag{3.5.14}$$

where the final equation is not conservative. The equation set is closed by computing the mixture γ from the volume fractions.

3.6 Riemann Solvers

In this section the Riemann solvers employed for each gas model is described. The derivations are restricted to Cartesian grids for simplicity, within the code they are implemented in a fully curvilinear manner. The mass fraction and ThCM models are solved in a fully coupled manner, and the derivation of the new approximate Riemann solvers are detailed here. For the quasi-conservative models, an outline of the Riemann solver is given, as the code employs the Roe scheme proposed in [4], and the HLLC scheme proposed by Johnsen and Colonius [97].

3.6.1 Mass Fraction Model

The Scalar Non-Conservative Invariants

To derive an approximate Riemann solver for each flux dimensional splitting is applied. Thus for the flux **E**

$$\frac{\partial \widetilde{\mathbf{U}}}{\partial t} + \frac{\partial \widetilde{\mathbf{E}}}{\partial x} = 0, \tag{3.6.1}$$

where the $\widetilde{\mathbf{U}}$ denotes the reconstructed conservative variables and $\widetilde{\mathbf{E}}$ the corresponding flux. Expanding (3.6.1) for each of the governing equations, and reducing to primitive variables

$$\frac{\partial \widetilde{\rho}}{\partial t} + \widetilde{u}\frac{\partial \widetilde{\rho}}{\partial x} + \widetilde{\rho}\frac{\partial \widetilde{u}}{\partial x} = 0, \tag{3.6.2}$$

$$\widetilde{\rho}\frac{\partial \widetilde{u}}{\partial t} + \widetilde{\rho}\widetilde{u}\frac{\partial \widetilde{u}}{\partial x} + \widetilde{\rho}\frac{\partial \widetilde{p}}{\partial x} = 0, \tag{3.6.3}$$

$$\widetilde{\rho}\frac{\partial \widetilde{v}}{\partial t} + \widetilde{\rho u}\frac{\partial \widetilde{v}}{\partial x} = 0, \tag{3.6.4}$$

$$\widetilde{\rho}\frac{\partial \widetilde{w}}{\partial t} + \widetilde{\rho u}\frac{\partial \widetilde{w}}{\partial x} = 0, \tag{3.6.5}$$

$$\frac{\partial \widetilde{p}}{\partial t} + \widetilde{u}\frac{\partial \widetilde{p}}{\partial x} + \widetilde{\rho}a^2\frac{\partial \widetilde{u}}{\partial x} = 0, \tag{3.6.6}$$

$$\widetilde{\rho}\frac{\partial \widetilde{Y}}{\partial t} + \widetilde{\rho u}\frac{\partial \widetilde{Y}}{\partial x} = 0. \tag{3.6.7}$$

where a is the speed of sound. The time derivative of the conservative variables is replaced to introduce the vector of the conservative variables evaluated at the next time step. We develop $\widetilde{\mathbf{U}}$ in Taylor series expansion around the time level t.

$$\widetilde{\mathbf{U}}(t + \Delta t) = \widetilde{\mathbf{U}}_l(t) + \widetilde{\Delta x}\widetilde{\mathbf{U}}_x + \widetilde{\mathbf{U}}_t\Delta t \ , \tag{3.6.8}$$

where $\widetilde{\mathbf{U_l}}$ ($l = 0, 1, 2$) are the variables along the characteristics, l, and the the interval $\widetilde{\Delta x}$ is defined by introducing a wave speed λ^{eig} such that:

$$\widetilde{\Delta x} = \lambda^{eig}\Delta t. \tag{3.6.9}$$

Eq. (3.6.8) can be solved with respect to $\widetilde{\mathbf{U}}(t)$

$$\widetilde{\mathbf{U}}_t = \frac{\widetilde{\mathbf{U}} - \widetilde{\mathbf{U}}_l}{\Delta t} - \lambda^{eig}\widetilde{\mathbf{U}}_x \ . \tag{3.6.10}$$

The characteristic derivative $\widetilde{\mathbf{U}}_t$ is substituted into equations (3.6.2) to (3.6.7):

$$\frac{(\widetilde{\rho} - \rho_l)}{\Delta t} + \widetilde{\rho}_x\left(\widetilde{u} - \lambda^{eig}\right) + \widetilde{\rho}u_x = 0, \tag{3.6.11}$$

$$\widetilde{\rho}\left(\frac{(\widetilde{u} - u_l)}{\Delta t} + \widetilde{u}_x\left(\widetilde{u} - \lambda^{eig}\right)\right) + \widetilde{p}_x = 0, \tag{3.6.12}$$

$$\widetilde{\rho}\left(\frac{(\widetilde{v} - v_l)}{\Delta t} + \widetilde{v}_x\left(\widetilde{u} - \lambda^{eig}\right)\right) = 0, \tag{3.6.13}$$

$$\widetilde{\rho}\left(\frac{(\widetilde{w} - w_l)}{\Delta t} + \widetilde{w}_\xi\left(\widetilde{u} - \lambda^{eig}\right)\right) = 0, \tag{3.6.14}$$

$$\frac{(\widetilde{p} - p_l)}{\Delta t} + \widetilde{p}_x\left(\widetilde{u} - \lambda^{eig}\right) + \widetilde{\rho}a^2u_x = 0, \tag{3.6.15}$$

$$\widetilde{\rho}\frac{\left(\widetilde{Y} - Y_l\right)}{\Delta t} + \widetilde{\rho}\widetilde{Y}_x\left(\widetilde{u} - \lambda^{eig}\right) = 0. \tag{3.6.16}$$

As each equation sums to zero, the method suggested by Courant and Hilbert [43] can be used. Multiply each equation by a constant and add them together:

$$\frac{1}{\Delta t}\left[c_1\left(\widetilde{\rho}-\rho_l\right)+c_5\left(\widetilde{p}-p_l\right)+\widetilde{\rho}\left\{c_2\left(\widetilde{u}-u_l\right)+c_3\left(\widetilde{v}-v_l\right)+c_4\left(\widetilde{w}-w_l\right)+f\left(\widetilde{Y}-Y_l\right)\right\}\right]+$$
$$c_1\widetilde{\rho}_x\left(\widetilde{u}-\lambda^{eig}\right)+\widetilde{\rho}\left[u_x\left\{\left(c_1+c_5a^2\right)X+c_2\left(\widetilde{u}-\lambda^{eig}\right)\right\}+v_xc_3\left(\widetilde{u}-\lambda^{eig}\right)+\right.$$
$$\left.w_xc_4\left(\widetilde{u}-\lambda^{eig}\right)+c_6\widetilde{Y}_x\left(\widetilde{u}-\lambda^{eig}\right)\right]+\widetilde{p}_x\left[c_2+c_5\left(\widetilde{u}-\lambda^{eig}\right)\right]=0. \quad (3.6.17)$$

As the coefficients c_{1-6} are arbitrary, then if (3.6.17) equals zero, each of the individual components must equal zero, giving:

$$c_1\left(\widetilde{\rho}-\rho_l\right)+c_5\left(\widetilde{p}-p_l\right)+\widetilde{\rho}\left\{c_2\left(\widetilde{u}-u_l\right)+c_3\left(\widetilde{v}-v_l\right)+c_4\left(\widetilde{w}-w_l\right)+c_6\left(\widetilde{Y}-Y_l\right)\right\}=0, \quad (3.6.18)$$

and,

$$c_1\left(\widetilde{u}-\lambda^{eig}\right)=0, \quad (3.6.19)$$
$$\left(c_1+c_5a^2\right)+c_2\left(\widetilde{u}-\lambda^{eig}\right)=0, \quad (3.6.20)$$
$$c_3\left(\lambda_0^{eig}-\lambda^{eig}\right)=0, \quad (3.6.21)$$
$$c_4\left(\lambda_0^{eig}-\lambda^{eig}\right)=0, \quad (3.6.22)$$
$$c_2+c_4\left(\widetilde{u}-\lambda^{eig}\right)=0, \quad (3.6.23)$$
$$c_6\left(\widetilde{u}-\lambda^{eig}\right)=0. \quad (3.6.24)$$

As the coefficients can be any constant, then $\lambda_0^{eig}=\widetilde{u}$ from (3.6.19). This implies that $c_1=-c_5a^2$ from (3.6.20), and $c_2=0$ from (3.6.23). Substituting this into (3.6.18) yields:

$$c_5\left[\left(\widetilde{p}-p_l\right)-a^2\left(\widetilde{\rho}-\rho_l\right)\right]-\widetilde{\rho}\left\{c_3\left(\widetilde{v}-v_l\right)+c_4\left(\widetilde{w}-w_l\right)+c_6\left(\widetilde{Y}-Y_l\right)\right\}=0. \quad (3.6.25)$$

As this equation must be true regardless of the choice of coefficients, they can be arbitrarily set to zero giving the following set of equations:

$$\left(\widetilde{p}-p_0\right)-a^2\left(\widetilde{\rho}-\rho_0\right)=0, \quad (3.6.26)$$
$$\left(\widetilde{v}-v_0\right)=0, \quad (3.6.27)$$
$$\left(\widetilde{w}-w_0\right)=0, \quad (3.6.28)$$
$$\left(\widetilde{Y}-Y_0\right)=0. \quad (3.6.29)$$

However, setting $c_1 = 0$ and consider equations (3.6.18) to (3.6.24) again:

$$c_2 = \frac{c_5 a^2}{\left(\lambda_0^{eig} - \lambda^{eig}\right)}, \tag{3.6.30}$$

Inserting the above into (3.6.23):

$$\left(\lambda_0^{eig} - \lambda^{eig}\right)^2 = a^2, \tag{3.6.31}$$

giving the eigenvalues $\lambda^{eig} = \lambda_1^{eig} = \lambda_0^{eig} + a$ and $\lambda_2^{eig} = \lambda_0^{eig} - a$. For λ_1^{eig},

$$(\widetilde{p} - p_1) + \widetilde{\rho} a (\widetilde{u} - u_1) = 0, \tag{3.6.32}$$

for λ_2^{eig},

$$(\widetilde{p} - p_2) - \widetilde{\rho} a (\widetilde{u} - u_2) = 0, \tag{3.6.33}$$

where $(.)_1$ and $(.)_2$ indicate values evaluated along the λ_1^{eig} and λ_2^{eig} characteristic lines, respectively. Thus there are now six characteristic equations for the six unknown averaged flow values needed to determine the flux at the cell face.

Converting to Conservative Form

The next step is to convert equations (3.6.26)-(3.6.33) to conservative variables. Up until this point the only assumption that is introduced is that the characteristic lines are straight, not curved as they are in reality. Now the differences can be expressed using the chain rule of differentiation (for example $\rho\Delta u + u\Delta\rho = \Delta(\rho u)$):

$$\Delta u = \frac{\Delta(\rho u) - u\Delta\rho}{\rho}, \quad \Delta v = \frac{\Delta(\rho v) - v\Delta\rho}{\rho}, \tag{3.6.34}$$

$$\Delta w = \frac{\Delta(\rho w) - w\Delta\rho}{\rho}, \quad \Delta Y = \frac{\Delta(\rho Y) - Y\Delta\rho}{\rho}. \tag{3.6.35}$$

For the pressure extra care must be taken, as in a multi-component flow the ratio of specific heats can vary across an interface. Adapting a methodology utilised in Drikakis and Tsangaris [54] for an arbitrary equation of state, the pressure difference is expressed as:

$$\Delta p = p_i \Delta i + p_\rho \Delta\rho + p_Y \Delta Y. \tag{3.6.36}$$

From (3.1.10) the difference in internal energy i can be written as:

$$\rho\Delta i = \Delta e - \left[u\Delta(\rho u) + v\Delta(\rho v) + w\Delta(\rho w)\right] - i\Delta\rho. \tag{3.6.37}$$

Substituting (3.6.37) into (3.6.36):

$$\Delta p = Q\Delta\rho + \frac{p_i}{\rho}\left[\Delta e - \left(u\Delta(\rho u) + v\Delta(\rho v) + w\Delta(\rho w)\right)\right] + \frac{p_Y}{\rho}\left(\Delta(\rho Y) - Y\Delta\rho\right), \quad (3.6.38)$$

$$Q = p_\rho + q_K\frac{p_i}{\rho} - i\frac{p_i}{\rho}, \qquad q_K = \frac{1}{2}(u^2 + v^2 + w^2). \quad (3.6.39)$$

Next these differences are substituted into equations (3.6.26)-(3.6.33), and renaming

$$(\rho u) = l, \ (\rho v) = m, \ (\rho w) = n, \ (\rho Y) = o, \quad (3.6.40)$$

Thus,

$$(\widetilde{\rho} - \rho_0)\left(Q - a^2 - Y\frac{p_Y}{\rho}\right) + \frac{p_i}{\rho}\left[(\widetilde{e} - e_0) - \left(u\left(\widetilde{l} - l_0\right) + v(\widetilde{m} - m_0) + w(\widetilde{n} - n_0)\right)\right] + \frac{p_Y}{\rho}(\widetilde{o} - o_0) = 0, \quad (3.6.41)$$

$$-(\widetilde{\rho} - \rho_0)v + (\widetilde{m} - m_0) = 0, \quad (3.6.42)$$

$$-(\widetilde{\rho} - \rho_0)w + (\widetilde{n} - n_0) = 0, \quad (3.6.43)$$

$$(\widetilde{o} - o_0) - Y(\widetilde{\rho} - \rho_0) = 0, \quad (3.6.44)$$

$$(\widetilde{\rho} - \rho_1)\left(Q - a\lambda_0^{eig} - Y\frac{p_Y}{\rho}\right) + \left(\widetilde{l} - l_1\right)\left(a - u\frac{p_i}{\rho}\right) - (\widetilde{m} - m_1)v\frac{p_i}{\rho} - (\widetilde{n} - n_1)w\frac{p_i}{\rho} + (\widetilde{e} - e_1)\frac{p_i}{\rho} + \frac{p_Y}{\rho}(\widetilde{o} - o_1) = 0, \quad (3.6.45)$$

$$(\widetilde{\rho} - \rho_2)\left(Q + a\lambda_0^{eig} - Y\frac{p_Y}{\rho}\right) - \left(\widetilde{l} - l_2\right)\left(a + u\frac{p_i}{\rho}\right) - (\widetilde{m} - m_2)v\frac{p_i}{\rho} - (\widetilde{n} - n_2)w\frac{p_i}{\rho} + (\widetilde{e} - e_2)\frac{p_i}{\rho} + \frac{p_Y}{\rho}(\widetilde{o} - o_2) = 0. \quad (3.6.46)$$

Repeating the technique by Courant and Hilbert [43], multiply the above equations by the coefficients c_{1-6}

$$\widetilde{\rho}\overline{\rho} + \widetilde{l}\overline{l} + \widetilde{m}\overline{m} + \widetilde{n}\overline{n} + \widetilde{e}\overline{e} + \widetilde{o}\overline{o} = \rho_0\overline{\rho} + l_0\overline{l} + m_0\overline{m} + n_0\overline{n} + o_0\overline{o} + e_0\overline{e} + 2a^2\left(c_5R_1 + c_6R_2\right), \quad (3.6.47)$$

Where,

$$\overline{\rho} = c_1\left(Q - a^2 - Y\frac{p_Y}{\rho}\right) - c_2v - c_3w + c_5\left(Q - a\lambda_0^{eig} - Y\frac{p_Y}{\rho}\right) + c_6\left(Q + a\lambda_0^{eig} - Y\frac{p_Y}{\rho}\right) - c_4Y, \quad (3.6.48)$$

$$\bar{l} = c_5\left(a - u\frac{p_i}{\rho}\right) - c_6\left(a + u\frac{p_i}{\rho}\right) - c_1 u\frac{p_i}{\rho}, \tag{3.6.49}$$

$$\overline{m} = -\left(c_1 + c_5 + c_6\right) v\frac{p_i}{\rho} + c_2, \tag{3.6.50}$$

$$\overline{n} = -\left(c_1 + c_5 + c_6\right) w\frac{p_i}{\rho} + c_3, \tag{3.6.51}$$

$$\overline{e} = \frac{p_i}{\rho}\left[c_1 + c_5 + c_6\right], \tag{3.6.52}$$

$$\overline{o} = c_4 + \frac{p_Y}{\rho}\left(c_1 + c_5 + c_6\right), \tag{3.6.53}$$

$$2a^2 R_1 = \left(\rho_0 - \rho_1\right)\left(a\lambda_0^{eig} - Q + Y\frac{p_Y}{\rho}\right) + \left(l_0 - l_1\right)\left(u\frac{p_i}{\rho} - a\right) + \left(m_0 - m_1\right) v\frac{p_i}{\rho} + \left(n_0 - n_1\right) w\frac{p_i}{\rho} - \left(e_0 - e_1\right)\frac{p_i}{\rho} - \left(o_0 - o_1\right)\frac{p_Y}{\rho}, \tag{3.6.54}$$

$$2a^2 R_2 = -\left(\rho_0 - \rho_2\right)\left(Q + a\lambda_0^{eig} - Y\frac{p_Y}{\rho}\right) + \left(l_0 - l_2\right)\left(u\frac{p_i}{\rho} + a\right) + \left(m_0 - m_2\right) v\frac{p_i}{\rho} + \left(n_0 - n_2\right) w\frac{p_i}{\rho} - \left(e_0 - e_2\right)\frac{p_i}{\rho} - \left(o_0 - o_2\right)\frac{p_Y}{\rho}. \tag{3.6.55}$$

This system of equations must be inverted to solve for c_5 and c_6. First combining (3.6.49) and (3.6.52):

$$c_5 - c_6 = \frac{\bar{l} + \lambda_0^{eig}\overline{e}}{a}. \tag{3.6.56}$$

Next add (3.6.48) to (3.6.49) multiplied by u, (3.6.50) multiplied by v, (3.6.51) multiplied by w, and (3.6.53) multiplied by Y:

$$c_5 + c_6 = \frac{\overline{\rho} + \bar{l}u + \overline{m}v + \overline{n}w + \overline{e}H + \overline{o}Y}{a^2}, \tag{3.6.57}$$

$$H = q_K + i + \frac{p}{\rho}, \qquad a^2 = p\frac{p_i}{\rho^2} + p_\rho. \tag{3.6.58}$$

Now c_5 and c_6 can be obtained by subtraction and additions of (3.6.56) and (3.6.57).

$$c_5 = \frac{1}{2\widetilde{a}^2}\left[\overline{\rho} + \bar{l}\left(u + a\right) + \overline{m}v + \overline{n}w + \overline{e}\left(H + a\lambda_0^{eig}\right) + \overline{o}Y\right],$$

$$c_6 = \frac{1}{2\widetilde{a}^2}\left[\overline{\rho} + \bar{l}\left(u - a\right) + \overline{m}v - +\overline{n}w + \overline{e}\left(H - a\lambda_0^{eig}\right) + \overline{o}Y\right].$$

Setting $\overline{\rho} = 1$, $\overline{l} = \overline{m} = \overline{n} = \overline{e} = \overline{o} = 0$, then:

$$c_5 = c_6 = \frac{1}{2a^2}.$$

Inserting this into (3.6.47), an equation for the cell face value of $\widetilde{\rho}$ is gained:

$$\widetilde{\rho} = \rho_0 + R_1 + R_2. \tag{3.6.59}$$

Likewise, setting $\overline{l} = 1$, $\overline{\rho} = \overline{m} = \overline{n} = \overline{e} = \overline{o} = 0$, then:

$$c_5 = \frac{(u + \widetilde{a})}{2a^2}, \tag{3.6.60}$$

$$c_6 = \frac{(u - \widetilde{a})}{2a^2}, \tag{3.6.61}$$

thus,

$$\widetilde{l} = l_0 + (u + a) R_1 + (u - a) R_2. \tag{3.6.62}$$

An identical operation for $\widetilde{m}$, $\widetilde{n}$, and $\widetilde{e}$ yields:

$$\widetilde{m} = m_0 + v (R_1 + R_2), \tag{3.6.63}$$

$$\widetilde{n} = n_0 + w (R_1 + R_2), \tag{3.6.64}$$

$$\widetilde{e} = e_0 + \left(H + a\lambda_0^{eig}\right) R_1 + \left(H - a\lambda_0^{eig}\right) R_2. \tag{3.6.65}$$

For $\widetilde{o}$,

$$c_5 = c_6 = \frac{Y}{2a^2},$$

$$\widetilde{o} = o_0 + Y (R_1 + R_2). \tag{3.6.66}$$

Compact Form

Now, examining the final equations, they can be rewritten in a more compact form suitable for computation. Starting with (3.6.59):

$$\widetilde{\rho} = \rho_0 + \overline{\rho} + r_1 + r_2, \tag{3.6.67}$$

$$\overline{\rho} = \frac{p_i}{\rho s^2}\left[\overline{e} - e_0 - \rho_0\left(Q\frac{\rho}{p_i} - Y\frac{p_Y}{p_i}\right) - \frac{p_Y}{p_i}o_0\right], \tag{3.6.68}$$

$$\overline{e} = l_0 u + m_0 v + n_0 w, \tag{3.6.69}$$

$$r_1 = \frac{1}{2a^2}\left\{\rho_1\left(Q - a\lambda_0^{eig} - Y\frac{p_Y}{\rho}\right) + l_1\left(a - u\frac{p_i}{\rho}\right) - \frac{p_i}{\rho}(m_1 v - n_1 w + e_1) + o_1\frac{p_Y}{\rho}\right\}, \tag{3.6.70}$$

$$r_2 = \frac{1}{2a^2}\left\{\rho_2\left(Q + a\lambda_0^{eig} - Y\frac{p_Y}{\rho}\right) - l_2\left(a + u\frac{p_i}{\rho}\right) - \frac{p_i}{\rho}(m_2 v - n_2 w + e_2) + o_2\frac{p_Y}{\rho}\right\}. \tag{3.6.71}$$

Similarly,

$$\widetilde{l} = l_0 + (u + a)\, r_1 + (u - a)\, r_2 + u\overline{\rho}, \tag{3.6.72}$$

$$\widetilde{m} = m_0 + v\,(r_1 + r_2 + \overline{\rho})\,, \tag{3.6.73}$$

$$\widetilde{n} = n_0 + w\,(r_1 + r_2 + \overline{\rho})\,, \tag{3.6.74}$$

$$\widetilde{e} = e_0 + \left(H + a\lambda_0^{eig}\right) r_1 + \left(H - a\lambda_0^{eig}\right) r_2 + H\overline{\rho}, \tag{3.6.75}$$

$$\widetilde{o} = o_0 + Y\,(\overline{\rho} + r_1 + r_2)\,. \tag{3.6.76}$$

Equations (3.6.67) to (3.6.76) give the characteristic based conservative variables which can then be used to calculate the interface flux following Godunov's method.

3.6.2 Total Enthalpy Conservation of the Mixture Model

The Scalar Non-Conservative Invariants

To derive an approximate Riemann solver for each flux the methodology in Section 3.6.1 can be followed in considering the dimensionally split fluxes in equation (3.6.1). Expanding for each of the governing equations, and reducing to primitive variables:

$$\frac{\partial\widetilde{\rho}}{\partial t} + \widetilde{u}\frac{\partial\widetilde{\rho}}{\partial x} + \widetilde{\rho}\frac{\partial\widetilde{u}}{\partial x} = 0, \tag{3.6.77}$$

$$\widetilde{\rho}\frac{\partial\widetilde{u}}{\partial t} + \widetilde{\rho}\widetilde{u}\frac{\partial\widetilde{u}}{\partial x} + \widetilde{\rho}\frac{\partial\widetilde{p}}{\partial x} = 0, \tag{3.6.78}$$

$$\widetilde{\rho}\frac{\partial\widetilde{v}}{\partial t} + \widetilde{\rho}\widetilde{u}\frac{\partial\widetilde{v}}{\partial x} = 0, \tag{3.6.79}$$

$$\widetilde{\rho}\frac{\partial\widetilde{w}}{\partial t} + \widetilde{\rho}\widetilde{u}\frac{\partial\widetilde{w}}{\partial x} = 0, \tag{3.6.80}$$

$$\frac{\partial\widetilde{p}}{\partial t} + \widetilde{u}\frac{\partial\widetilde{p}}{\partial x} + \widetilde{\rho}a^2\frac{\partial\widetilde{u}}{\partial x} = 0, \tag{3.6.81}$$

$$\widetilde{\rho}\frac{\partial\widetilde{\chi}}{\partial t} + \widetilde{\rho}\widetilde{u}\frac{\partial\widetilde{\chi}}{\partial x} = 0, \tag{3.6.82}$$

$$\widetilde{\rho}\frac{\partial}{\partial t}\frac{1}{\widetilde{\mathcal{M}}} + \widetilde{\rho}\widetilde{u}\frac{\partial}{\partial x}\frac{1}{\widetilde{\mathcal{M}}} = 0. \tag{3.6.83}$$

where a is the speed of sound. The time derivative of the conservative variables is replaced to introduce the vector of the conservative variables evaluated at the next time step, as detailed in Section 3.6.1:

$$\frac{(\widetilde{\rho}-\rho_l)}{\Delta t}+\widetilde{\rho}_x\left(\widetilde{u}-\lambda^{eig}\right)+\widetilde{\rho}u_x=0, \tag{3.6.84}$$

$$\widetilde{\rho}\left(\frac{(\widetilde{u}-u_l)}{\Delta t}+\widetilde{u}_x\left(\widetilde{u}-\lambda^{eig}\right)\right)+\widetilde{p}_x=0, \tag{3.6.85}$$

$$\widetilde{\rho}\left(\frac{(\widetilde{v}-v_l)}{\Delta t}+\widetilde{v}_x\left(\widetilde{u}-\lambda^{eig}\right)\right)=0, \tag{3.6.86}$$

$$\widetilde{\rho}\left(\frac{(\widetilde{w}-w_l)}{\Delta t}+\widetilde{w}_\xi\left(\widetilde{u}-\lambda^{eig}\right)\right)=0, \tag{3.6.87}$$

$$\frac{(\widetilde{p}-p_l)}{\Delta t}+\widetilde{p}_x\left(\widetilde{u}-\lambda^{eig}\right)+\widetilde{\rho}a^2u_x=0, \tag{3.6.88}$$

$$\widetilde{\rho}\frac{(\widetilde{\chi}-\chi_l)}{\Delta t}+\widetilde{\rho}\widetilde{\chi}_x\left(\widetilde{u}-\lambda^{eig}\right)=0, \tag{3.6.89}$$

$$\widetilde{\rho}\frac{\left(\frac{1}{\widetilde{\mathcal{M}}}-\frac{1}{\mathcal{M}_l}\right)}{\Delta t}+\widetilde{\rho}\left(\frac{1}{\widetilde{\mathcal{M}}}\right)_x\left(\widetilde{u}-\lambda^{eig}\right)=0. \tag{3.6.90}$$

Multiply each equation by a constant and add them together:

$$\begin{aligned}\frac{1}{\Delta t}\Big[c_1(\widetilde{\rho}-\rho_l)+c_5(\widetilde{p}-p_l)+\widetilde{\rho}\{c_2(\widetilde{u}-u_l)+c_3(\widetilde{v}-v_l)+\\ c_4(\widetilde{w}-w_l)+c_6(\widetilde{\chi}-\chi_l)+c_7\left(\frac{1}{\widetilde{\mathcal{M}}}-\frac{1}{\mathcal{M}_l}\right)\}\Big]+c_1\widetilde{\rho}_x\left(\widetilde{u}-\lambda^{eig}\right)+\\ \widetilde{\rho}\Big[u_x\left\{\left(c_1+c_5a^2\right)X+c_2\left(\widetilde{u}-\lambda^{eig}\right)\right\}+v_xc_3\left(\widetilde{u}-\lambda^{eig}\right)+\\ w_xc_4\left(\widetilde{u}-\lambda^{eig}\right)+c_6\widetilde{\chi}_x\left(\widetilde{u}-\lambda^{eig}\right)+c_7\left(\frac{1}{\widetilde{\mathcal{M}}}\right)_x\left(\widetilde{u}-\lambda^{eig}\right)\Big]+\widetilde{p}_x\left[c_2+c_5\left(\widetilde{u}-\lambda^{eig}\right)\right]=0.\end{aligned} \tag{3.6.91}$$

As the coefficients are arbitrary, then if (3.6.91) equals zero, each of the individual components must equal zero, giving:

$$\begin{aligned}c_1(\widetilde{\rho}-\rho_l)+c_5(\widetilde{p}-p_l)+\widetilde{\rho}\{c_2(\widetilde{u}-u_l)+c_3(\widetilde{v}-v_l)+\\ c_4(\widetilde{w}-w_l)+c_6(\widetilde{\chi}-\chi_l)+c_7\left(\frac{1}{\widetilde{\mathcal{M}}}-\frac{1}{\mathcal{M}_l}\right)\}=0,\end{aligned} \tag{3.6.92}$$

and,

$$c_1\left(\widetilde{u}-\lambda^{eig}\right)=0, \tag{3.6.93}$$

$$\left(c_1+c_5a^2\right)+c_2\left(\widetilde{u}-\lambda^{eig}\right)=0, \tag{3.6.94}$$

$$c_3\left(\lambda_0^{eig}-\lambda^{eig}\right)=0, \tag{3.6.95}$$

$$c_4\left(\lambda_0^{eig}-\lambda^{eig}\right)=0, \tag{3.6.96}$$

$$c_2+c_4\left(\widetilde{u}-\lambda^{eig}\right)=0, \tag{3.6.97}$$

$$c_5\left(\widetilde{u}-\lambda^{eig}\right)=0, \tag{3.6.98}$$

$$c_7\left(\widetilde{u}-\lambda^{eig}\right)=0, \tag{3.6.99}$$

As the coefficients can be any constant, then $\lambda_0^{eig}=\widetilde{u}$ from (3.6.93). This implies that $c_1=-c_5a^2$ from (3.6.94), and $c_2=0$ from (3.6.97). Substituting this into (3.6.92) yields:

$$c_5\left[\left(\widetilde{p}-p_l\right)-a^2\left(\widetilde{\rho}-\rho_l\right)\right]-\widetilde{\rho}\left\{c_3\left(\widetilde{v}-v_l\right)+ c_4\left(\widetilde{w}-w_l\right)+c_6\left(\widetilde{\chi}-\chi_l\right)+c_7\left(\frac{1}{\widetilde{\mathcal{M}}}-\frac{1}{\mathcal{M}_l}\right)\right\}=0. \tag{3.6.100}$$

As this equation must be true regardless of the choice of coefficients, these can be arbitrarily set to zero giving the following set of equations:

$$\left(\widetilde{p}-p_0\right)-a^2\left(\widetilde{\rho}-\rho_0\right)=0, \tag{3.6.101}$$

$$\left(\widetilde{v}-v_0\right)=0, \tag{3.6.102}$$

$$\left(\widetilde{w}-w_0\right)=0, \tag{3.6.103}$$

$$\left(\widetilde{\chi}-\chi_0\right)=0, \tag{3.6.104}$$

$$\left(\frac{1}{\widetilde{\mathcal{M}}}-\frac{1}{\mathcal{M}_0}\right)=0. \tag{3.6.105}$$

However, if setting $c_1=0$ and considering equations (3.6.92) to (3.6.99) again:

$$c_2=\frac{c_5a^2}{\left(\lambda_0^{eig}-\lambda^{eig}\right)}, \tag{3.6.106}$$

Inserting the above into (3.6.97):

$$\left(\lambda_0^{eig}-\lambda^{eig}\right)^2=a^2, \tag{3.6.107}$$

giving the eigenvalues $\lambda^{eig} = \lambda_1^{eig} = \lambda_0^{eig} + a$ and $\lambda_2^{eig} = \lambda_0^{eig} - a$. For λ_1^{eig},

$$(\widetilde{p} - p_1) + \widetilde{\rho} a\,(\widetilde{u} - u_1) = 0, \tag{3.6.108}$$

for λ_2^{eig},

$$(\widetilde{p} - p_2) - \widetilde{\rho} a\,(\widetilde{u} - u_2) = 0, \tag{3.6.109}$$

where $(.)_1$ and $(.)_2$ indicate values evaluated along the λ_1^{eig} and λ_2^{eig} characteristic lines, respectively. There are now six characteristic equations for the six unknown averaged flow values needed to determine the flux at the cell face.

Converting to Conservative Form

The next step is to convert equations (3.6.101)-(3.6.109) to conservative variables. The differences can be expressed using the chain rule of differentiation:

$$\Delta u = \frac{\Delta(\rho u) - u\Delta\rho}{\rho}, \quad \Delta v = \frac{\Delta(\rho v) - v\Delta\rho}{\rho}, \quad \Delta w = \frac{\Delta(\rho w) - w\Delta\rho}{\rho}, \tag{3.6.110}$$

$$\Delta\chi = \frac{\Delta(\rho\chi/\mathcal{M}) - \chi\Delta\rho/\mathcal{M}}{\rho/\mathcal{M}}, \quad \Delta\left(\frac{1}{\mathcal{M}}\right) = \frac{\Delta(\rho/\mathcal{M}) - (1/\mathcal{M})\Delta\rho}{\rho}. \tag{3.6.111}$$

Utilising the methodology from Drikakis and Tsangaris [54] for an arbitrary equation of state, the pressure difference is expressed as:

$$\Delta p = p_i \Delta i + p_\rho \Delta\rho + p_\chi \Delta\chi. \tag{3.6.112}$$

From (3.1.10) the difference in internal energy i can be written as:

$$\rho\Delta i = \Delta e - [u\Delta(\rho u) + v\Delta(\rho v) + w\Delta(\rho w)] - i\Delta\rho. \tag{3.6.113}$$

Substituting (3.6.113) into (3.6.112):

$$\Delta p = Q\Delta\rho + \frac{p_i}{\rho}\left[\Delta e - (u\Delta(\rho u) + v\Delta(\rho v) + w\Delta(\rho w)\right] + \frac{p_\chi}{\rho}\left(\Delta(\rho\chi) - \chi\Delta\rho\right), \tag{3.6.114}$$

$$Q = p_\rho + q_K\frac{p_i}{\rho} - i\frac{p_i}{\rho}, \quad q_K = \frac{1}{2}(u^2 + v^2 + w^2). \tag{3.6.115}$$

Next these differences are substituted into equations (3.6.101)-(3.6.109), and renaming

$$(\rho u) = l,\ (\rho v) = m,\ (\rho w) = n,\ (\rho\chi/\mathcal{M}) = o,\ (\rho/\mathcal{M}) = q \tag{3.6.116}$$

giving,

$$(\widetilde{\rho}-\rho_0)\left(Q-a^2\right)+\frac{p_i}{\rho}\left[(\widetilde{e}-e_0)-\left(u\left(\widetilde{l}-l_0\right)+v\left(\widetilde{m}-m_0\right)+w\left(\widetilde{n}-n_0\right)\right)\right]+$$
$$\frac{p_\chi}{q}\left[(\widetilde{o}-o_0)-\chi\left(\widetilde{q}-q_0\right)\right]=0, \quad (3.6.117)$$

$$-(\widetilde{\rho}-\rho_0)\,v+(\widetilde{m}-m_0)=0, \quad (3.6.118)$$

$$-(\widetilde{\rho}-\rho_0)\,w+(\widetilde{n}-n_0)=0, \quad (3.6.119)$$

$$(\widetilde{o}-o_0)-\chi\left(\widetilde{\rho}-\rho_0\right)=0, \quad (3.6.120)$$

$$(\widetilde{\rho}-\rho_1)\left(Q-a\lambda_0^{eig}\right)+\left(\widetilde{l}-l_1\right)\left(a-u\frac{p_i}{\rho}\right)-(\widetilde{m}-m_1)\,v\frac{p_i}{\rho}-(\widetilde{n}-n_1)\,w\frac{p_i}{\rho}+$$
$$(\widetilde{e}-e_1)\,\frac{p_i}{\rho}+\frac{p_\chi}{q}\left[(\widetilde{o}-o_1)-\chi\left(\widetilde{q}-q_1\right)\right]=0, \quad (3.6.121)$$

$$(\widetilde{\rho}-\rho_2)\left(Q+a\lambda_0^{eig}\right)-\left(\widetilde{l}-l_2\right)\left(a+u\frac{p_i}{\rho}\right)-(\widetilde{m}-m_2)\,v\frac{p_i}{\rho}-(\widetilde{n}-n_2)\,w\frac{p_i}{\rho}+$$
$$(\widetilde{e}-e_2)\,\frac{p_i}{\rho}+\frac{p_\chi}{q}\left[(\widetilde{o}-o_2)-\chi\left(\widetilde{q}-q_2\right)\right]=0. \quad (3.6.122)$$

Next, repeating the technique by Courant and Hilbert [43], multiply the above equations by the coefficients c_{1-7}

$$\widetilde{\rho}\overline{\rho}+\widetilde{l}\overline{l}+\widetilde{m}\overline{m}+\widetilde{n}\overline{n}+\widetilde{e}\overline{e}+\widetilde{o}\overline{o}+\widetilde{q}\overline{q}=\rho_0\overline{\rho}+l_0\overline{l}+m_0\overline{m}+n_0\overline{n}+o_0\overline{o}+q_0\overline{q}+e_0\overline{e}+2a^2\left(c_6R_1+hR_2\right), \quad (3.6.123)$$

Where,

$$\overline{\rho}=c_1\left(Q-a^2\right)-c_2v-c_3w+c_6\left(Q-a\lambda_0^{eig}\right)+c_7\left(Q+a\lambda_0^{eig}\right)-\frac{c_5}{\mathcal{M}}, \quad (3.6.124)$$

$$\overline{l}=c_6\left(a-u\frac{p_i}{\rho}\right)-c_7\left(a+u\frac{p_i}{\rho}\right)-c_1u\frac{p_i}{\rho}, \quad (3.6.125)$$

$$\overline{m}=-\left(c_1+c_6+c_7\right)v\frac{p_i}{\rho}+c_2, \quad (3.6.126)$$

$$\overline{n}=-\left(c_1+c_6+c_7\right)w\frac{p_i}{\rho}+c_3, \quad (3.6.127)$$

$$\overline{e}=\frac{p_i}{\rho}\left[c_1+c_6+c_7\right], \quad (3.6.128)$$

$$\overline{o}=c_4+\frac{p_\chi}{q}\left(c_1+c_6+c_7\right), \quad (3.6.129)$$

$$\overline{q} = c_5 - \frac{\chi p_\chi}{q}\left(c_1 + c_6 + c_7\right) - c_4\chi, \tag{3.6.130}$$

$$\begin{aligned} 2a^2 R_1 = {} & \left(\rho_0 - \rho_1\right)\left(a\lambda_0^{eig} - Q\right) + \left(l_0 - l_1\right)\left(u\frac{p_i}{\rho} - a\right) + \left(m_0 - m_1\right)v\frac{p_i}{\rho} + \\ & \left(n_0 - n_1\right)w\frac{p_i}{\rho} - \left(e_0 - e_1\right)\frac{p_i}{\rho} - \frac{p_\chi}{q}\left[\left(o_0 - o_1\right) - \chi\left(q_0 - q_1\right)\right], \end{aligned} \tag{3.6.131}$$

$$\begin{aligned} 2a^2 R_2 = {} & -\left(\rho_0 - \rho_2\right)\left(Q + a\lambda_0^{eig}\right) + \left(l_0 - l_2\right)\left(u\frac{p_i}{\rho} + a\right) + \left(m_0 - m_2\right)v\frac{p_i}{\rho} + \\ & \left(n_0 - n_2\right)w\frac{p_i}{\rho} - \left(e_0 - e_2\right)\frac{p_i}{\rho} - \frac{p_\chi}{q}\left[\left(o_0 - o_2\right) - \chi\left(q_0 - q_2\right)\right]. \end{aligned} \tag{3.6.132}$$

This system of equations must be inverted to solve for c_6 and c_7. First combining (3.6.125) and (3.6.128):

$$c_6 - c_7 = \frac{\overline{l} + \lambda_0^{eig}\overline{e}}{a}. \tag{3.6.133}$$

Next add (3.6.124) to (3.6.125) multiplied by u, (3.6.126) multiplied by v, (3.6.127) multiplied by w, (3.6.129) multiplied by $\chi/\mathcal{M}$, and (3.6.130) multiplied by $1/\mathcal{M}$:

$$c_6 + c_7 = \frac{\overline{\rho} + \overline{l}u + \overline{m}v + \overline{n}w + \overline{e}H + \overline{o}\chi/\mathcal{M} + \overline{q}/\mathcal{M}}{a^2}, \tag{3.6.134}$$

$$H = q_K + i + \frac{p}{\rho}, \qquad a^2 = p\frac{p_i}{\rho^2} + p_\rho. \tag{3.6.135}$$

Now c_6 and c_7 can be obtained by subtraction and additions of (3.6.133) and (3.6.134).

$$c_6 = \frac{1}{2\widetilde{a^2}}\left[\overline{\rho} + \overline{l}\left(u + a\right) + \overline{m}v + \overline{n}w + \overline{e}\left(H + a\lambda_0^{eig}\right) + \overline{o}\frac{\chi}{\mathcal{M}} + \frac{\overline{q}}{\mathcal{M}}\right], \tag{3.6.136}$$

$$c_7 = \frac{1}{2\widetilde{a^2}}\left[\overline{\rho} + \overline{l}\left(u - a\right) + \overline{m}v - +\overline{n}w + \overline{e}\left(H - a\lambda_0^{eig}\right) + \overline{o}\frac{\chi}{\mathcal{M}} + \frac{\overline{q}}{\mathcal{M}}\right]. \tag{3.6.137}$$

Setting $\overline{\rho} = 1$, $\overline{l} = \overline{m} = \overline{n} = \overline{e} = \overline{o} = \overline{q} = 0$, then:

$$c_6 = c_7 = \frac{1}{2a^2}. \tag{3.6.138}$$

Inserting this into (3.6.123), an equation for the cell face value of $\widetilde{\rho}$ is gained:

$$\widetilde{\rho} = \rho_0 + R_1 + R_2. \tag{3.6.139}$$

Likewise, setting $\bar{l} = 1$, $\bar{\rho} = \bar{m} = \bar{n} = \bar{e} = \bar{o} = 0 = \bar{q} = 0$, then:

$$c_6 = \frac{(u + \widetilde{a})}{2a^2}, \tag{3.6.140}$$

$$c_7 = \frac{(u - \widetilde{a})}{2a^2}, \tag{3.6.141}$$

thus,

$$\widetilde{l} = l_0 + (u + a) R_1 + (u - a) R_2. \tag{3.6.142}$$

An identical operation for $\widetilde{m}$, $\widetilde{n}$, and $\widetilde{e}$ yields:

$$\widetilde{m} = m_0 + v (R_1 + R_2), \tag{3.6.143}$$

$$\widetilde{n} = n_0 + w (R_1 + R_2), \tag{3.6.144}$$

$$\widetilde{e} = e_0 + \left(H + a\lambda_0^{eig}\right) R_1 + \left(H - a\lambda_0^{eig}\right) R_2. \tag{3.6.145}$$

For $\widetilde{o}$,

$$c_6 = c_7 = \frac{\chi}{2\mathcal{M}a^2}, \tag{3.6.146}$$

$$\widetilde{o} = o_0 + \frac{\chi}{\mathcal{M}} (R_1 + R_2). \tag{3.6.147}$$

For $\widetilde{q}$,

$$c_6 = c_7 = \frac{1}{2\mathcal{M}a^2}, \tag{3.6.148}$$

$$\widetilde{o} = q_0 + \frac{1}{\mathcal{M}} (R_1 + R_2). \tag{3.6.149}$$

Compact Form

Now, examining the final equations, they can be rewritten in a more compact form suitable for computation. Starting with (3.6.139):

$$\widetilde{\rho} = \rho_0 + \bar{\rho} + r_1 + r_2, \tag{3.6.150}$$

$$\bar{\rho} = \frac{1}{a^2} \left[\frac{p_i}{\rho} (\bar{e} - e_0) + \frac{p_\chi}{q} (\chi q_0 - o_0) - \rho_0 Q \right], \tag{3.6.151}$$

$$\bar{e} = l_0 u + m_0 v + n_0 w, \tag{3.6.152}$$

$$r_1 = \frac{1}{2a^2} \left\{ \rho_1 \left(Q - a\lambda_0^{eig}\right) + l_1 \left(a - u\frac{p_i}{\rho}\right) - m_1 v \frac{p_i}{\rho} - n_1 w \frac{p_i}{\rho} + e_1 \frac{p_i}{\rho} - \frac{p_\chi}{q} (\chi q_1 - o_1) \right\}, \tag{3.6.153}$$

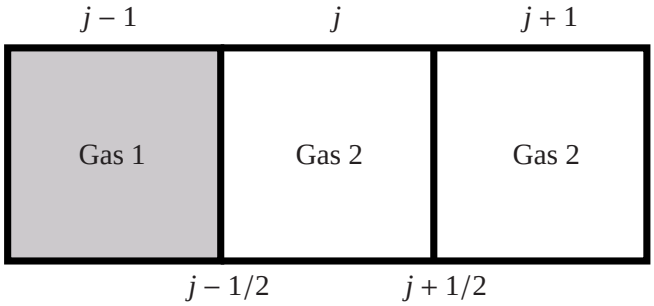

Figure 3.1: Diagram illustrating the position of the contact surface with respect to cells $j-1$, j and $j+1$

$$r_2 = \frac{1}{2a^2}\left\{\rho_2\left(Q + a\lambda_0^{eig}\right) - l_2\left(a + u\frac{p_i}{\rho}\right) - m_2 v\frac{p_i}{\rho} - n_2 w\frac{p_i}{\rho} + e_2\frac{p_i}{\rho} - \frac{p_\chi}{q}\left(\chi q_2 - o_2\right)\right\}. \tag{3.6.154}$$

Similarly,

$$\widetilde{l} = l_0 + (u+a)\, r_1 + (u-a)\, r_2 + u\overline{\rho}, \tag{3.6.155}$$

$$\widetilde{m} = m_0 + v\,(r_1 + r_2 + \overline{\rho}), \tag{3.6.156}$$

$$\widetilde{n} = n_0 + w\,(r_1 + r_2 + \overline{\rho}), \tag{3.6.157}$$

$$\widetilde{e} = e_0 + \left(H + a\lambda_0^{eig}\right) r_1 + \left(H - a\lambda_0^{eig}\right) r_2 + H\overline{\rho}, \tag{3.6.158}$$

$$\widetilde{o} = o_0 + \frac{\chi}{\mathcal{M}}\left(\overline{\rho} + r_1 + r_2\right). \tag{3.6.159}$$

$$\widetilde{q} = q_0 + \frac{1}{\mathcal{M}}\left(\overline{\rho} + r_1 + r_2\right). \tag{3.6.160}$$

Equations (3.6.150) to (3.6.160) give the characteristic based conservative variables which can then be used to calculate the inter-cell flux following Godunov's method.

Conservation of Pressure Equilibrium

It has been shown previously that the Mass Fraction model does not maintain pressure equilibrium, e.g., see [1, 31, 38, 85, 93, 103, 104, 114]. However, it was reported by Wang *et al.* [191] that the ThCM model conserved pressure equilibrium. This is not the case, as will be demonstrated in this subsection. In the original paper by Wang *et al.* the error was introduced as they only examined the case where the density is equal on both sides of the contact surface.

Considering the flow through the three computational cells shown in Figure 3.1, where the contact surface is located at $j-1/2$, it can be shown that the pressure equilibrium within the cell is not maintained. The contact surface between two gases is located at $j-1/2$ and is moving at a constant velocity u. Assume $(.)_2$ quantities in the cell j and $j+1$, and $(.)_1$ in cell $j-1$ at time level n. Using the approximate Riemann solver derived here the characteristics-based variables computed are exact. Given a first order in time and space discretisation, the pressure at the next time step in cell j can be written as

$$\frac{p^{n+1}}{p^n} = \frac{\left[(\gamma_1 - 1)(1 - \nu u) + (\gamma_2 - 1)\nu u\right]\left[T_1(1 - \nu u) + T_2 \nu u\right]}{T_1(1 - \nu u)(\gamma_1 - 1) + T_2 \nu u(\gamma_2 - 1)}, \tag{3.6.161}$$

where the identities $c_v = R/(\gamma - 1)$ and $\rho = p\mathcal{M}/R_u T$ have been utilised, where T is the temperature, R the specific gas constant, R_u the universal gas constant, and $\nu = \Delta t/\Delta x$. This result is similar to that gained by Jenny *et al.* [93] for the γ model. Thus for either the Mass Fraction or ThCM two-equation model, pressure equilibrium is maintained if any of the following conditions are satisfied:

- The two temperatures are equal,
- νu equals one or zero.

In [191] the authors suggest using the one-equation ThCM model, however the performance is much worse with the one-equation model as pressure oscillations occur if the two densities are different. This is much more restrictive than temperature equivalence.

3.6.3 Quasi-Conservative Methods

Roe Scheme

The equations of Abgrall [2] are solved using a Roe scheme of similar nature to that proposed by Allaire *et al.* [4], except that it has been extended to three dimensions from their one dimensional description. This is described here for multicomponent flows consisting of two perfect gases. Details of the derivation of the standard Roe scheme is given in Toro [184]. The derivation of the Roe scheme requires knowledge of the flux Jacobian of the system, the eigenvalues and eigenvectors, and the wave strengths. Given a direction split system of the form,

$$\frac{\partial \mathbf{U}}{\partial t} + \mathbf{A}(\mathbf{U})\frac{\partial \mathbf{U}}{\partial x} = 0, \tag{3.6.162}$$

the flux Jacobian $\mathbf{A}$ is given by,

$$\mathbf{A} = \begin{bmatrix} uY_2 & -uY_1 & Y_1 & 0 & 0 & 0 & 0 \\ -uY_2 & uY_1 & Y_2 & 0 & 0 & 0 & 0 \\ \beta_1 - u^2 & \beta_2 - u^2 & \left(2 - \frac{1}{\kappa}\right)u & -\frac{v}{\kappa} & -\frac{w}{\kappa} & \frac{1}{\kappa} & M \\ -uv & -uv & v & u & 0 & 0 & 0 \\ -uw & -uw & w & 0 & u & 0 & 0 \\ u(\beta_1 - H) & u(\beta_2 - H) & H - \frac{u^2}{\kappa} & -\frac{uv}{\kappa} & -\frac{uw}{\kappa} & \left(1 + \frac{1}{\kappa}\right) & uM \\ 0 & 0 & 0 & 0 & 0 & 0 & u \end{bmatrix}, \tag{3.6.163}$$

$$\beta_{1,2} = \frac{1}{\kappa}\left(q_K - \delta_{1,2}\right), \qquad \kappa_{1,2} = \frac{\partial \rho_{1,2} i_{1,2}}{\partial p_{1,2}}, \qquad \delta_{1,2} = \frac{\partial \rho_{1,2} i_{1,2}}{\partial \rho_{1,2}}, \tag{3.6.164}$$

$$\kappa = \alpha_1 \kappa_1 + \alpha_2 \kappa_2, \qquad M = \frac{1}{\kappa}\left(\rho_1 \delta_1 - \rho_1 i_1\right) - \frac{1}{\kappa}\left(\rho_2 \delta_2 - \rho_2 i_2\right), \tag{3.6.165}$$

This Jacobian gives five repeated eigenvalues

$$\lambda_2^{eig} = \lambda_3^{eig} = \lambda_4^{eig} = \lambda_5^{eig} = \lambda_6^{eig} = u, \tag{3.6.166}$$

and two non-repeated

$$\lambda_1^{eig} = u - a \qquad \lambda_7^{eig} = u + a, \tag{3.6.167}$$

where the speed of sound a is defined as

$$a^2 = \left(H - q_K\right)\kappa^{-1}. \tag{3.6.168}$$

The eigenvectors are not unique, as there are five repeated eigenvalues. This means that any linear combination of the first five eigenvectors of the system is itself an eigenvector (replacing one of the original five). With some manipulation the eigenvectors can be cast into the following form

$$\mathbf{K^1} = \begin{bmatrix} Y_1 \\ Y_2 \\ u - a \\ v \\ w \\ H - ua \\ 0 \end{bmatrix}, \quad \mathbf{K^2} = \begin{bmatrix} 1 \\ 0 \\ u \\ v \\ w \\ q_K + \delta_1 \\ 0 \end{bmatrix}, \quad \mathbf{K^3} = \begin{bmatrix} 0 \\ 1 \\ u \\ v \\ w \\ q_K + \delta_2 \\ 0 \end{bmatrix}, \quad \mathbf{K^4} = \begin{bmatrix} 0 \\ 0 \\ 0 \\ 1 \\ 0 \\ v \\ 0 \end{bmatrix}, \tag{3.6.169}$$

$$\mathbf{K^5} = \begin{bmatrix} 0 \\ 0 \\ 0 \\ 0 \\ 1 \\ w \\ 0 \end{bmatrix}, \quad \mathbf{K^6} = \begin{bmatrix} 0 \\ 0 \\ 0 \\ 0 \\ 0 \\ -M\kappa \\ 1 \end{bmatrix}, \quad \mathbf{K^7} = \begin{bmatrix} Y_1 \\ Y_2 \\ u + a \\ v \\ w \\ H + ua \\ 0 \end{bmatrix}. \tag{3.6.170}$$

The Roe flux can be written as

$$F_{i+1/2} = \frac{1}{2}\left(F_L + F_R\right) - \frac{1}{2}\sum_{j=1}^{7}\left|\lambda_j^{eig}\right|\delta_j \mathbf{K}^j. \tag{3.6.171}$$

The Roe scheme uses Roe averages to compute the wave strengths δ across each linearised wave in the Riemann problem. Defining the Roe average quantity as

$$\overline{a} = \frac{\sqrt{\rho}_L a_L + \sqrt{\rho}_R a_R}{\sqrt{\rho}_L + \sqrt{\rho}_R}, \qquad \underline{a} = \frac{\sqrt{\rho}_L a_R + \sqrt{\rho}_R a_L}{\sqrt{\rho}_L + \sqrt{\rho}_R}. \tag{3.6.172}$$

The wave strengths are

$$\begin{aligned}
\delta_1 &= \left(\Delta p - \underline{\rho} a \Delta u\right)/2a^2, && (3.6.173)\\
\delta_2 &= \Delta\left(\rho_1\alpha_1\right) - \frac{\overline{Y}_1}{a^2}\Delta p, && (3.6.174)\\
\delta_3 &= \Delta\left(\rho_2\alpha_2\right) - \frac{\overline{Y}_2}{a^2}\Delta p, && (3.6.175)\\
\delta_4 &= \Delta\left(\rho v\right) - \overline{v}\Delta\rho, && (3.6.176)\\
\delta_5 &= \Delta\left(\rho w\right) - \overline{w}\Delta\rho, && (3.6.177)\\
\delta_6 &= \Delta\alpha, && (3.6.178)\\
\delta_7 &= \left(\Delta p + \underline{\rho} a \Delta u\right)/2a^2. && (3.6.179)
\end{aligned}$$

where the speed of sound of the mixture a is estimated numerically as

$$a^2 = \sum_{i=1}^{2}\frac{\overline{Y_i \kappa_i a_i^2}}{\overline{\kappa}}. \tag{3.6.180}$$

from the wave strengths and the eigenvalues the last term in Equation (3.6.171) can be rewritten as

$$\frac{1}{2}\sum_{j=1}^{7}\left|\lambda_j^{eig}\right|\delta_i \mathbf{K}^j = \left|\overline{u} - a\right|\delta_1\begin{bmatrix}\overline{Y}_1\\ \overline{Y}_2\\ \overline{u} - a\\ \overline{v}\\ \overline{w}\\ \overline{H} - \overline{u}a\end{bmatrix} + \left|\overline{u}\right|\begin{bmatrix}\delta_2\\ \delta_3\\ \overline{u}\left(\delta_2 + \delta_3\right)\\ \overline{v}\left(\delta_2 + \delta_3\right) + \delta_4\\ \overline{w}\left(\delta_2 + \delta_3\right) + \delta_5\\ B + \delta_4\overline{v} + \delta_5\overline{w}\end{bmatrix} + \left|\overline{u} + a\right|\delta_7\begin{bmatrix}\overline{Y}_1\\ \overline{Y}_2\\ \overline{u} + a\\ \overline{v}\\ \overline{w}\\ \overline{H} + \overline{u}a\end{bmatrix}, \tag{3.6.181}$$

$$B = \Delta\left(\rho i\right) + \frac{\overline{u}^2 + \overline{v}^2 + \overline{w}^2}{2}\Delta\rho - \frac{\overline{H}\Delta p}{a^2}. \tag{3.6.182}$$

It should be noted that as the equation for the evolution of α_1 is decoupled from the other equations it is not solved using the Roe scheme. Instead, it is solved separately at using a simple upwind scheme following Allaire *et al* [4]. If the scheme is at first order this is

$$F_{i+1/2} = \frac{1}{2}(\overline{u} + |\overline{u}|)\Delta\alpha_1, \tag{3.6.183}$$

$$F_{i-1/2} = \frac{1}{2}(|\overline{u}| - \overline{u})\Delta\alpha_1. \tag{3.6.184}$$

If it is second or higher order

$$F_{i+1/2} = \frac{1}{2}(u_R\alpha_{1,R} + u_L\alpha_{1,L}) - \frac{1}{4}|u_R + u_L|(\alpha_{1,R} - \alpha_{1,L}) - \frac{\alpha_1}{2}(u_R + u_L). \tag{3.6.185}$$

As the Roe scheme does not prevent unphysical expansion shocks, the standard 'entropy fix' proposed by Harten and Hyman [77] is applied to the eigenvalues to prevent this occurring.

HLLC Scheme

The HLLC method proposed by Johnsen and Colonius has been implemented to solve the single equation version of the quasi-conservative system. The single species version of the HLLC method is detailed in Toro [184], and the addition of the equation for the transport of κ requires only slight modification. Firstly, the direction split transport equation for κ is recast as,

$$\frac{\partial\kappa}{\partial t} + \frac{\partial u\kappa}{\partial\xi} - \kappa\frac{\partial u}{\partial\xi} = 0. \tag{3.6.186}$$

The first two terms of this equation are conservative, and the flux for this can be solved in an identical manner to the flux of density in the continuity equation. The third term is added as a source term. This is reformulated as a finite volume flux by integrating over a volume giving (in one dimension)

$$\int_{i-1/2}^{i+1/2} \kappa\frac{\partial u}{\partial x}dx \approx \kappa_i(u^{HLLC}_{i+1/2} - u^{HLLC}_{i-1/2}), \tag{3.6.187}$$

where the integral has been evaluated to second order accuracy in κ. Finally, the velocities are computed using

$$u^{HLLC} = \frac{1 + sign(s*)}{2}(u^L + s^-(\beta^{*L} - 1)) + \frac{1 - sign(s*)}{2}(u^R + s^+(\beta^{*R} - 1)), \tag{3.6.188}$$

$$\beta^{*L,R} = \frac{s^{L,R} - u^{L,R}}{s^{L,R} - s^*}, \qquad s^- = min(0, s^L), \qquad s^+ = max(0, s^R), \tag{3.6.189}$$

where the required wave speeds are estimated using a primitive variable Riemann solution to the pressure and velocity in the intermediate region of the Riemann problem, exactly as detailed in [184], pp.303-305.

3.7 Numerical Test cases

In this section four test cases are presented to validate the new Riemann solvers and highlight the strengths and weaknesses of each multi-component model. The test cases have been chosen to be representative of the three dimensional compressible problems which are the focus of this thesis. These are shock interactions, typically with a stationary interface. It is important that spurious oscillations are minimised, and that the solution is as accurate as possible. Air is the most commonly employed driver gas, however shock tube experiments also employ Helium or Sulphur-Hexafluoride (SF_6) as the second gas. This generates a relatively large density ratio, and hence Atwood number.

The number of points $N_x = 100$ for all simulations, however the ThCM model has been run with $N_x = 400$ at fifth-order accuracy for each test case as a reference solution. This reference solution is independent of model employed (excepting pressure oscillations, where present). The Courant number $C = 0.6$ to aid direct comparison to previous papers. Piecewise constant reconstruction (first order in space) is employed, along with third order TVD Runge-Kutta in time (see section 3.3 for full details). The coarse grid and low order scheme has been chosen to highlight the performance of the Riemann solvers.

Throughout this section Mass Fraction is abbreviated to 'MF', Total Enthalpy Conservation of the Mixture to 'ThCM', the Allaire *et al.* quasi-conservative method is denoted by 'QCA', and the Johnsen and Colonius quasi-conservative method 'JC'. The ThCM reference results are denoted by 'REF'.

3.7.1 Test A: Modified Sod Shock Tube Problem

A modified version of the Sod shock tube problem [171] is used to compare the performance of the schemes with previous work with the same or similar test case, such as Abgrall and Karni [3], Chargy *et al.* [31], Karni [103], and Larrouturou [114]. The Riemann problem is defined initially as:

$$(\rho, u, p, \gamma)_L = (1, 0, 1, 1.4)\,,$$
$$(\rho, u, p, \gamma)_R = (0.125, 0, 0.1, 1.2)\,.$$

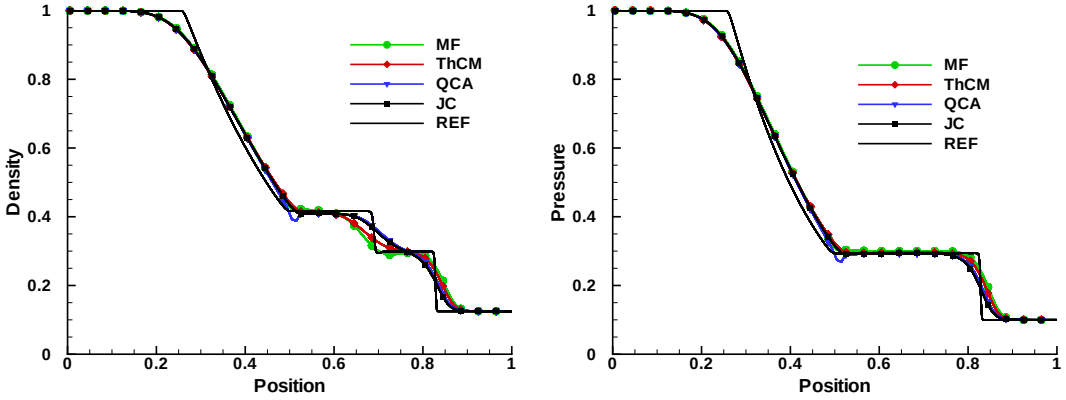

(a) Density

(b) Pressure

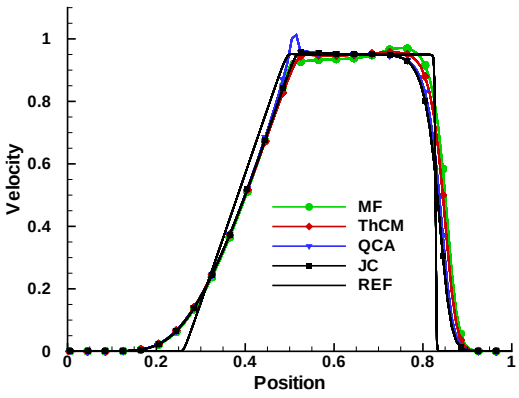

(c) Velocity

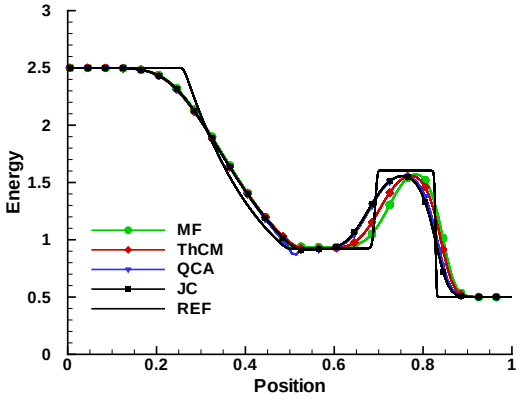

(d) Energy

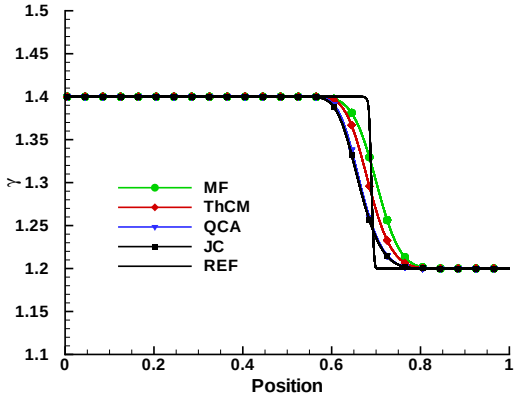

(e) γ

Figure 3.2: Results for Test A

Additionally $c_{v,L} = c_{v,R}$ completely defines the problem.

Figure 3.2 compares the performance of the models at time $t = 0.2s$. As a broad observation, all models perform well. The MF model suffers from an undershoot in density profile (Figure 3.2(a)), and a non-physical jump in velocity over the contact surface as illustrated in Figure 3.2(c). This jump in velocity across the contact surface is analogous to the behaviour observed in first-order simulations by Karni [103]. Karni showed that the rate of convergence of this error as mesh resolution increases is extremely slow. The ThCM model is superior to the MF model in this example, showing no density undershoot at the contact surface and a reduced velocity jump. QCA and JC perform the best, effectively reducing this error to zero. The slight overshoot in the velocity at the tail of the expansion wave in the QCA solution is a remnant of the initial discontinuity and is not considered to be indicative of any particular weakness in the model.

The two quasi-conservative models capture the position of the shock most accurately, however the ThCM model performs much better at the contact surface, and along with the MF model appear to be the least diffusive.

3.7.2 Test B: Helium Slab

This problem is a right facing shock wave passing through a slab of stationary Helium located at $0.4 < x < 0.6$, producing a series of reflected and transmitted shock waves inside the slab. This is a more complex problem, however, it is representative of many scenarios of practical interest such as Richtmyer Meshkov instabilities and shock-bubble interactions. The problem is defined as follows:

$$
\begin{aligned}
(\rho, u, p, \gamma, c_v)_{x<0.25} &= (1.3765, 0.3948, 1.57, 1.4, 717.2)\,, \\
(\rho, u, p, \gamma, c_v)_{0.25<x<0.4} &= (1, 0, 1, 1.4, , 717.2)\,, \\
(\rho, u, p, \gamma, c_v)_{0.4<x<0.6} &= (0.138, 0, 1, 1.67, 3114.9)\,, \\
(\rho, u, p, \gamma, c_v)_{0.6<x<1.0} &= (1, 0, 1, 1.4, , 717.2)\,.
\end{aligned}
$$

and has been presented previously in [2, 191]. The results are detailed in Figure 3.3 for time $t = 0.3s$. At this low resolution there is very little difference between the different models, indeed, they form a single line. However, oscillations can be seen in the higher-order, higher resolution ThCM reference simulation. This is due to the difference in temperature as the shock passes through the material interface, and is completely inhibited by numerical dissipation in the lower resolution simulation.

A refined simulation was conducted by increasing the number of cells in the x direction N_x to 400, and using the van Leer second-order limiter. A close up of the pressure and velocity profiles in the central region of the problem is shown in Figure 3.4. There are oscillations in the pressure and velocity field for the MF model are generated as the

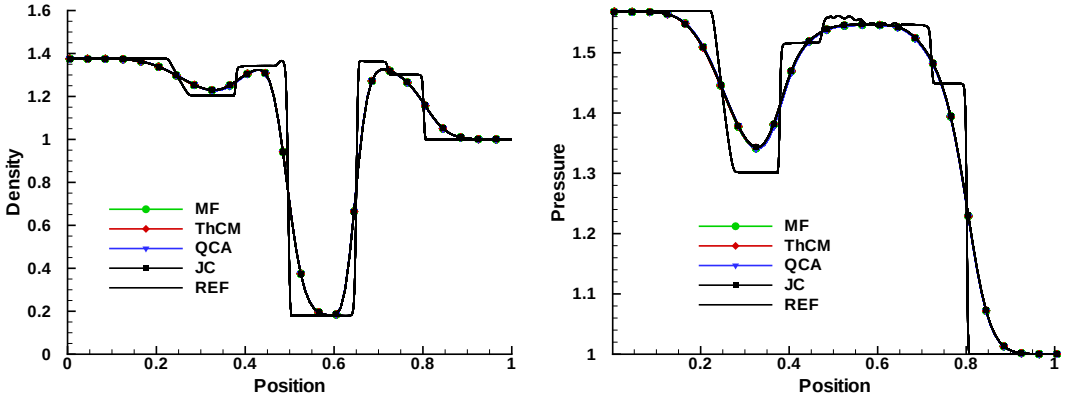

(a) Density

(b) Pressure

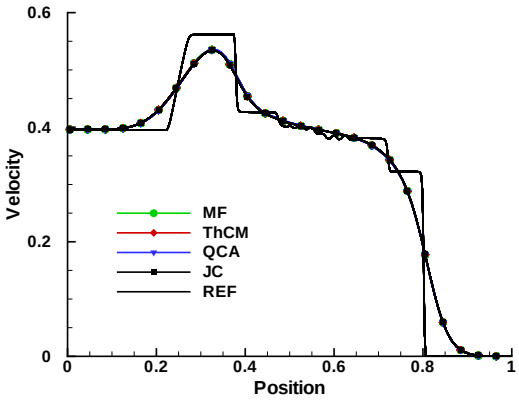

(c) Velocity

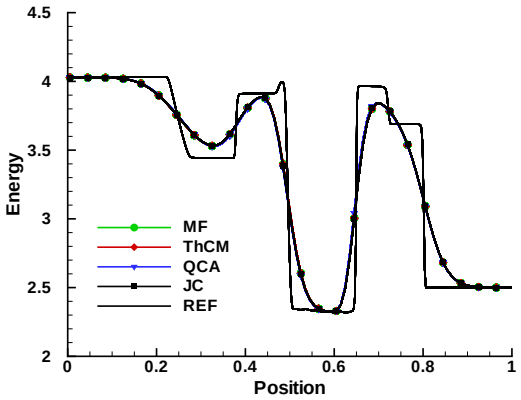

(d) Energy

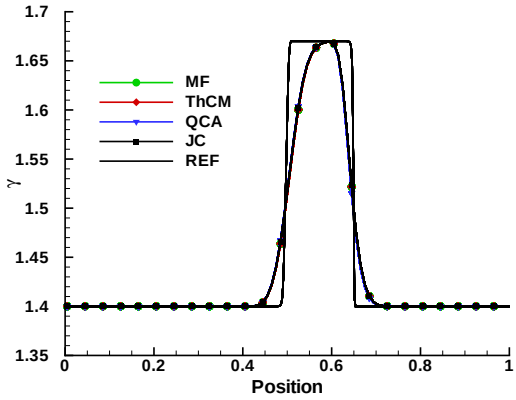

(e) γ

Figure 3.3: Results for Test B

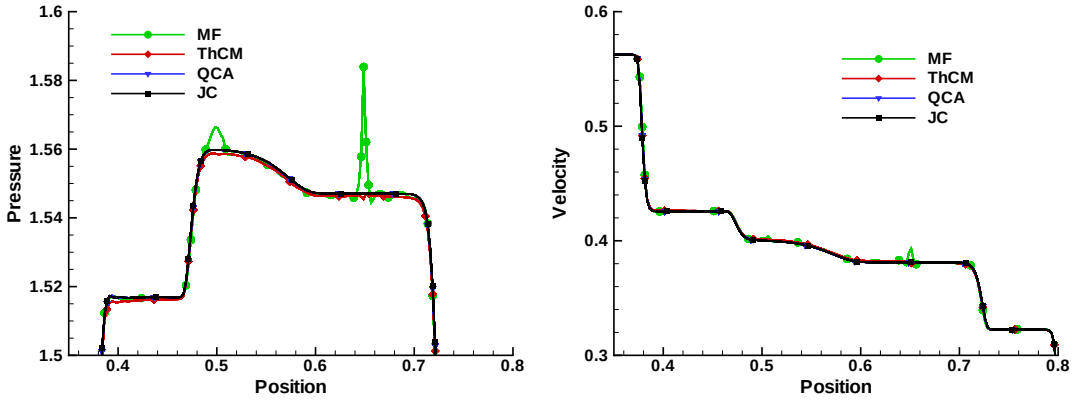

(a) Pressure (b) Velocity

Figure 3.4: Pressure and velocity fields for Test B at second-order accuracy and $N_x = 400$

shock passes through the material interface. In the ThCM model these oscillations significantly smaller, however, they are still present. These one-dimensional oscillations would translate to the spurious generation of vortices in two and three dimension. Both quasi-conservative methods conserve pressure equilibrium excellently at low and high orders of accuracy.

3.7.3 Test C: Shock - SF_6 Slab

This problem is a right facing shock wave passing through a slab of stationary SF_6 located at $0.4 < x < 0.6$, producing a series of reflected and transmitted shock waves inside the slab. This test case highlights schemes which have slight deviations from the actual γ, which is very close to one in SF_6. The initial conditions are,

$$(\rho, u, p, \gamma, c_v)_{x<0.25} = (1.3765, 0.3948, 1.57, 1.4, 717.2)\,.$$
$$(\rho, u, p, \gamma, c_v)_{0.25<x<0.4} = (1, 0, 1, 1.4, , 717.2)\,,$$
$$(\rho, u, p, \gamma, c_v)_{0.4<x<0.6} = (5.5, 0, 1, 1.076, 686.3)\,,$$
$$(\rho, u, p, \gamma, c_v)_{0.6<x<1.0} = (1, 0, 1, 1.4, , 717.2)\,.$$

and the output time is $t = 0.4s$. Once more, all models perform well, only QCA giving a discrepancy in the speed of the reflected shock wave. As with the previous problem, the reference solution has an oscillation at the material interface. The error in the physical model is not dissipated by the numerical scheme at high resolution.

The results from the same simulation with a second order van Leer limiter and $N_x = 400$ for all methods is shown in Figure 3.6. This illustrates that the pressure spike when using the MF model is significant when computing a realistic test problem. With less dissipative limiters the pressure spikes represent a significant problem and can

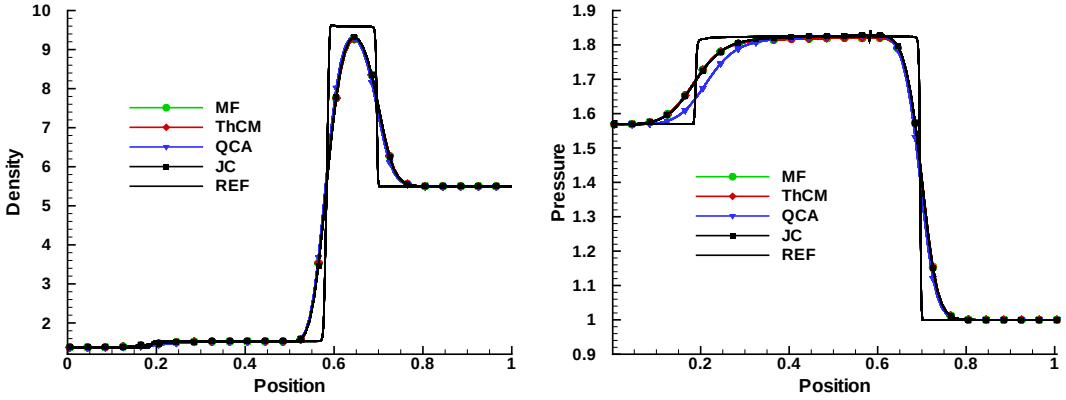

(a) Density

(b) Pressure

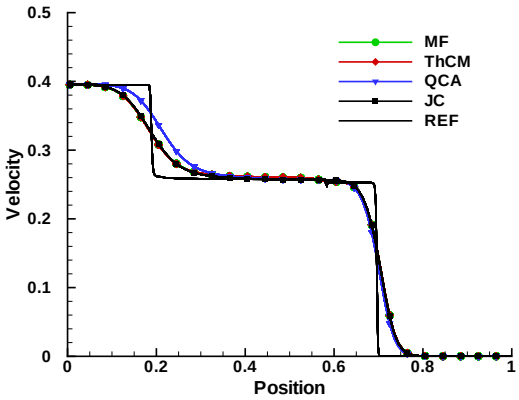

(c) Velocity

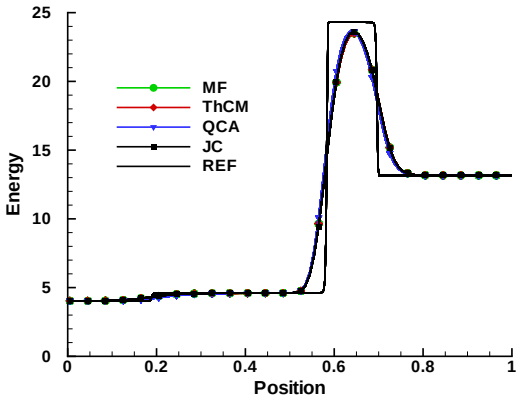

(d) Energy

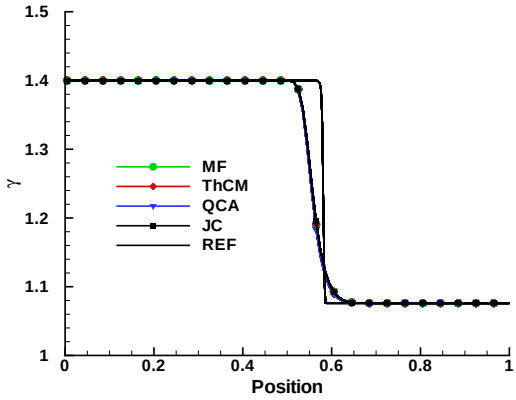

(e) γ

Figure 3.5: Results for Test C

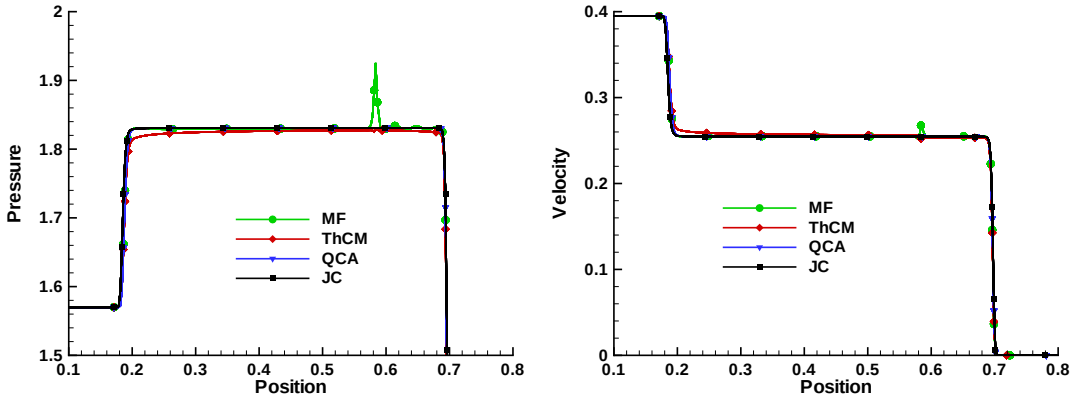

(a) Pressure (b) Velocity

Figure 3.6: Pressure and velocity fields for Test C at second-order accuracy and $N_x = 400$

cause negative energies. The more closely coupled ThCM model gives lower oscillations, and the quasi-conservative models are without oscillation. More importantly, the quasi-conservative models are significantly better resolved in the regions between the reflected and transmitted shocks, whereas the ThCM model does not achieve the plateau values. This shows a long time and distant influence of the small oscillations generated at the material interface on the overall flow structure.

3.7.4 Test D: Strong Shock Wave

Some important situations involve strong shock waves, a typical example of this would be the strengthening of a curved shock. This could occur via diffraction of an initially plane shock wave, or as a result of a converging cylindrical or spherical shock.

To test the performance of the schemes in this case, Test C has been run again but with a Mach 10 shock wave. This is defined as follows:

$$(\rho, u, p, \gamma, c_v)_{x<0.25} = (5.714, 9.762, 116.5, 1.4, 717.2)\,.$$

where the rest of the domain is initialised as for Test C. Results are shown in Figure 3.7 for time $t = 0.1s$. The main purpose of this test case is to demonstrate that the JC method does not perform well in the presence of strong shocks. The non-conservative formulation, and the method of solution give strong variations in γ as the shock changes form across a material interface, and also as it initially smears to the grid. There is a variation of greater than 3% for shocks above Mach=3.5, and this becomes worse with increasing resolution and order of accuracy. Indeed, this problem could not be run at $N_x = 400$ for the JC model as pressure becomes negative when γ drops below 1.

The results for MF, ThCM and QCA are good, however there is a difference in the position of the reflected shock. The MF and ThCM models perform better than the QCA

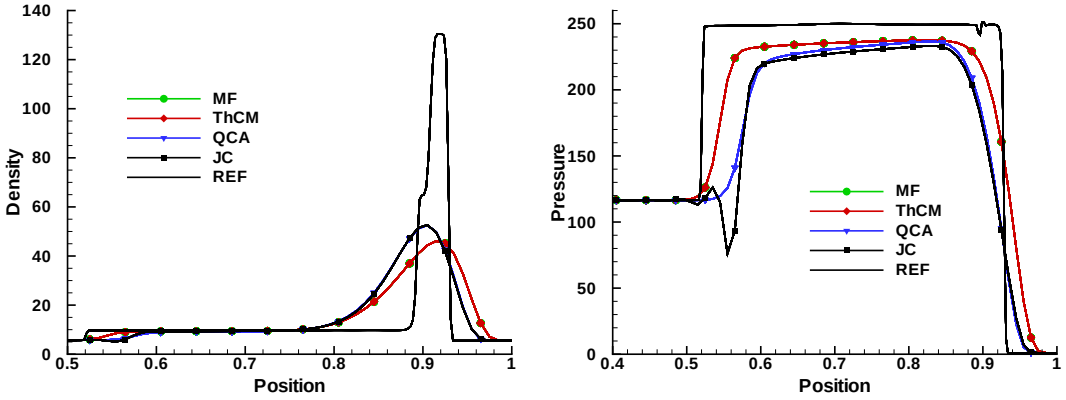

(a) Density

(b) Pressure

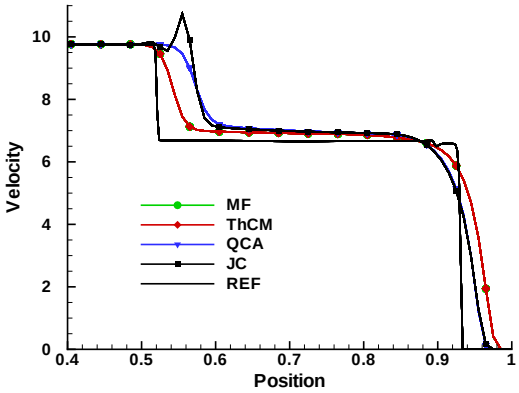

(c) Velocity

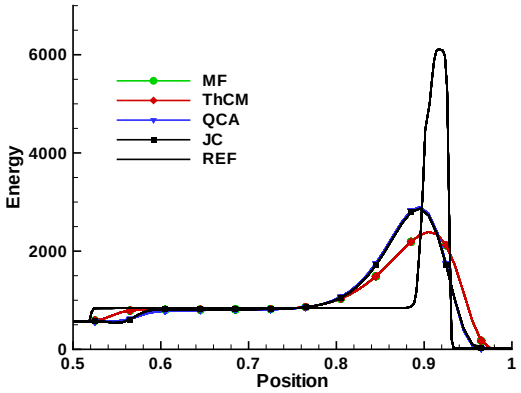

(d) Energy

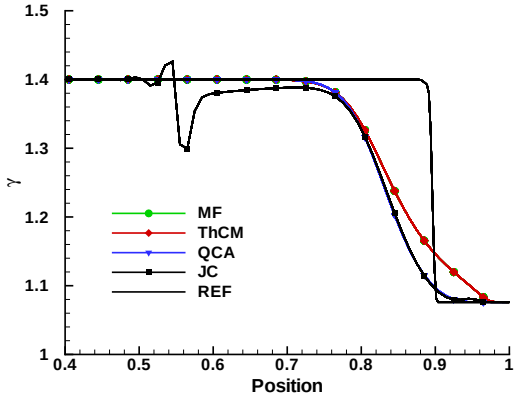

(e) γ

Figure 3.7: Results for Test D

model as they have closer shock speeds to the converged solution, and match better to the pressure profile. However, the QCA model does not have pressure oscillations at the material interface which exist in the MF and ThCM models.

3.7.5 Discussion

Several observations can be made about the multicomponent models tested. The MF model generates significant oscillations at the material interface due to imperfections in the physical model. Closer coupling of the molecular weight and γ in regions dominated by numerical dissipation leads to reduced pressure oscillations when employing the ThCM model. The oscillations are eliminated in the QCA and JC quasi-conservative methods.

The JC quasi-conservative method is generally superior to the other methods, giving more sharply resolved features, especially in the shock-SF_6 test case. However, it performs badly for strong shock waves due to the treatment of the non-conservative additional equation. This could be prohibitative in simulations with strongly converging shock waves.

Based on the test cases in this section, the ThCM model using the new characteristics based Riemann solver appears to be the best compromise for flows where reasonably strong shocks are present and it is important to get signal speeds as accurate as possible, but the JC HLLC Riemann solver is clearly much better in all other cases. The ThCM model is employed primarily within this thesis as a conservative choice ensuring that the values of γ remain within the prescribed bounds, preventing problems created if γ drops below one.

3.8 Numerical Methods for Unsteady Turbulent Flows

3.8.1 Direct Numerical Simulation

Direct Numerical Simulation (DNS) involves the use of an extremely fine grid such that all of the fluid motion from the largest energy containing scales to the smallest flow features at the Kolmogorov scale are resolved. In this method there are no approximations introduced by statistical closure of the Navier-Stokes equations and thus an 'exact' solution is gained. Unfortunately huge computational resources are required to perform DNS for typical engineering problems with the present computational power. The approximate size of the smallest eddies is the Kolmogorov scale η_K, computed as follows, where ℓ is the integral length scale:

$$\eta_k = \ell \left(\frac{u\ell}{\nu} \right)^{-3/4} = Re^{-3/4} \ell$$

Assuming that this is the required order of magnitude of the mesh, then the total number of points must be the volume of the domain divided by the 'Kolmogorov volume':

$$N_x \sim \frac{L_{box}^3}{\eta_K^3} \sim \frac{L_{box}^3}{\ell^3} Re^{9/4}$$

Thus:

$$Re \leq N_x^{4/9}$$

The maximum typical permissable time step is of the order of $\Delta t = \Delta x/u$, thus the number of time iterations can be written as:

$$N_t \sim \frac{T}{\Delta t} \sim \frac{T}{\eta_K/u} \sim \frac{T}{\ell/u} Re^{3/4}$$

The total simulation time is thus:

$$\text{Computer Time} \propto N_t N_x \propto \left(\frac{T}{\ell/u}\right)\left(\frac{L_{box}}{\ell}\right)^3 Re^3 \tag{3.8.1}$$

This equation demonstrates that the computational time of any simulation increases proportionally with the Reynolds number cubed. Using relationship (3.8.1) it has been shown that on a Teraflop computer a simulation of box size $L_{box} = 10\ell$ at $Re = 50,000$ would take 24 years to complete [44, 148]. As many large scale simulations easily run into $Re \sim 1 \times 10^6$ the limitations of DNS are clearly illustrated.

As the small scales typically contain little energy compared to the larger scales, this computational expense can be reduced by modelling the contribution of the smaller eddies. This approach is called Large Eddy Simulation (LES).

3.8.2 Large Eddy Simulation

Large Eddy Simulations (LES) reduce the computational expense of simulating turbulent flows by assuming that at high Reynolds numbers the small scales are 'universal'. This concept assumes that the small scales are the same in every flow, whether the initial large scale eddies are formed from separation from a transonic airfoil, or in a tidal channel. Considering the kinetic energy spectrum in Figure 2.5, a LES will aim to resolve all of the energy containing scales (which vary in form from problem to problem), and some of the inertial range. The rest of the inertial range and the dissipation range is modelled in such a way that energy is removed from the 'resolved' vortices in an identical manner as it would be removed if the 'unresolved' vortices were present. An example LES applied to two dimensional shock-induced mixing is shown in Figure 3.8. The fine scale structures present in the experiment are not directly simulated by the numerical method, but the dissipation of the numerical method is employed to model their effects.

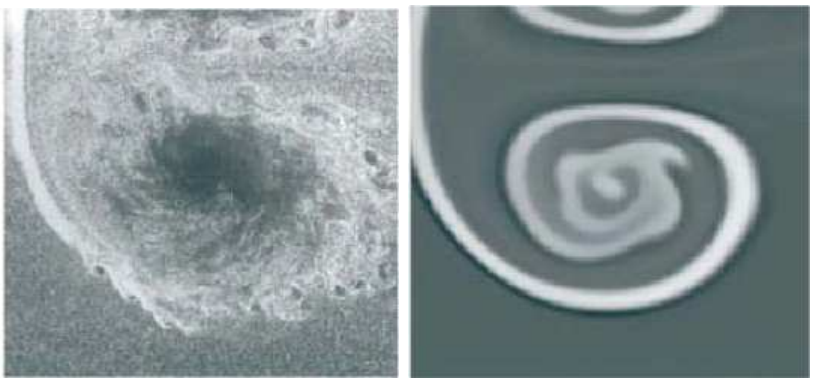

Figure 3.8: Experimental (left) and numerical (right) solutions for development of a shocked gas column RM instability [58]

Mathematically, the Navier Stokes equations are filtered spatially (with assumed temporal correspondence), giving:

$$\frac{\partial \overline{\rho}}{\partial t} + \nabla (\overline{\rho}\tilde{u}) = 0 \tag{3.8.2}$$

$$\frac{\partial \overline{\rho}\tilde{u}}{\partial t} + \nabla \cdot (\overline{\rho}\tilde{u}\tilde{u}) = \overline{f} + \nabla \cdot \sigma - \nabla \cdot \tau_{SGS} \tag{3.8.3}$$

$$\frac{\partial \overline{E}}{\partial t} + \nabla \cdot \left[(\overline{E} + \overline{p})\tilde{u}\right] = \overline{Q} + \nabla \cdot \left(\kappa_\theta \nabla \tilde{T} + \tilde{u} \cdot \sigma\right) - \nabla \cdot F_{SGS} \tag{3.8.4}$$

$$\sigma = 2\overline{\mu}\tilde{S} + \overline{\mu_b} \nabla \cdot \tilde{u} \tag{3.8.5}$$

$$S = \left[\nabla\tilde{u} + (\nabla\tilde{u})^T\right]/2 - (\nabla \cdot \tilde{u})/3 \tag{3.8.6}$$

where:

$$\tau_{SGS} = \overline{\rho u u} - \overline{\rho}\tilde{u}\tilde{u} \tag{3.8.7}$$

$$F_{SGS} = \overline{(E + p)u} - \left(\overline{E} + \overline{p}\right)\tilde{u} \tag{3.8.8}$$

and $\overline{(.)}$ indicates spatially averaged and $\tilde{(.)}$ is the Favre weighted average, i.e. $\tilde{u} = \overline{\rho u}/\overline{\rho}$. These equations are exact for a given equal spaced filter, however they are not in closed form. The quantities labelled $(.)_{SGS}$ rely on information from the unresolved scales, where SGS stands for 'sub-grid scale'. This data is not available within the simulation, and thus has to be modelled.

In the traditional form of LES, these sub-grid scale terms are modelled explicitly by addition extra terms to close the system of equations. LES has had great success when applied to incompressible flows however compressible flows with discontinuities continue to be a source of immense difficulty.

There are several key issues. Firstly, existing models are known to provide excessive dissipation in flows where the growth of an initially small perturbation to fully turbulent flow must be resolved [120, 148]. There are currently very few subgrid models

capable of capturing a shock wave, most require additional numerical dissipation to stabilise the numerical scheme in regions of rapid change. It is also noted that results are often insensitive to the model employed [61], which significantly increases the complexity of defining the 'correct' numerical scheme for a given problem, as there are a number of empirical coefficients to fix, especially for compressible problems. Indeed, it was shown in [64] that the optimum choice for the coefficients of a subgrid model are not only problem dependent, but also grid dependent.

With the large number of uncertainties, some practitioners opt to run simulations without the subgrid model, allowing the numerical method to dissipate turbulent kinetic energy where necessary. This approach has become known as Implicit Large Eddy Simulation (ILES).

3.8.3 Implicit Large Eddy Simulation

It has been recognised that some numerical schemes gain good results in complex flows without the explicit addition of a subgrid model [120]. This was first observed by Boris *et al.* [24] and Youngs [195] who point out that simulating the unfiltered flow equations instead of the filtered equations gives good results in both decaying homogeneous turbulence and mixing flows. Fureby *et al.* [61] compared and contrasted eight modelling strategies (including no model) using grid sizes of 16^3, 32^3 and 64^3 in the simulation of homogeneous decaying turbulence. The turbulent kinetic energy spectra were compared with the DNS of Jimenez *et al.* [96], and demonstrated that there were only small differences in the macroscopic behaviour of the flow for simulations with and without a subgrid model.

The basis of this approach is that the numerical truncation error associated with discretising the governing equations results in terms of similar form or action to sub-grid models, with the filter size being adjusted automatically to the grid size. As justification of the approach, one of two assumptions are made - either the subgrid model is implicitly designed into the limiting method of the numerical scheme, based on the observation that an upwind numerical scheme can be rewritten as a central scheme plus a dissipative term (see [51, 53, 71] and references therein), or that the details of the dissipation is irrelevant and that the flow has a 'self adjusting mechanism' which yields the correct dissipation of kinetic energy.

Such implicit subgrid models fall into the class of structural models, as there is no assumed form of the nature of the subgrid flow thus the subgrid model is entirely determined by the structure of the resolved flow [159]. An important element of ILES is the choice of Finite Volume methods. These have an inherent structural model as the reconstruction phase recovers subgrid velocities up to the order of accuracy of the numerical scheme. This is because the Finite Volume method computes the cell averaged flow quantities (exact quantities filtered by the mesh size) based on exact fluxes computed at the cell interface. However, it cannot recover modes beyond the Nyquist frequency, and these are modelled through the numerical dissipation of the

scheme itself.

Using ILES, excellent results have been gained in simulation of flows as varied as Rayleigh-Taylor and Richtmyer Meshkov instability [197, 195, 183], Free jets [24, 70], channel flow [70], open cavity flow [75, 51], geophysical flows [129, 170], delta wings [67] and decaying turbulence [52, 61, 149, 60, 130, 81, 182].

There has been a large growth in ILES simulations, however, as with LES simulations there has not been consensus on the appropriate form of the discretisation 'error' in ILES. Thus there is substantial potential for further formalisation and improvement.

The Implicit Subgrid Model

ILES is a so-called 'no model' turbulence model. It is assumed that the numerics provide sufficient modelling of the subgrid terms to allow the 'correct' dissipation of turbulent kinetic energy. As pointed out in the introduction, the subgrid model embedded onto the numerical method used in the discretisation of the convective terms is determined entirely by the structure of the flow. This has obvious benefits in the simulation of transitional flows where excess dissipation can damp the growth of critical modes. A detailed description of the implicit subgrid model would be too lengthy to include (see, for example [53, 128, 24, 127, 71]), however, an outline of the current analysis of the ILES model will be given in this section.

The finite volume fluxes for the Godunov method can be written in the following format [184]

$$\mathbf{F_{i+1/2}} = \frac{1}{2}\left(\mathbf{F_L} + \mathbf{F_R}\right) - \frac{1}{2}\left|\mathbf{A}\right|\left(\mathbf{U_R} - \mathbf{U_L}\right), \tag{3.8.9}$$

$$\left|\mathbf{A}\right| = \mathbf{K}\left|\mathbf{\Lambda}\right|\mathbf{K^{-1}}, \tag{3.8.10}$$

where $\mathbf{A}$ is the flux Jacobian, $\mathbf{\Lambda}$ is a diagonal array of eigenvalues, $\mathbf{F}$ is the vector of fluxes and the subscripts R and L indicate the right and left side of the interface, respectively. Using this expression it can be seen that the influence of the extrapolation method on the kinetic energy dissipation rate can be understood as the combination of two effects.

The first term on the right hand side of (3.8.9) is directly computed from the extrapolated quantities thus it is an approximation of the flux to a certain order of accuracy. In finite volume methods the filtered quantity is inverted to recover the continuous function to estimate the extrapolated cell interface values. The numerical grid is assumed to be equivalent to a top hat filter in physical space, i.e.

$$\bar{U} = \frac{1}{\Delta Vol}\int_0^{\Delta v} U \Delta Vol, \tag{3.8.11}$$

where $\bar{U}$ indicates the cell averaged quantity, and $\Delta Vol = \Delta x \Delta y \Delta z$. The inversion is usually done using a Taylor series expansion of the top hat filter, and shows that the

leading order difference between the cell averaged quantity and continuous function measured at the cell centre are at second order, i.e. in one dimension (for more details see [159, 128, 28])

$$U = \bar{U} - \frac{\Delta x^2}{24}\bar{U}_{xx} + O\Delta x^4, \tag{3.8.12}$$

where $(.)_x$ indicates a derivative with respect to x. In the construction of schemes with accuracy higher than second-order, this conversion has to be taken into account in the design of the scheme. This implies that higher order schemes inherently include some leading order influences of the subgrid variations for the resolved modes (either turbulent or laminar variations). For example, at third-order accuracy the leading order kinetic energy dissipation term can be determined from Modified Equation Analysis (MEA) following the methodology in [126, 128].

To date published results have focused on the incompressible Euler equations, but extensions to compressible are currently in progress by Rider and Margolin. The first step in this process is to write the extrapolated quantities as a function of the cell averaged quantity, expanding the interface value in a Taylor series as is done when deriving truncation terms for the linear advection equation. Next, subtract the exact Euler equations and gather together the leading order terms in powers of Δx, Δy and Δz. These remaining terms form the truncation error. As an example, taking third-order accurate extrapolated quantities, the leading order terms can be written as the divergence of a tensor τ. In two dimensions

$$\tau^{xx} = -\frac{\Delta x^2}{12}u_x^2 - \frac{\Delta y^2}{12}u_y^2, \tag{3.8.13}$$

$$\tau^{xy} = \tau^{yx} = -\frac{\Delta x^2}{12}u_x v_x - \frac{\Delta y^2}{12}u_y v_y, \tag{3.8.14}$$

$$\tau^{yy} = -\frac{\Delta x^2}{12}v_x^2 - \frac{\Delta y^2}{12}v_y^2. \tag{3.8.15}$$

An equivalent results is also achieved through Approximate Deconvolution, as detailed in [28, 159]. The dissipation of kinetic energy due to this stress tensor is

$$\frac{dE_D}{dt} = -\int_D \left(u_x\tau^{xx} + u_y\tau^{xy} + v_x\tau^{yx} + v_y\tau^{yy}\right) DXDY, \tag{3.8.16}$$

where E_D now indicates the kinetic energy in a domain of size $DXDY$ without external forces . This gives

$$\frac{dKE}{dt} = \frac{\Delta x^2}{12}\left[\left\langle u_x^3\right\rangle + \left\langle u_x u_y v_x\right\rangle\right] + \frac{\Delta y^2}{12}\left[\left\langle v_y^3\right\rangle + \left\langle u_y v_x v_y\right\rangle\right] \tag{3.8.17}$$

The leading order terms are proportional to the skewness of the velocity derivative, which is negative in turbulent flows thus providing dissipation of resolved kinetic energy. Naturally, higher order extrapolation methods will approximate the subgrid variations to a higher order of accuracy for modes which can be resolved on a given grid.

The extrapolation method also influences the second term in (3.8.9) through the difference of the left and right extrapolated quantities. Ideally this should remove kinetic energy from the system in a form similar to the action of subgrid vortices on the resolved vortices. Kolmogorov proposed the following similarity hypothesis [110, 111]

$$L\bar{\epsilon_L} = \frac{5}{4}\overline{\Delta u^3} \tag{3.8.18}$$

where $\bar{\epsilon_L}$ is the dissipation rate averaged over the distance L, and Δu is the velocity increment. This represents the dissipation due to homogeneous isotropic turbulence per unit time per unit area.

The only time that kinetic energy is irreversibly changed into heat in the solution of a Riemann problem is between a shock wave and contact surface. All other flow features are isentropic. As determined in [19, 98] the entropy change ΔS due to the passage of a shock wave can be written as

$$\Delta S = -\left.\frac{\partial^2 p}{\partial V^2}\right|_S \frac{\Delta V^3}{12T}, \tag{3.8.19}$$

where V is the specific volume, p is the pressure, and T is the temperature. Using the Hugoniot relations and under the assumption of a perfect gas this can be written as

$$T\Delta S = -\frac{(\gamma+1)\,a^2}{12}\left(\frac{\Delta u_s}{u_1}\right)^3, \tag{3.8.20}$$

where γ is the ratio of specific heats, a is the sound speed, Δu_s is the velocity jump over the shock wave and u_1 the pre-shock velocity relative to the shock. This gives a measure of the irreversible dissipation of kinetic energy in the Riemann solution, an increase of specific internal energy at the cost of specific kinetic energy. Thus at an interface where the solution of a Riemann problem lies between the contact surface and shock wave there will be an effective dissipation of kinetic energy proportional to Δu^3 - analogous to (3.8.18). The choice of extrapolation method directly influences the magnitude of the velocity jump, thus modifying the dissipative properties of the numerical scheme.

An important implication of this is that the differences between the extrapolated quantities (i.e. $U_R - U_L$) are as important as the formal order of accuracy of the extrapolation in characterising the dissipative properties of the scheme.

An additional component to consider is the behaviour of the extrapolation methods as regards monotonicity. MUSCL schemes are strictly monotonic, however WENO

methods are not. Oscillations in one dimension are manifested as vortex breakdown in two and three dimensions. This dispersive behaviour of the very high-order methods can inject energy at the small scales, altering the kinetic energy spectrum.

Given a perfect subgrid model, an LES at several different resolutions should be identical given that the cutoff wave number lies within the inertial range. However, it is expected that the model is not perfect, thus increasing the resolution should have the effect of reducing the effects of the numerical method on a given mode, shifting it to higher wave numbers. Thus any errors induced via the subgrid model should decrease with increased resolution and order of the schemes.

The numerical methods employed here satisfy the second law of thermodynamics on a global level. This is one of the main advantages of employing shock capturing methods, as conventional LES typically employs a scheme which is not shock capturing and hence generates spurious oscillations in violation of the second law of thermodynamics.

3.9 Flow Field Initialisation

3.9.1 Initialisation of Non-Divergent Homogeneous Turbulence

This section will describe the method utilised to initialise a turbulent flow field with a prescribed mean square velocity, kinetic energy, and with a kinetic energy spectrum given by

:

$$E(k) = Ck^4 \exp\left(-2\left(k/k_p\right)^2\right). \tag{3.9.1}$$

This spectrum is derived considering the case of dominating viscous effects in a homogeneous turbulent velocity field [82]. The peak in the energy spectrum is predefined by changing the peak k_p in the exponential.This field could then be superimposed on top of a mean flow, or to provide a homogeneous turbulent field for fundamental studies of turbulent decay. The following derivation and computational method was provided by D. Youngs of AWE.

To guarantee the generation of a non-divergent (i.e. incompressible) velocity field, the velocity can be formed from components of a vector potential Φ, which satisfies the following relationship:

$$u = \nabla \times \Phi. \tag{3.9.2}$$

As the divergence of a curl is identically equal to zero, then this forms a non-divergent velocity field. By considering the form of the energy spectrum in equation (3.9.1) an expression for the vector potential Φ can be formed. Firstly, the total kinetic energy KE in the flow can be calculated:

$$\begin{aligned} KE &= \frac{1}{2}\int_0^\infty [u(k)]^2\, dk \\ &= \int_0^\infty E(k)dk \\ &= \int_0^\infty \int_0^\infty \int_0^\infty E(k)/\,|k|^2\, dk_x dk_y dk_z. \end{aligned} \tag{3.9.3}$$

Using equation (3.9.1):

$$KE(\mathbf{k}) = \int_0^\infty \int_0^\infty \int_0^\infty \left[\, \sqrt{C}k \exp\left(-\left(k/k_p\right)^2\right)\right]^2 dk_x dk_y dk_z. \tag{3.9.4}$$

Comparing equations (3.9.3) and (3.9.4) it is clear that the velocity is of the form $\sqrt{C}k \exp\left(-\left(k/k_p\right)^2\right)$.

As the velocity is the first derivative of the vector potential, the components of $\overrightarrow{\Phi(k)}$ are of the form:

$$\Phi(\mathbf{k}) = \sqrt{C} \exp\left(-\left(k/k_p\right)^2\right). \tag{3.9.5}$$

Due to the Gaussian form of the vector potential, the higher wave numbers contribute very little to the overall magnitude in real space. As an example, if k_p=4, the contribution to the overall energy at k=30 is sixteen orders of magnitude lower than the peak. To economise on computing time and memory resources, the inverse Fourier transform of equation (3.9.5) can be truncated at a small multiple of k_p. Noting that the vector potential is a real function:

$$\Phi(x,y,z) = \sum_{l,m,n=-\infty}^{\infty} \text{Real}\left\{c_{l,m,n} \exp\left[Ik_0\left(lx + my + nz\right)\right]\right\}, \tag{3.9.6}$$

where $k_0 = 2\pi/L$. To satisfy the given energy spectrum, equations (3.9.5) and (3.9.6) must be identical in the limit of infinite l, m and n. For this to occur the complex coefficients $c_{l,m,n}$ must have the Gaussian distribution of the form shown in equation (3.9.5). Firstly, equation (3.9.6) can be simplified considerably by expanding using the Euler formula, and considering only the real part of the equation:

$$\Phi(x,y,z) = \sum_{l,m,n=-\infty}^{\infty} r_{l,m,n} \cos\left[k_0\left(lx + my + nz\right) + \phi_{l,m,n}\right], \tag{3.9.7}$$

where $c_{l,m,n} = c_1 + Ic_2$, thus $r_{l,m,n} = \sqrt{c_1^2 + c_2^2}$ and $\phi = \tan\left(c_2/c_1\right)$. Next, the cosine term is expanded using trigonometric relations giving:

$$\begin{aligned}\Phi(x,y,z) &= 2\sum_{l,m,n=-\infty}^{\infty} r_{l,m,n}\cos\phi \times \\ &\{[\cos(k_0 lx)\cos(k_0 my) - \sin(k_0 lx)\sin(k_0 my)]\cos(k_0 nz) - \\ &[\cos(k_0 lx)\sin(k_0 my) + \sin(k_0 lx)\cos(k_0 my)]\sin(k_0 nz)\} + \\ &r_{l,m,n}\sin\phi \times \\ &\{[\sin(k_0 lx)\sin(k_0 my) - \cos(k_0 lx)\cos(k_0 my)]\sin(k_0 nz) - \\ &[\cos(k_0 lx)\sin(k_0 my) + \sin(k_0 lx)\cos(k_0 my)]\cos(k_0 nz)\}.\end{aligned} \tag{3.9.8}$$

This has the advantage that all of the data can be stored in two dimensional arrays of maximum size $k_{max} \times N_{max}$. To initialise a random field $c_{l,m,n}$ must be chosen from a distribution randomly such that the mean $\langle c_{l,m,n} \rangle$ gives the Fourier coefficients in equation (3.9.5). In this case they are selected from a Gaussian distribution with mean of zero and standard deviation of one - but with non-unitary area. This is selected so that the peak of the Gaussian is one. The Gaussian curve of the real part c_1 and imaginary part c_2 of $c_{l,m,n}$ is therefore:

$$G = \exp\left[-\left(c_1^2 + c_2^2\right)/2\right]. \tag{3.9.9}$$

Assuming that $c_{l,m,n} = c_1 + ic_2$:

$$c_1 = r\cos\phi, \tag{3.9.10}$$

$$c_2 = r\sin\phi. \tag{3.9.11}$$

G can now be rewritten as:

$$G = \exp\left[-r^2/2\right]. \tag{3.9.12}$$

Given two random numbers R_1 and R_2 between 0 and 1, a method of sampling a Gaussian distribution is used. First a random direction is chosen in the $r - \phi$ plane, then the magnitude of r is determined by rearranging equation (3.9.12) after setting $G = R_2$:

$$\phi = 2\pi R_1, \tag{3.9.13}$$

$$r = \sqrt{-2\ln(R_2)}, \tag{3.9.14}$$

The computational expense can be further reduced by utilising eight coefficients and summing over one of the eight octants, leading to the final expression utilised in the code.

$$\begin{aligned}\Phi(x,y,z) \;=\; & \sum_{l,m,n=0}^{\infty} a_{l,m,n}\cos(k_0 lx)\cos(k_0 my)\cos(k_0 nz) + \\ & b_{l,m,n}\cos(k_0 lx)\cos(k_0 my)\sin(k_0 nz) + \\ & c_{l,m,n}\cos(k_0 lx)\sin(k_0 my)\cos(k_0 nz) + \\ & d_{l,m,n}\cos(k_0 lx)\sin(k_0 my)\sin(k_0 nz) + \\ & e_{l,m,n}\sin(k_0 lx)\cos(k_0 my)\cos(k_0 nz) + \\ & f_{l,m,n}\sin(k_0 lx)\cos(k_0 my)\sin(k_0 nz) + \\ & g_{l,m,n}\sin(k_0 lx)\sin(k_0 my)\cos(k_0 nz) + \\ & h_{l,m,n}\sin(k_0 lx)\sin(k_0 my)\sin(k_0 nz)\,.\end{aligned} \tag{3.9.15}$$

Now equation (3.9.15) has to be modified to compensate for the doubling of contributions from the zeroth wave number. If it is assumed that $l, m, n > 0$ then the total kinetic energy can be written following equation (3.9.4):

$$KE = \int_0^{\infty} |\mathbf{k}|^2 \left[k\overline{\Phi(\mathbf{k})}\right]^2 d\mathbf{k}, \tag{3.9.16}$$

where $\overline{\Phi(\mathbf{k})}$ is the mean of the contributions of the Fourier coefficients. As:

$$\sqrt{\overline{cos(x)^2}} = 1/2, \tag{3.9.17}$$

then:

$$\sqrt{\overline{\left(a_{l,m,n}\cos(k_0 lx)\cos(k_0 my)\cos(k_0 nz)\right)^2}} = \overline{a_{l,m,n}^2}/8, \tag{3.9.18}$$

so the root mean square contribution of the coefficients $a_{l,m,n}$, $b_{l,m,n}$... at one mode of $l, m, n > 0$ to the total kinetic energy is:

$$KE = \int_0^{\infty} |\mathbf{k}|^2 \left[0.125k^2\left(\overline{a_{l,m,n}^2 + b_{l,m,n}^2 + c_{l,m,n}^2 + d_{l,m,n}^2 + e_{l,m,n}^2 + f_{l,m,n}^2 + g_{l,m,n}^2 + h_{l,m,n}^2}\right)\right] d\mathbf{k}. \tag{3.9.19}$$

Now if $l = 0$, the contributions from the $\sin(k_0 lx)$ can be neglected, thus the total contribution is:

$$KE = \int_0^{\infty} |\mathbf{k}|^2 \left[0.25k^2\left(\overline{a_{l,m,n}^2 + b_{l,m,n}^2 + c_{l,m,n}^2 + d_{l,m,n}^2}\right)\right] d\mathbf{k}, \tag{3.9.20}$$

as the mean of $\cos(0) = 1$. This is not correct, as it counts the contributions from the zeroth mode twice in the summation in equation (3.9.15). To compensate for this each coefficient is calculated as follows, using $a_{l,m,n}$ as an example:

$$a_{l,m,n} = RS(l)S(m)S(n)\exp\left(-\left(k/k_p\right)^2\right), \tag{3.9.21}$$

where S(p)=1/ $\sqrt{2}$ if $p = 0$, 1 if $p > 0$ and R is a random number picked from a Gaussian distribution (e.g. c_1). Thus when $l = 0$ and $m, n > 0$ the contribution is now correct, given by:

$$KE = \int_0^\infty |\mathbf{k}|^2 \left[0.125k^2\left(\overline{a_{l,m,n}^2 + b_{l,m,n}^2 + c_{l,m,n}^2 + d_{l,m,n}^2}\right)\right] d\mathbf{k}. \tag{3.9.22}$$

As a final step the kinetic energy is rescaled linearly to equal a known constant, and the mean velocities shifted to equal zero (for the homogeneous turbulence case).

3.9.2 Initialisation of a Multimode Perturbed Interface

The most realistic method of representing a two-dimensional interface between two materials is as the summation of a number of individual modes in accordance with a certain spectra. The method of initialisation is similar to that employed to initialise homogeneous turbulence in Section 3.9.1. The typical inertial confinement capsule has a surface power spectrum expressed as:

$$\begin{aligned} P = sd^2 &= \int_0^\infty [A(k)]^2\, dk && (3.9.23)\\ &= \int_0^\infty \frac{1}{k^2} dk \\ &= \int_0^\infty \int_0^\infty \frac{1}{k^2}\frac{1}{2\pi|k|} dk_y dk_z \\ &\propto \int_0^\infty \int_0^\infty \frac{1}{k^3} dk_y dk_z, && (3.9.24) \end{aligned}$$

where sd is the standard deviation of the perturbation, and $A(\mathbf{k})$ the amplitude of the perturbation. The specified power spectrum gives an equivalent amplitude $A(\mathbf{k})$ in wave space:

$$A(\mathbf{k}) \propto \frac{1}{k^{3/2}}. \tag{3.9.25}$$

To initialise modes within a certain band, the inverse Fourier transform of equation (3.9.25) can be taken, noting that the amplitude is a real function:

$$A(y,z) = \sum_{m,n=-\infty}^{\infty} Real\left\{c_{m,n}\exp\left[Ik_0(my+nz)\right]\right\}, \tag{3.9.26}$$

where $k_0 = 2\pi/L$. To satisfy the given power spectrum, equations (3.9.25) and (3.9.26) must be identical. For this to occur, the complex coefficients $c_{m,n}$ must have the form shown in equation (3.9.25). Firstly, equation (3.9.26) can be simplified considerably by expanding using the Euler formula, and considering only the real part of the equation:

$$A(y,z) = \sum_{m,n=-\infty}^{\infty} r_{m,n} \cos\left[k_0 \left(my + nz\right) + \phi_{m,n}\right], \tag{3.9.27}$$

where $c_{m,n} = c_1 + ic_2$, thus $r_{m,n} = \sqrt{c_1^2 + c_2^2}$ and $\phi = \tan\left(c_2/c_1\right)$. Next, the cosine term is expanded using trigonometric relations giving:

$$\begin{aligned} A(y,z) = \sum_{m,n=-\infty}^{\infty} & r_{m,n} \cos\phi \times \left[\cos\left(k_0 my\right)\cos\left(k_0 nz\right) - \sin\left(k_0 my\right)\sin\left(k_0 nz\right)\right] - \\ & r_{m,n} \sin\phi \times \left[\sin\left(k_0 my\right)\cos\left(k_0 nz\right) + \cos\left(k_0 my\right)\sin\left(k_0 nz\right)\right]. \end{aligned} \tag{3.9.28}$$

This has the advantage that all of the data can be stored in two dimensional arrays of maximum size $k_{max} \times N_{max}$. The computational expense can be further reduced by utilising four coefficients and summing over one of the four quadrants, leading to the final expression utilised in the code.

$$\begin{aligned} A(y,z) = \sum_{m,n=0}^{\infty} & a_{m,n} \cos\left(k_0 my\right)\cos\left(k_0 nz\right) + b_{m,n} \cos\left(k_0 my\right)\sin\left(k_0 nz\right) + \\ & c_{m,n} \sin\left(k_0 my\right)\cos\left(k_0 nz\right) + d_{m,n} \sin\left(k_0 my\right)\sin\left(k_0 nz\right). \end{aligned} \tag{3.9.29}$$

To initialise a random field $a_{m,n}$, $b_{m,n}$.... must be chosen from a distribution randomly so that the mean gives the Fourier coefficients in equation (3.9.25). The random variables are selected from a Gaussian distribution as detailed in Section 3.9.1. Now equation (3.9.29) must be modified to compensate for the doubling of contributions from the zeroth wave number as done previously for homogeneous turbulence. Each coefficient is calculated as follows, using $a_{m,n}$ as an example:

$$a_{m,n} = RS\left(m\right)S\left(n\right)\frac{1}{k^{3/2}}, \tag{3.9.30}$$

where $S\left(p\right) = 1/\sqrt{2}$ if $p = 0$, 1 if $p > 0$ and R is a random number picked from a Gaussian distribution. Equation (3.9.30) is calculated as part of the initialisation process, and as a final step the standard deviation is rescaled linearly to equal a predefined value, and the mean amplitude shifted to equal zero.

Once the interface has been defined, it is necessary to set up the initial conditions as accurately as possible. In most simulations the perturbations are at a sub-grid scale,

so they must be represented to reasonable accuracy. To achieve this, cells located on the interface are initialised as a mixture, and not simply as one component or another. The volume fraction of one gas within a cell is computed as the average position of the interface at each face of the cell. As an example, if the interface defined by $\mathcal{S}_{i,j,k}$ is located in the $y-z$ plane, with cell indices i, j and k for the x, y, and z plane respectively, the volume fraction is estimated via a linear interpolation:

$$\alpha = \frac{x_{i+1/2,j,k} - \left[\mathcal{S}_{i,j-1/2,k} + \mathcal{S}_{i,j+1/2,k} + \mathcal{S}_{i,j,k-1/2} + \mathcal{S}_{i,j,k+1/2}\right]/4}{x_{i+1/2,j,k} - x_{i-1/2,j,k}}. \tag{3.9.31}$$

CHAPTER 4

Homogeneous Decaying Turbulence

4.1 Introduction

One of the key requirements for a numerical scheme used to investigate shock-induced turbulent mixing is that it can accurately simulate low Mach turbulent features. This chapter assesses the performance of high-order Godunov-type methods for turbulent applications via simulations of low Mach number ($M = 0.1$) homogeneous decaying turbulence. The study does not intend to prove that ILES is a better approach than standard LES, based on explicit subgrid scale models, for the flow in question. It is intended as a starting point for further development by identifying quantitatively the strengths and weaknesses of high-resolution methods used in ILES by comparing the ILES results with experimental studies, DNS and previous LES.

It is a complementary extension of the work of Garnier *et al.* [62], where the ability of shock-capturing schemes was tested for resolutions up to 128^3 and for six extrapolation methods from second- to fifth-order. The authors concluded that the dissipation rate of the ILES methods is too high, and that the behaviour of the schemes is more akin to a low Reynolds DNS than an LES. In the present work, the extrapolation methods employed are less diffusive and range from MUSCL second-order through to WENO ninth-order accurate. Each of these extrapolation methods have been run on grids from 32^3 to 256^3 to examine the behaviour and convergence (if any) of turbulent statistics and spectra.

The layout of the chapter is as follows. Section 4.2 details the numerical scheme employed, and the method used to initialise a homogeneous, isotropic turbulent field. The effect of non-zero velocity divergence in the flow field is discussed. Section 4.3 compares the quantitative behaviour of the seven ILES variants in terms of fundamental properties of a turbulent flow field; growth of the integral length scale; decay rate of turbulent kinetic energy; time variation of enstrophy; skewness and flatness of the velocity derivative; velocity increment and pressure fluctuation probability distribution functions; kinetic energy spectra; effective numerical filter and spectral numerical viscosity. Section 4.4 concludes this chapter.

4.2 Simulation Details

4.2.1 Governing Equations

For all simulations in this chapter it is considered that the Kolmogorov scale is significantly smaller that the mesh size, equivalent to stating that the viscous effects are negligible. Therefore, the Reynolds number $Re \rightarrow \infty$ and the Navier-Stokes equations reduce to the Euler equations. The system of equations is completed with the specification of an equation of state for an ideal gas.

4.2.2 Numerical Scheme

The computations were carried out using a finite volume Godunov-type method. The flux terms are evaluated by a characteristics-based Riemann solver [55]. TVD time stepping is required for the WENO schemes to retain numerical stability, thus time advancement is achieved using a third-order TVD Runge Kutta method [69]. Simulations using both the TVD time-stepping and third-order extended stability Runge-Kutta [69] with MUSCL limiters show that the kinetic energy decay exponent and mean velocity derivative moments up to sixth-order vary by less than 1%. This is expected as the CFL condition ensures that the time step is significantly smaller than the spatial step.

In this chapter the full range of extrapolation methods detailed in Section 3.4 are tested; MUSCL second-order methods Minmod (MM), van Leer (VL) and van Albada (VA) ([184, 53]; MUSCL third-order method (M3); MUSCL fifth-order,(M5) [107]; and finally WENO fifth- and ninth-order (W5 and W9)[11]. The details of these limiting methods are presented in Section 3.4.

4.2.3 Initialisation

The flow field was initialised using the method derived in section 3.9.1, and utilised in previous simulations of decaying turbulence [195, 197]. The flow field has an initial kinetic energy spectrum given by the analytical solution in the case of dominating viscous effects [82]

$$E(k) = u_{rms}^2 \frac{k^4}{k_p^4} \sqrt{\frac{8}{k_p^2 \pi}} \exp\left(-2\left(k/k_p\right)^2\right), \tag{4.2.1}$$

where k is the wave number, and the peak in the energy spectrum is defined by changing the peak k_p in the exponential. Unless otherwise stated the peak of the energy spectrum was chosen at $k_p = 4$ to aid comparison with previous results from Youngs [195, 197]. To ensure the generation of an almost non-divergent (i.e. incompressible) velocity field, the velocity is formed from components of a vector potential Φ, which satisfies the following relationship:

$$u = \nabla \times \Phi \tag{4.2.2}$$

As the divergence of a curl is identically equal to zero this gives a non-divergent velocity field. The vector potential is initialised with a Gaussian distribution of amplitudes and random phases which is rescaled linearly to give a velocity field satisfying

$$KE = \frac{3}{2} u_{rms}^2 = 0.5, \tag{4.2.3}$$

$$M = \frac{u_{rms}}{a} = 0.1, \tag{4.2.4}$$

where u_{rms} is the mean turbulent velocity. Further details of the initialisation can be found in Section 3.9.1. Although this gives zero velocity divergence in the initial condition, the rate of change of divergence of velocity is not necessarily zero, as has been reported by several authors [22, 56, 149, 160, 168]. The effectiveness of this method was investigated by decomposing the compressible and incompressible velocity fields in Fourier space using the Helmholtz decomposition. This splits an arbitrary vector into solenoidal (i.e. incompressible) and dilational (compressible) components [22, 56, 149, 160, 168]. The velocity in Fourier space can be written as a sum of the solenoidal and dilational velocity components:

$$u(\mathbf{k}) = u_s(\mathbf{k}) + u_d(\mathbf{k}), \tag{4.2.5}$$

where,

$$\nabla \cdot u_s(\mathbf{k}) = 0, \tag{4.2.6}$$

which in Fourier space can be written as,

$$\mathbf{k} \cdot u_s(\mathbf{k}) = 0. \tag{4.2.7}$$

Now the Fourier transform of the velocity field can be written with respect to the normal and parallel components of the wave vector $\mathbf{k}$

$$u(\mathbf{k}) = \underbrace{c_1(\mathbf{k})\mathbf{k}_n}_{u_s} + \underbrace{c_2(\mathbf{k})\mathbf{k}_p}_{u_d} \tag{4.2.8}$$

Next take the dot product of (4.2.8) with the wave vector $\mathbf{k}$

$$\mathbf{k} \cdot u(\mathbf{k}) = \mathbf{k} \cdot c_2(\mathbf{k})\mathbf{k}_p = c_2 |\mathbf{k}|^2 \tag{4.2.9}$$

$$c_2 = \frac{\mathbf{k} \cdot u(\mathbf{k})}{|\mathbf{k}|^2}, \tag{4.2.10}$$

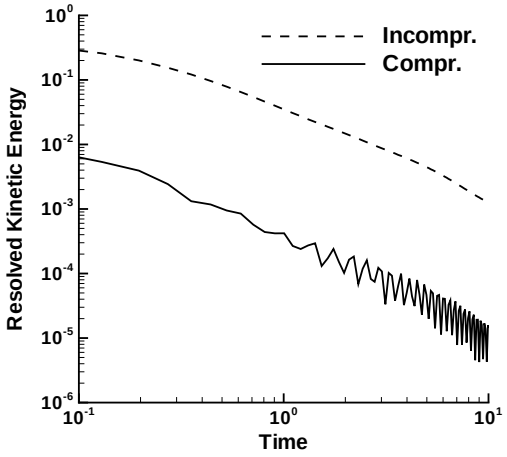

Figure 4.1: The amount of kinetic energy contained in the incompressible and compressible modes in a 32^3 simulation using VL extrapolation

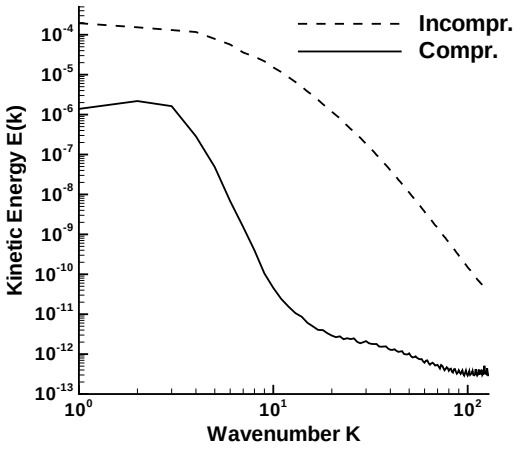

Figure 4.2: The compressible and incompressible kinetic energy spectra for a 256^3 using VL extrapolation

this gives the compressible part of the velocity field. The solenoidal and dilational components can be calculated given the three dimensional Fourier transform of the velocity field

$$u_s(\mathbf{k}) = u(\mathbf{k}) - \frac{\mathbf{k} \cdot u(\mathbf{k})}{|\mathbf{k}|^2}\mathbf{k}, \tag{4.2.11}$$

$$u_d(\mathbf{k}) = u(\mathbf{k}) - u_s(\mathbf{k}). \tag{4.2.12}$$

Figure 4.1 shows the total resolved kinetic energy in the compressible and incompressible modes respectively for a 32^3 VL simulation. The energy in the compressible modes is about three orders of magnitude less than the energy in the incompressible modes and decreases as the simulation continues. It was found that even for Mach

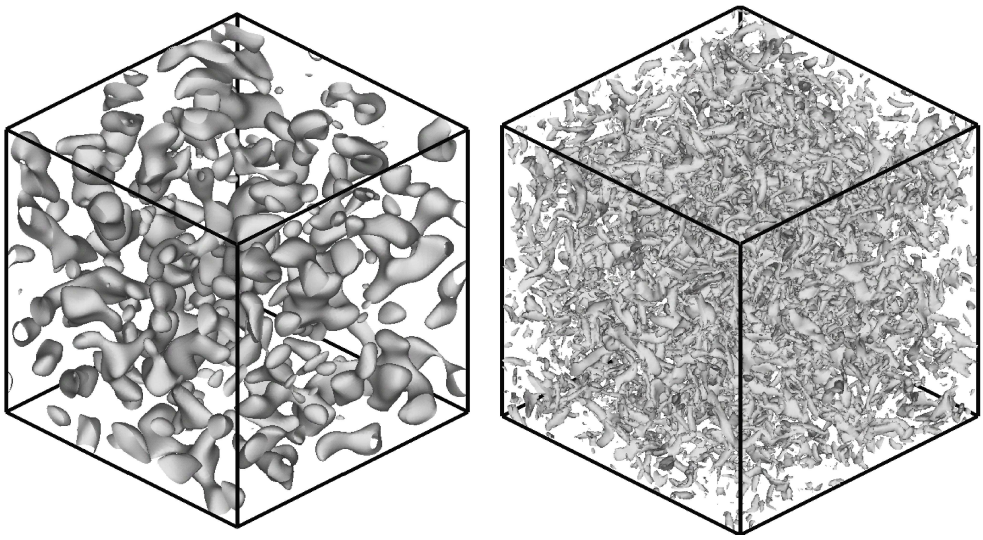

(a) $t = 0$ (b) $t = 1$

Figure 4.3: Iso-vorticity surfaces at $\sqrt{\omega^2} = 5$ illustrating the initial condition and fully developed homogeneous turbulence in a 128^3 using M5 extrapolation

$= 0.5$ the compressible component at initialisation is less than 1%. Comparisons with previous results [22, 56, 149, 160, 168] show that the initial conditions are effectively reducing the influence of velocity divergence effects. A key observation of the evolution of the kinetic energy in the compressible component is that it is highly oscillatory. Kovasnay [112] showed that in the absence of viscosity and at low Mach number the vorticity, pressure and entropy are decoupled; viscosity acts to couple the pressure and entropy, but the vorticity remains decoupled. This decoupling leads to the oscillations in compressible kinetic energy at late times. The spectra shown in Figure 4.2 illustrate that the energy in the compressible modes is largely restricted to the lower wave numbers. The undesirable aspect of this is that on the short time scales the rate of change of energy at low wave numbers is oscillatory due to the compressible modes. Hence, the kinetic energy dissipation rate at a given point in time must be computed as an average of the rate of change centred on the time point of interest.

Figure 4.3 shows isosurfaces of equal vorticity magnitude taken at $t = 0$ and $t = 1$ for the 128^3 case with M5 extrapolation. This shows the initial flow field composed of low wave number modes, and the fine scale worm like vortical structures present in the fully developed turbulent flow field. The form of the structures present in the flow field does not change at later times. Figure 4.4 shows the development of the skewness at each of the mesh resolutions for M5 demonstrating that a steady state is achieved after a relatively short period of time allowing for good statistical averages, especially at the higher resolutions. The simulations were run to a non-dimensional time of $t = 5$ for all mesh resolutions, corresponding to approximately 8 eddy turnover times.

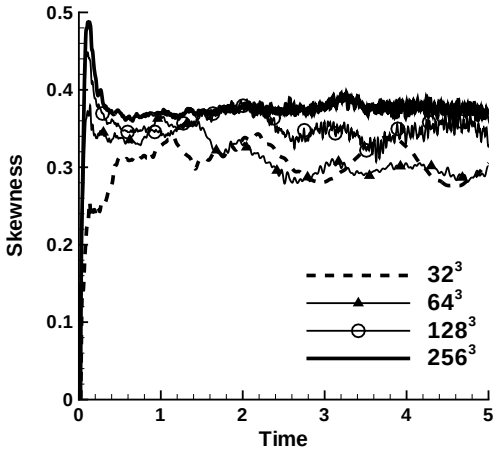

Figure 4.4: Velocity derivative skewness as a function of time at several resolutions using M5 extrapolation

4.3 Results and Discussion

4.3.1 Turbulent Isotropy

It is important to quantify turbulent isotropy, as turbulent theory relies on this assumption to derive analytical expressions for kinetic energy decay rates and growth of the length scales. The integral length was calculated from the longitudinal and transverse energy spectra using [44, 178]

$$\ell = \frac{\pi}{u_{rms}^2} E_{11}(k=0), \tag{4.3.1}$$

$$\ell = \frac{2\pi}{u_{rms}^2} E_{22}(k=0), \tag{4.3.2}$$

where,

$$E_{11}(k_1) = \frac{1}{\pi}\left\langle u_1^2 \right\rangle \int_0^\infty dx_1 f(x_1)\cos k_1 x_1, \tag{4.3.3}$$

$$E_{22}(k_1) = \frac{1}{\pi}\left\langle u_1^2 \right\rangle \int_0^\infty dx_1 g(x_1)\cos k_1 x_1, \tag{4.3.4}$$

and f and g are the second-order longitudinal and lateral correlation functions relative to the 1-direction. These are then averaged in all three directions. Both definitions of the integral length agree to within ten percent throughout the period of the simulations, however, it is observed that the simulations become increasingly more anisotropic at late times. There is a considerable anisotropy evident in the mean velocities for the 32^3, as it is extremely under-resolved. At this resolution there are only 8 cells per wavelength even at the peak of the energy spectrum. Above 32^3 the maximum mean square

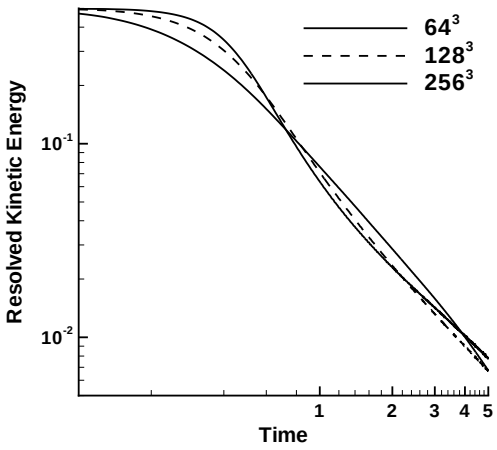

Figure 4.5: Resolved kinetic energy in simulations using the MUSCL 5th order limiter at different resolutions

turbulent velocities in each direction match the mean turbulent velocity to within 6% throughout the simulation.

4.3.2 Kinetic Energy Decay Rate and Growth of the Length Scales

It is widely accepted that the evolution of kinetic energy in homogeneous isotropic turbulence can be written as follows [82]:

$$\frac{3}{2}u_{rms}^2 = A(t - t_0)^{-\mathcal{P}}, \tag{4.3.5}$$

where A is a constant, t_0 is the virtual origin in time, and $\mathcal{P}$ is a positive constant. If the exponent is not in a physically realistic range then the simulations will rapidly decorrelate with reality. In addition to this, the growth of the energy containing scales, i.e. the integral length scale, must be represented accurately, as these eddies typically represent the dominating structures in the flow. The growth of the integral length scale is

$$\ell = B\,(t - t_0)^q\,, \tag{4.3.6}$$

and q is a positive constant [144]. To facilitate comparison with conventional LES studies, the virtual origin in time $t_0 = 0$ when computing the mean kinetic energy decay exponent and growth of the integral length scales.

Figure 4.5 shows the total resolved kinetic energy using the MUSCL fifth-order extrapolation method. Only resolutions of above 32^3 are shown for clarity. There is very little decay in kinetic energy in the first instant as the energy is being transferred from the

Table 4.1: Mean kinetic energy decay exponent $\mathcal{P}$

Resolution	MM	VA	VL	M3	M5	W5	W9
32^3	0.96	1.19	1.33	1.17	1.32	1.48	1.56
64^3	1.32	1.45	1.39	1.36	1.58	1.44	1.47
128^3	1.27	1.52	1.49	1.47	1.41	1.44	1.28
256^3	1.28	1.43	1.36	1.32	1.25	1.30	1.16

low to high wave numbers. Once the high wave numbers are populated, the numerical dissipation increases until an approximately constant power law decay is seen.

Wind tunnel experiments using grid generated turbulence have measured kinetic energy decay rates $\mathcal{P} \approx 1.2 - 1.3$ [41, 138, 140, 169, 100]. Theoretical analysis does not give a clear solution, however, it is expected that the decay should lie between $\mathcal{P} \approx 1.2$ [21, 144] and $\mathcal{P} \approx 1.4$ [119, 193, 192]. Recent DNS at $Re_{\lambda_{tay}} < 250$ by Ishida *et al.* [90] with an initial spectrum proportional to k^4 gave $\mathcal{P} = 10/7$. The mean decay exponent $\mathcal{P}$ from t=1 to 5 for each extrapolation method is detailed in Table 4.1.

At 32^3 all second and third-order methods exhibit a decay rate which is significantly less than physically expected. As will be discussed in the following section, the velocity derivative moments for these schemes at this resolution returns rapidly to Gaussian, thus no turbulent field exists. Excessive numerical dissipation acts on the resolved modes, as even at the peak of the kinetic energy spectrum there are only 8 cells per wavelength. It should be noted that the decay rate alone cannot characterise a numerical method as the decay rate depends on the resolved features. For example, a method may have a low mean decay rate simply because all short wave perturbations have been dissipated from the system at an early time - this is the case with the Minmod limiter at 32^3.

The decay exponent for the Minmod limiter at 64^3 is in excellent agreement with the quoted value of $\mathcal{P} = 1.3$ for 64^3 in Garnier *et al.* [62], thus confirming the consistency of the comparison. However, the other schemes exhibit a less diffusive behaviour. At higher resolutions, and at higher orders of accuracy, the decay exponent lies between 1.16 and 1.58 for all methods employed, whereas [62] report $\mathcal{P} > 2$. The results here are in good agreement with the previous study by Youngs [195] which reported $\mathcal{P} = 1.41$ using a Lagrangian based ILES code with the same initialisation method.

Compared to the experimentally determined decay exponents these results are higher, however, there is uncertainty in the choice of the virtual origin t_0 in both simulation and experiment. The ILES methods compare favourably with conventional LES, where the decay exponent $\mathcal{P} = 1.17 - 2$ [135, 27, 190, 9, 87, 179, 78, 35].

In comparing the limiters, the two fifth-order methods and W9 give the most physically realistic kinetic energy decay rates at low resolution. At all other resolutions the decay rate remains within a physically realistic range for all limiters, given the uncertainties in determining t_0.

Two additional simulations of 256^3 resolution were carried out with the Minmod lim-

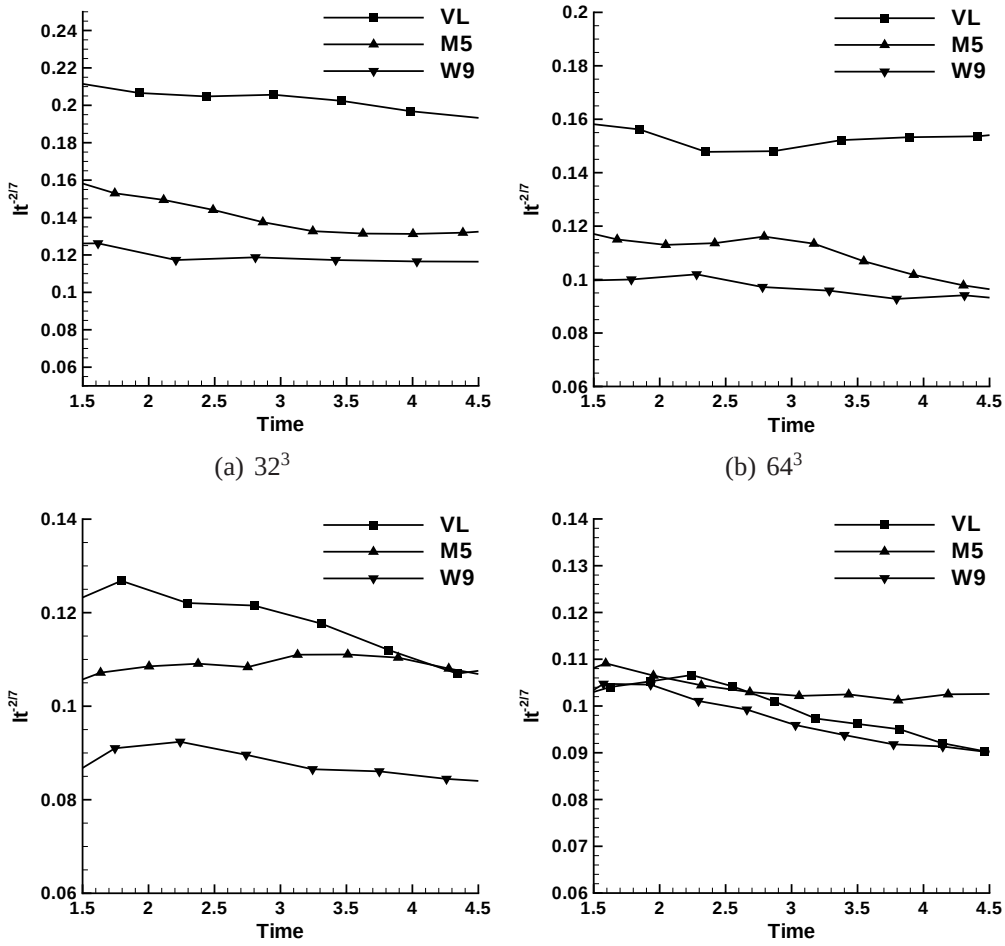

Figure 4.6: Normalised integral length $\ell t^{-2/7}$ plotted against time for different resolutions

iter, where the peak of the initial energy spectrum were chosen $k_p = 1$ and 12, respectively. The two simulations differ quite significantly in flow structure and behaviour. The lower the initial peak of the spectrum, the longer the period of redistribution of energy before a power-law decay of kinetic energy begins. The average decay exponent $\mathcal{P}$ is 2.12 for $k_p = 1$ and 1.29 for $k_p = 12$. The theoretical decay rate of constrained turbulence (i.e. when the energy containing scales are close to the size of the box) is $\mathcal{P} = 2$, which is in good agreement with the decay rate for the case where $k_p = 1$. This behaviour is nearly identical to that seen in the symmetry breaking turbulent decay of the Taylor Green vortex, where initially large coherent structures develop instabilities and break down [52, 25].

Given an initial spectrum of k^4 at low wave numbers it is expected that the integral length should grow proportional to $t^{2/7}$ [82, 144], potentially moving to $t^{2/5}$ if the low wave numbers take on a k^2 form at late time. Figure 4.6 shows the normalised integral length scale $\ell t^{-2/7}$ for all grid resolutions for three extrapolation methods. These plots are representative of the behaviour of all of the extrapolation methods employed in this

Table 4.2: Velocity structure functions computed from DNS

Quantity	[146]	[106]	[147]	[188]	[135]	[32]	[96]	[190]	[160]	[68]
$Re_{\lambda_{tay}}$	45	83	64	150	< 51	202	168	195	175	460
S_3	0.47	0.51	0.4	0.5	0.58	0.44	0.52	0.54	0.45	0.55
S_4	-	-	4.05	5.9	4.31	-	6.1	6.7	-	7.91

Table 4.3: Velocity structure functions computed from LES

Quantity	[27]	[61]	[9]	[87]	[100]	Gaussian
$Re_{\lambda_{tay}}$	∞	248	< 71	∞	720	-
S_3	0.4	-	0.4	0.22	0.42	0.00
S_4	2.73	3.6	-	-	-	3.00

study. The lines do not lie on top of each other as each numerical scheme has a different time origin for the decay of kinetic energy and the growth of the integral length scale. It can be seen that the integral length grows proportional to $t^{2/7}$ as expected, and that this relationship becomes more accurate as the resolution and order of the method increases.

4.3.3 Structure Functions and Enstrophy

The velocity structure functions are typically used to quantify if the flow is turbulent, and its characteristics. These are computed as [148]

$$S_n = (-1)^n \frac{\langle (\partial u/\partial x)^n \rangle}{\left\langle (\partial u/\partial x)^2 \right\rangle^{n/2}}, \tag{4.3.7}$$

where n is a positive integer, and the derivatives are computed using second-order accurate centred differences and then averaged over all three directions. The third-order velocity structure function ($n = 3$), or skewness, is directly related to enstrophy in isotropic homogenous turbulence, and the fourth-order structure function ($n = 4$), or flatness, gives a measure of the probability of occurrence of extreme or mild events. Typically, the lower the absolute value, the higher the numerical dissipation.

The flatness increases consistently with Reynolds number, at a rate approximately $S_4 \propto 3+1/2Re^{0.25}$. The most recent experimental results measured $S_3 = 0.34$, and $S_4 = 3.75$ for $Re_{\lambda_{tay}} = 720$ [100], both lower than previous experiments. Computational results from previous DNS and LES simulations are summarised in Tables 4.2 and 4.3.

Table 4.4 details the average skewness functions in the present study, listed in approximate order of decreasing dissipative behaviour of the numerical scheme. It is expected that increasing the resolution should increase the skewness until it reaches the state expected for fully developed homogeneous decaying turbulence. Sreenivasan

Table 4.4: Third order velocity structure functions

Resolution	MM	VA	VL	M3	M5	W5	W9
32^3	0.08	0.11	0.19	0.14	0.31	0.30	0.26
64^3	0.22	0.32	0.30	0.31	0.31	0.33	0.31
128^3	0.31	0.35	0.33	0.34	0.36	0.36	0.32
256^3	0.34	0.37	0.36	0.36	0.38	0.40	0.35

Table 4.5: Fourth order velocity structure functions

Resolution	MM	VA	VL	M3	M5	W5	W9
32^3	4.09	3.78	3.62	5.17	4.17	3.58	3.33
64^3	4.07	4.25	3.94	5.49	4.37	3.95	3.47
128^3	4.34	4.38	4.09	5.80	4.55	4.32	3.55
256^3	4.56	4.61	4.27	4.74	4.96	4.81	3.98

and Antonia [176] have compiled many experimental velocity structure function measurements. The skewness appears constant at approximately 0.5 between Reynolds 10 and 1000, but increases above this threshold. In the current study, as the mesh resolution increases, the skewness increases converging towards a value of around 0.37. This is in good agreement with the most recent experimental results of 0.34 for $Re_{\lambda_{tay}} = 720$ [100] and previous ILES results [62], but lower than DNS results. The close agreement with the results of Kang *et al.* [100] is interesting as the integral length scale in the experiments is approximately $1/4$ the size of the wind tunnel - and in the current simulations it is approximately $1/4$ of the box size.

At the lowest resolution the skewness factor for all second and third-order limiting methods is much lower than the experimental values and tends rapidly back to a Gaussian distribution. The numerical dissipation of the scheme does not allow an adequate number of undamped modes to represent a turbulent flow field. However, at fifth-order and higher the numerical schemes capture the non-Gaussian behaviour well. As the majority of simulations around complex geometries are not well resolved this is an important point to note. As is generally accepted, Minmod is very dissipative, and not a good extrapolation method to use for turbulent flow. This is illustrated in the skewness values, which remain much lower than expected until resolutions of 128^3. At 64^3 the van Albada, van Leer and MUSCL third-order have physically realistic skewness values, close to experimental results. Surprisingly, the skewness decreases when using W9 methods, indicating that the M5 and W5 perform best at all resolutions.

The mean flatness is detailed in Table 4.5. Comparing the results to experimental results reported in [176] the flatness should increase consistently with Reynolds number, at a rate approximately $S_4 \propto 3 + 1/2Re^{0.25}$. This implies that the ILES simulations are achieving average Taylor Reynolds numbers of approximately one hundred over the course of the simulation, during which the mean turbulent velocities decrease by one fifth. However, the experiments of Kang *et al.* measured lower flatness of 3.75 at

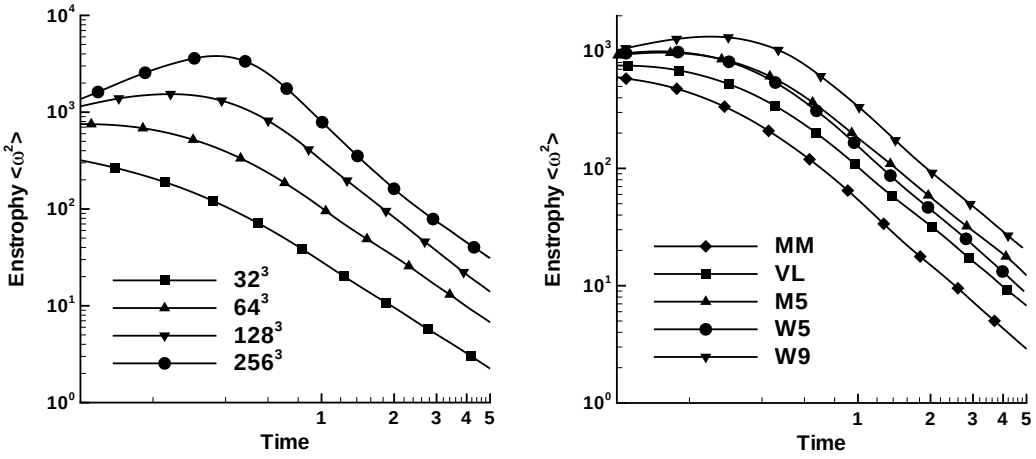

(a) (b)

Figure 4.7: Variation of the enstrophy with time; a) Van Leer limiter at $32^3 \rightarrow 256^3$ b) with extrapolation method

$Re_{\lambda_{tay}} = 720$, which would give the simulations a much higher effective $Re_{\lambda_{tay}}$ within the simulations. The flatness does not change significantly with increasing resolution, or increasing order of the numerical scheme. M3 has the highest mean value at low resolution, however at higher resolutions there is little difference between the schemes. This indicates that the probability of extreme events is not increasing with increasing resolution, contradictory to expected behaviour.

Figure 4.7a) shows the time variation of the enstrophy ($< \omega^2 >$, where ω is the vorticity) for each mesh resolution for the van Leer limiter. Figure 4.7b) shows the variation with method at a 64^3 resolution. Above 128^3 resolution for the second and third-order methods, and 64^3 for the higher-order methods there are two clear stages as reported in previous studies [119, 80]. In the first stage the entrophy increases due to vortex stretching which transfers energy to the smaller, faster moving vortices. Once the energy spectrum is fully developed, the enstrophy reduces with time as numerical dissipation decreases the resolved kinetic energy. In comparing the different methods, the higher the order of the method, the higher the enstrophy peak, reflecting the decreasing dissipation. W9 is the least dissipative via this measure, followed by W5 and M5. W9 is equivalent to van Leer at double the mesh resolution, whereas W5 and M5 are slightly less than double. At late times M5 has higher enstrophy than W5, indicating that setting local minima and maxima to first-order accuracy does not significantly influence the accuracy of the scheme.

4.3.4 Probability Distribution Functions

The velocity increment probability distribution functions (PDFs) have been computed for each grid resolution and method, where the velocity increment is defined as $\Delta u_i = u_i(x + \Delta x) - u(x)$. Figures 4.8 and 4.9 show the PDFs normalised by Δu_{rms} plotted with

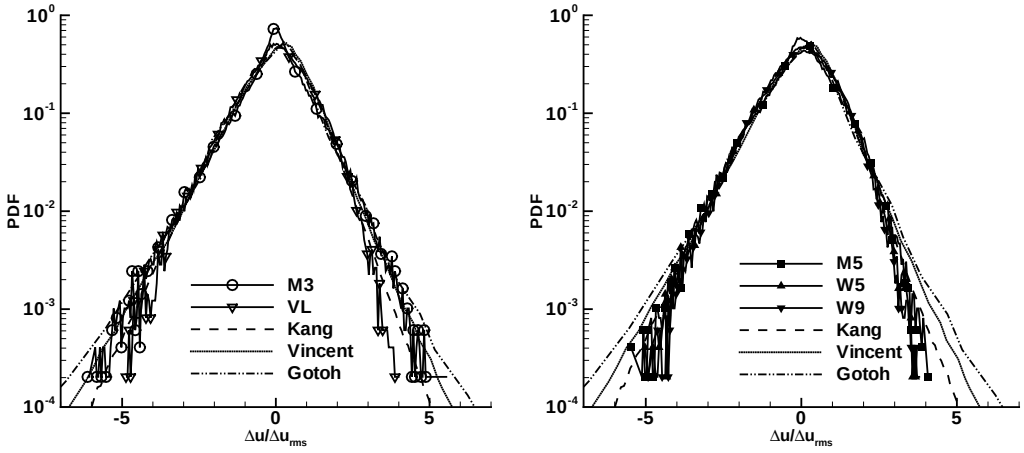

(a) 32^3

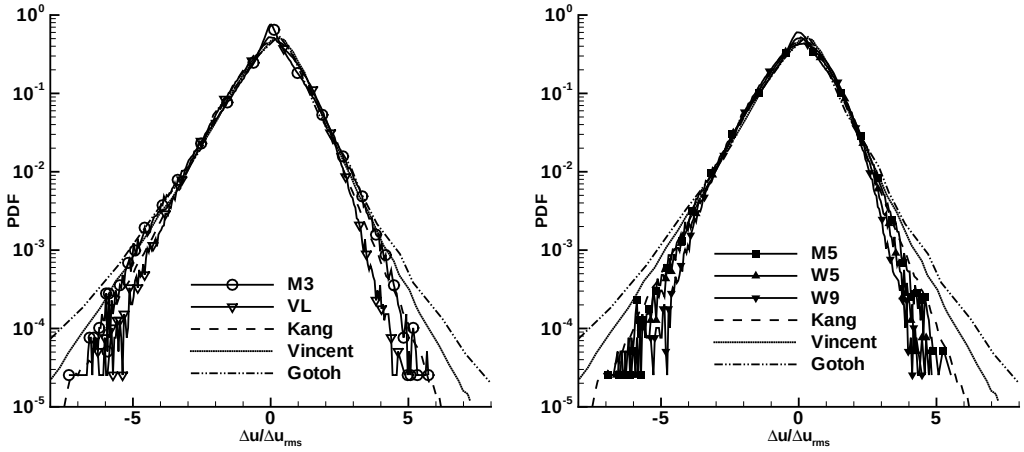

(b) 64^3

Figure 4.8: Velocity increment PDFs compared to experimental results by Kang *et al.* [100], and DNS by Vincent and Meneguzzi [188] and Gotoh *et al.* [68] at $t = 2$

experimental results by Kang *et al.* [100] taken at $Re_{\lambda_{tay}} = 626$, and DNS by Vincent and Meneguzzi [188] ($Re_{\lambda_{tay}} \approx 150$) and Gotoh *et al.* [68] ($Re_{\lambda_t ay} \approx 381$). Note that the van Albada, Minmod and van Leer give very similar results hence the first two are not shown. All methods capture the non-Gaussian behaviour of the velocity increments, the fifth-order MUSCL limiter giving best agreement with the experimental results. Indeed, at 256^3 resolution the M3 and M5 limiters lie almost directly on top of the experimental results for negative increments, and follow the positive increments up to $\Delta u/\Delta u_{rms} = 5$. Surprisingly, the ninth-order WENO has the least activity in the wings compared to the other very high order schemes. The van Leer, Minmod and van Albada limiters give exponential wings, but less intermittent than both experimental and DNS results.

The results shown here demonstrate that the shock capturing schemes give velocity increment PDFs in very good agreement with experimental results at $Re_{\lambda_{tay}} \approx 626$.

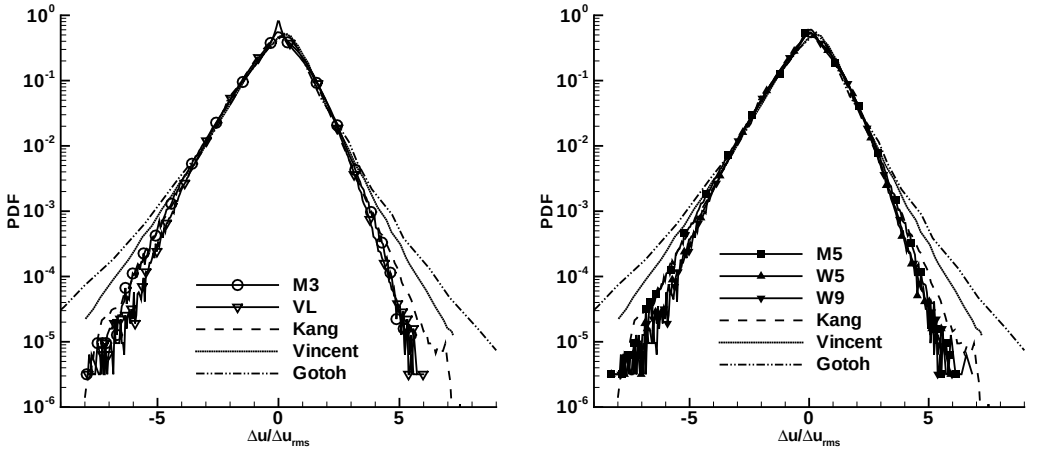

(a) 128^3

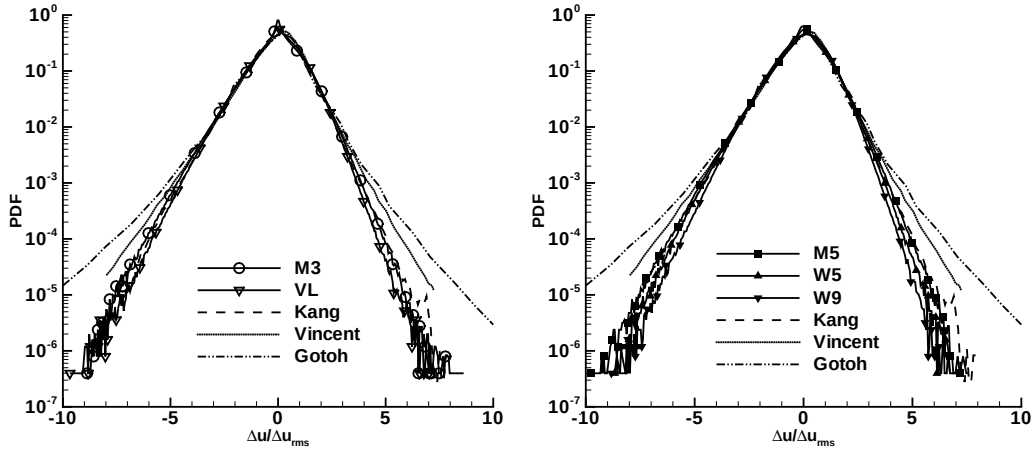

(b) 256^3

Figure 4.9: Velocity increment PDFs compared to experimental results by Kang *et al.* [100], and DNS by Vincent and Meneguzzi [188] and Gotoh *et al.* [68] at $t = 2$

This appears contradictory to the results in Garnier *et al.* who show that the velocity increment PDFs are close to DNS results at $Re_{\lambda_{tay}} \approx 20$. Comparing DNS of Vincent and Meneguzzi [188] and Gotoh *et al.* [68], and the experimental results of Kang *et al.* [100] it is clear that there is a large discrepancy in the behaviour of the PDFs. The DNS results have a PDF which differs by more than an order of magnitude at the exponential wings from the experimental results, and appears to be increasing with $Re_{\lambda_{tay}}$. Thus, from comparison with DNS results, a low numerical Reynolds number of ≈ 20 appears reasonable as in [62], however comparison with experiment gives the numerical Reynolds number significantly higher at approximately 626.

The pressure PDFs are shown in Figure 4.10 for the VL, M5 and W9 schemes at 256^3, where they follow a Gaussian distribution, demonstrating that the pressure is decorrelated from the vorticity. This Gaussian distribution of pressure is found for all schemes at all resolutions. The source of this decorrelation is believed to be the

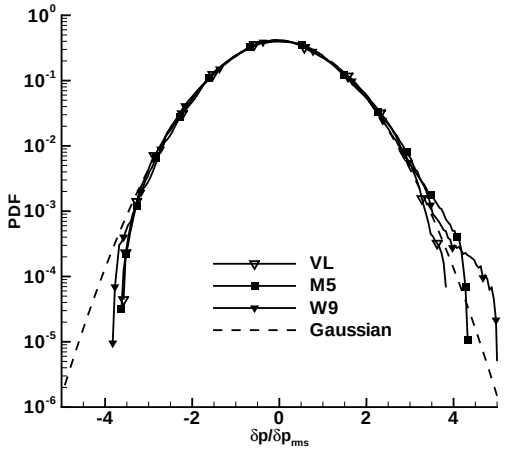

Figure 4.10: Pressure fluctuation PDF from the 256^3 simulation at $t = 2$

decoupling of pressure and vorticity as described in Section 4.2.3.

4.3.5 Turbulent Kinetic Energy Spectra

The three dimensional energy spectrum $E(k)$ is defined as [44]

$$E(k) = 2\pi k^2 \phi_{ii}(k), \tag{4.3.8}$$

where $k = \sqrt{k_x^2 + k_y^2 + k_z^2}$ and the spectrum tensor ϕ is

$$\phi_{ij}(\mathbf{k}) = \frac{1}{(2\pi)^3} \int_{-\infty}^{\infty} \mathbf{Q}_{ij}(\mathbf{r}) \exp^{-I\mathbf{kr}} d\mathbf{r}, \tag{4.3.9}$$

where Q_{ij} is the second-order velocity correlation tensor. The three dimensional resolved kinetic energy spectrum for all resolutions and methods at $t = 5$ are shown in Figure 4.11 for the second and third-order methods, and in Figure 4.12 for the fifth and ninth-order methods. Ideally, the high wave number part of the spectrum should form a straight line in log-log axis with a power law of $k^{-5/3}$ as predicted by Kolmogorov [110]. At 32^3 all limiters except W9 are too dissipative at high wave numbers, leading to lower kinetic energy than ideal. The W9 simulation has a reasonable inertial range to the cutoff. Given that the degrees of freedom within the system are low, this is an excellent result. However, increasing the resolution to 64^3 does not give a corresponding increase in the $k^{-5/3}$ range, although at this resolution there also is a short inertial range in simulations using the fifth-order methods. Interestingly, the M5 method is less dissipative than W5 at high wave numbers, leading to a slightly 'fuller' spectrum.

The trend towards increasing size of the range with approximate Kolmogorov scaling continues for 128^3 and 256^3 for the higher order schemes, with very little or no inertial range for the second and third order limiters until the highest resolution. Table 4.6

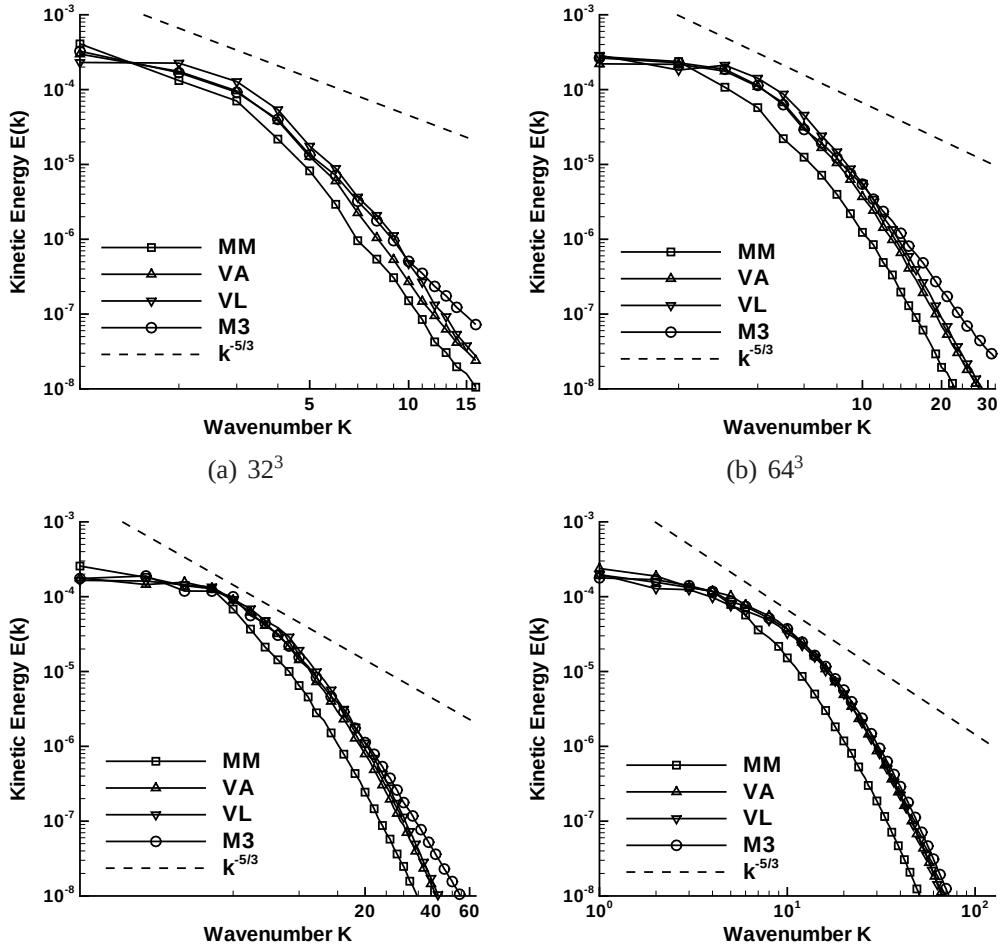

(a) 32^3 (b) 64^3

(c) 128^3 (d) 256^3

Figure 4.11: Three-dimensional kinetic energy spectrum E_{3D} at t=5 for the second- and third-order methods at different resolutions

details the ratio of the wave number at which the energy spectrum deviates more than 10% from an assumed $k^{-5/3}$ to the maximum wave number k_{max} for the given grid. At the grid resolutions considered, this appears to be reaching a value independent of grid resolution, indicating that the simulations are of a large-eddy nature, and not following a constant dissipation Kolmogorov range scaling, where k/k_{max} would decrease with increasing effective Reynolds number [82].

In comparing the schemes, Minmod shows effectively no inertial range, and the data in Table 4.6 is representative of this. It gives consistently worse resolution of high wave number modes when compared to the other second-order limiters. As stated in Section 3.8.3 the leading order difference between the limited quantities for MM is second order, however for VA, VL and M3 the difference is third order. As the dissipation in a Godunov scheme is proportional to the difference of extrapolated quantities, the lower the leading order of the difference, the higher the dissipation. Examining the spectra in Figure 4.11 it is clear that the MM limiter is more dissipative, and that the

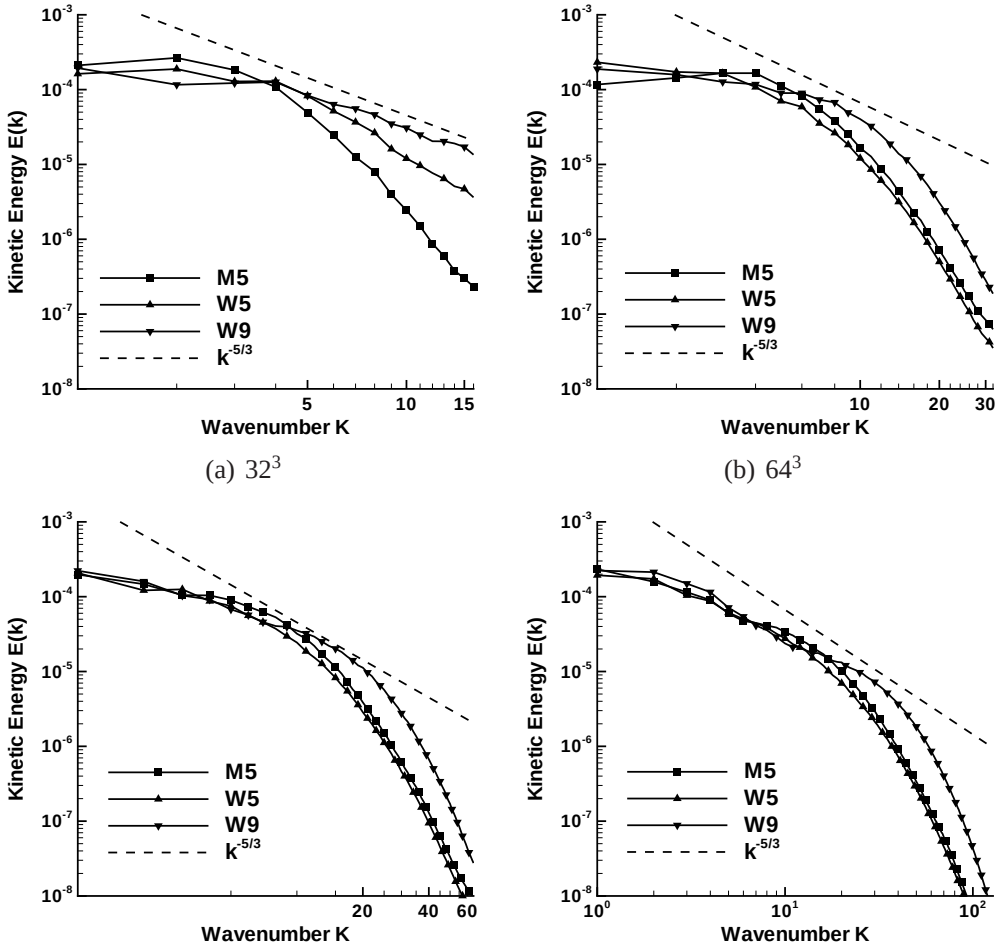

(a) 32^3 (b) 64^3

(c) 128^3 (d) 256^3

Figure 4.12: Three-dimensional kinetic energy spectrum E_{3D} at t=5 for the fifth- and ninth-order methods at different resolutions

formally second-order accurate VL and VA methods have behaviour closer to that of the third order accurate M3. These resolve a short inertial range up to $k_{max}/10$, defined as the highest normalised wave number (k/k_{max}) at which the resolved kinetic energy spectrum deviates more than 10% from an assumed $k^{-5/3}$ law.

Significant improvements are seen at fifth-order where the dissipative ranges begin at $k_{max}/6$ and at ninth order at $k_{max}/3$. From this it can be seen that using fifth and higher order methods are comparable to increasing the resolution by a factor of two in each direction when compared to the second and third order limiters, thus easily justifying the increase in computational time. As turbulent velocities scale as $k^{-1/3}$ then if it is assumed that a $k^{-5/3}$ range exists to the cutoff then even at the maximum grid resolution the smallest eddies still have a mean turbulent velocity one fifth of that at the peak. This is an extremely noisy signal and very difficult to capture accurately using any numerical method in physical space. Results gained here for the higher-order schemes indicate that the simulations capture modes of wavelength of 10 cells with reasonable

Table 4.6: Highest normalised wave number (k/k_{max}) at which the resolved kinetic energy spectrum deviates more than 10% from an assumed $k^{-5/3}$ law

Resolution	MM	VA	VL	M3	M5	W5	W9
32^3	0.19	0.19	0.19	0.19	0.25	0.31	1.0
64^3	0.09	0.13	0.16	0.13	0.22	0.25	0.34
128^3	0.05	0.10	0.13	0.11	0.19	0.19	0.31
256^3	0.05	0.10	0.10	0.10	0.16	0.16	0.31

statistical accuracy, which is considered to be a good result.

The Kolmogorov constant has been computed and it is found that $C_k \approx 1.9$ for the three dimensional spectrum. This is in good agreement with the 'bump' at the beginning of the sub-inertial range where $C_k \approx 2$, as reported in recent DNS [99, 68], and experimental results [175, 100, 158, 140, 29], but higher than the theoretical value of $C_k \approx 1.6$ expected. It should be noted that these are single time spectra from decaying turbulence not averaged from statistically stationary forced turbulence.

A further measurement of the presence of a sub-inertial range is by computing Kolmogorov's four-fifth's law. As the problem is not stationary (i.e. it is decaying) the results were calculated from the Karman-Howarth equation for an inviscid fluid, hence including a contribution from the time variation of the second order structure function [148],

$$-\left[\frac{3}{r^4}\int_0^r s^4 \frac{\partial}{\partial t} D_{LL}(s,t)ds + D_{LLL}(r,t)\right]/\epsilon r = \frac{4}{5} = \mathcal{B}, \tag{4.3.10}$$

where $D_{LL} = \overline{\left[u(x_1 + e_1\frac{4}{5} = r, t) - u(x_1,t)\right]^2}$, $D_{LLL} = \overline{[u(x_1 + e_1 r, t) - u(x_1,t)]^3}$ and s is a dummy integration variable. In forced turbulence this relationship holds at $Re_{\lambda_{tay}} > 1170$ [139], and Antonia and Burattini [10] suggest that for decaying isotropic turbulence the asymptotic value of four-fifths is not reached until $Re_{\lambda_{tay}} > 10^6$.

$\mathcal{B}$ is plotted in Figure 4.13 at a grid resolution of 256^3 results for the van Leer, M3, M5, and WENO methods. The four-fifths law is not satisfied for any of the methods. Comparing the results with experiment suggest $Re_{\lambda_{tay}} < 100$.

The short extent of the sub-inertial range (if present at all) indicates that the ILES approach using standard compressible finite volume methods would not be appropriate for accurate resolution of flow where the features of interest are less than several mesh cells in size.

4.3.6 Spectral Distribution of Numerical Viscosity

From the previous subsections it appears that the M3, M5 and W9 limiters are the optimum choices compared to schemes of similar order of accuracy. To further quantify the performance of these schemes the spectral behaviour of the numerical viscosity is

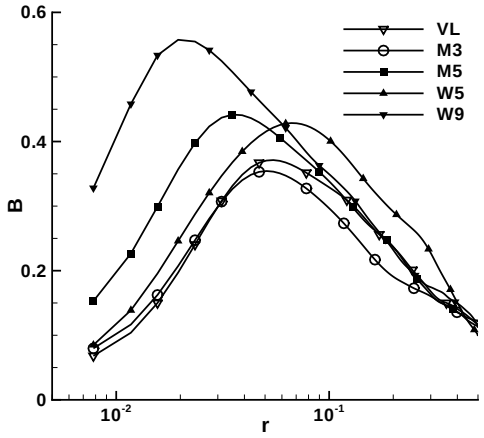

Figure 4.13: $\mathcal{B}$ plotted for the 256^3 grid resolution at $t = 5$

examined. Garnier *et al.* [62] computed the amplification factor for upwind fluxes, showing that a unique filter length cannot be defined for the Euler equations. This will be examined here. Secondly, the numerical viscosity is computed in the form of a numerical spectral eddy viscosity as proposed by Domaradzki *et al.* [49]. This is compared to the theoretical 'ideal' eddy viscosity for homogeneous decaying turbulence computed by Chollet [33] via the test field model and eddy damped quasi-normal Markovian approximation. This method of comparison has been employed by Hickel *et al.* [81] to optimise incompressible implicit LES.

Following Garnier *et al.* [62] the amplification of the Fourier modes due to discretisation errors can be computed as the ratio of the Fourier transform of the finite volume fluxes over the spectral fluxes,

$$\mathcal{A} = \frac{\sum_{k-1/2<|\mathbf{k}|<k+1/2} \mathrm{FFT}\,|(\partial\mathbf{E}/\partial x + \partial\mathbf{F}/\partial y + \partial\mathbf{G}/\partial z)|^2}{\sum_{k-1/2<|\mathbf{k}|<k+1/2} |Ik_1\mathrm{FFT}(\mathbf{E}) + Ik_2\mathrm{FFT}(\mathbf{F}) + Ik_3\mathrm{FFT}(\mathbf{G})|^2}, \tag{4.3.11}$$

which can be rewritten using Equation (3.1.1) as,

$$\mathcal{A} = \frac{\sum_{k-1/2<|\mathbf{k}|<k+1/2} \mathrm{FFT}\,|-\partial\mathbf{U}/\partial t|^2}{\sum_{k-1/2<|\mathbf{k}|<k+1/2} |Ik_1\mathrm{FFT}(\mathbf{E}) + Ik_2\mathrm{FFT}(\mathbf{F}) + Ik_3\mathrm{FFT}(\mathbf{G})|^2}. \tag{4.3.12}$$

The numerator is computed as a central difference approximation for the derivative of the conserved variables with respect to time, i.e. $(\mathbf{U}^{n+1} - \mathbf{U}^{n-1})/\Delta t$, and the spectral divergence as a function of the conserved variables at time level n. Figure 4.14 shows the ratio of the fluxes computed for the M3, M5 and W9 schemes for 64^3 to 256^3 for the continuity and ρu momentum equation. The results for the energy equation are very similar to those of the continuity equation, and the ρv and ρw momentum equations match the ρu equation.

As shown in [62] the effective filter length is different for the continuity and momentum equations. Increasing the resolution of the numerical scheme does not significantly

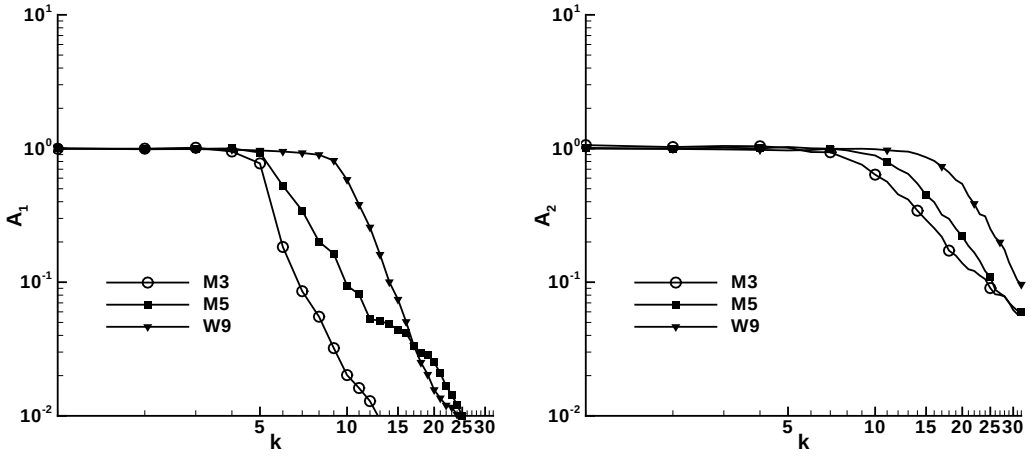

(a) 64^3

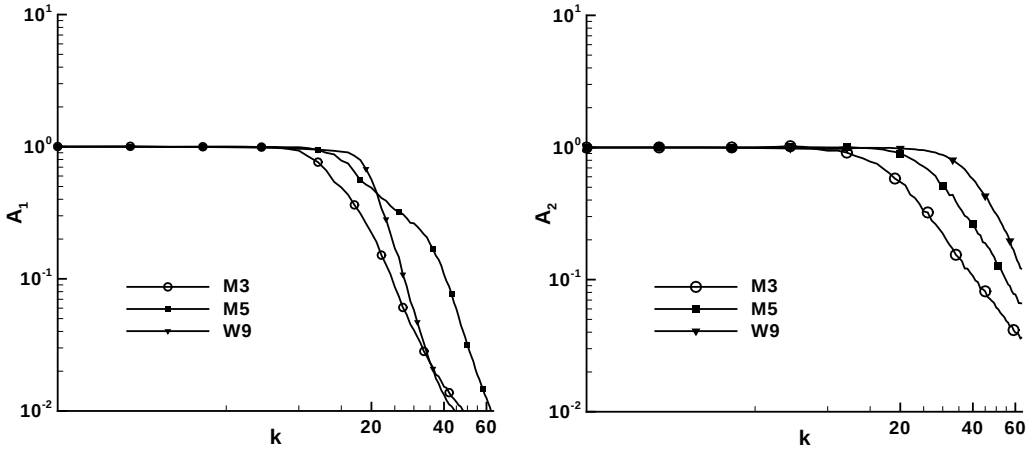

(b) 128^3

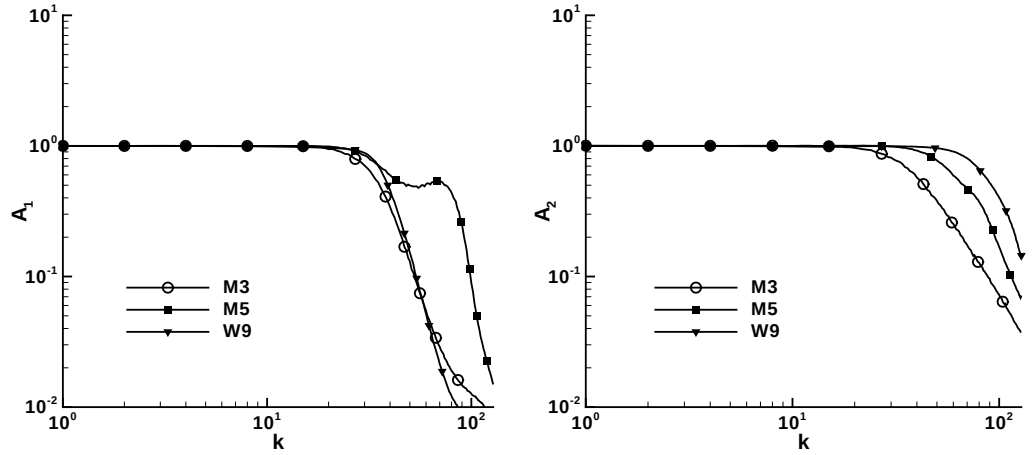

(c) 256^3

Figure 4.14: The ratio of the fluxes computed using the FV schemes to spectral fluxes at $t = 5$ for the continuity equation (left) and u-momentum equation (right)

Table 4.7: Highest normalised wave number (k/k_{max}) at which $\mathcal{A} > 0.9$

	64^3		128^3		256^3	
Scheme	$\mathcal{A}_1$	$\mathcal{A}_2$	$\mathcal{A}_1$	$\mathcal{A}_2$	$\mathcal{A}_1$	$\mathcal{A}_2$
M3	0.16	0.25	0.17	0.20	0.18	0.20
M5	0.19	0.31	0.19	0.31	0.22	0.33
W9	0.28	0.46	0.28	0.46	0.23	0.48

improve the resolution of the continuity and energy equations, and at the highest resolution there is only a 20% difference in cut-off wave number for $\mathcal{A}_1$ over all methods.

Table 4.7 details the cut-off filter length, which is defined as the highest wave number for which $\mathcal{A} > 0.9$, normalised by k_{max}. Comparing these to the results in Table 4.6 it can be seen that for M3 and M5 the cut-off point for the $k^{-5/3}$ range is at a lower wave number than the effective cut-off wave number for the continuity and energy equation ($\mathcal{A}_1$ and $\mathcal{A}_5$). However, the WENO ninth-order inertial range cut-off lies between the effective filter length for the continuity and momentum equations. The normalised effective filter length appears to be converging to a constant value independent of grid size, being approximately $k_{max}/5$ for M3, $k_{max}/3$ for M5 and $k_{max}/2$ for W9. All three schemes are dissipative, the maximum amplification of a given wave number is 6% for M3, 2.5% for M5 and 0.1% for W9 at 64^3, becoming negligible at higher grid resolutions. This is likely to be due to the accuracy of the central difference approximation of the change in conserved quantities over the time, hence explaining why the maximum amplification decreases as grid size increases.

Next, the effective numerical viscosity is assessed for it's suitability as a turbulent eddy viscosity. The momentum equations can be written in spectral form as

$$\left(\frac{\partial}{\partial t} + \nu k^2\right) u_n(\mathbf{k}, t) = -\frac{I}{2} P_{nlm}(\mathbf{k}) \int u_l(\mathbf{p}, t) u_m(\mathbf{k} - p, t) d^3 p, \tag{4.3.13}$$

where the projection tensor is defined as,

$$P_{nlm}(\mathbf{k}) = k_m(\delta_{nl} - k_n k_l / k^2) + k_l(\delta_{nm} - k_n k_m / k^2). \tag{4.3.14}$$

The evolution equation for kinetic energy as a function of wave number is derived by multiplying Equation (4.3.13) by $u_n^*(\mathbf{k}, t)$, where * indicates the complex conjugate, giving

$$\frac{\partial \frac{1}{2}|u(\mathbf{k}, t)|^2}{\partial t} = -2\nu k^2 \frac{1}{2}|u(\mathbf{k}, t)|^2 + T(\mathbf{k}, t), \tag{4.3.15}$$

$$T(\mathbf{k}, t) = \frac{1}{2} \mathrm{Im}\left[u_n^*(\mathbf{k}, t) P_{nlm}(\mathbf{k}) \int u_l(\mathbf{p}, t) u_m(\mathbf{k} - p, t) d^3 p\right]. \tag{4.3.16}$$

The spectra can be integrated in spherical shells to give the Transfer function $T(k)$ and Energy spectrum $E(k)$ as a function of wave vector magnitude k,

$$E(k) = 4\pi k^2 \frac{1}{2} < |u(\mathbf{k}, t)|^2 >, \tag{4.3.17}$$

$$T(k) = 4\pi k^2 < T(\mathbf{k}, t) > . \tag{4.3.18}$$

Equation (4.3.15) can be rewritten as

$$\frac{\partial}{\partial t} E(k, t) = -2\nu k^2 E(k, t) + T(k, t). \tag{4.3.19}$$

By assuming that the numerical viscosity behaves in a manner analogous to physical viscosity, an effective numerical viscosity for inviscid simulations can be computed using

$$\nu_n = \frac{T(k, t) - \frac{\partial}{\partial t} E(k, t)}{2k^2 E(k, t)}, \tag{4.3.20}$$

computed numerically as [49]

$$\nu_n = \frac{T(k, t^n) - (E(k, t^{n+1}) - E(k, t^{n-1}))/2\Delta t}{2k^2 E(k, t^n)}, \tag{4.3.21}$$

where modes are included in the computation only if the magnitude of the wave vector is smaller than a cut-off wave number k_c. It is normalised using the energy at the cutoff wave number $E(k_c)$ and k_c

$$\nu_n^+(k|k_c) = \frac{\nu_n}{\sqrt{E(k_c)/k_c}}. \tag{4.3.22}$$

This is compared to the theoretical result fitted by the expression of Chollet [33]

$$\nu_n^+(k|k_c) = C_K^{-3/2} \left(0.441 + 15.2 \exp^{-3.03 k_c/k}\right). \tag{4.3.23}$$

The computation of the effective numerical viscosity is quite sensitive to the choice of the cut-off wave number k_c. Plotted in Figure 4.15 are the effective numerical viscosities for $k_c = k_{max}/2$. Also plotted are the effective numerical viscosities where k_c is the average of the filter cut-offs measured from $\mathcal{A}(k)$.

At $k/k_c > 0.3$ in all simulations there is a very good qualitative agreement in terms of the shape of the numerical spectral viscosity in comparison to the theoretical curve. Both numerical and theoretical lines have a region of approximately constant viscosity at intermediate wave numbers, and increasing viscosity as $k/k_c \to 1$. The effective dissipation is consistent with the previous results, showing the W9 scheme as the least dissipative, and M3 as the most dissipative. At the cut-off wave numbers chosen here

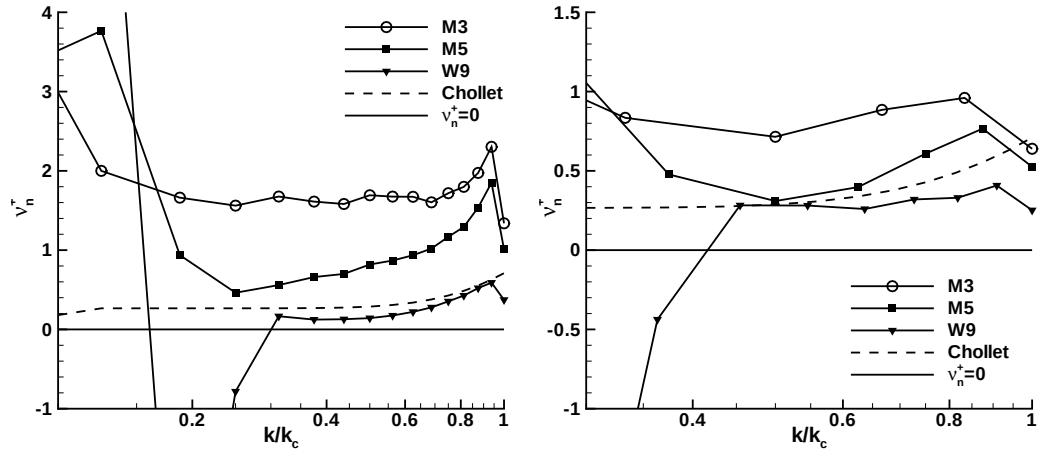

(a) 64^3

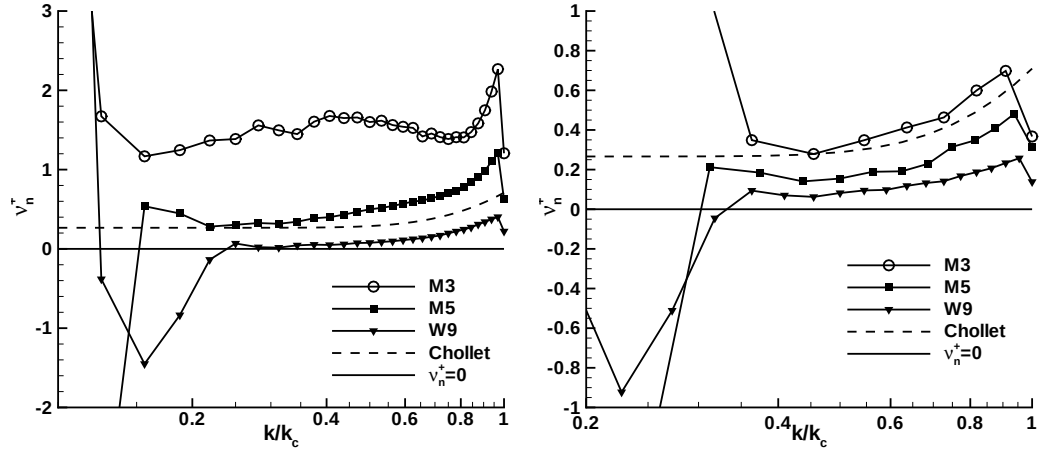

(b) 128^3

Figure 4.15: The effective normalised numerical viscosity at $t = 5$ compared to the ideal normalised eddy viscosity from Chollet [33]. Cut-off wave number $k_c = k_{max}/2$ (left), k_c determined from filter cutoff (right)

the effective viscosity of the W9 scheme is lower than the ideal spectral eddy viscosity, which implies that the scheme could benefit from the addition of a sub-grid model. However, if a higher wave number cut-off is chosen, the effective numerical viscosity increases above the theoretical line.

The agreement with the theoretical results of Chollet is reasonable, however, when employing the effective cut-off from $\mathcal{A}(k)$, the number of modes between the energy containing modes (approximately $1 < k < 5$) and the cut-off is very low, even for ninth-order methods at 128^3. This can be seen in Figure 4.15, where each symbol represents a mode. At 64^3 each method has less than 10 wave numbers in this range, at 128^3 less than 20.

These results imply that given a high enough grid resolution it is possible to select a cut-off wave number for each method which gives a spectral viscosity in agreement

with Chollet's theory. The key issue at present is that the required grid resolution is prohibitively large for many practical situations of industrial interest.

At low wave numbers the effective numerical viscosity becomes negative for some wave numbers, positive for others, and increases in magnitude. This increase in effective viscosity can also be seen in Ciardi *et al.* [36]. It is interesting that for some modes the effective viscosity becomes negative. This occurs for modes where the net transfer of kinetic energy ($T(k)$) is negative, yet the turbulent kinetic energy at that mode increases. As all schemes have been shown to be dissipative at all modes on average (Figure 4.14), it is possible that this is due to compressibility effects as discussed in Section 4.2.3. There can be an increase in kinetic energy at some points in the flow due to a local exchange of energy from pressure to kinetic energy in the acoustic modes. When there are statistically few modes (i.e. at low wave numbers) this local exchange could cause an increase in total turbulent kinetic energy at a given wave number. This is not taken into account in Equation (4.3.15) as this expression is valid only for incompressible flows.

4.4 Conclusions

The ability of high-order finite volume Godunov-type ILES schemes to simulate homogeneous decaying turbulence at low Mach number has been investigated quantitatively using a number of different parameters. The homogeneous isotropic flow field is initialised using the divergence of a vector potential to minimise the compressible component of the kinetic energy spectrum.

It has been demonstrated that the behaviour of the large scales is captured well at resolutions greater than 32^3, or when using numerical methods of higher than third-order accuracy. With this constraint satisfied the turbulent kinetic energy decay exponent lies close to the theoretical and experimental results, and is as accurate as results reported for conventional large-eddy simulation. The integral length scale is expected to grow as $t^{2/7}$ for the initialised energy spectrum, and this is shown to hold for all methods. Additionally, velocity increment PDFs are found to have exponential wings, but pressure PDFs are essentially Gaussian.

Examining the spectra indicate that all methods are too dissipative at high wave numbers, giving a slope steeper than the expected $k^{-5/3}$, and there is no agreement with the Kolmogorov four-fifths law. All methods have effective filters at less than $k_{max}/2$ for the momentum equations and $k_{max}/4$ for the continuity and energy equation, indicating that a single filter length cannot be defined for all equations. When the numerical viscosity is assessed as a spectral eddy viscosity it is in good qualitative agreement with the theoretical solution, having a plateau at intermediate wave numbers and a peak at the cut off. However, unless the cut-off wave number is chosen below $k_{max}/2$ then all methods are too dissipative.

It is difficult to define a single effective Reynolds number for the simulations. Com-

paring the PDF's to experimental results gives an estimated $Re_{\lambda_{tay}} \approx 600$, however, compared to DNS it is an order of magnitude lower. Examining the four-fifths law shows $Re_{\lambda_{tay}} \approx 30 - 100$ for all methods except WENO ninth-order which is approximately 200.

In comparing the numerical methods, the fifth and ninth-order methods have a clear advantage in that they are capable of resolving non-Gaussian turbulent behaviour at lower resolutions than the second and third-order methods. Of the second and third-order methods the third-order limiter M3 performs the best - giving a velocity derivative skewness close to experimental for all resolutions greater than 32^3 whilst maintaining a reasonable kinetic energy decay rate. Additionally, the third-order limiter has marginally higher kinetic energy at the high wave numbers, and gives a better match to experimental velocity increment PDFs. Considering computational time, however, the complexity of this limiter would make it undesirable as it is more expensive than the fifth-order methods.

Of the very high-order methods, plots of enstrophy show that using a ninth-order scheme gives a similar solution to the second and third-order methods at double the resolution. The two fifth-order schemes give a solution equivalent to slightly less than twice the effective grid size. This is confirmed by calculating the effective numerical filter length, where the WENO ninth-order method resolves double the wave numbers of the M3 method. Interestingly, there is only a marginal improvement in resolution of the energy and continuity equation at the higher grid sizes. The M5 limiter gives excellent agreement with experimental results in predicting the intermittency in the tails of the velocity increment PDFs, whereas the WENO methods drop off steeply at the tails. Examining the kinetic energy spectra shows that the ninth-order method resolves an approximate $k^{-5/3}$ to $k_{max}/3$, the fifth-order method up to $k_{max}/6$, and lower-order methods up to $k_{max}/10$. This means that fifth and higher-order methods at 128^3 perform better than the second-order methods at 256^3. The increase in accuracy via this measure is greater than the increase in computational time.

In summary, the numerical methods ranked in order of decreasing performance with respect to accuracy for a given computational time are WENO ninth-order, followed by MUSCL fifth-order, WENO fifth-order, MUSCL third-order, van Leer, van Albada and Minmod. For a given simulation it is expected that an optimum choice would be either WENO ninth-order or MUSCL fifth-order depending on the monotonicity constraints of a given problem. Finally, it is clear that all of the numerical methods are too dissipative at the high wavenumbers. The following chapter investigates in depth the mechanism for this overly-dissipative behaviour of Godunov-type schemes, demonstrating the leading order source of dissipation of turbulent kinetic energy.

CHAPTER 5

Theoretical Analysis of Kinetic Energy Dissipation in Godunov Schemes

5.1 Introduction

The Finite Volume (FV) Godunov method has proven extremely successful in the simulation of high Mach number flows, and is an essential tool in many applications involving high speed flows and shock waves. The Euler equations can form steep discontinuities in compressible flows, and in order to provide a stable and non-oscillatory solution a certain level of artificial dissipation is added to the solution. In a Godunov method this dissipation is added through the upwind behaviour of the numerical scheme. Unfortunately, the dissipation required to stabilise the solution also dissipates kinetic energy, and it is the rate of dissipation which is the subject of this chapter. It is especially important in describing the poor performance of Godunov methods in simulations of low Mach flows, determining the implicit subgrid model for Implicit Large Eddy Simulations (ILES), and in errors associated with strong shock interactions. Issues such as convergence problems and difficulties due to round off errors are not dealt within this chapter, for further information see, for example, [72, 108, 161, 185] and references within.

Several previous papers have discussed the influence of the introduction of artificial viscosity on the simulation of inviscid flows. Noh [143] detailed the behaviour of finite difference schemes, highlighting the sometimes undesirable effects of the von Neumann and Richtmyer type viscosity when simulating strong shock waves, due to the overly dissipative nature of certain formulations, especially in the absence of heat conduction. Christensen [34] draws parallels between the dissipation inherent in a Godunov method, and that due to artificial viscosity method. The different forms of artificial viscosity are further discussed in Benson [18] with respect to their performance in capturing shocks. Volpe [189] demonstrated using several numerical examples that FV methods provide inaccurate results at low Mach due to excess numerical dissipation. Later, Menikoff [131] noted that artificial viscosity is responsible for the entropy errors associated with a diffused shock, and that this error does not disappear with mesh refinement. Several papers by Guillard [74, 73, 72] examine the low Mach

problem, demonstrating that at low Mach numbers the artificial viscosity present in Godunov schemes leads to an undesirable scaling of the pressure with respect to the Mach number, and proposing a form of preconditioning of the governing equations to correct this. However, to the authors knowledge, an analytical form of the dissipation of kinetic energy in Godunov schemes has not been yet been derived.

Two factors have increased the importance of the dissipation of kinetic energy by Godunov schemes. Firstly, as computational power and grid size increases, simulations which were typically high Mach now resolve relatively low Mach perturbations. An example of this is in the simulation of compressible turbulent flows. The large scales are at a relatively high Mach number, whereas small instabilities can occur at low Mach. These can grow in size and affect the development of the larger scales (especially in fundamental instabilities such as Rayleigh Taylor, Richtmyer-Meshkov and Kelvin-Helmholtz). It is important to understand the mechanism of dissipation of turbulent kinetic energy within compressible schemes, to better represent the growth of these small instabilities, and hence reliably model the actual flow physics.

Secondly, there has been a rapid increase in the use of Implicit Large Eddy Simulation in a variety of applications [24, 51, 61, 67, 70, 75, 129, 149, 170, 195, 197] where the dissipation inherent within the numerical method is employed 'in lieu' of an explicit subgrid model. To design future implicit models, an analytical description of the leading order dissipative terms is required so that this can be matched to the expected dissipation rate (such as that due to Kolmogorov's refined similarity hypothesis [111]).

It is expected that a useful description of kinetic energy dissipation rate should describe both the increase in dissipation at low Mach number as well as the behaviour of implicit subgrid models at more moderate Mach numbers. It is typically assumed that the dissipation in the Godunov scheme arises from the presence of shock waves in the solution of the Riemann problem at the cell interface. Section 5.2 derives an equation to link the increase of entropy with dissipation of kinetic energy. Using this, Section 5.3 shows that the dissipation due to a shock of fixed strength is constant with Mach at leading order, thus this cannot be the leading source of dissipation of kinetic energy. Next, the possibility that there are more shocks in the discrete Riemann problem at low Mach is investigated in Section 5.4. It is shown that although the structure of the problem does change at low Mach, this is not the direct source of increase of dissipation as it does not change significantly below Mach ≈ 0.2. Finally, Section 5.5 demonstrates via an asymptotic analysis of the discrete problem that the leading order dissipation is due primarily to the reaveraging process, and that the irreversible dissipation of kinetic energy is proportional to Δu^2 and the speed of sound a. This is validated numerically using several different Riemann solvers, exact and approximate. Additionally, the applicability of these results to higher order methods is discussed.

An important point to note is that this chapter analyses the entropy change and dissipation of kinetic energy specifically for a Godunov method, however the approach is relatively universal and, in principal, the results are applicable to all standard compressible methods.

5.2 The Relationship Between Kinetic Energy and Entropy

Before commencing the analysis, it is important to clarify the governing equations, and essential to discuss the relationship between kinetic energy and entropy. This chapter is concerned solely with the analysis of the Euler equations of gas flow, where viscosity is assumed negligible ($Re \rightarrow \infty$). The homogeneity property of the Euler equations means that the properties can be analysed using the following governing equations in each principal direction,

$$\frac{\partial \mathbf{U}}{\partial t} + \frac{\partial \mathbf{E}}{\partial x} = 0, \tag{5.2.1}$$

where,

$$\mathbf{U} = [\rho,\ \rho u,\ \rho v,\ \rho w,\ e]^T, \tag{5.2.2}$$

$$\mathbf{E} = \left[\rho u,\ \rho u^2 + p,\ \rho uv,\ \rho uw,\ (e + p)u\right]^T, \tag{5.2.3}$$

$$e = \rho i + \frac{1}{2}\rho\left(u^2 + v^2 + w^2\right), \tag{5.2.4}$$

and ρ, i, u, v, w are the density, specific internal energy per unit volume and Cartesian velocity components, respectively. Throughout this chapter it is assumed that the fluid satisfies the ideal gas equation of state

$$p = \rho i\,(\gamma - 1), \tag{5.2.5}$$

where γ is the ratio of specific heats. In a Godunov method the governing equations are solved in integral form where the cell averaged conserved variables at the new time step, $\overline{\mathbf{U}}^{n+1}$ are computed according to

$$\overline{\mathbf{U}}^{n+1} = \overline{\mathbf{U}}^{n} - \frac{\Delta t}{\Delta x}\left(\mathbf{E}_{j+1/2} - \mathbf{E}_{j-1/2}\right) = 0, \tag{5.2.6}$$

where Δt and Δx are the time step and width of the cell. The time averaged numerical fluxes $\mathbf{E}_{j\pm1/2}$ are computed from the Riemann problem at the cell interface. This is typically seen as the solution of the Riemann problem along the line $x = 0$, where x is centred at the interface. The structure of a typical solution is illustrated in Figure 5.1. At any interface where the velocity or pressure differs from one side to the next, the solution will normally split into three waves, a contact surface sandwiched by two waves which are either a shock or rarefaction. Only the shock wave adds irreversible dissipation, as the rarefaction and contact surface are isentropic phenomena. Thus irreversible dissipation occurs only when the solution to the Riemann problem at $x = 0$

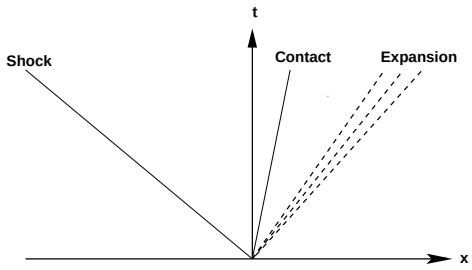

Figure 5.1: An example of the solution to a Riemann problem

(the star quantities) lies between the contact surface and the shock wave, as is the case in Figure 5.1.

Understanding the role of entropy in the context of dissipation of specific kinetic energy is key to understanding the dissipative properties of Godunov schemes. Entropy is a quantity which is usually defined by a difference, expressed as

$$\Delta S = \frac{R}{\gamma - 1} ln \left[\left(\frac{p}{\rho^{\gamma}} \right)^{n+1} \left(\frac{\rho^{\gamma}}{p} \right)^{n} \right], \tag{5.2.7}$$

where R is the specific gas constant, n the time step level and ΔS the change in entropy per unit mass.

The numerical solution to the Euler equations is constructed in a such a form that mass, momentum and total energy are conserved, but, kinetic energy is not conserved, due to numerical dissipation. The behaviour of the change of kinetic energy within a compressible fluid is similar to that of a damped spring. There are changes of kinetic energy which are accompanied by an isentropic change in pressure, as is the case for an ideal inviscid flow without shocks. In this case, although the kinetic energy has changed, there has been no actual dissipation of kinetic energy, and thus the flow behaves like an undamped spring. However, if the entropy increases then there has been an irreversible dissipation of specific kinetic energy which acts as a dampener to the isentropic motion.

A direct relationship between kinetic energy and entropy will now be derived. Beginning with the conservation equation for mechanical energy in vector notation without external forces [142]:

$$\rho \frac{D}{Dt} (q_K) = -[\nabla \cdot (p\mathbf{u}) - p\nabla \cdot \mathbf{u}] + [\nabla \cdot (\tau^{\nu} \cdot \mathbf{u}) - \tau^{\nu} : \nabla \mathbf{u}], \tag{5.2.8}$$

where ρ is the density, $q_K = 1/2 \sqrt{u^2 + v^2 + w^2}$, τ^{ν} is the shear stress tensor, p the pressure, $\mathbf{u}$ is the vector of velocities, and D/Dt represents the material or total derivative. The first group of terms on the right hand side relate to flow work due to the pressure on the control volume minus that work which does not increase kinetic energy, the third term is the total work which the surroundings do on the fluid through the viscous stress

and the fourth term is the portion of the work due to viscous stresses which dissipates kinetic energy. This is a sink of kinetic energy, and is also written as

$$\tau^{\nu} : \nabla \mathbf{u} = \tau^{\nu}_{ij} \frac{\partial u_i}{\partial x_j}. \tag{5.2.9}$$

This relationship is originally developed for physical viscosity but can be applied to numerical viscosity, as it was shown by Margolin *et al.* [128] that the truncation error terms can also be written as the divergence of a stress tensor. By subtracting the kinetic energy equation from the energy equation, a conservation equation for internal energy i without external sources can be written

$$\rho \frac{Di}{Dt} = -\nabla \cdot \mathbf{q} - p \nabla \cdot \mathbf{u} + \tau^{\nu} : \nabla \mathbf{u}. \tag{5.2.10}$$

Note that the viscous sink term present in the kinetic energy equations appears identically in the internal energy equation as a source term. There is an additional source term due to the heat diffusion flux $\mathbf{q}$, and due to pressure work compressing the element.

Entropy is a scalar quantity which is transported with the heat flow rate $\mathbf{q}$. The transport equation for entropy is [142]

$$\rho \frac{DS}{Dt} = -\nabla \cdot \left(\frac{\mathbf{q}}{T} \right) + \dot{\mathcal{P}}_s, \tag{5.2.11}$$

where the first term on the right hand side represents flux of entropy via heat conduction, $\dot{\mathcal{P}}_s$ is the production rate of entropy, and T the temperature. Next, using the Gibbs equation

$$\rho \frac{Ds}{Dt} = \frac{\rho}{T} \frac{Di}{Dt} - \frac{p}{\rho T} \frac{D\rho}{Dt}. \tag{5.2.12}$$

and combining this with the continuity equation and equation for the evolution of internal energy gives [17]

$$\dot{\mathcal{P}}_s = \frac{\kappa_\theta}{T^2} (\nabla T \cdot \nabla T) + \frac{\tau^{\nu} : \nabla \mathbf{u}}{T}, \tag{5.2.13}$$

where Fourier's Law of heat conduction has be used to express $\mathbf{q}$ in terms of temperature. The second term on the right hand side refers to a production of entropy via viscous stresses, and is identical to the sink term in the kinetic energy equation divided by temperature. Consider a typical low Mach number flow, where it is assumed that production of entropy due to thermal conduction is small in comparison to production via viscous stresses. For this case, temperature multiplied by production of entropy is equal to the irreversible viscous dissipation in Equation (5.2.8), or

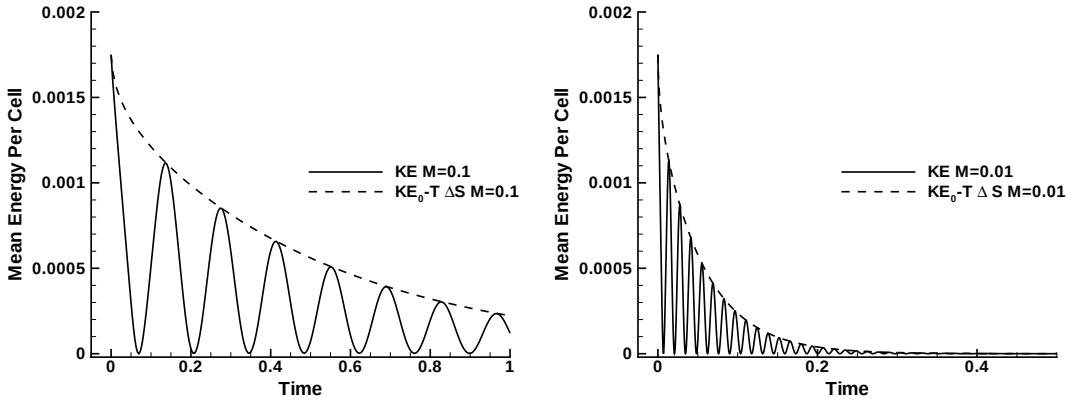

(a) $M = 0.1$ (b) $M = 0.01$

Figure 5.2: Actual change of kinetic energy plotted with the predicted change using the initial kinetic energy minus $T\Delta S$ for a shock tube problem

$$T\dot{\mathcal{P}}_s = \tau^{\nu} : \nabla \mathbf{u} = -\frac{1}{2}\rho\left(\frac{D(q^2)}{DT}\right)_{irreversible}. \tag{5.2.14}$$

The result directly relates the increase of entropy with the dissipation of kinetic energy pointwise within a system due to a stress tensor τ^{ν}, under the assumption that the cell is not located on an inlet or outlet boundary where there is a net flux of shear stress into or out of the system.

A useful feature of the directional split Godunov methods is that many of the properties of the scheme can be illustrated through simple one dimensional test cases, such as the combination of isentropic and non-isentropic behaviour. Consider the shock tube problem

$$x < 0.5, \qquad p_L = p_R = p_0\left(1 + \tfrac{\gamma-1}{2}M^2\right)^{\frac{\gamma}{(\gamma-1)}}, \qquad u = Ma/2, \tag{5.2.15}$$

$$x > 0.5, \qquad \rho_L = \rho_R = \rho_0\left(1 + \tfrac{\gamma-1}{2}M^2\right)^{\frac{1}{(\gamma-1)}}, \qquad u = -Ma/2, \tag{5.2.16}$$

where a is the speed of sound, M the Mach number. The computational domain is 200 cells in a region of dimension 1, and the boundary conditions are periodic. First order time stepping and first order piecewise constant in space reconstruction is used. This problem is formulated so that the left and right hand quantities are isentropic realisations of the same flow, and that the mean momentum is zero. Figure 5.2 a) shows the variation of specific kinetic energy with time compared to the variation of $T\Delta S$ where the values of p_0 and ρ_0 are chosen such that the Mach number of the flow is 0.1. The kinetic energy behaves as a damped spring as described previously, where the isentropic variations in kinetic energy are much more rapid than the non-isentropic variations. However, it is clear that the irreversible decrease in kinetic energy is mirrored exactly by an increase in $T\Delta S$. Figure 5.2 b) shows the same test case for

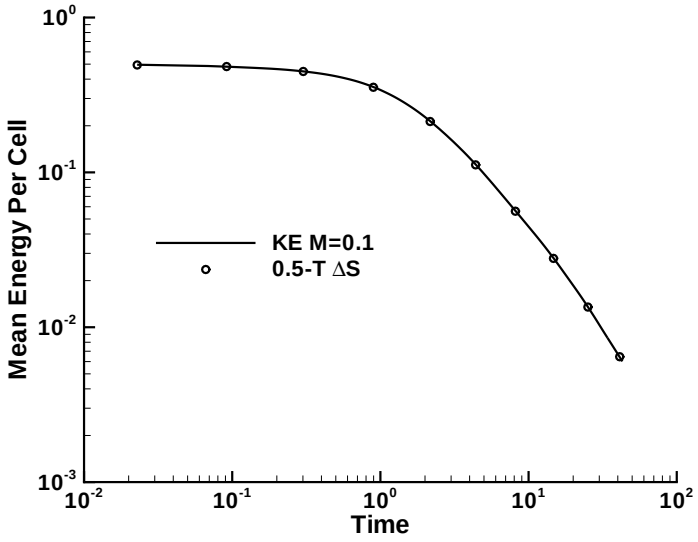

Figure 5.3: Actual change of kinetic energy plotted with the predicted change using the initial kinetic energy minus $T\Delta S$ for homogeneous decaying turbulence in a cube

a Mach of 0.01. The same relationship can be seen however the rate of decrease of kinetic energy is much more rapid, illustrating the severe Mach number dependence of dissipation of kinetic energy.

As a more complex case, consider homogeneous decaying turbulence in a periodic cube at resolution 32^3 using the 5th order MUSCL reconstruction in space and 3rd order TVD Runge-Kutta. Specify the initial condition following [195, 197] as a summation of Fourier modes of random phase corresponding to the kinetic energy spectra

$$E(k) = u^2 \frac{k^4}{k_p^4} \sqrt{\frac{8}{k_p^2 \pi}} \exp\left(-2\left(k/k_p\right)^2\right), \tag{5.2.17}$$

where k is the wavenumber, and the peak of the energy spectrum was chosen at $k_p = 4$. Additionally, the initial kinetic energy magnitude and Mach number are chosen as

$$KE = \frac{3}{2} u_{rms}^2 = 0.5, \tag{5.2.18}$$

$$M = \frac{u_{rms}}{a} = 0.1, \tag{5.2.19}$$

where u is the mean turbulent velocity. Figure 5.3 shows the time variation of kinetic energy compared to the initial kinetic energy minus $T\Delta S$. The agreement is exact. From these two examples it is clear that if the behaviour of entropy is understood, then an understanding of the dissipation of kinetic energy by Godunov schemes follows naturally.

5.3 The Dissipation of Kinetic Energy Across a Shock

The passage of a shock wave causes an increase in entropy, thus leads to irreversible dissipation of kinetic energy. Consider a stationary shock wave with pre-shock velocity u, specific volume V, Temperature T and pressure p. Bethe [19] (Reproduced in [98]) utilised the Hugoniot relations to derive the leading order entropy increase as

$$\Delta S = -\left.\frac{\partial^2 p}{\partial V^2}\right|_S \frac{\Delta V^3}{12T}. \tag{5.3.1}$$

This relationship is accurate to within 15% where $\Delta u/u$ and $\Delta\rho/\rho$ are less than 10%, and shock Mach number $M_s < 1.05$. From thermodynamic principles the second derivative of the pressure with respect to the specific volume can be expressed as [132]

$$\left.\frac{\partial^2 p}{\partial V^2}\right|_S = \frac{2\mathcal{G}\gamma p}{V^2}, \tag{5.3.2}$$

where $\mathcal{G}$ is the curvature of the isentrope. Using Equation (5.3.2) in (5.3.1) gives

$$\Delta S = -\frac{\mathcal{G}a^2}{6T}\left(\frac{\Delta V}{V}\right)^3. \tag{5.3.3}$$

Considering conservation of momentum across a stationary shock

$$\frac{u_1}{V} = \frac{u_2}{V_2}, \tag{5.3.4}$$

where u_1 and u_2 are the pre- and post-shock flow velocities, V and V_2 the pre- and post-shock specific volumes, the difference in specific volume ΔV can be related to the difference in velocity

$$\frac{\Delta V}{V} = \frac{\Delta u_s}{u_1}, \tag{5.3.5}$$

where Δu_s is the velocity jump at the shock. The change of entropy can now be written as

$$\Delta S = -\frac{\mathcal{G}a^2}{6T}\left(\frac{\Delta u_s}{u_1}\right)^3. \tag{5.3.6}$$

Finally, as noted in [132] the curvature of the isentrope for an ideal gas is

$$\mathcal{G} = \frac{1}{2}(\gamma + 1), \tag{5.3.7}$$

Inserting this into Equation (5.3.6), the irreversible increase of specific internal energy $T\Delta S$ is

$$T\Delta S = -\frac{(\gamma+1)\,a^2}{12}\left(\frac{\Delta u_s}{u_1}\right)^3. \tag{5.3.8}$$

As this is relative to a stationary shock, then as the Mach number tends to zero, $u_1 \to a$, showing that the dissipation of a shock of fixed Mach number decreases proportionally to $1/a$. However, the shock wave travels at a speed proportional to a thus the dissipation *rate* due to the passage of a shock of fixed Mach number is constant in time and independent of flow Mach number. This demonstrates that the increase in dissipation at low Mach number cannot be explained as dissipation inherent within the governing equations, and is a property of the discrete system.

5.4 The Form of the Solution to the Discrete Riemann Problem

As the dissipation due to a shock wave is not dependent on the flow Mach number, then a second possibility is that the number of interfaces where the solution of the Riemann problem lies between the shock and contact surface increases as the Mach number decreases. To compute the solution to the Riemann problem exactly an iterative process must be employed to determine the velocity v^*, density ρ^* and pressure p^* between the waves. However, at low Mach number or where the jumps are not extreme, the solution to the Riemann problem can be attained with reasonable accuracy using the primitive variable linearised solution [184] for p^*

$$p^* = \frac{1}{2}(p_L + p_R) + \frac{1}{2}(u_L - u_R)\overline{\rho a}, \tag{5.4.1}$$

which can be rearranged as,

$$p^* = p_R + \underbrace{\frac{\Delta p}{2}}_{O(M^2)} + \underbrace{\frac{\Delta u}{2}\overline{\rho a}}_{O(M)}. \tag{5.4.2}$$

Scaling arguments can be used to deduce the behaviour of the flow field at low Mach number. It is commonly accepted that in an incompressible flow field the pressure differences scale with M^2, and velocity difference scales with M [108]. The second term on the left hand side of Equation (5.4.2) is $O\left(M^2\right)$ whereas the final term scales as $O(M)$. This means that in low Mach flows it is expected that the majority of Riemann problems will result in a two-shock or two-rarefaction configuration, as pointed out in [73]. These are generated when $p^* < max(p_L, p_R)$ or $p^* < min(p_L, p_R)$ respectively. Indeed, examining each cell interface for the homogeneous decaying turbulence

problem shows that at Mach 0.2 the structure of the field is 46% two-shock, 46 % two-rarefaction and 7 % single shock single rarefaction solutions. Reducing the Mach number to 0.02 gives 48 % two-rarefaction and 52 % two-shock. This does not change as Mach decreases. As expected, as the Mach decreases the occurrence of single shock, single rarefaction solutions becomes increasingly rare. The typical structure of the solution to the Riemann problem changes as the Mach number decreases, however, once $M < 0.1$ the structure does not change significantly and so is not likely to be the direct cause of increased dissipation.

5.5 Irreversible Dissipation due to Solution Reaveraging

5.5.1 Linear Advection Equation

The linear advection equation is particularly useful to demonstrate the irreversible dissipation of kinetic energy in the FV framework. Consider

$$u_t + a u_x = 0, \tag{5.5.1}$$

where u can be taken as a velocity, and a the signal speed, assumed positive. In this case there are no dissipative terms thus the exact solution conserves kinetic energy. The problem can be discretised at first order accuracy in time and upwind in space as follows

$$u_j^{n+1} = u_j^n - \nu a \left(u_j^n - u_{j-1}^n \right), \tag{5.5.2}$$

where $\nu = \Delta t / \Delta x$. Taking the initial conditions as $u_{j-1}^n = -\Delta u/2$ and $u_j^n = u_{j+1}^n = \Delta u/2$, consider the solution in cell j at time $n+1$

$$u_j^{n+1} = \frac{\Delta u}{2} (1 - 2\nu a). \tag{5.5.3}$$

The theoretical change in kinetic energy is zero, but computationally it is

$$\left(u_j^{n+1} \right)^2_{exact} - \left(u_j^{n+1} \right)^2_{numerical} = \frac{1}{2} \Delta u^2 \nu a (1 - \nu a), \tag{5.5.4}$$

giving a dissipation rate increasing proportional to Δu^2 and the speed of sound a. Note that this result can also be gained via standard modified equation analysis [184]. It was shown by Merriam [133] that the production of entropy (defined by the entropy pair $S = -u^2$ and $F = -au^2$) for the wave equation in this first order scheme is proportional to Δu^2 and a, mirroring the decrease in kinetic energy shown here. As the flux is exact, the dissipation is due solely to the reaveraging process where $\overline{u}^2 \neq \overline{(\overline{u} + u')^2}$. This

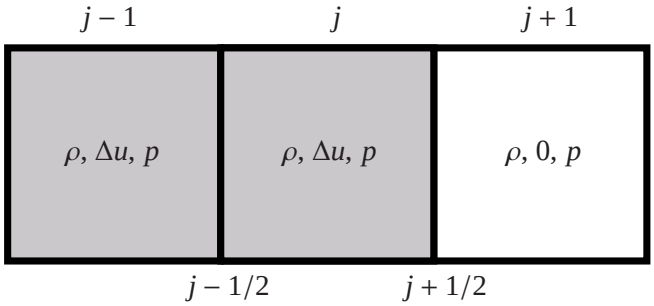

Figure 5.4: Schematic of the flow under consideration

implies that a similar dissipation due to the reaveraging process should occur in the FV representation of the Euler equations. The following section investigates this by examining the variation of the entropy over a single time step.

5.5.2 The Euler Equations

To derive the actual change of entropy in the discrete system, the entropy change in a single computational cell in a single time step is considered. The derivation of the leading order entropy change for the case of an isolated jump in velocity is detailed in full in Appendix B.1 to allow the reader to repeat the analysis. This solution was first gained by hand, and was subsequently used to validate solutions gained using the symbolic manipulation software Mathematica for the more complex but common case of a jump in all primitive variables.

Isolated Velocity Discontinuity

In this section the change of entropy is derived for an interface where there is a velocity jump Δu, but ρ and p remain constant. Consider flow through three computational cells, where the discontinuity is located at $j + 1/2$ as shown in Figure 5.4. The flow variables are evolved over one time step for a first order in space and time upwind Godunov scheme. It is assumed that the solution of the Riemann problem can be approximated using the linearised solution ([184], p.279), an assumption which is validated in subsequent numerical test cases. Assuming quantities ρ, Δu, and p in the cell $j - 1$ and j, and ρ, 0, and p in cell $j + 1$ at time level n, the solution of the Riemann problem at the cell interface $j + 1/2$ can be written as

$$p^* = p + \frac{\Delta u \rho a}{2}, \tag{5.5.5}$$

$$u^* = \frac{\Delta u}{2}, \tag{5.5.6}$$

$$\rho^* = \rho + \frac{\Delta u \rho}{2a}. \tag{5.5.7}$$

Table 5.1: Rate of increase of $T\Delta S$ for an isolated velocity jump per unit time

$\Delta u/a$	Eqn. (5.5.10)	Exact	PVRS	HLLC
0.5	0.00024	0.00026	0.00025	0.00026
0.1	0.0011	0.0011	0.0011	0.0011
0.01	0.01	0.01	0.01	0.01
0.001	0.104	0.104	0.104	0.104

The leading order entropy increase over a single time step given by an asymptotic expansion in Δu and a is (See Appendix B.1 for full details)

$$\Delta S = \frac{R}{\gamma - 1}\frac{\gamma\nu\Delta u^2}{8a}\left[2\gamma - 2 + 2\nu a\left(1-\gamma\right)\right] + O\left(\Delta u^3\right). \tag{5.5.8}$$

As the irreversible increase of specific internal energy is $T\Delta S = \left(a^2/R\gamma\right)\Delta S$ then

$$T\Delta S = \frac{\Delta u^2 \nu a}{4}\left(1-\nu a\right) + O\left(\Delta u^3\right). \tag{5.5.9}$$

It can be seen that the increase of entropy is only positive as long as $1 - \nu a > 0$, which is low Mach limit of the familiar CFL condition. Equation (5.5.9) can be converted to time rate of dissipation, given that $\nu = \Delta t/\Delta x \approx C/a$, where C is the Courant-Friedrichs-Levy number,

$$\epsilon_{\Delta u} = T\Delta S/\Delta t = \frac{\Delta u^2 a}{4\Delta x}\left(1-\nu a\right) + O\left(\Delta u^3\right). \tag{5.5.10}$$

where ϵ is the irreversible change of kinetic energy per unit time. This is consistent with analysis of the increase of entropy by Barth [13], which also points to an increase of entropy proportional to the jump size squared. The asymptotic analysis has been validated using a one dimensional test case for a first order in time and space Godunov method solving the Riemann problem with an exact Riemann solver, the HLLC solver, and the Primitive Variable Riemann Solver (for details about these Riemann solvers consult [184]). Table 5.1 shows the rate of entropy increase in the first time step for a shock tube case where the left and right states are defined as

$$p_L = p_R = \rho a^2, \qquad \rho_L = \rho_R = \rho, \qquad u_L = \Delta u, \qquad u_R = 0. \tag{5.5.11}$$

The results show excellent agreement with all numerical schemes even where the Mach number of the velocity jump is as high as 0.5. This agreement is to be expected as Equation (5.5.10) is a leading order approximation in terms of Mach number of the velocity jump and in terms of order of the velocity jump itself, thus it is applicable beyond the strictly incompressible regime.

The dependence of the dissipation rate on the speed of sound and Δu^2 is clearly different from the dissipation inherent in the solution of the Euler equations (Equation (3.8.20)). Equation (3.8.20) was derived assuming the validity of the Hugoniot relations [88], which only hold true when all gradients of the flow exiting the control volume are zero, and the rate of change of these gradients is zero in a given frame of reference. Clearly, this is not the general case for an arbitrary interface where there is a difference in all primitive variables. Thus, the Hugoniot relations hold in a global sense, but the above expansion applies in the case of unsteady flow for an interface with a local variation in velocity from the left to right state.

Taking the initialisation of a shock wave on a grid as an example, the validity of the result becomes clear. In the first time step a dissipation proportional to Δu_s^2 acts on the initialised velocity jump. This is larger than the dissipation rate for an ideal shock wave derived by Bethe and thus the shock is diffused. After several time steps a steady state solution is gained where the sum of several smaller Δu^2 equals the entropy gain of a single global increase proportional to Δu^3. In this process the excess entropy produced in the first time step at a rate of Δu_s^2 manifests itself as an entropy 'anomaly'. A similar process occurs when shock waves interact, and causes excess heating in the Noh test case which can be viewed as a shock interaction problem [143].

The dependence on Δu^2 is due to an interaction of both the governing equations and the reaveraging process. If the increase of entropy was solely due to the reaveraging of the continuous function to a fixed mesh, then the leading order error terms would be of order Δu. However, the governing equations are constructed in such a manner that the leading order fluctuations (i.e. Δp and $\Delta \rho$) are isentropic in nature and so cancel in the asymptotic expansion.

Menikoff [131] examined the variation of entropy when initialising a shock wave, or when shock waves interact and demonstrated that an entropy anomaly occurs due to the finite width of a viscous shock profile, which is a special case of the general asymptotic expansion presented here.

As also observed numerically in [131], under refinement of the mesh the spatial extent of the anomaly reduces, but the magnitude does not. In employing a Godunov method to simulate a turbulent flow field, there is no steady frame of reference, and these entropy 'anomalies' occur throughout the field providing a dissipation rate proportional to Δu^2 and a. It is then expected that ILES simulations using a Godunov scheme would have a subgrid model more akin to a physical viscosity than proportional to Δu^3 as ideally desired. As the numerical viscosity increases above that required to mimic the behaviour of the subgrid scales then a greater separation is required between the highest wave number captured on the grid and the beginning of the sub-inertial range. When simulating low Mach turbulence with Godunov methods this effect means that a large number of finite volumes must be employed to give the required separation. This explains why the kinetic energy spectra gained using shock capturing methods are typically overly dissipative in the high wavenumber range (See, for example, [62, 182]).

Isolated Velocity and Pressure Discontinuity

The analytical methodology followed in Appendix B.1 to give the leading order dissipation rate for an isolated velocity discontinuity has been implemented into Mathematica, a symbolic manipulation software package. The use of symbolic manipulation software enabled the derivation of leading order dissipation rates for more complex cases including jumps in all primitive variables. This was validated using the analytical solution for the isolated velocity jump and numerical test cases. The Mathematica script used to compute the leading order terms in the dissipation rate for the case of a jump in all primitive variables is reproduced in Appendix B.2.

Extending the previous test case but now including a jump in pressure, such that

$$p_L = p + \Delta p/2 \qquad p_R = p - \Delta p/2, \qquad \rho_L = \rho_R = \rho, \qquad u_L = \Delta u, \qquad u_R = 0., \tag{5.5.12}$$

the leading order dissipation rate in the presence of a jump Δp and Δu, $\epsilon_{\Delta p,\Delta u}$, can be written as

$$\epsilon_{\Delta u,\Delta p} = \frac{(1-\nu a)}{\Delta x}\frac{(\Delta p - \rho a \Delta u)^2}{4a\rho^2} + ... \tag{5.5.13}$$

The time rate of irreversible dissipation of specific kinetic energy in the case of an isolated pressure jump decreases with Mach number (assuming a fixed pressure jump). Table 5.2 details the rate of entropy increase in the first time step for a first order in time and space shock tube test case where the initial conditions are

$$p_L = p + \Delta p/2 \qquad p_R = p - \Delta p/2, \qquad \rho_L = \rho_R = \rho, \qquad u_L = u_R = 0, \tag{5.5.14}$$

and Δp is constant in magnitude, the ratio $\Delta p/p$ is adjusted by increasing the pressure p. The highest change tested is a jump of half the magnitude of the mean pressure of the left and right side. In all cases the error between the leading order entropy increase in Equation (5.5.13) and the exact solution is less than 1%. The rate of entropy production scales with the inverse of the speed of sound as expected. Comparing this with the results in Table 5.1 it is clear that the terms due to the velocity jump dominate in low Mach flows. Interestingly, the leading order approximation in Equation (5.5.13) is valid for such a large pressure jump even though the PVRS Riemann solver produces negative entropy due to the higher order terms.

In this case, the variations in density do not affect the rate of entropy production - they only modify the magnitude of production in the presence of a velocity or pressure jump due to the influence of the term $\rho = (\rho_L + \rho_R)/2$ in the linearised solution.

It is interesting to note that the dissipation is proportional to the square of the departure from the characteristic relation along the $\lambda_{eig} = u + a$ eigenvalue, $\Delta p - \rho a \Delta u = 0$.

Table 5.2: Rate of increase of $T\Delta S$ for an isolated pressure jump per unit time

$\Delta p/p$	Eqn. (5.5.13)	Exact	PVRS	HLLC
0.5	0.00048	0.00048	−0.0001	0.00048
0.1	0.00021	0.00021	0.00016	0.00021
0.01	6.6×10^{-5}	6.6×10^{-5}	6.5×10^{-5}	6.6×10^{-5}
0.001	2.1×10^{-5}	2.1×10^{-5}	2.1×10^{-5}	2.1×10^{-5}

The analysis within this subsection has assumed that u^* is positive, i.e. that the solution at $x = 0$ lies to the left of the contact surface and thus can be described by Equation (5.5.7), but there is no assumption in the direction of the jumps as long as this criteria remains valid. If it is assumed that the velocity jump is sufficiently negative, or that the pressure increases from left to right such that $u* < 0$ then the solution for $\rho*$ changes to ([184], p. 297)

$$\rho* = \rho_R + (u* - u_R)\rho/a. \tag{5.5.15}$$

Utilising the script in Appendix B.1, the leading order rate of dissipation in this case is

$$\epsilon_{u*<0} = \epsilon_{\Delta u,\Delta p} + \frac{\Delta p\left(\Delta p - a^2\Delta\rho\right)}{2\Delta x\rho^2 a\left(\gamma - 1\right)} + ... \tag{5.5.16}$$

For a constant pressure and density jump there is an additional component of dissipation which increases as the Mach number decreases, proportional to $\Delta p\Delta\rho$. However, this would scale as M^{-4} in incompressible flows or at least M^{-2} for un-preconditioned compressible FV schemes so would not dominate over the terms in Δu^2. The characteristic invariant along the $\lambda_{eig} = u$ eigenvalue also appears in this expression, so it appears that dissipation is minimised only when all jumps are zero, or when the jumps correspond exactly to the characteristic equations for the waves which pass into the cell.

Shear Waves

For a three dimensional direction split method the shear waves are typically advected passively. This means that the accuracy of the projected value of the velocities parallel to the interface, in this case the v velocity, will also affect dissipation. In the case of a single isolated jump in v velocity dissipation will only occur if the contact wave enters the cell under consideration. This is because the components parallel to the interface only change across the contact surface. For example, if the jump in v velocity takes place at the right hand interface, dissipation occurs only if u^* is negative.

Following the methodology detailed in Appendix B.1, the leading order irreversible dissipation rate has been derived given the initial conditions in Equation (5.5.12) and

additionally $v_L = \Delta v/2$, $v_R = -\Delta v/2$. The leading order term associated with the shear wave is constant with respect to the speed of sound,

$$\epsilon_{\Delta v} = \frac{\Delta v^2 \left(\Delta\rho - 2\rho\right) u}{4\rho\Delta x} + ... \tag{5.5.17}$$

thus it does not influence the asymptotic behaviour of the system. In a simple shock tube case with constant u, p, ρ and a step discontinuity in the v velocity component Equation (5.5.17) is accurate to within 1% in validation cases where $\Delta v/a < 0.5$.

5.5.3 Higher Order Methods

The previous subsections discuss only the first order in time and space Godunov scheme. The majority of practical simulations are conducted with second or even higher order methods, and so it is useful to discuss the applicability of the above analysis to more general Godunov schemes.

In smooth regions, a higher order interpolation in space would act to reduce the magnitude of the jumps between the left and right quantities. The irreversible dissipation will still depend on Δu^2 and increase as $1/M$, however Δu^2 would now be estimated via a Taylor series expansion of the interpolation function. This confirms that a key parameter in the design of numerical schemes is to minimise the difference between the left and right quantities, not necessarily the formal order of accuracy. As an example of this, the Minmod and van Leer limiters have the same formal order of accuracy when used in a MUSCL formulation. Despite this the van Leer limiter will normally resolve interfaces much more sharply. The underlying reason for this difference is that although both limiters have second order accurate interpolation, the jump from the left to right side interpolated values is second order for Minmod, but third order for van Leer. This gives the observed improvement in performance.

An additional property of the various extrapolation methods is that they increase the kinetic energy within a given cell via the process of interpolation itself. This will also affect the entropy, however in a more complex manner, the analysis of which is beyond the scope of this chapter. It is expected that methods which give overall dissipative truncation errors represent interpolation methods which do not increase the kinetic energy with respect to the continuous function in the interpolation stage.

The analysis in section 5.5 is not valid for higher order time stepping methods, and would have to be repeated for each different time stepping method. As all higher order methods are multi-step then it is expected that the resulting expressions would be quite complex. However, the asymptotic behaviour can be easily examined numerically. Table 5.3 shows the velocity jump test case in Section 5.5.2 repeated using second order Total Variation Diminishing (TVD) Runge-Kutta method [164], implict-explicit dual time-stepping (DT) method [92], third order TVD Runge Kutta method [69], and third order extended stability (ES) Runge-Kutta [173] with first order spatial reconstruction using the exact Riemann solver. These results demonstrate that the dissipation

Table 5.3: Rate of increase of $T\Delta S$ for a fixed magnitude velocity jump (varying the speed of sound) for several different time stepping methods

$\Delta u/a$	2nd TVD RK	2nd DT	3rd TVD RK	3rd ES RK
0.5	0.00028	0.00023	0.00029	0.0003
0.1	0.0012	0.0010	0.0012	0.0014
0.01	0.011	0.010	0.013	0.013
0.001	0.118	0.103	0.130	0.130

Table 5.4: Rate of increase of $T\Delta S$ for a variable velocity jump (fixed speed of sound) for several different time stepping methods

$\Delta u/a$	2nd TVD RK	2nd DT	3rd TVD RK	3rd ES RK
0.1	0.0012	0.0010	0.0012	0.0014
0.2	0.0052	0.0043	0.0055	0.0056
0.4	0.023	0.019	0.023	0.023

increases linearly with speed of sound with all time stepping methods as was the case for the first order in time computations. Additional tests varying the magnitude of isolated velocity discontinuities whilst holding the speed of sound constant are detailed in Table 5.4. It confirms that the dissipation rate is proportional to Δu^2 for all higher order time stepping methods examined. This confirms that the same trends detailed for the first order schemes apply to higher order in time computations.

5.6 Conclusions

The analytical results derived within this chapter demonstrate that the rate of dissipation of a Godunov scheme for a typical unsteady flow is not of the same form as the irreversible dissipation in the governing Euler equations. In shock tube cases the global dissipation of the solution for a shock wave can be computed using the Hugoniot relations, and has been shown previously to be proportional to the velocity jump across the shock wave cubed. However, in the case of an unsteady flow feature, the local increase in entropy is dependent on the numerical viscosity which in the FV Godunov method is proportional to the velocity jump, Δu, squared and the speed of sound a. Under the assumption of low production of entropy due to thermal gradients, this corresponds to a kinetic energy dissipation rate proportional to $a\Delta u^2$, explaining directly the poor performance of Godunov methods at low Mach.

This has important ramifications in the simulation of low Mach number flows, where excess damping of flow structures leads to extremely inaccurate solutions. The analysis is presented for Godunov-type methods, however it is likely that a similar mechanism is present in all compressible finite volume methods which include a reconstruction phase. It is also of importance for Implicit Large Eddy Simulation. The expressions within this chapter can be used to derive new variable extrapolation methods, tailored

to mimic classic sub grid models through the size of the jumps in primitive variables.

CHAPTER 6

Low Dissipation Numerical Method

6.1 Introduction

Increasing computational power and improvements in numerical methods has meant that simulations of compressible flow configurations are now at such high resolution that it is increasingly important to capture relatively low Mach number features with the same compressible scheme. An example of such combined flows could include a super-critical airfoil with a turbulent wake, shock-induced shear instabilities, or Rayleigh-Taylor instabilities.

In the previous chapter, it was demonstrated that the leading order kinetic energy dissipation rate in a Finite Volume Godunov scheme can be expressed as

$$\epsilon = \frac{(1-C)}{\Delta x}\frac{(\Delta p - \rho a \Delta u)^2}{4a\rho^2} + ... \tag{6.1.1}$$

where p, ρ, u and a are the pressure, density, velocity normal to the cell interface and speed of sound respectively. Δx is the length of the computational cell, C the Courant-Friedrich-Levy (CFL) number and Δ indicates a difference between the left and right quantities at the cell interface. The key observations regarding this result is that the dissipation is proportional to the speed of sound and the velocity jump squared at leading order. Thus any low Mach features are heavily dampened by the numerical scheme.

The modification proposed in this chapter is intended for use in flows with both compressible and low Mach features, such that the time step size is not constrained by the low Mach features. It includes a simple local modification to the reconstruction process which effectively removes the Mach number dependence of the leading order dissipation rate of kinetic energy, hence significantly improving the resolution of low Mach portions of a compressible flow. It is applied in this chapter to a Godunov-type method however, in principal, there is no reason why it cannot be extended to any compressible method which employs a reconstruction phase. The main feature of the modified numerical method proposed here is that it *locally* adapts the reconstruction method to allow good resolution of low Mach features and shocks at the same time

without modifying the formulation of the governing equations. It is thus more readily applicable to flows including complex physical processes than methods based on low Mach number expansions of the Euler equations (such as the pressure projection methods of [109, 5]), or preconditioned schemes (such as [72, 117]) which typically require significant modification to add the effects of multiple fluid components, reactions, strongly compressible features or other additional physics. The modification requires negligible additional computational expense.

The layout of this chapter is as follows. Section 6.2 proposes a simple modification of the reconstruction method applied only to the velocity jumps across the cell interface. It is shown analytically that the leading order dissipation rate is constant as Mach number tends to zero, instead of tending to infinity as with the original scheme. This method has been implemented in a fifth-order in space, third-order in time MUSCL based Finite Volume Godunov method, which is also detailed in section 6.2. The original fifth-order method and the modified scheme are applied to one dimensional test cases in Section 6.3.1, which demonstrate that the modified scheme can capture weak acoustic waves, moderate and strong shock waves, and advect density layers with a reasonably low level of diffusion. Section 6.3.2 presents a single mode Kelvin-Helmholtz instability showing that the modified scheme extends the ability of the Godunov method to Mach numbers as low as 10^{-4} and recovers the expected M^2 scaling of pressure and density fluctuations. Two complex three dimensional test cases are detailed in Section 6.3.3. The modified scheme is shown to significantly reduce dissipation at the high wavenumber modes in homogeneous decaying turbulence. It is then applied to a high resolution simulation of the Richtmyer-Meshkov instability where the turbulent kinetic energy spectra are in excellent agreement with theoretical predictions, especially considering the lack of an explicit subgrid model. Finally, Section 6.4 gives conclusions and discusses the possible directions of future work.

It should be noted that an additional numerical method based on a modified Roe scheme has been proposed which has gained good results at low Mach flow. However, as the approach proposed in this chapter is more general (i.e. applicable to a range of different schemes), the modified Roe scheme is not described here. For further details on it see Appendix C or [181].

6.2 Numerical Method

This chapter is concerned with the simulation of the Euler equations, where viscosity is assumed negligible ($Re \to \infty$). The three-dimensional compressible Euler equations are solved using the direction split method. This involves solving in each principal direction the following governing equations,

$$\frac{\partial \mathbf{U}}{\partial t} + \frac{\partial \mathbf{E}}{\partial x} = 0, \tag{6.2.1}$$

where,

$$\mathbf{U} = [\rho,\ \rho u,\ \rho v,\ \rho w,\ e]^T, \tag{6.2.2}$$

$$\mathbf{E} = \left[\rho u,\ \rho u^2 + p,\ \rho uv,\ \rho uw,\ (e+p)u\right]^T, \tag{6.2.3}$$

$$e = \rho i + 0.5\rho\left(u^2 + v^2 + w^2\right), \tag{6.2.4}$$

and ρ, i, u, v, w are the density, specific internal energy per unit volume and Cartesian velocity components, respectively. It is assumed that the fluid satisfies the ideal gas equation of state

$$p = \rho i\,(\gamma - 1), \tag{6.2.5}$$

where γ is the ratio of specific heats. The Kelvin-Helmholtz and Richtmyer-Meshkov simulations also advect a passive scalar to track the two fluid components, assumed to be miscible. The fluxes are obtained by solving the Riemann problem at the cell interface using left and right limited quantities. The HLLC approximate Riemann solver is employed as detailed in Toro [184]. Higher order accuracy is achieved using MUSCL extrapolation [187],

$$\mathbf{P}^L_{i+1/2} = \mathbf{P}_i + \frac{1}{2}\phi^{lim}\left(r_i^{lim,L}\right)(\mathbf{P}_i - \mathbf{P}_{i-1}), \tag{6.2.6}$$

$$\mathbf{P}^R_{i+1/2} = \mathbf{P}_{i+1} - \frac{1}{2}\phi^{lim}\left(r_i^{lim,R}\right)(\mathbf{P}_{i+2} - \mathbf{P}_{i+1}), \tag{6.2.7}$$

where $\mathbf{P}$ is the vector of cell averaged primitive variables, and the cells are labelled by the integer i. Also,

$$r_i^{lim,L} = \frac{\mathbf{P}_{i+1} - \mathbf{P}_i}{\mathbf{P}_i - \mathbf{P}_{i-1}}, \quad r_i^{lim,R} = \frac{\mathbf{P}_i - \mathbf{P}_{i-1}}{\mathbf{P}_{i+1} - \mathbf{P}_i}. \tag{6.2.8}$$

The fifth-order limiter proposed by Kim and Kim [107] is employed

$$\phi*^{lim}_{M5,L} = \frac{-2/r_{i-1}^{lim,L} + 11 + 24 r_i^{lim,L} - 3 r_i^{lim,L} r_{i+1}^{lim,L}}{30}, \tag{6.2.9}$$

$$\phi*^{lim}_{M5,R} = \frac{-2/r_{i+2}^{lim,R} + 11 + 24 r_{i+1}^{lim,R} - 3 r_{i+1}^{lim,R} r_i^{lim,R}}{30}, \tag{6.2.10}$$

where monotonicity is maintained by limiting the above extrapolations using

$$\phi^{lim}_{M5,L} = \max(0, \min(2, 2r_i^{lim,L}, \phi*^{lim}_{M5,L})), \tag{6.2.11}$$

$$\phi^{lim}_{M5,R} = \max(0, \min(2, 2r_i^{lim,R}, \phi*^{lim}_{M5,R})). \tag{6.2.12}$$

This completes the description of the standard fifth-order method which will be denoted 'M5' throughout this chapter. The fifth-order method gives significantly better resolution that typical second-order schemes, for example, in the Sod shock tube case the extent of diffusion of the contact surface is typically reduced by one third compared to MUSCL with the second-order van Leer limiter.

As shown by Guillard *et al.* [73] the scaling of the pressure differences is incorrect at low Mach for the standard Godunov scheme. This can be shown by examining the solution to the Riemann problem for the interface pressure, where

$$p = p + \frac{M}{2}\sqrt{\gamma p \rho}\Delta u \tag{6.2.13}$$

at the cell interface once the Riemann problem is solved. The theoretical analysis in the previous chapter demonstrated that this is caused by the specification of an artificially large velocity jump at the cell interface when using piecewise constant variable extrapolation.

The solution to this problem can be approached in two different ways. One method would be to modify the Riemann solver itself in an attempt to compensate for the strength of the acoustic waves. This approach would lead to a preconditioned method such as that proposed by Guillard *et al.* [73]. However, a second approach is to consider that the Riemann solver is acting upon artificially large jumps in the primitive variables. These jump sizes have been determined through purely mathematical reasoning (i.e. via extrapolation at a specified order of accuracy of cell centred quantities) without regard for the physical nature of the flow being simulated. In this chapter it is proposed to modify the extrapolated, or 'limited' quantities in order to take into account the flow physics at low Mach.

As has been demonstrated analytically in Chapter 5, the kinetic energy dissipation rate can be gained by analysis of the generation of entropy over a single time step, using the Taylor series expansion of the extrapolated variables. This is based on the observation that in the absence of strong thermal conduction, the generation of entropy change by temperature is equal to the dissipation of kinetic energy.

The Taylor series expansion of MUSCL reconstruction using the M5 interpolation method on the vector of cell averaged primitive variables $\mathbf{P}$ gives

$$\tilde{\mathbf{P}}(x) = \mathbf{P}^i + \frac{\Delta x}{2}\mathbf{P}^i_x + \frac{\Delta x^2}{12}\mathbf{P}^i_{xx} - \frac{\Delta x^4}{720}\mathbf{P}^i_{xxxx} + \frac{\Delta x^5}{60}\mathbf{P}^i_{xxxx} + ..., \tag{6.2.14}$$

where $\mathbf{P}^i$ indicates functions evaluated at the cell centre. The exact expansion from the cell averaged quantity to the continuous function gives

$$\mathbf{P}(x) = \mathbf{P}^i + \frac{\Delta x}{2}\mathbf{P}^i_x + \frac{\Delta x^2}{12}\mathbf{P}^i_{xx} + \frac{\Delta x^2}{12}\mathbf{P}^i_{xx} - \frac{\Delta x^4}{720}\mathbf{P}^i_{xxxx} + O(\Delta x^6), \tag{6.2.15}$$

confirming that the extrapolation method is fifth order accurate. From this point on the

superscripts $(.)^i$ will be omitted for clarity. It was shown in Chapter 5 that the leading order dissipation rate arises due to the velocity jump normal to the cell interface. Thus, for simplicity, a flow field consisting of constant density, pressure and shear velocities but continuously varying normal velocity component u is considered. The following derivation is complex even for first order in time and space methods, hence following verification of the methodology (detailed in the previous chapter), a Mathematica script was used for the analysis.

The fluxes at the $i + 1/2$ and $i - 1/2$ interfaces are computed from the Taylor series expansion of the M5 extrapolation. These are then evolved at first order in time, and the change of entropy over the time step computed. Next, this process was repeated using the exact solution at the cell interfaces (i.e. the same process but with the exact Taylor series expansion). The leading order change in entropy in the discrete solution with van Leer limiting is then subtracted from the exact solution, giving the kinetic energy dissipation rate due to the errors in the spatial discretisation. Remarkably this consists of only a single term

$$\epsilon^{M5} = \frac{\Delta x^5}{60} a u_x u_{xxxxx} + H.O.T. \tag{6.2.16}$$

This term is proportional to Δx^5 as expected from the leading order of the difference between the left and right quantities in the expansion of the limiting function. Additionally, the dissipation rate increases with speed of sound a, as was previously demonstrated for the first order limiter in Chapter 5.

A simple solution to the problem of the excessive numerical dissipation is sought by modifying the velocity jump at the cell interface by a function z, where the reconstructed velocities $\mathbf{u}$ are now defined by

$$\begin{aligned} \mathbf{u}_{L,M5+LM} &= \frac{\mathbf{u}_L + \mathbf{u}_R}{2} + z\frac{\mathbf{u}_L - \mathbf{u}_R}{2}, \\ \mathbf{u}_{R,M5+LM} &= \frac{\mathbf{u}_L + \mathbf{u}_R}{2} + z\frac{\mathbf{u}_R - \mathbf{u}_L}{2}, \end{aligned} \tag{6.2.17}$$

Repeating the above analysis but for the new modified velocity extrapolation given by Equation (6.2.17) gives,

$$\epsilon^{M5+LM} = \frac{\Delta x^5}{60} z a u_x u_{xxxxx} + H.O.T., \tag{6.2.18}$$

where $H.O.T.$ are higher order in terms of spatial derivative, but lower order in terms of speed of sound. It can be seen that by choosing $z = min(M_{local}, 1))$, $M_{local} = \max(M_L, M_R)$ the leading order dissipation rate becomes

$$\epsilon^{M5+LM} = \frac{\Delta x^5}{60} |u| u_x u_{xxxxx} + H.O.T. \tag{6.2.19}$$

This ensures that the dissipation does not exceed that of the original scheme and reverts to the standard upwind form in supersonic flows. The new treatment of the velocity jumps can be considered more 'realistic', in that the standard Godunov method sets up artificially large jumps which would not be present in a low Mach flow field. It can also been seen as a progressive central differencing of the velocity components as Mach number tends to zero. The left and right densities or pressures are not modified, as this will cause excessive diffusion in stationary contact surfaces, which is not desirable. Importantly, as the sign of the fifth derivative is the same as the sign of the first derivative, the leading order term is still absolutely dissipative locally. A key observation is that the reconstruction is modified based on the local properties of the flow field, hence the same governing equations are solved throughout the domain.

By assuming that the flow field consists of a single sinusoidal perturbation, where $u(x) = \tilde{u}\sin(kx)$ and $k = 1/n\Delta x$, the dissipation rate can be written as

$$\epsilon^{M5+LM} \approx \frac{1}{60n^6}\frac{|\tilde{u}|^3}{\Delta x}, \tag{6.2.20}$$

which shows a similar functional form to Kolmogorov's four-fifths law (which gives $\epsilon \propto |u|^3/l$), whereas the standard method gives a dissipation rate of the form $\epsilon \propto u^2 a/\Delta x$. This chapter includes some fully turbulent test cases to investigate if this functional change in the dissipation rate improves performance in the framework of Implicit Large Eddy Simulation. From this relation it is clear that the dissipation rate decreases steeply as n increases, i.e. as the wavelength of the mode under consideration increases, as is expected of a higher order method.

The leading order dissipation rate gives increasing entropy as long as the standard CFL criteria is held, thus the numerical method does not suffer the severe instability of preconditioned methods when used in conjunction with explicit time stepping [20]. Additionally, substituting the modified velocity jump according to Equation (6.2.17) into Equation (6.2.13) recovers the expected M^2 scaling of the pressure and density variations. This numerical method is denoted 'M5+LM' throughout this chapter.

It should be noted that not all interpolation methods can be modified in this way. A similar modification applied to the van Leer limiter gives a leading order truncation error

$$\epsilon^{VL+LM} = \frac{\Delta x^2}{12}uu_x u_{xx} + \frac{\Delta x^3}{12}Cau_x u_{xxx}, \tag{6.2.21}$$

demonstrating that one of the leading order terms still increases with speed of sound.

Finally, third-order accurate Runge-Kutta time-stepping method is employed [173]

$$U_i^1 = U_i^n + \frac{1}{2}\frac{\Delta t}{\Delta x}f\left(U_i^n\right), \tag{6.2.22}$$

$$U_i^2 = U_i^n + \frac{1}{2}\frac{\Delta t}{\Delta x}[f\left(U_i^1\right)], \tag{6.2.23}$$

$$U_i^{n+1} = \frac{1}{3}\left(2U_i^2 + U_i^n + \frac{\Delta t}{\Delta x}[f\left(U_i^2\right) + f\left(U_i^1\right)]\right). \tag{6.2.24}$$

where $f\left(U_i^n\right)$ indicates the net flux into the cell evaluated using the array of conserved variables at time n in cell position i (see also [53]). This has an extended stability region to a theoretical limit of $CFL = 2$.

6.3 Test cases

6.3.1 One-Dimensional Test Cases

Modified Sod Shock Tube

To demonstrate that the proposed modification does not affect the ability of the scheme to capture shock waves and contact surfaces the original and modified method have been applied to the Sod shock tube test case modified to include stationary flow within the rarefaction fan. This modification is used to test the scheme for unphysical rarefaction shocks when the leading order dissipation is decreased significantly within the fan. The initial conditions are

$$(\rho, u, p)_L = (1, -0.5, 1), \qquad (\rho, u, p)_R = (0.125, 0, 0.1), \qquad \gamma = 1.4 \tag{6.3.1}$$

where the initial discontinuity is placed at $x = 0.5$. The domain is of length 1 and was discretised using 100 cells. The CFL number was chosen as 1.4, and the results were taken at $t = 0.17$. Figure 6.1 shows the pressure, density and velocity profiles using both the modified and original limiting methods. The pressure and density profiles are almost indistinguishable from the original fifth-order scheme. There is only a slight change in position of the first point in the shock wave, and the modified scheme gives sharper profiles at the head and tail of the rarefaction.

Density Layer

The second test case is taken from Klein [109] and is used to validate that the scheme can advect large density variations at Mach=0.02 at very low dissipation, whilst resolving a low wavelength acoustic wave which passes through the density layer. The initial conditions are defined by

$$\rho(x, 0) = 1 + \Phi \sin(40\pi x/L) + M(1 + \cos(\pi x/L)) \tag{6.3.2}$$
$$p(x, 0) = 1 + \gamma M(1 + \cos(\pi x/L)) \tag{6.3.3}$$
$$u(x, 0) = \sqrt{\gamma} M(1 + \cos(\pi x/L)) \tag{6.3.4}$$

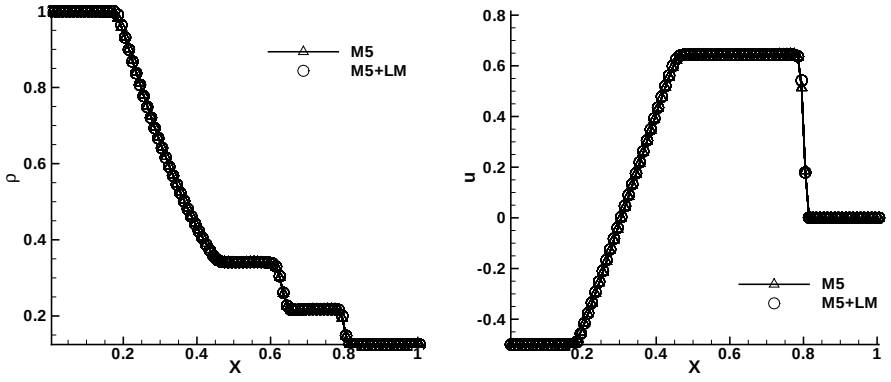

(a) Density (b) Velocity

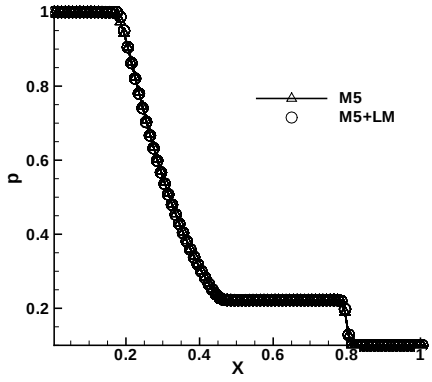

(c) Pressure

Figure 6.1: Results from the modified Sod shock tube test case

and the domain size is $-L \leq x \leq L = 1/M$ where $M = 1/51$. Finally, the domain is discretised with 1020 points, $CFL = 1.4$, and $\gamma = 1.4$. Figure 6.2 shows the pressure, velocity and density distributions at time $t = 5.071$ for both the original fifth-order scheme and the modified scheme, corresponding to about two and a half passages of the long wave acoustic perturbation. Again, both modified and unmodified schemes perform extremely well, the total density variation has been reduced by only 7% compared the initial amplitude. This is far better than the Superbee results reported in [109], and as good as the low dissipation implicit scheme presented there. The total density variation between the standard and modified scheme is only 10^{-3}%. This was the only test case examined here where the modified scheme was less stable than the original scheme, which would run up to $CFL = 1.6$.

Noh

The third test case is taken from Noh [143] and consists of two infinite strength shocks moving out from the centre. This is employed to test the performance of the scheme for very strong shocks. The initial conditions are

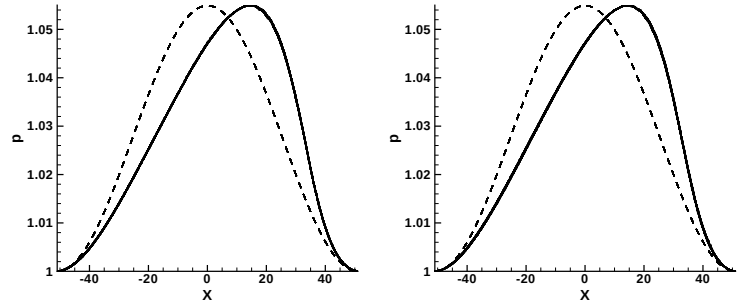

(a) Pressure

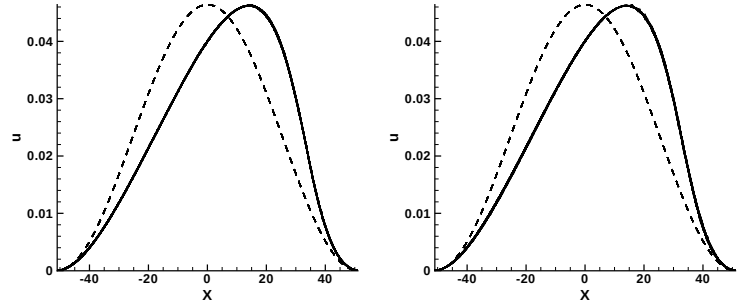

(b) Velocity

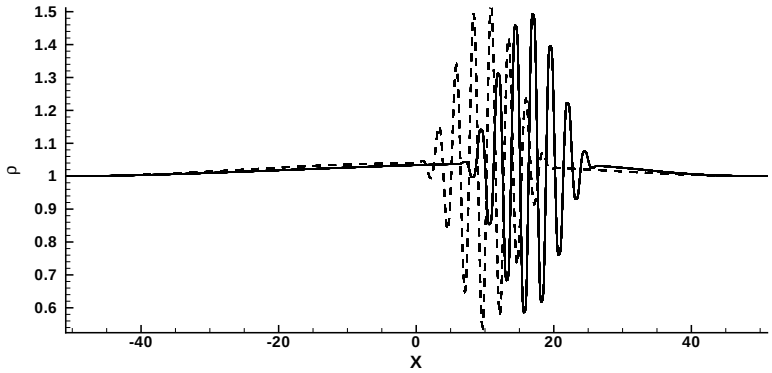

(c) Density M5

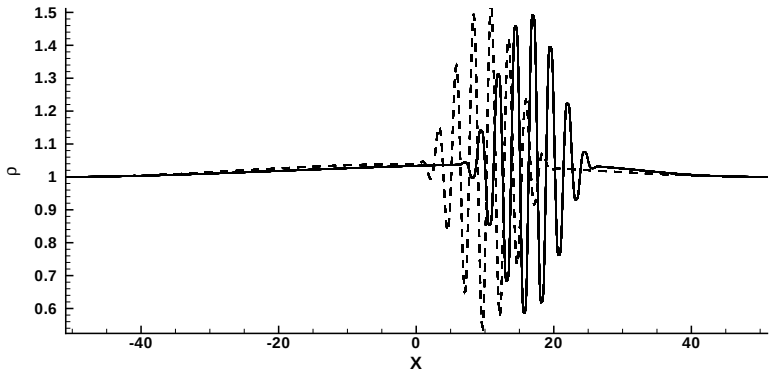

(d) Density M5+LM

Figure 6.2: Results from the density layer test case, left column M5, right column modified scheme M5+LM. The initial conditions are shown as dashed lines

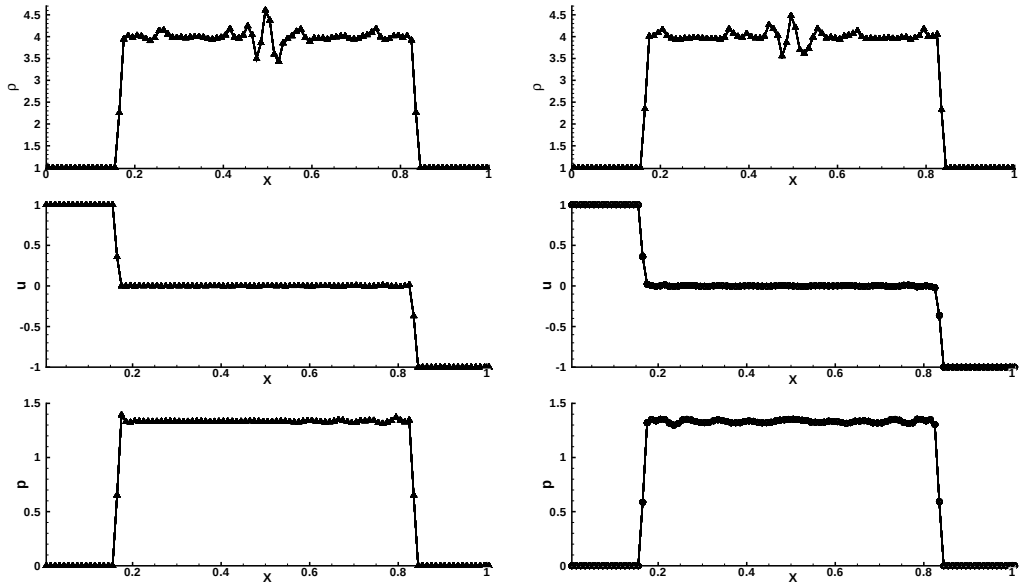

(a) M5 (b) M5+LM

Figure 6.3: Results from the Noh test case

$$(\rho, u, p)_L = (1, 1, 10^{-6}), \qquad (\rho, u, p)_R = (1, -1, 10^{-6}), \qquad \gamma = 5./3. \tag{6.3.5}$$

where the initial discontinuity is placed at $x = 0.5$. The domain is of length 1 and was discretised using 100 cells. The CFL number was chosen as 1.5, and the results were taken at $t = 1$. Figure 6.3 shows the density profiles using both the modified and original limiting methods. Both original and modified schemes demonstrate excellent shock capturing, however both schemes break symmetry (as do many high order schemes in this test case (see Liska and Wendroff [122]), and are oscillatory behind the strong shock. Performance in this test case can be improved by employing TVD time stepping method. This is demonstrated in Figure 6.4, which shows the results gained with the same reconstruction method but employing the third order TVD Runge-Kutta time stepping of Gottlieb and Shu [69] at CFL 0.5. The spread of the oscillations away from the centre is significantly reduced for both reconstruction methods, with the modified scheme giving the best results in the uniform region behind the shock.

6.3.2 Two-Dimensional Test Cases

Single Mode Kelvin-Helmholtz

The effective resolution of a numerical scheme can be determined by examining the ability to resolve the a single mode instability. In this case, an initially small perturbation velocity of one tenth the free stream Mach number triggers the development of a Kelvin-Helmholtz vortex. It is initialised following [199]

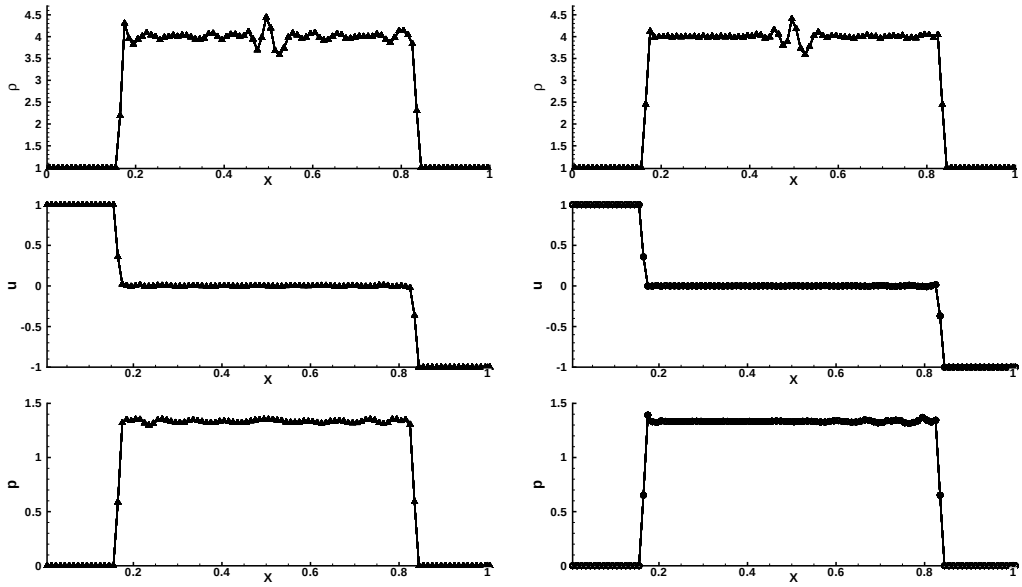

(a) M5 (b) M5+LM

Figure 6.4: Results from the Noh test case using 3rd order TVD Runge-Kutta

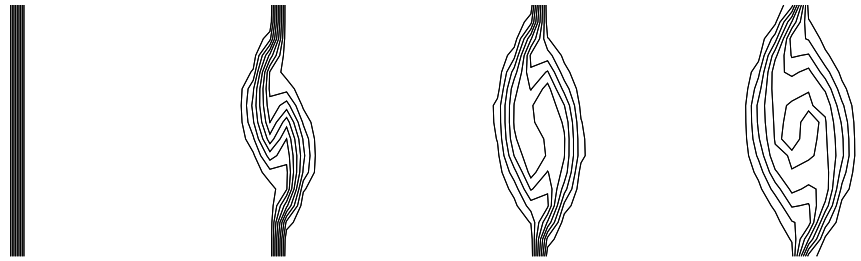

(a) t=0 (b) t=1 (c) t=2 (d) t=3

Figure 6.5: Contour lines at mass fraction 0.1 through to 0.9 with increments of 0.1 showing the development of the Kelvin-Helmholtz instability at Mach=0.2 using scheme M5

$$u = \frac{\partial A_z}{\partial y}, \qquad v = -\frac{\partial A_z}{\partial x}, \qquad A_z = \frac{U_0}{k} cos(ky) exp^{-k|x|}, \qquad U_0 = 0.1\Delta U, \tag{6.3.6}$$

where ΔU is the difference in mean flow velocity U across the mixing layer. In this example $\Delta U = 1$, hence $v = -\Delta U/2$ for $-0.5 < x < 0$ and $v = \Delta U/2$ for $0 < x < 0.5$. The Mach number, defined by $\Delta U/a$, is adjusted by changing the pressure. Density is fixed at $\rho = 1$, and $\gamma = 5/3$. The size of the domain is 1×1 and is discretised with 16 cells in each direction. The coarse resolution is deliberately chosen to highlight the scheme's ability to capture what would be a high wavenumber perturbation on a larger grid. It also allows easy demonstration of the low Mach behaviour of the dissipation of kinetic energy.

Figure 6.5 shows the development of the single mode vortex using the original fifth-order method at $M = 0.2$. The characteristic rolled up vortex is clearly visible, high-

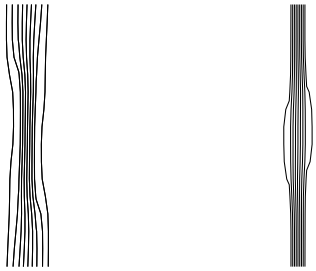

(a) $M = 0.02$ (b) $M = 0.002$

Figure 6.6: Contour lines at mass fraction 0.1 through to 0.9 with increments of 0.1 at t=3 for Mach numbers 0.02 and 0.002 using scheme M5

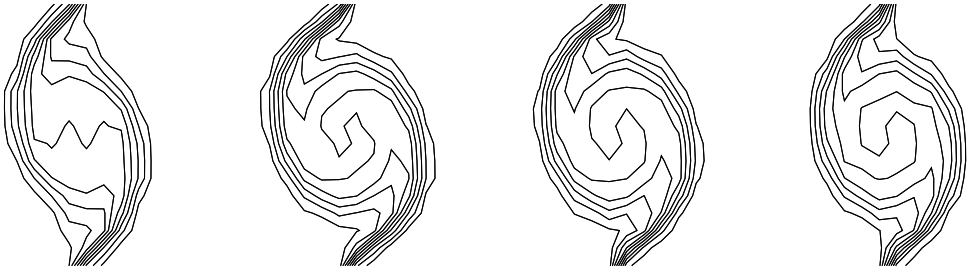

(a) $M = 0.2$ (b) $M = 0.02$ (c) $M = 0.002$ (d) $M = 0.0002$

Figure 6.7: Contour lines at mass fraction 0.1 through to 0.9 with increments of 0.1 using M5+LM at $t = 3$

lighted by the transport of a passive scalar into the spirals. It should be noted that this is already a reasonable result - using a second order limiter such as van Leer at this grid resolution would give no visible roll up.

If the Mach number is reduced by increasing the background pressure, then excessive dissipation prevents growth of the initial instability. Figure 6.6 shows the development of the mixing layer at Mach= 0.02 and 0.002. At flow Mach numbers of less than 0.2 the perturbation is dissipated, preventing the growth of the instability.

Applying the low Mach correction to the velocity jumps improves the resolution of the perturbation, as shown in Figure 6.7. At $M = 0.2$ the vortex roll-up is greater, however the 0.5 contour line has merged in the central cells thus creating the 'kink' in vortex centre. As Mach $\rightarrow 0$ the spiral structure of the vortex is perfectly intact and appears to be reaching a relatively Mach-independent structure. At the lowest Mach number there is a very slight asymmetry in the results, which is due to the use of a small number to prevent a divide by zero in the limiting stage of the calculation.

As pointed out in Guillard *et al.* [74, 73] it is important that the pressure and density fluctuations follow the correct scaling. They demonstrate clearly that the standard finite volume scheme contains pressure fluctuations of order M, contrary to the incompressible limit which should only support perturbations of order M^2. The relative pressure and density difference are defined as

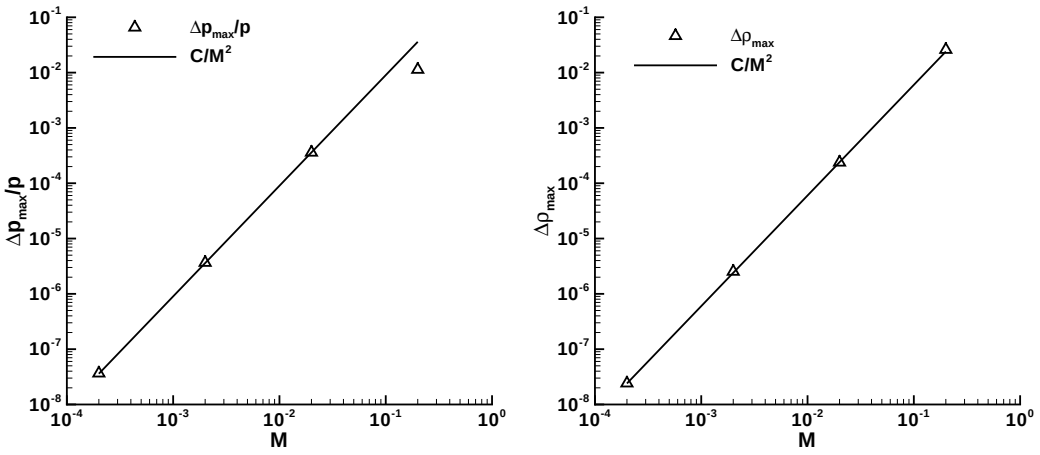

(a) Pressure (b) Density

Figure 6.8: Scaling of the maximum pressure and density variations with Mach number at $t = 3$ for scheme M5+LM

$$\Delta p = \frac{p_{max} - p_{min}}{p}, \qquad \Delta\rho = \rho_{max} - \rho_{min}, \tag{6.3.7}$$

and are plotted in Figure 6.8 for Mach 0.2 to Mach 0.0002 at $t = 3$ for scheme M5+LM. Below Mach 0.2 the maximum pressure variation follows a M^2 scaling as required from incompressible theory, as does the scaling of density variation.

6.3.3 Three-Dimensional Test Cases

Homogeneous Decaying Turbulence

In this section the schemes are tested for the ability to resolve a turbulent flow where all flow properties vary continuously throughout the flow field. The canonical numerical test case for which theoretical results are available for comparison is that of homogeneous decaying turbulence in a periodic cube. From the results in section 6.3.2 it is expected that the modified scheme will be significantly less dissipative. This would be a great advantage as it is well known that Godunov schemes dissipate heavily at high wavenumbers [62, 182].

The flow field was initialised using a method derived by Youngs and utilised in previous simulations of decaying turbulence [195, 197]. The flow field has an initial kinetic energy spectrum given by [82]

$$E(k) = u'^2 \frac{k^4}{k_p^4} \sqrt{\frac{8}{k_p^2 \pi}} \exp\left(-2\left(k/k_p\right)^2\right), \tag{6.3.8}$$

where k is the wavenumber, and the peak in the energy spectrum is defined by changing

the peak k_p in the exponential. The peak of the energy spectrum was chosen at $k_p = 4$. To ensure the generation of an almost non-divergent (i.e. incompressible) velocity field, the velocity is formed from components of a vector potential Φ, which satisfies the following relationship:

$$u = \nabla \times \Phi. \tag{6.3.9}$$

As the divergence of a curl is identically equal to zero this gives a non-divergent velocity field. The vector potential is initialised with a Gaussian distribution of amplitudes and random phases which is rescaled linearly to give a velocity field satisfying

$$KE = \frac{3}{2} u_{rms}^2 = 0.5, \tag{6.3.10}$$

$$M = \frac{u_{rms}}{a} = 0.1. \tag{6.3.11}$$

The chosen Mach number is low for a Godunov method, and thus it highlights more clearly the advantages of the modified MUSCL reconstruction proposed. The simulations were run at 32^3, 64^3 and 128^3 using both M5 and M5+LM, and the viscous terms were neglected ($Re \to \infty$). Figure 6.9 plots the mean kinetic energy per unit volume versus time for each grid resolution up to $t = 5$ which corresponds to about eight eddy turnover times. At lower grid resolutions the M5+LM scheme resolves more kinetic energy, and begins decay at a later time, which is a typical feature of increased resolution of the scheme. Figure 6.9d) compares the kinetic energy decay rate of the 32^3 modified scheme with the performance of the 64^3 scheme showing that the modified scheme behaves very close to the unmodified scheme at double the resolution.

Three dimensional kinetic energy spectra have been calculated following [44]

$$E(k) = 2\pi k^2 \phi_{ii}(k), \tag{6.3.12}$$

where $k = \sqrt{k_x^2 + k_y^2 + k_z^2}$ and the spectrum tensor ϕ is

$$\phi_{ij}(\mathbf{k}) = \frac{1}{(2\pi)^3} \int_{-\infty}^{\infty} \mathbf{Q}_{ij}(\mathbf{r}) \exp^{-I\mathbf{kr}} d\mathbf{r}, \tag{6.3.13}$$

where Q_{ij} is the second-order velocity correlation tensor. The instantaneous three dimensional energy spectra are shown in Figure 6.10 for several time instants using both methods at each resolution. The original method shows the dissipative nature of the unaltered Godunov method for high wavenumber modes. There is a significant improvement in the turbulent spectra at all grid resolutions indicating much higher energy in the high wavenumbers when modifying the velocity increments at low Mach. The original numerical dissipation was clearly too high (due to the speed of sound dependence) and thus generated a much larger dissipation range than desirable when

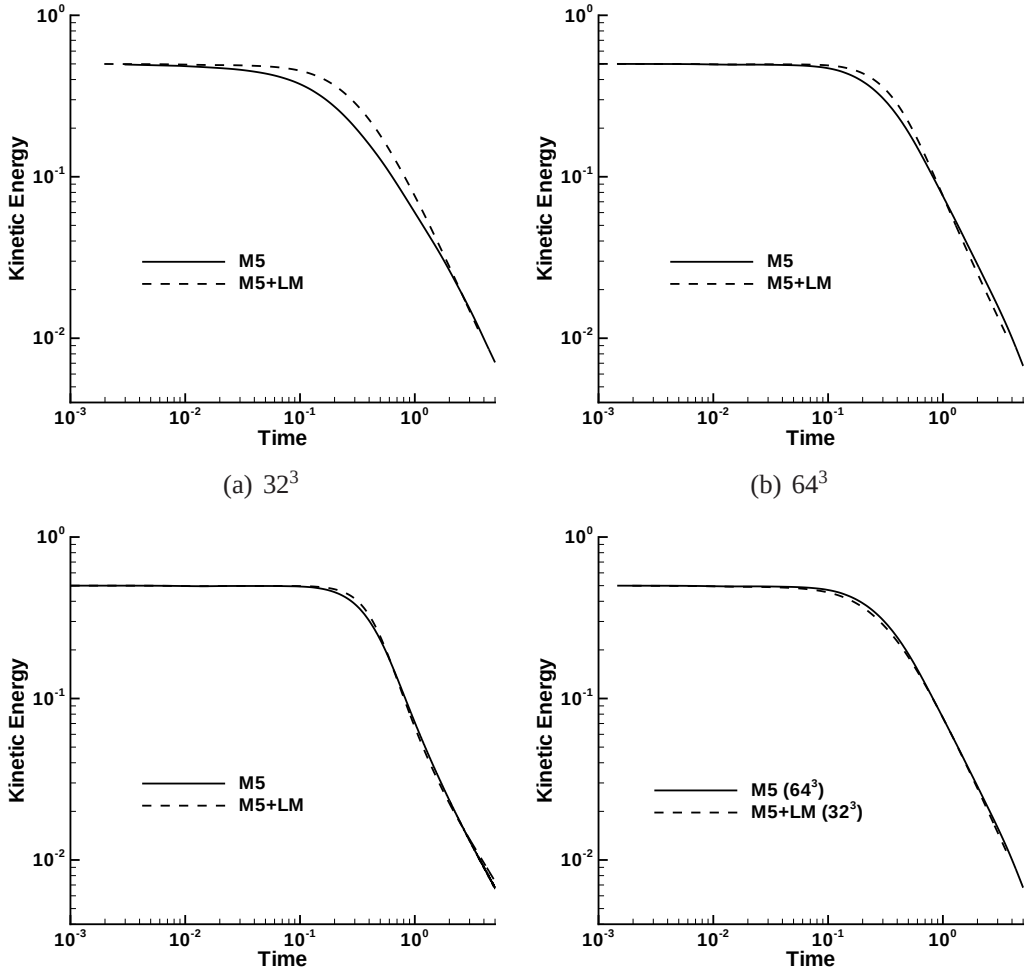

(a) 32^3 (b) 64^3

(c) 128^3 (d) 32^3 M5+LM vs. 64^3 M5

Figure 6.9: Kinetic energy versus time for the modified (M5+LM) and original (M5) scheme

simulating turbulent flow. There is a good match to a $k^{-5/3}$ spectrum when using the modified scheme despite there being no subgrid model employed - indicating that the modified scheme is potentially a good candidate for Implicit Large Eddy Simulation.

To assess this, the effective spectral accuracy and spectral eddy viscosity detailed in Section 4.3.6 have been computed for the standard scheme and the modified scheme. The results are shown in Figure 6.11 and 6.12. Surprisingly, the effective spectral accuracy for the continuity equations ($\mathcal{A}_1$) is actually reduced for the modified scheme, however for the momentum equations ($\mathcal{A}_2$) the spectral accuracy is significantly increased - and is better than the standard ninth-order WENO methods. It appears that the improved spectra and numerical results at low Mach are primarily due to improved resolution in the momentum equations. It was already noted in Chapter 4 that the resolution of the continuity equation is generally worse than that of the momentum equations, but the ramifications of this are the subject of ongoing work. Figure 6.12 shows that the modified limiting method provides dissipation closer in both form and

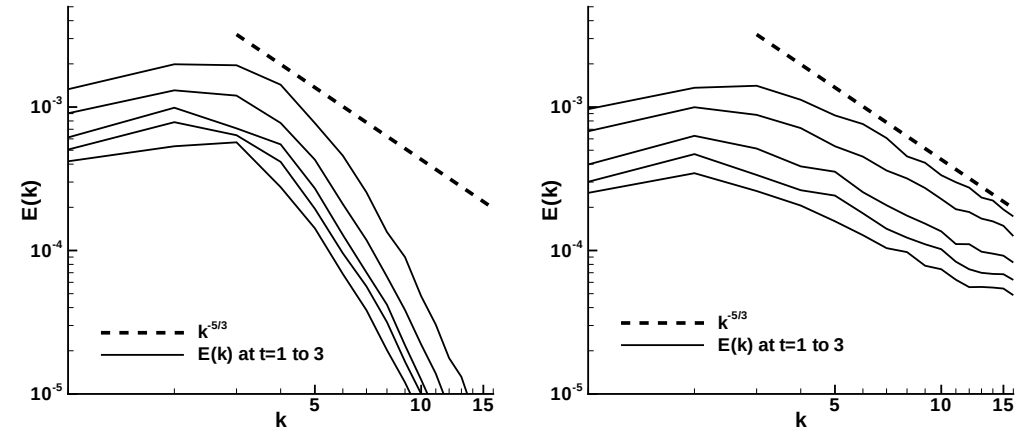

(a) 32^3

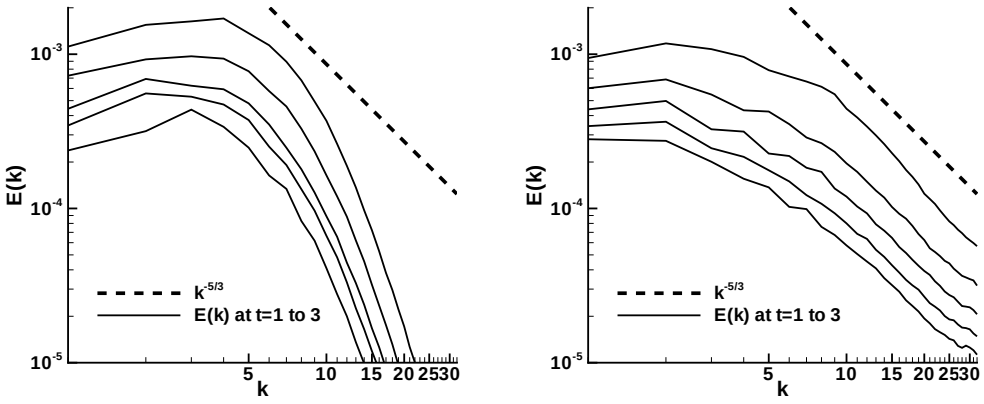

(b) 64^3

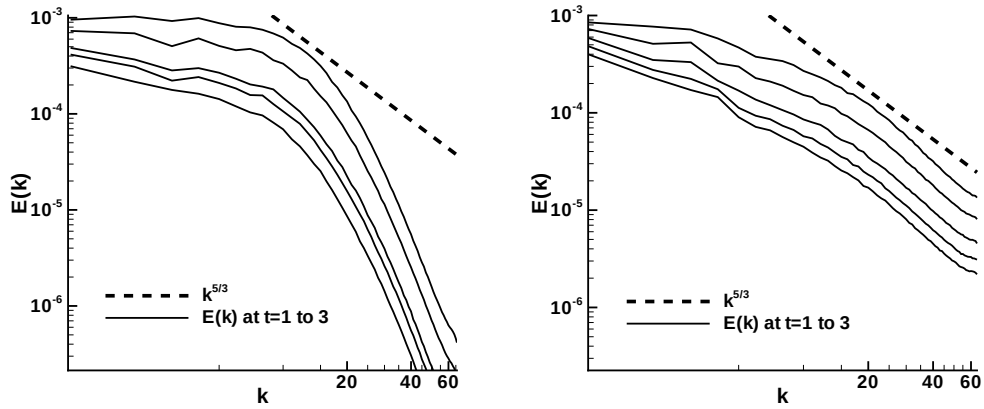

(c) 128^3

Figure 6.10: Instantaneous three dimensional energy spectra taken at t = 1 to 3 in increments of 0.5, where the highest solid line is the earliest time. Results for M5 are in the left column, M5+LM in the right column

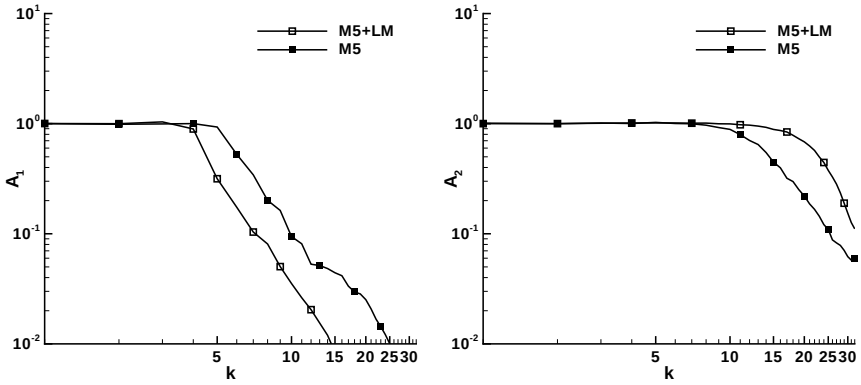

Figure 6.11: Effective spectral accuracy computed from Equation (4.3.12) for the continuity equation (left) and momentum equation (right) at 64^3 resolution

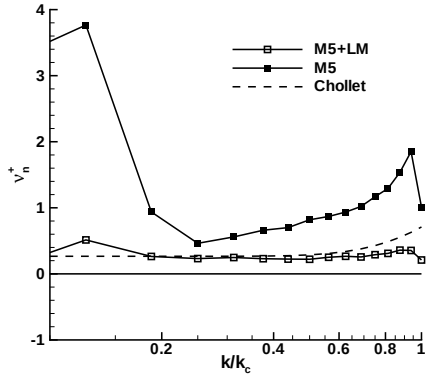

Figure 6.12: Effective spectral eddy viscosity computed from Equation (4.3.21) at the 64^3 simulation

value to that predicted by Chollet. Additionally, at low wavenumber the effective eddy viscosity is low, implying that the rapid acoustic fluctuations at a large scale are not present in the simulation.

Richtmyer-Meshkov Mixing

Finally the numerical scheme is applied to a three dimensional mixing problem where the sharp and accurate treatment of shock waves and contact surfaces is of paramount importance. Richtmyer-Meshkov mixing is generated when a perturbed interface between two gases is impulsively accelerated, typically by a shock wave [155, 134]. These instabilities first grow linearly, and then transition to turbulence, and are of importance in the study of supernovae explosions, wakes of jet engines, combustion chambers and inertial confinement fusion. This type of interaction is typically at very high Reynolds numbers thus the viscous terms are neglected. This subsection focusses on the high wavenumber performance of the numerical method, the flow physics is discussed in more detail in Section 7.3.

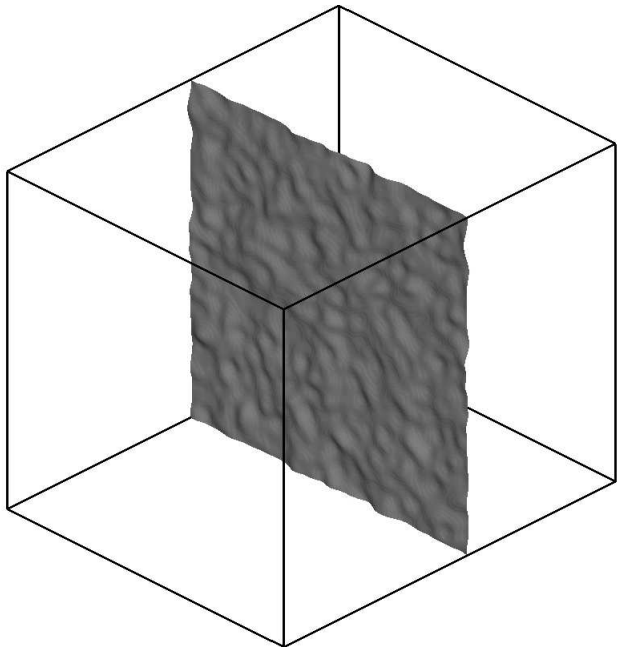

Figure 6.13: Iso-surface of mass fraction $Y_1 = 0.5$ illustrating the initial condition for the Richtmyer-Meshkov test case

The test case uses the initial conditions derived by Youngs [198] to examine the influence of initial conditions on the growth of the resultant mixing layer. The flow field consists a heavy and light gas separated by a perturbed interface where the perturbation satisfies a given power spectrum and mean amplitude. The incident shock wave is of Mach= 1.84, equivalent to a four-fold pressure increase across the shock wave. The domain chosen is of size $[0, 0, 0] \times [2.4\pi, 2\pi, 2\pi]$ where additional length is given in the x direction to allow for growth of the mixing layer. The initial conditions are

$$x < 2.3 \qquad (\rho, u, p) = (6.375, -61.4875, 4 \times 10^5) \tag{6.3.14}$$

$$2.3 < x < 3.35 + \mathcal{S} \qquad (\rho, u, p) = (3.0, -291.575, 10^5) \tag{6.3.15}$$

$$3.35 + \mathcal{S} < x \qquad (\rho, u, p) = (1.0, -291.575, 10^5) \tag{6.3.16}$$

where an initial velocity is given to the material interface such that the mean velocity of the interface is stationary after passage of the shock wave. The ratio of specific heats, γ, is set to $5/3$. The initial interface perturbation $\mathcal{S}$ is given as the sum of modes of random phase conforming to an initial power spectrum $P \propto c/k^2$. The modes excited are restricted between $\lambda_{min} = 16\Delta x$ and $\lambda_{max} = 2\pi/3$ and the standard deviation of the perturbation amplitude is $0.1\lambda_{min}$. Figure 6.13 shows the isosurface of mass fraction $Y_1 = 0.5$ at $t = 0$, illustrating the nature of the perturbation. The grid size employed is $360 \times 300 \times 300$ and simulations were run with both the original M5 limiter and modified M5+LM scheme at $CFL = 0.75$.

Once the shock wave has passed, the maximum Mach number within the mixing layer

is approximately 0.25 and decreases with time, thus the standard boundary conditions utilised in a compressible code cannot be applied in the x direction. To prevent excessive reflection of the incident and reflected shock wave, an extended one dimensional domain is employed as inlet and outlet conditions in the x direction. This does not completely eliminate completely the reflected wave as this is impossible where the mesh size changes (see Menikoff [131]), but reduces the magnitude of the reflected wave to 0.03% of the initial velocity, which is then transmitted without reflection through the inlet boundary condition. In the y and z direction periodic boundaries are applied. Note that in the following discussion all length scales are non-dimensionalised by λ_{min}, time scales by λ_{min} and $\Delta u = 291.575$ (the initial velocity impulse applied to the interface by the shock wave).

Figure 6.14 shows three time instances in the development of the mixing layer for each scheme. The large scale structures are in similar locations in both of the schemes, however it is clear that there is significantly improved resolution of fine scale features, as expected from the previous test cases. Figure 6.15 shows a plane slice of the domain showing contours of mass fraction at $t = 240$ for both numerical schemes, further highlighting the increased resolution of the modified scheme.

Next the growth of the mixing layer is examined. It is expected that the mixing layer integral width W, defined as

$$W = \int_x < \alpha_1 >< \alpha_2 > dx, \tag{6.3.17}$$

where $< \alpha_1 >$ is the $y - z$ plane averaged volume fraction of species one, and it is expected that W should grow as t^θ. Theoretical analysis suggests that at late times $\theta \approx 1/3 - 2/3$ [37, 202, 196]. Figure 6.16 shows the non-dimensional mixing layer width. The lines of best fit show $\theta \approx 0.35$ for the original scheme, and ≈ 0.38 for the modified scheme, in reasonable agreement. The increased resolution of fine scale structure does not significantly affect the integral mixing layer width, which is to be expected as simulations with single mode perturbations demonstrate that the mixing layer width can usually be captured on a very coarse grid [183].

Finally, the two-dimensional turbulent kinetic energy spectra have been calculated in the $y-z$ plane (parallel to the initial interface) and averaged over 10 slices in the x direction (direction of shock propagation). Each spectra is computed for a slice 256 by 256, and the 10 slices are symmetric across the centre of the mixing layer. Figure 6.17 compares the spectra obtained using the two numerical methods at several time instances during the decay of turbulent kinetic energy. A $k^{-3/2}$ line has been plotted on the charts which is the theoretical form of the turbulent kinetic energy spectra determined by extending the Kolmogorov-Kraichnan phenomenology to take into account the 'driven' nature of the turbulent mixing zone [202]. There is an excellent match between the theoretical result and the M5+LM scheme between $8 < k < 100$, indicating that excess dissipation at low Mach effectively removed small perturbations from the original fifth-order scheme thus preventing development of a fully turbulent flow regime. This is an excellent result, especially considering the lack of an explicit subgrid model, and

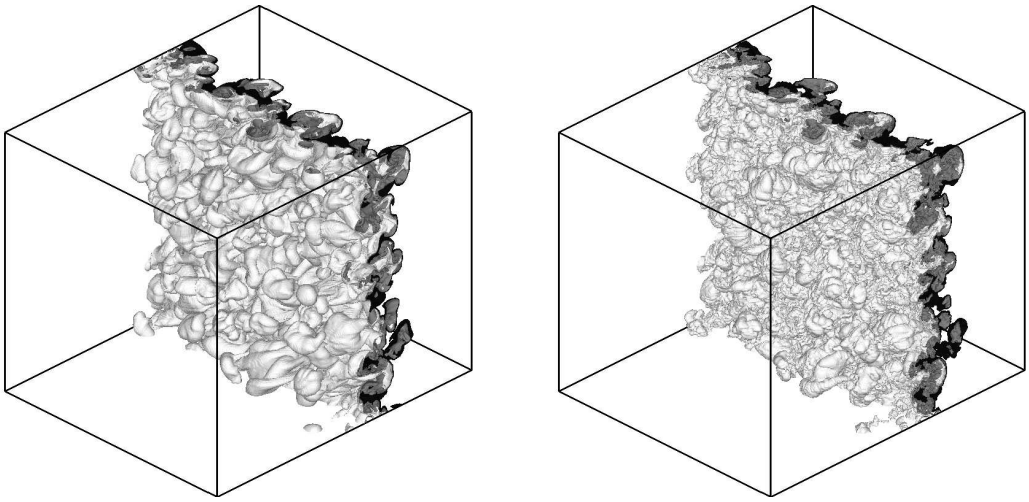

(a) $t = 80$

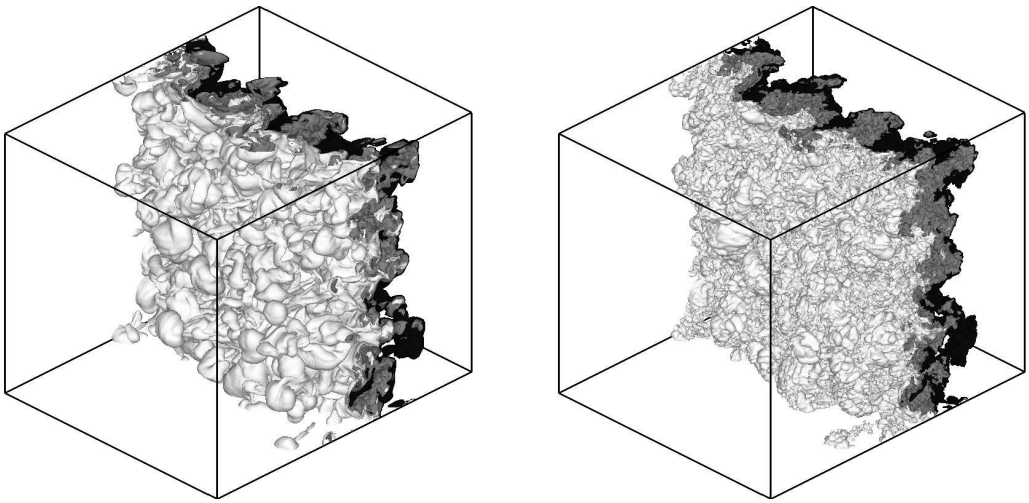

(b) $t = 160$

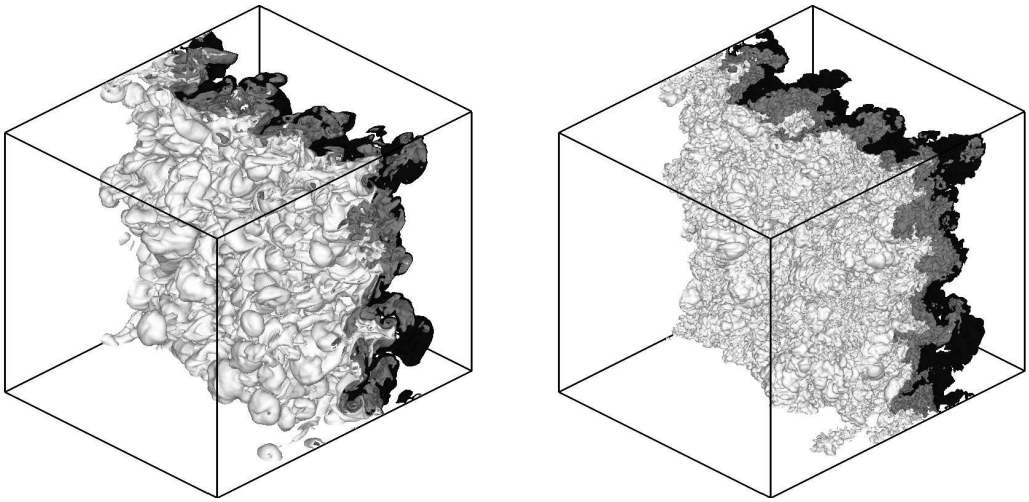

(c) $t = 240$

Figure 6.14: Iso-surface of mass fraction $Y_1 = 0.05$, 0.5 and 0.95 showing the time development of the turbulent mixing layer. Results for M5 are in the left column, M5+LM in the right column

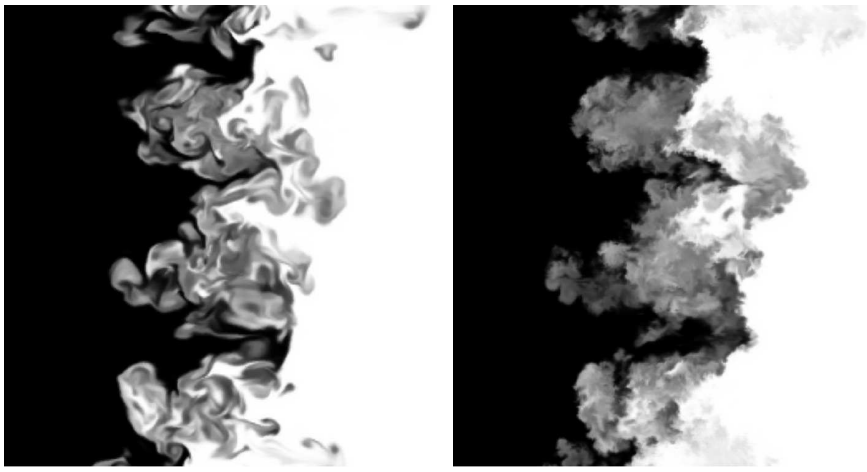

(a) M5 (b) M5+LM

Figure 6.15: Contour flood of mass fraction at $t = 240$ illustrating the fine scale structures present

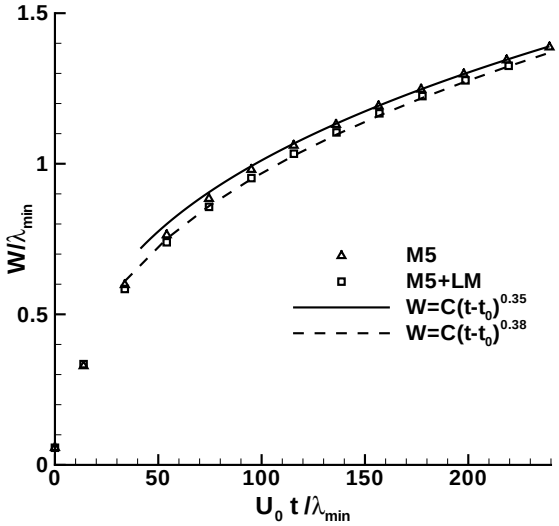

Figure 6.16: Variation of the integral mixing width W with time for the two numerical schemes

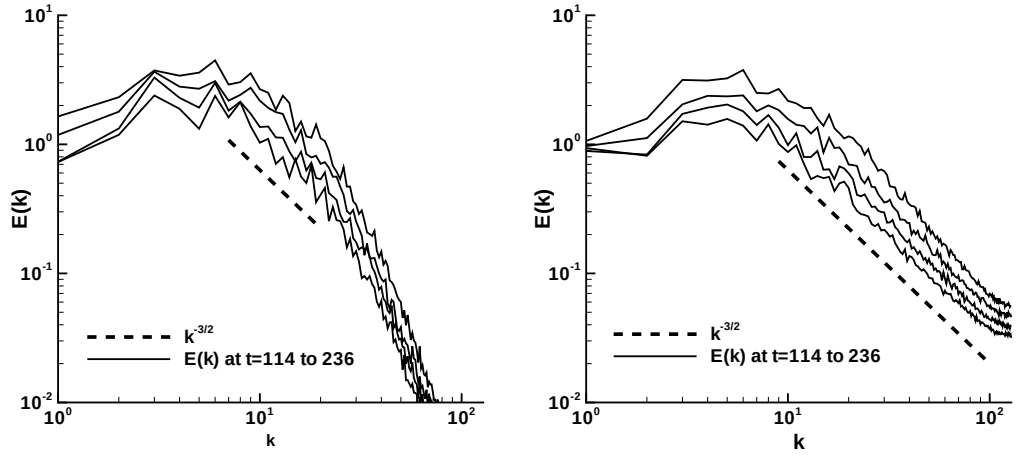

(a) M5 (b) M5+LM

Figure 6.17: Two-dimensional turbulent kinetic energy spectra taken at t = 114, 154, 195, and 236 plotted with a $k^{-3/2}$ line

a huge improvement on the original scheme. To the author's knowledge, such a large inertial range has not been seen in simulations less than 1024^3 [39] with other high resolution schemes. It could be suggested that there is a short inertial range present for $8 < k < 20$ for the original scheme however at such low wavenumbers there is only a small statistical sample thus any power law dependence is masked by statistical fluctuations.

Such a large influence of the low Mach correction on the high wavenumbers is surprising. If it is assumed that the turbulent kinetic energy spectra conforms to a $k^{-3/2}$ form, then the characteristic velocity for a given wavenumber falls as $k^{-1/4}$. Assuming the peak of the spectrum is at $k = 4$, for $k = 100$ the mean velocity would be ≈ 0.4 of the peak velocity, which is not an excessively low Mach number in this test case (Mach≈ 0.1). Thus the simulations have demonstrated that the seed instabilities resulting in such a spectrum are at a Mach number much less than the characteristic Mach number of the modes resolved on the grid assuming an inertial range form to the grid cut-off. These instabilities are damped at a very early stage in their growth by the original fifth-order method.

6.4 Conclusions

This chapter has presented a simple modification of the Finite Volume Godunov method to significantly improve performance at low Mach and in turbulent flows. It is shown analytically and through numerical test cases that the dissipation of the numerical scheme becomes constant in the limit of zero Mach, as opposed to tending to infinity as is the case for the traditional scheme. In addition, this modification recovers the correct scaling of the pressure and density fluctuations as Mach decreases. The key

feature of the numerical scheme is that the reconstruction is modified *locally*, hence the scheme can capture both shock waves and low Mach features in the same computational domain using the same formulation of the governing equations. The numerical modification adds negligible computational cost.

The modified method has been implemented in a fifth-order finite volume code using the HLLC Riemann solver, and several numerical testcases validate the performance compared to the original fifth-order method. The ability to capture shock waves in a non-oscillatory manner was demonstrated using the Sod shock tube test case, and the scheme can advect low Mach density variations without excessive dissipation. A two dimensional Kelvin-Helmholtz test case showed that the dissipation is reasonably Mach independent, and that the pressure and density fluctuations scale with M^2 as expected. Finally, two complex three dimensional turbulent simulations demonstrate significant improvement in the resolution of flow features, especially in the representation of high wavenumber modes. Results presented for the three-dimensional Richtmyer-Meshkov instability show instantaneous two dimensional turbulent kinetic energy spectra in excellent agreement with the predicted $k^{-3/2}$ form for three quarters of the wavenumber range. Previous published results with high resolution methods gain an inertial range of this length typically only with three times the number of grid points in each direction. It has also demonstrated that the accurate simulation of turbulent flows of Mach ≈ 0.1 relies on the numerical scheme capturing the growth of very low Mach instabilities.

This paper has presented the results from applying such a modification to a standard Godunov-type method, however, in principal there is no reason why equivalent results would not be gained in a wider class of fully compressible schemes which rely on reconstruction of the conserved or primitive variables at the cell interface.

CHAPTER 7

Compressible, Turbulent Flows

7.1 Open Cavity Flow

7.1.1 Introduction

Although the primary aim of this thesis is to analyse and develop numerical methods for shock induced turbulent mixing, there is a severe lack of detailed quantitative experimental data in this area against which the methods can be validated. The aim of this section is to validate the new fifth-order low Mach numerical scheme for simulations of compressible turbulent flow by comparison with experimental data and conventional LES with an advanced subgrid scale model.

It was decided to use the detailed experimental results of Forestier *et al.* [59] for compressible flow over a deep open cavity. This type of flow is of interest in many applications from vehicle sunroofs to simulations of aircraft undercarriage, weapons bays and scramjet combustion. A key feature of cavity flow is the feedback mechanism between strong acoustic waves, and the shear layer shed from the upstream edge of the cavity. In deep cavities, strong acoustic waves are generated as the coherent vortices strike the downstream corner of the cavity. These then propagate upstream to influence the developing shear layer.

A schematic of the experimental setup is shown in Figure 7.1. The flow enters the test section with a freestream velocity U of 258 m/s, equivalent to Mach 0.8. The stagnation pressure and temperature were 0.98×10^5Pa and 293K respectively. The cavity length L is 0.05m, depth is 0.12m, and width is 0.12m. The Reynolds number based on cavity length $Re_c = UL/\nu_{vis} = 860,000$. Boundary layer transition was triggered well before the cavity and the incompressible shape factor and momentum thickness were measured as approximately 1.3 and 0.65mm respectively.

The experiment measured velocity components using a two-dimensional laser-Doppler velocimeter, which were then post-processed to separate mean flow and Reynolds stresses. In addition, pressure data was taken from a sensor mounted 0.035m below the lip of the cavity on the upstream face. This measured a strong fundamental mode at a frequency of $1990 \pm 6Hz$ of magnitude $155dB$, and several subsequent harmonics. A

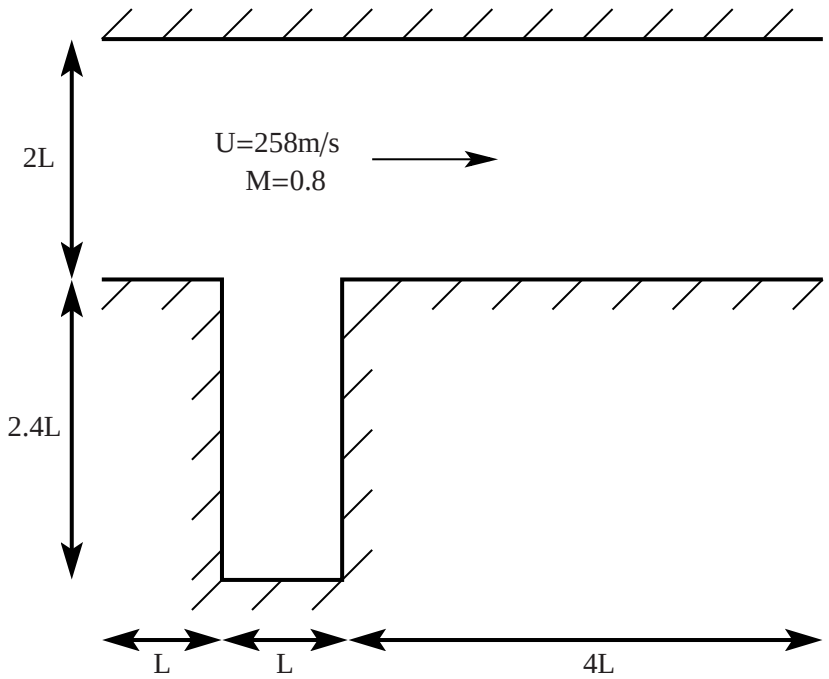

Figure 7.1: Schematic of the cavity flow experimental setup. The width of the channel is 2.4L. .

semi-empirical formula proposed by Rossiter [157] is commonly used to estimate the frequency of the fundamental mode,

$$f_n = \frac{U_c}{L}\frac{n-\alpha}{M+1/\kappa} \tag{7.1.1}$$

where n is the mode, M is the Mach number and U is the freestream velocity. Finally, κ and α are parameters which are recommended to be 0.57 and 0.25 respectively for this geometry [157]. However, using the standard coefficients for this geometry gives a predicted fundamental mode at 1515Hz, an error of almost 30%. This highlights the case for numerical simulation, as for this geometry the standard empirical formulae are very inaccurate. Following their experimental results, Forestier *et al.* [59] suggest using $\alpha = 0$ for this specific geometry, giving the fundamental mode at 2020Hz.

As the cavity flow is at high Reynolds number it is not computationally viable to employ Direct Numerical Simulation. It is pointed out by Larcheveque *et al.* [113] that Reynolds Averaged Navier Stokes (RANS) methods can predict successfully the location of the first mode, but not the magnitude. This is due to the excess dissipation of the RANS method in the developing mixing layer, which is inherently unsteady on a short timescale. Although LES is more expensive, it is capable of resolving the time dependent behaviour of the flow, simulating the acoustic field directly. This method is sometimes denoted as Computational Aeroacoustics, as the full Navier-Stokes equations are solved to gain the acoustic field. Previous LES by Larcheveque *et al.* [113] of this flow configuration gained excellent results using both LES with a selective mixed scale model and ILES. However, the underlying compressible schemes employed were

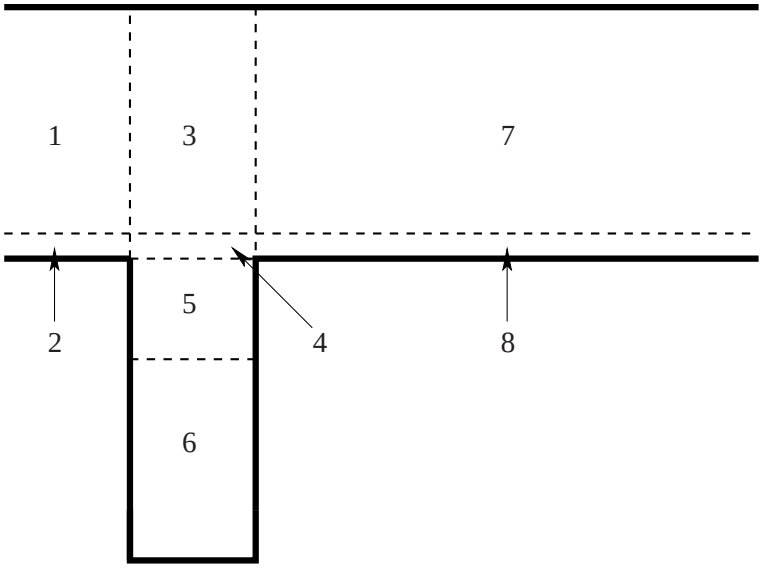

Figure 7.2: Schematic illustrating the different clustering regions employed in the cavity grid

.

not shock capturing, hence generate oscillatory behaviour in regions of discontinuities.

7.1.2 Numerical Methods

For this test case the governing equations are the Navier-Stokes equations. The air used in the experiment is modelled as an ideal gas with ratio of specific heats $\gamma = 1.4$.

The numerical method chosen is the fifth order MUSCL method with low Mach correction. No explicit subgrid modelling was employed, hence these simulation fall into the class of ILES. The grid size follows that of Larcheveque *et al.* [113], and takes the dimensions shown in Figure 7.1. The origin of the chosen co-ordinate system is on the upstream bottom corner of the cavity, where positive x is in the direction of the mean flow, positive z is vertical in the wind-tunnel, and y is the width of the domain, chosen as 0.05m.

Three different grid sizes have been employed, the grid consists of 0.8×10^6, 1.4×10^6 and 3×10^6 cells for the coarse, medium and fine simulations respectively. The domain was split into two blocks, and several different regions, the upper domain is the first block, and the cavity the second block. A schematic of the different regions in the grid is shown in Figure 7.2. The upper block is split into six regions, defined by being either before the cavity, above the cavity, or after the cavity, and then split in the z direction if they are located above the boundary and shear layer, or within the boundary and shear layer - defined as $z/L < 0.2$. Next the cavity block was split into two regions, region 5 contains the shear layer and associated recirculations close to the top of the cavity, extending to $z/L = -0.8$. Region 6 is the bottom of the cavity where the grid was relatively coarse.

Table 7.1: Details of the grid clustering exponents in the x direction, where x_R and x_L indicate clustering becoming finer in the downstream or upstream direction respectively

Regions	1, 2	3, 4, 5, 6	7, 8
Direction	x_R	$x_{L,R}$	x_L
Coarse	0.2	0.3	0.7
Medium	0.4	0.3	0.75
Fine	0.35	0.35	0.77

Table 7.2: Details of the grid clustering exponents in the z direction, where z_R and z_L indicate clustering becoming finer in the positive z or negative z directions

Regions	1, 3, 7	2, 4, 8	5	6
Direction	z_L	z_L	z_R	z_R
Coarse	0.6	0.2	0.2	0.5
Medium	0.6	0.2	0.15	0.4
Fine	0.6	0.3	0.2	0.5

An exponential clustering function was employed in the following form, taking the x direction as an example:

$$x(i) = x_{initial} + (x_{max} - x_{initial})\frac{\exp(0.1\mathcal{R}(i-1)) - 1}{\exp(0.1\mathcal{R}(i_{max} - 1)) - 1} \tag{7.1.2}$$

where i is the grid co-ordinate, $\mathcal{R}$ is the clustering exponent, i_{max} is the maximum number of points in the i direction in that region, and $x_{initial}$, x_{max} are the start and end points of the region in the x direction. Tables 7.1 and 7.2 list the grid clustering exponents in the x and z direction for each region, for each of the three grid levels employed, where several regions have the same clustering exponent. Table 7.3 details the number of points in total in the upper and lower blocks, and then number of points in the z direction in the boundary layer region above the cavity (Regions 2, 4, 8), and the mixing and recirculation zone within the cavity (region 5).

It is not considered that the development of the shear layer over the cavity is sensitive to the exact nature of the turbulent boundary layer. Hence, although the simulation is greatly under-resolved (even at the finest grid level $y^+ \approx 20$, the medium and coarse grids have y^+ of 42 and 55 respectively), no turbulent wall model was employed, and

Table 7.3: Number of grid points in each block for the different grid sizes

	Upper Block			Cavity Block			Upper b/layer	Cavity layer
Direction	x	y	z	x	y	z	z	z
Coarse	170	40	70	60	40	100	30	70
Medium	220	50	80	100	50	150	40	110
Fine	260	60	100	120	60	160	55	120

the walls of the wind tunnel were modelled as non-slip. Inlet boundary conditions were fixed assuming isentropic expansion from the experimental reservoir conditions ($p_0 = 98000$Pa, $T_0 = 293K$) to Mach 0.8. This gives a pressure of 64304Pa, density of 0.8623kg/m^3, and a velocity equal to 258m/s. The experiment measured turbulent noise levels of 1.5% of the freestream velocity, however numerical test with imposed white noise on the inlet boundary condition up to 15% of the freestream velocity showed no significant influence on the flow physics of the separated mixing layer.

The boundary layer at the inlet is defined using the experimentally measured incompressible shape factor and momentum thickness to define the power-law profile. Hence, for $y/\delta < 1$

$$< U >= U\left(\frac{y}{\delta}\right)^{1/n}, \tag{7.1.3}$$

where $n = 2/(H-1)$ is determined from the incompressible shape factor $H = 1.3$, and δ is determined using the momentum thickness $\theta = 0.65mm$,

$$\delta = \frac{\theta(n+1)(n+2)}{n}. \tag{7.1.4}$$

The exit boundary condition is extrapolated from the internal flow. As the flow is subsonic this condition is not rigorous as there are waves propagating upstream, however strong grid stretching the in x-direction damps acoustic perturbations far downstream of the cavity. The constant velocity flow field is maintained by a pressure drop which is imposed on the initial condition, aimed to compensate for momentum losses due to viscous drag at the wall, and losses due to the cavity. Assuming that the losses in the boundary layer are similar to that over a flat plate the shear stress can be estimated from the empirical relation [8]

$$\tau_w = \frac{1}{2}\rho U^2 C_f, \qquad C_f = 0.074/Re^{0.2}, \tag{7.1.5}$$

and the required pressure drop is given by

$$\Delta p = 2\tau_w A_{xy}/A_{yz}. \tag{7.1.6}$$

where A_{xy} is the area of the top and bottom walls, A_{yz} is the cross-sectional area of the domain. The mean flow is 258m/s, ratio of areas is 3, giving $\tau_w = 32$Pa and an imposed pressure drop of $\Delta p = 198$Pa. This pressure drop is imposed linearly throughout the domain at initialisation.

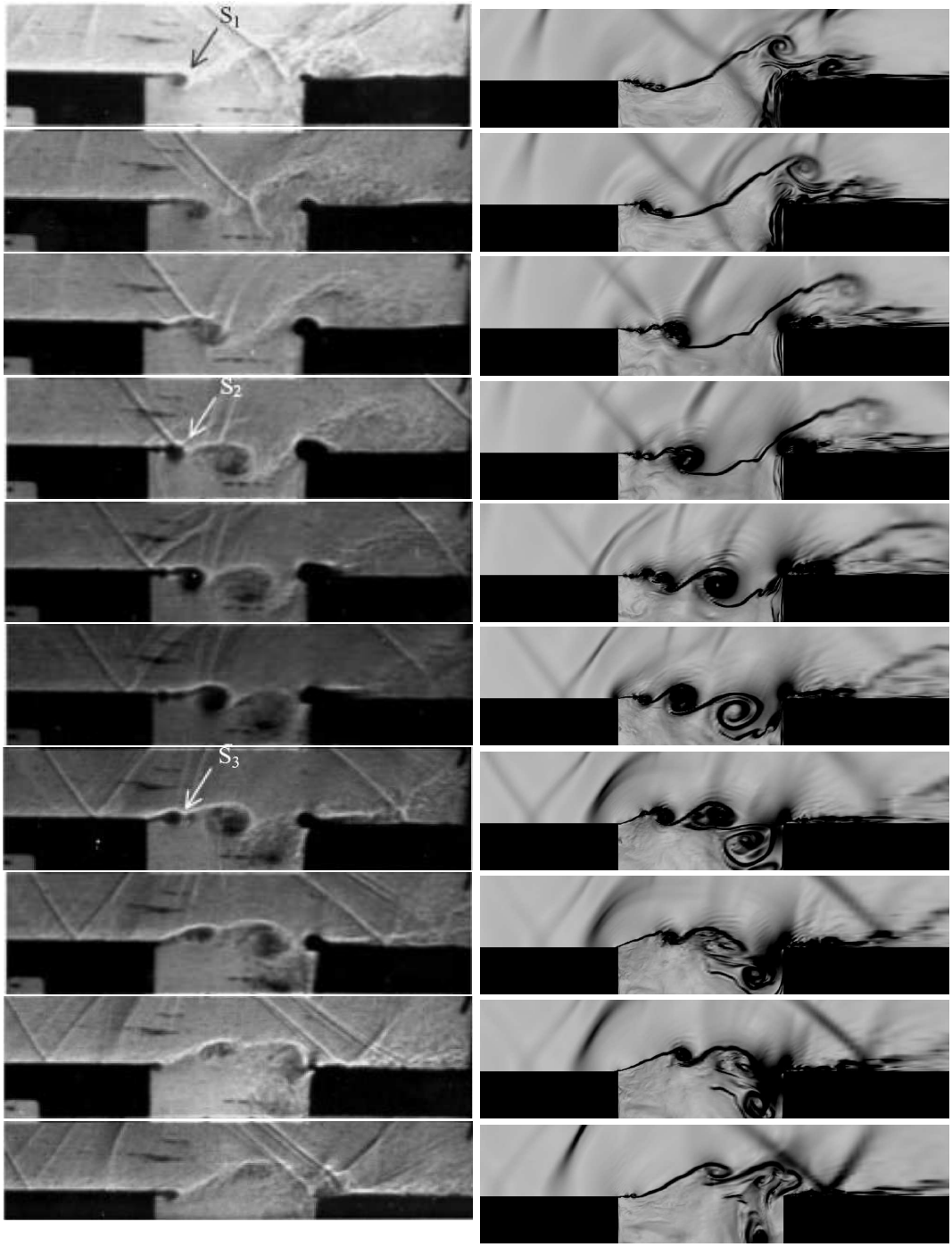

Figure 7.3: Comparison of experimental Schlieren images (left) and computational schlieren $|\nabla\rho|$ (right) at approximately the same time within the vortex shedding cycle

7.1.3 Results and Discussion

Flow Phenomenology

High speed schlieren images taken during the experiment demonstrated that the mixing layer undergoes a clear periodic cycle. This cycle is illustrated in Figure 7.3 which compares experimental schlieren images and computational schlieren results on the finest grid level ($|\nabla\rho|$). The first vortex (labelled S_1 on the experimental images) forms where the boundary layer separates from the upstream edge of the cavity. It then growth rapidly in size, an propagates downstream. As the same time the second structure (labelled S_2) begins to form at the separation point. At the third image in the sequence there is strong shock-vortex interaction resulting in deformation of the acoustic wave as it passes through the leading vortical structure. This releases a cylindrical sound wave as the vortex core is compressed into an elliptical shape during the passage of the wave, releasing acoustic waves as it returns to circular shape (these can be seen in the fifth and sixth images).

The third vortex is visible in the sixth frame, at which time the first vortex is approaching the downstream wall, and is deflected downwards. As the first vortex is strong, as it is shifted down the wall it induces an upward velocity on the developing second and third vortical structures, lifting them. In the final few images the second vortical structure strikes the downstream corner of the cavity, whereas the third vortex is lifted over the edge and continues downstream. The sequence of vortex shedding is broken by a strong pressure wave which reflects from the bottom of the cavity, cutting the shedding process close to the upstream corner of the cavity. This pressure wave can be seen passing the upstream corner in the final five images of Figure 7.3.

Acoustic waves are generated as the vortices impact on the downstream corner, and they propagate upstream and downstream, and in an additional complexity they are reflected off the top of the wind tunnel. These waves are seen clearly in the experimental and numerical images, however in the numerical images the reflected acoustic waves (leaning towards the upstream direction) are not as sharp due to grid stretching at the upper boundary. The prediction of the location of the acoustic waves is excellent when compared to experimental images. The network of emitted and reflected waves can be seen clearly in Figure 7.4 which shows the full computational domain.

Figure 7.5 and Figure 7.6 show a three dimensional view of the vortices, visualised as isosurfaces ‘Q’ criteria [94],

$$Q = -\frac{1}{2}\frac{\partial u_i}{\partial x_j}\frac{\partial u_j}{\partial x_i}, \tag{7.1.7}$$

demonstrating the complexity of the flow close to the shear layer. It also illustrates the dampening effect of grid stretching both at the bottom of the cavity, and in the boundary layer downstream of the cavity. Figure 7.6 shows the isosurfaces of $Q = 0.5\times10^6$, half the value taken for Figure 7.5 to illustrate the complex, three dimensional turbulent

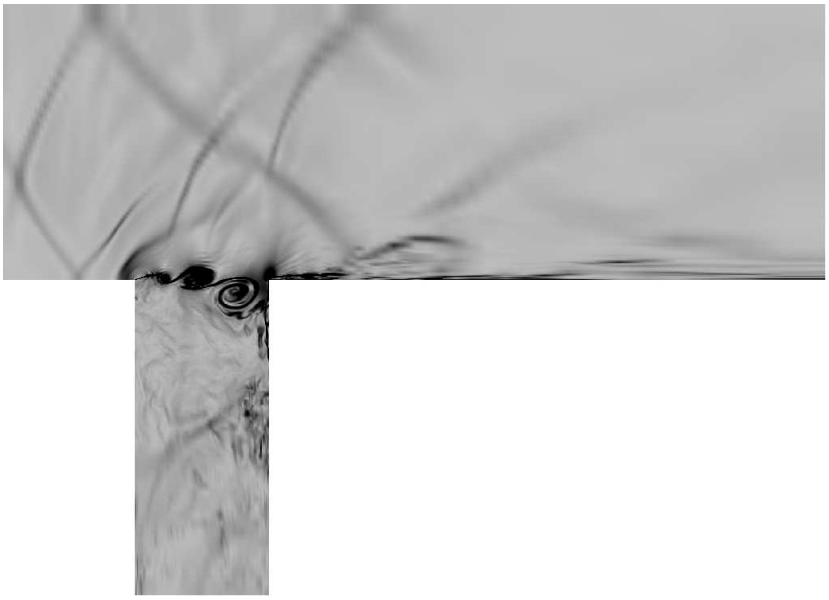

Figure 7.4: Computational schlieren $|\nabla\rho|$ showing the full computational domain at the finest grid resolution

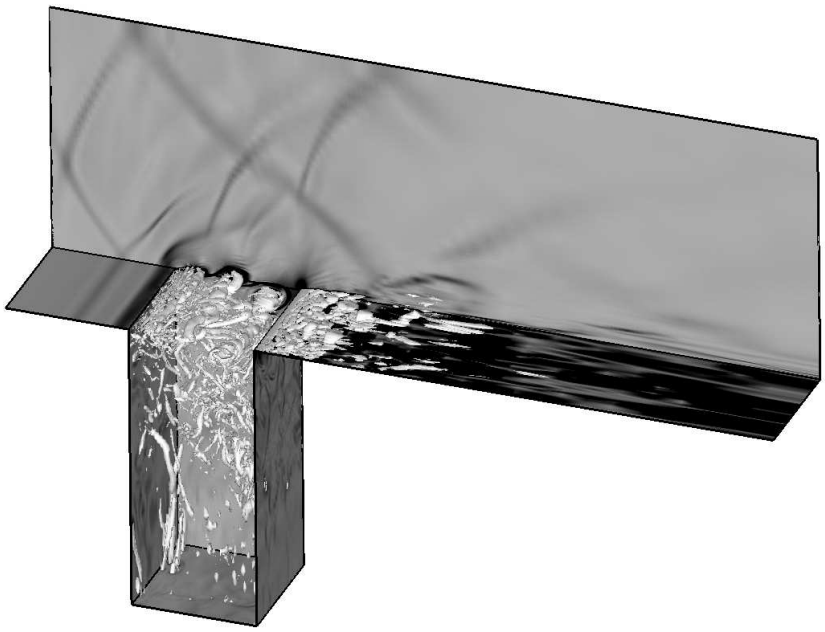

Figure 7.5: Three dimensional visualisation of isosurfaces of $Q = 10^6$ at the same time as Figure 7.4. Contour flood shows pseudo-schlieren field ($|\nabla\rho|$)

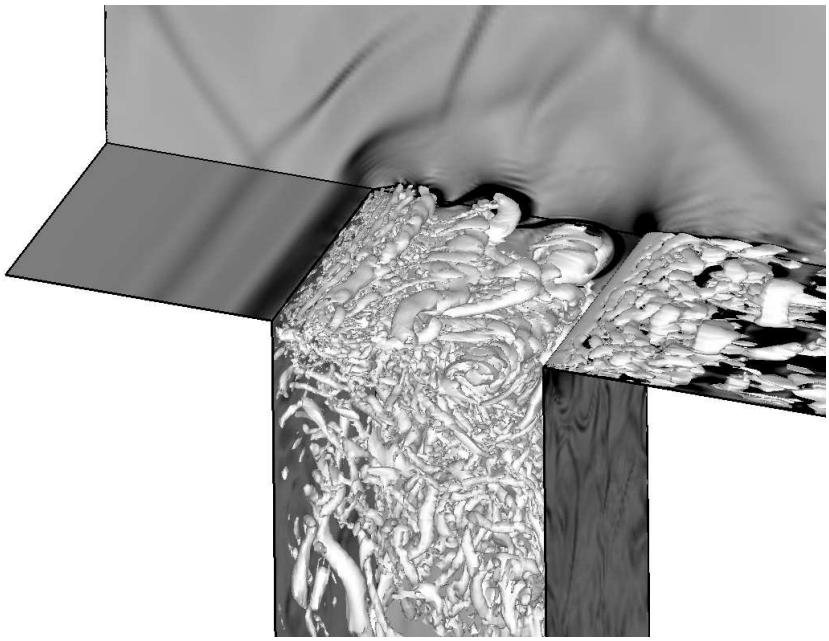

Figure 7.6: Close up of the cavity, showing visualisation of isosurfaces of $Q = 0.5 \times 10^6$ at the same time as Figure 7.5, but with an isosurface at half the value. Contour flood shows pseudo-schlieren field ($|\nabla\rho|$)

nature of the flow. The mixing layer is dominated by the three quasi-two dimensional vortices, however between these vortices are smaller streamwise vortices. There is also evidence that finer scale vortices, resulting from turbulent motion within the cavity, are subsequently entrained into the mixing layer.

Mean Flow

The Reynolds averaged mean flow data has been computed from data outputted for approximately 30 shedding cycles for the coarse and fine data, and 60 shedding cycles for the medium resolution simulation. The results are presented in Figure 7.7 and Figure 7.8, compared to experimental data measured using Laser Doppler Velocimetry along the developing mixing layer for several thousand shedding cycles, and the fine grid results from the LES study by Larcheveque *et al.*[113].

The overall agreement with experiment is excellent, especially considering the minimal approach to modelling the incoming boundary layers, and strong grid stretching at the upper wall. Comparing the results at $x/l = 0.05$, it appears that the initialised boundary layer at the inlet of the numerical domain is slightly thicker than required. There is a u-momentum loss between $z/L = 2.4$ and $z/L = 2.5$ when compared to the experimental results, which in turn will causes the centre of the mixing layer to be slightly higher.

The agreement at subsequent points is excellent, the only slight discrepancy is a consistent under-estimation of the u velocity above the cavity, which is due to the initial thickness of the upstream boundary layer. There are discrepancies close to the down-

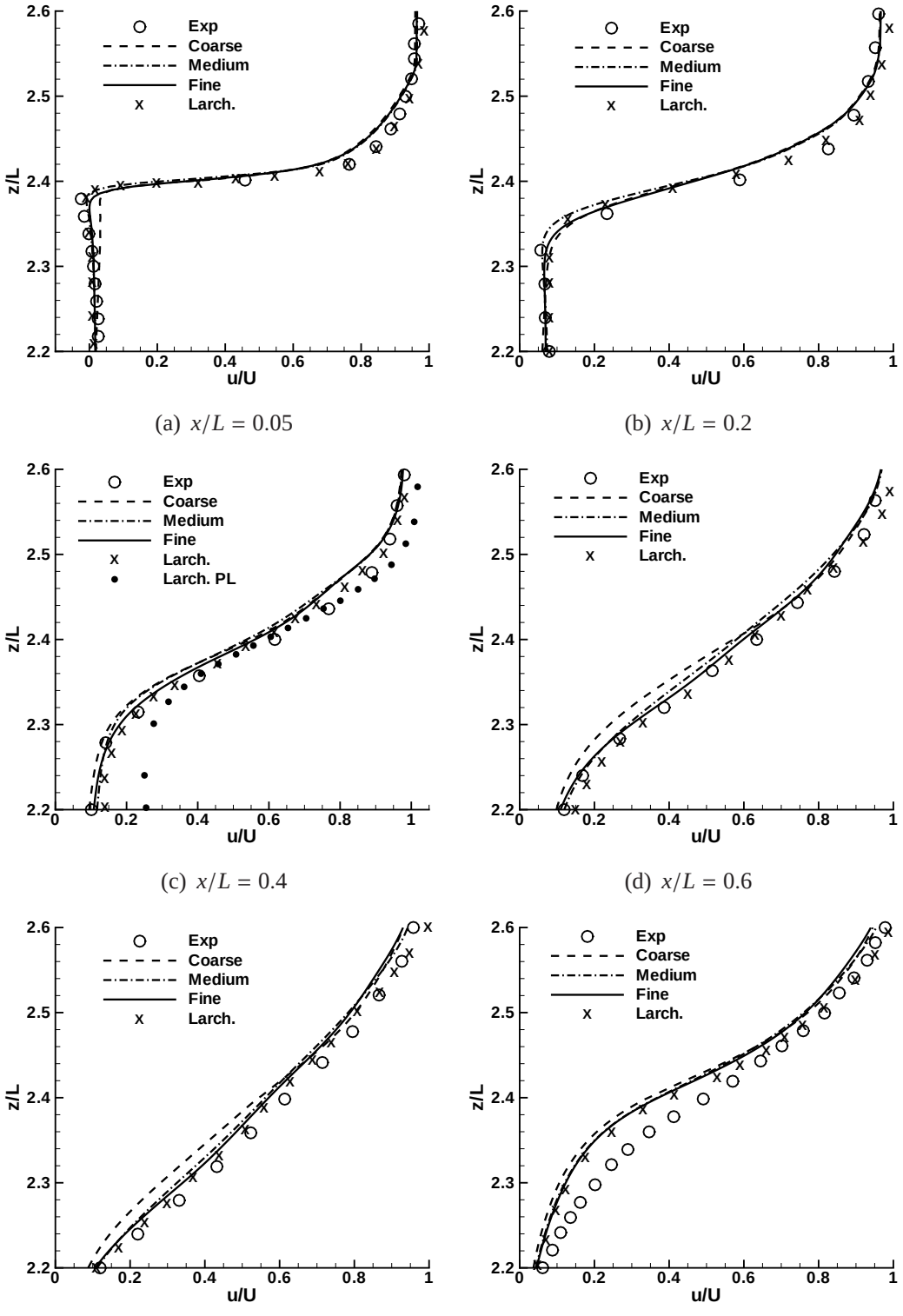

(a) $x/L = 0.05$ (b) $x/L = 0.2$

(c) $x/L = 0.4$ (d) $x/L = 0.6$

(e) $x/L = 0.8$ (f) $x/L = 0.95$

Figure 7.7: Comparison of mean longitudinal velocity $\overline{u}/U$ with experiment and previous LES [113]. For $x/L = 0.4$ the results from [113] gained using a power law boundary layer profile are plotted with solid circles

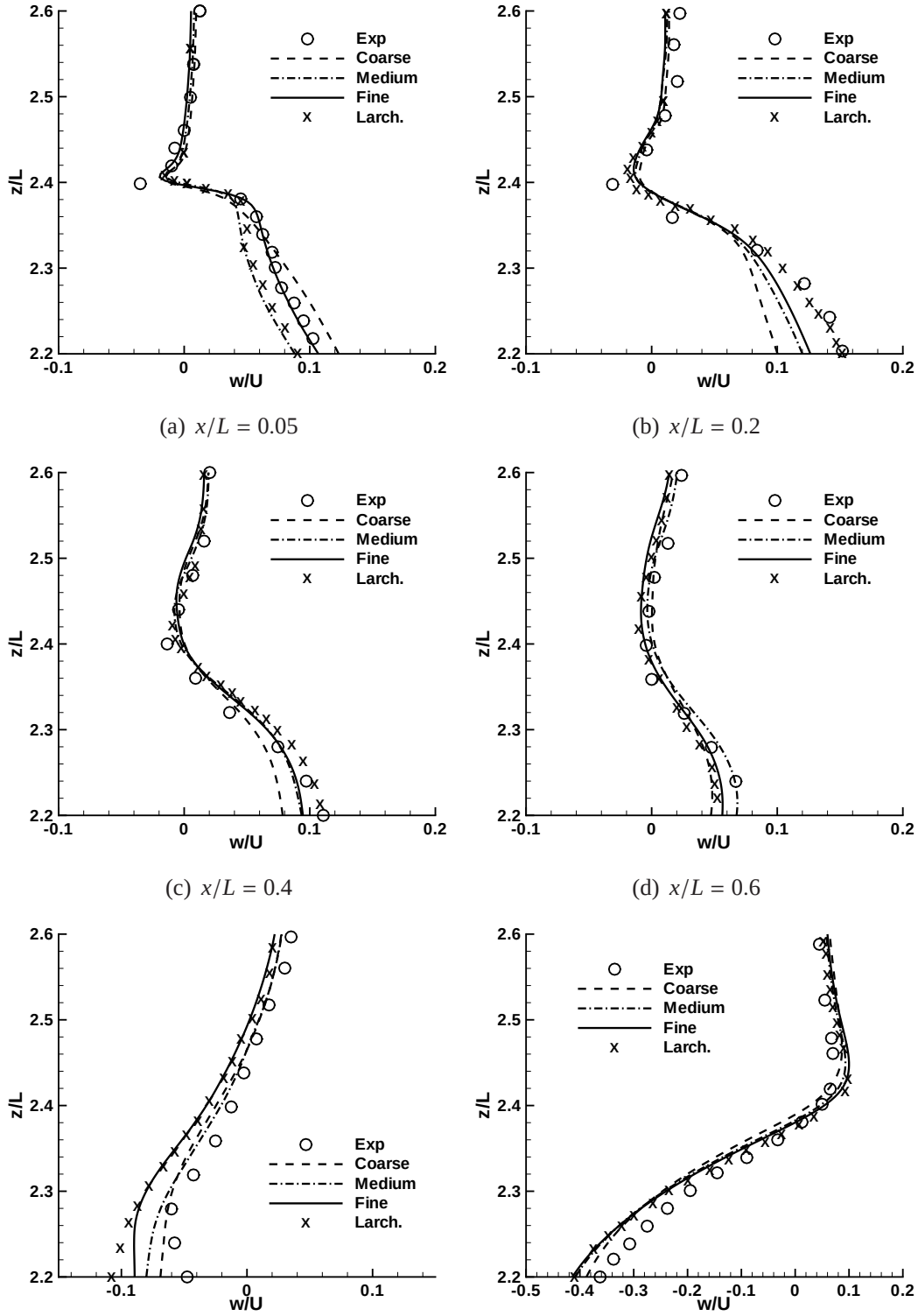

(a) $x/L = 0.05$ (b) $x/L = 0.2$

(c) $x/L = 0.4$ (d) $x/L = 0.6$

(e) $x/L = 0.8$ (f) $x/L = 0.95$

Figure 7.8: Comparison of mean longitudinal velocity $\overline{w}/U$ with experiment and previous LES [113]

stream edge of the cavity wall, however in this region there is a complex, fine scale interaction between the developing vortices and the downstream wall which is not well resolved.

The vertical velocities presented in Figure 7.8 are approximately one order of magnitude smaller than the freestream velocity. At the first measurement station, $x/L = 0.05$ the mean velocities are extremely well predicted on the fine grid, however the peak velocities in the centre of the layer are not predicted as accurately as in the other locations. At the other locations both the qualitative and quantitative behaviour are captured well, indicating the mixing layer is growing in a physically realistic manner.

At the majority of measurement planes there is a clear trend in improvement of the numerical results are resolution increases, converging towards the experimental measurements.

Comparison with the previous LES of Larcheveque *et al.* [113] show that on equivalent grids (medium grid in the current study with fine in the Larcheveque *et al.* case) the agreement with experiment is not as good for the longitudinal velocities, but as good for the vertical velocities. It is believed that the reason for the improved agreement with LES is that the inlet boundary layer was specified more accurately by rescaling the boundary layer profile measured from experiment. The rescaling was calibrated such that the mean boundary layer profile at the cavity was an excellent match for experimental measurements.

To support this conclusion, the solid circles in Figure 7.7c) show the results gained by Larcheveque *et al.* using ILES on a grid equivalent to the coarse grid employed here, but with a power law inlet boundary condition for the turbulent boundary layer. This is the same type of inlet boundary condition employed in the current simulations, but the results are substantially worse. This indicates that to some extent the ILES results presented here are less sensitive to the initial modelling assumptions, and that the proposed numerical method gives a better representation of the the expected flow physics.

Reynolds stresses

The time and space (in the periodic direction) averaged longitudinal Reynolds stresses are plotted against experiment in Figure 7.9. As with the mean flow velocities, there is good agreement with experimental results at all stations. The centre of the mixing layer in the numerical simulations is slightly higher than that in the experiment (See Figures 7.9 a) and b)), which is consistent with a thicker boundary layer upstream of the cavity.

The vertical Reynolds stress $\overline{w'^2}/U$ plotted in Figure 7.10 shows similar results to the longitudinal stresses. The peak of the vertical Reynolds stress indicates that the centre of the developing mixing layer is too high by about 1mm in comparison to experimental results. The cross-stress $\overline{u'w'}/U$ presented in Figure 7.11 also confirms this observation.

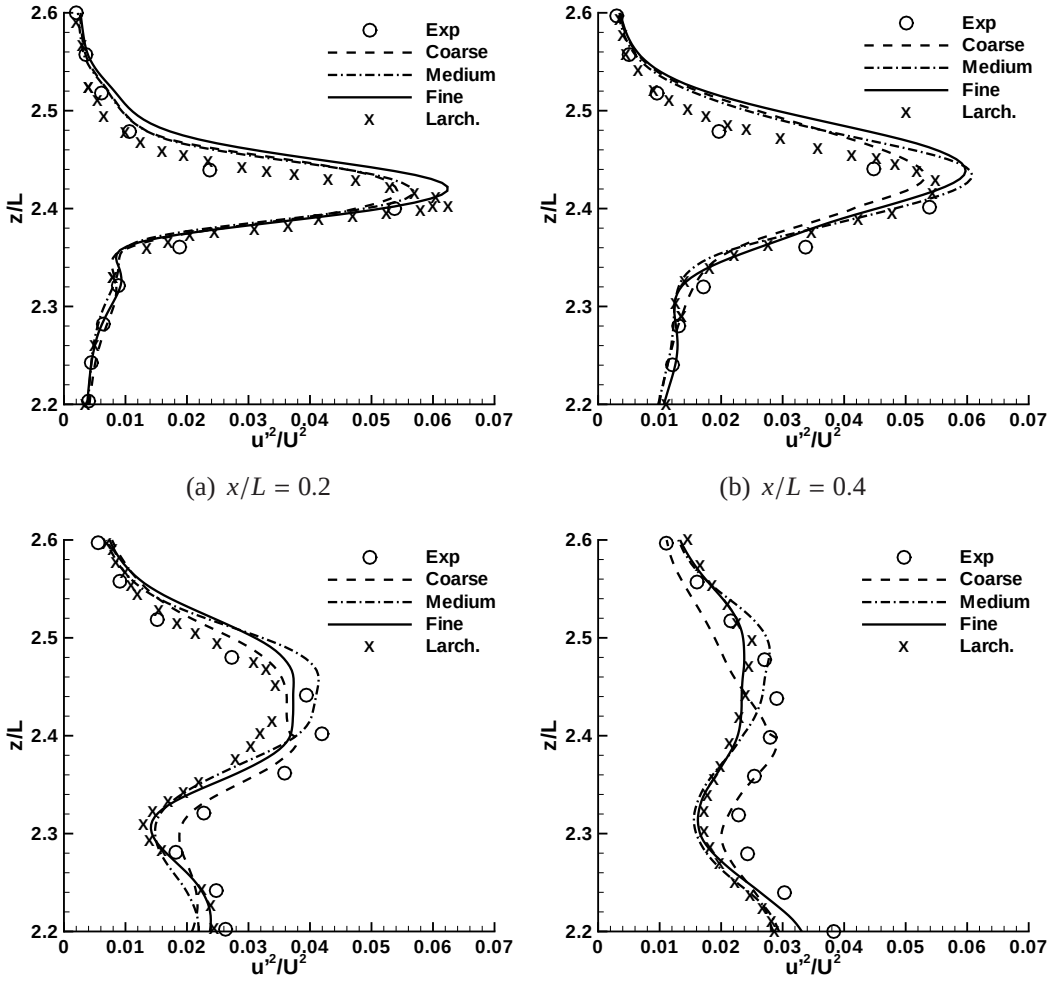

(a) $x/L = 0.2$ (b) $x/L = 0.4$

(c) $x/L = 0.6$ (d) $x/L = 0.8$

Figure 7.9: Comparison of $\overline{u'^2}/U$ with experiment and previous LES [113]

Finally, Figure 7.12 shows the two dimensional fluctuating kinetic energy close the upstream and downstream wall respectively. There is a slight overestimation of the turbulent kinetic energy at all grid resolutions - which is opposite to the results presented by [113], where conventional LES underestimated the fluctuating kinetic energy. This demonstrates that the numerical scheme is suitable for LES, as it does not excessively damp turbulent motions.

At this point it worth discussing the relative modelling effort in the classical and ILES simulations, and the properties of the numerical schemes. The key difference between the two simulations is visible in Figure 7.7 a). The inlet boundary layer profile used in [113] was not that reported in Forestier *et al.*, but a least squares fit to their experimental data. This was then rescaled to allow for growth up to the start of the cavity to give the best match to experimental data at $x/L = 0.4$, in conjunction with turbulent wall modelling. The simulations detailed here initialised the inlet boundary layer profile

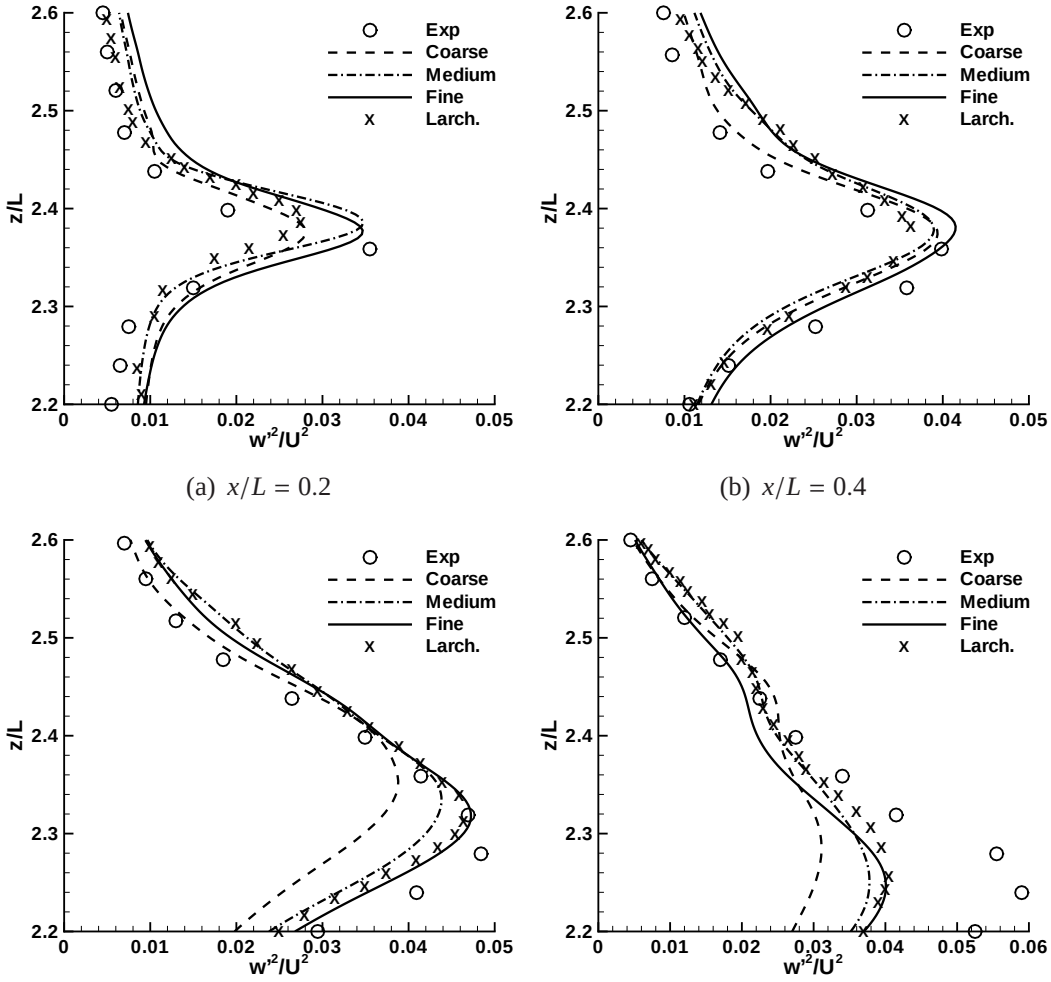

(a) $x/L = 0.2$ (b) $x/L = 0.4$

(c) $x/L = 0.6$ (d) $x/L = 0.8$

Figure 7.10: Comparison of $\overline{w'^2}/U$ at with experiment and previous LES [113]

directly from experimental measurements without such compensation, which meant that the initial boundary layer thickness is greater than that in the computation. This is a point which should be improved in future simulations.

The subgrid model employed by Larcheveque *et al.* is a selective mixed scale model, described in detail in [118]. This uses a nonlinear combination of a Smagorinsky and mixing length model. It requires the choice of two constants, the Smagorinsky coefficient and the nonlinear combination parameter. In addition, the Smagorinsky coefficient is modified for use in the mixing length model close to walls via the van Driest dampening function. To improve intermittency, an additional selective function is employed which premultiplies the eddy viscosity computed via the subgrid models. A further correction is employed for the filter length Δ to compensate for the fact that the mesh is highly stretched. Finally, the subgrid models themselves are evaluated numerically to second order accuracy. The Smagorinsky coefficient, the nonlinear

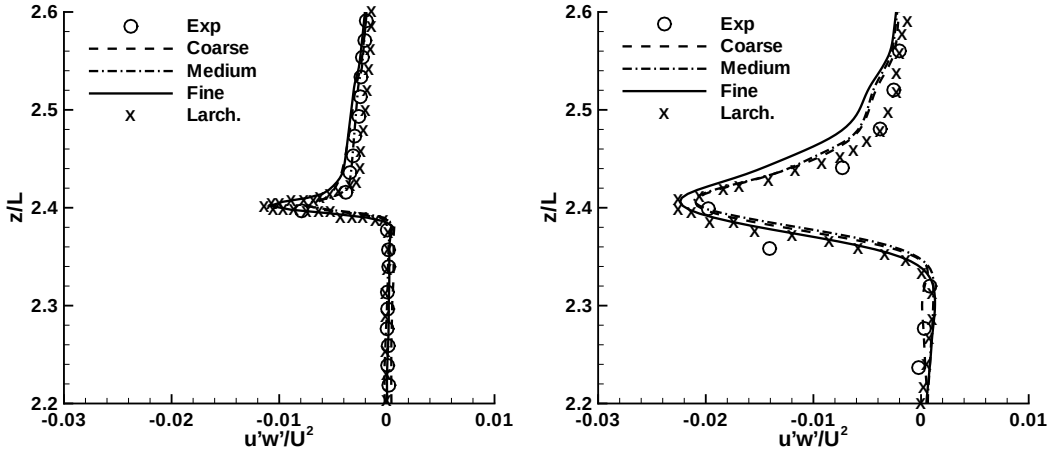

(a) $x/L = 0.05$ (b) $x/L = 0.2$

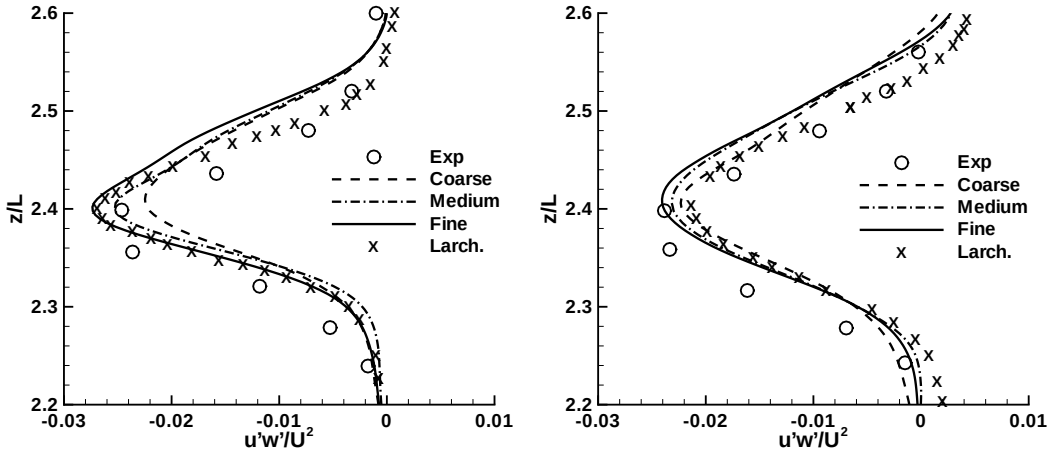

(c) $x/L = 0.3$ (d) $x/L = 0.6$

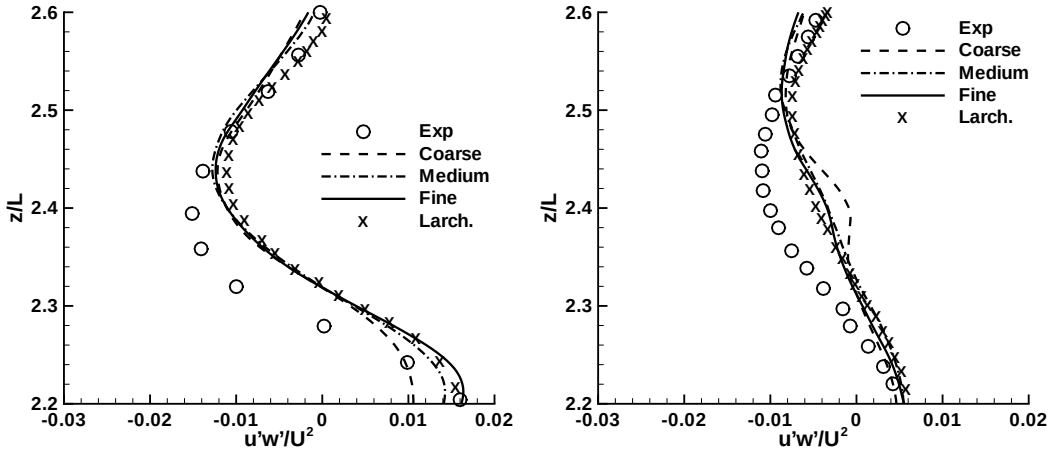

(e) $x/L = 0.8$ (f) $x/L = 0.95$

Figure 7.11: Comparison of $\overline{u'w'}/U$ with experiment and previous LES [113]

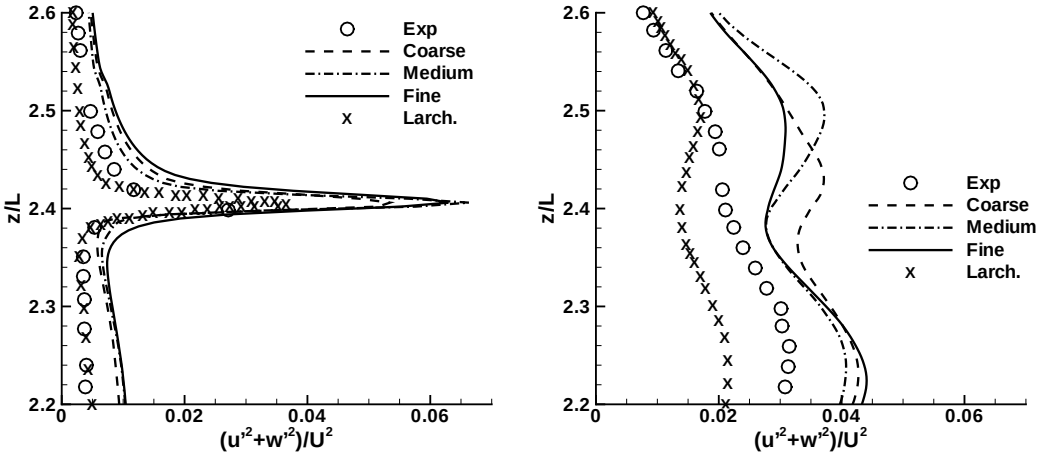

(a) $x/L = 0.05$ (b) $x/L = 0.95$

Figure 7.12: Comparison of $(\overline{u'^2} + \overline{w'^2})/U^2$ with experiment and previous LES [113]

combination parameter, and the selective function are all calibrated through comparison of numerical results with experiment [118]. The underlying numerical method is a combination of a second order central difference scheme with dissipation added to stabilise the numerical scheme by upwinding where oscillations occur. The numerical scheme is not shock capturing due to this oscillitory nature.

In contrast, the ILES approach appears very stark. No explicit subgrid models were employed, correction functions are not applied, and the scheme is shock capturing as demonstrated in the previous chapter. However, it is clear that a turbulent wall model (or improved inlet conditions) should be implemented in future simulations, as the results in this section have demonstrated that there is some sensitivity to the details incoming boundary layer profile on the location of the centre of the mixing layer and the exact match with experiment.

Pressure Spectra

In the experiment the average pressure power spectrum was measured at the upstream wall over approximately 5000 to 8000 shedding periods. As the time simulated is limited by computational power, the results presented within this section correspond to 30 shedding periods. To examine the influence of sampling time the medium grid level was run for 60 shedding periods. All pressure spectra are presented as frequency vs. Sound Pressure Level (SPL) in units of decibels (dB), where the conversion to decibel is

$$\mathrm{SPL}(dB) = 10\log_{10}\left(\frac{\mathrm{Power}}{4\times 10^{-10}}\right). \tag{7.1.8}$$

There are several different methods for computing the pressure power spectra, the three

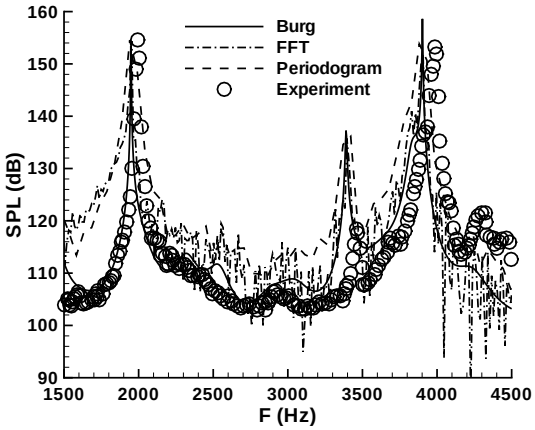

Figure 7.13: Pressure spectrum for the medium grid computed with three different methods

main being via a simple FFT process (as done for the turbulent kinetic energy spectrum). This is computed as the square of the Fourier transform of the pressure fluctuations, rescaled to satisfy Parseval's theorem. Parseval's theorem states that the integral of the power in the pressure power spectrum should be equal to the total power in the real signal. A problem with this method is that the power at a discrete part of the pressure spectrum can 'leak' to adjacent parts, a leakage which is not necessarily restricted to a narrow locality - indeed for a general function the leakage extends significantly.

The second method reduces this problem by explicitly 'windowing' the data such that this leakage is significantly reduced. This involves splitting the data into several chunks, and multiplying it by a specified window function before the Fourier transform. The disadvantage of this method is that it reduces the lowest frequency sampled, hence effectively reducing the number of periods over which the signal is averaged.

Finally, the third common method is Burg's method, which does not employ an explicit Fourier transform. This employs linear prediction theory, which was initially developed for predicting the value of a function at one instant using a combination of all previous instants. The coefficients of the linear prediction can be directly related to the power spectrum of the function, and provide an excellent method of extracting sharp peaks from short data samples - and does not rely on a data set which is a power of 2 in length. A key component of employing this method is selecting the number of 'poles' (coefficients in the expansion). If too many poles are selected the method can split a single peak into two peaks, or make several peaks where no peak exists. Further details on the three methods can be found in the Chapter 13 of [151].

In light of these observations, all three methods were implemented, and the results compared in Figure 7.13 for the medium grid resolution simulation. The circles show the experimental results up to the second harmonic. Several observations can be made. Firstly the standard FFT transform is extremely noisy, however it appears to resolve peaks well. The Periodogram method reduces the noise, however it suffers from low resolution due to the windowing process. Finally, Burg's method with $15,000$ poles captures the peaks accurately, and agrees well with the basic FFT transform. On this

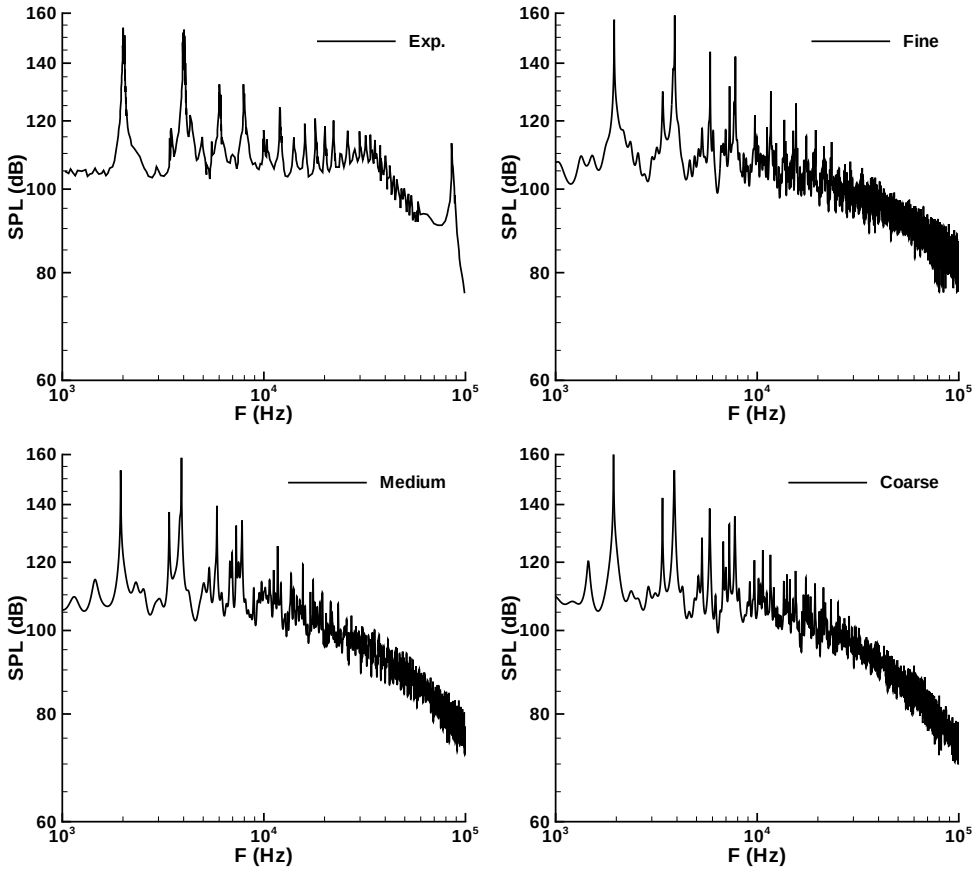

Figure 7.14: Pressure power spectrum up to 10kHz for simulations and experiment

basis the Burg method is employed throughout this section.

Figure 7.14 shows the pressure power spectrum for each of the three grid resolutions, and that of the experiment for the full range. A close up of the first two peaks is shown in Figure 7.15, comparing the different methods. It should be noted that the peak in the experimental results at about 90kHz is believed to be due to resonance of the sensor itself. Experimental measurements recorded the fundamental mode at 1975Hz (no error bars are given in [59]) at approximately 155dB sound pressure level. The coarse, medium and fine grid predict this peak at 1940Hz, 1948Hz and 1954Hz, with a sound pressure level of 160dB, 153dB and 157dB respectively. This is equivalent to errors compared to experiment of less than 5dB at all grid levels. These are excellent results considering that the boundary layers were not modelled, and that extremely coarse grids were used in the upper half of the wind tunnel, and bottom of the cavity.

As can be seen in Figure 7.15, the frequency of the second mode is also predicted to within 2%, but the sound pressure level is overestimated by 6dB at the highest grid level. Additionally, the small peak between the first two modes is overestimated significantly, however as the scale is logarithmic, this would not affect total sound pressure significantly. The source of the smaller peak is a longitudinal wave which is

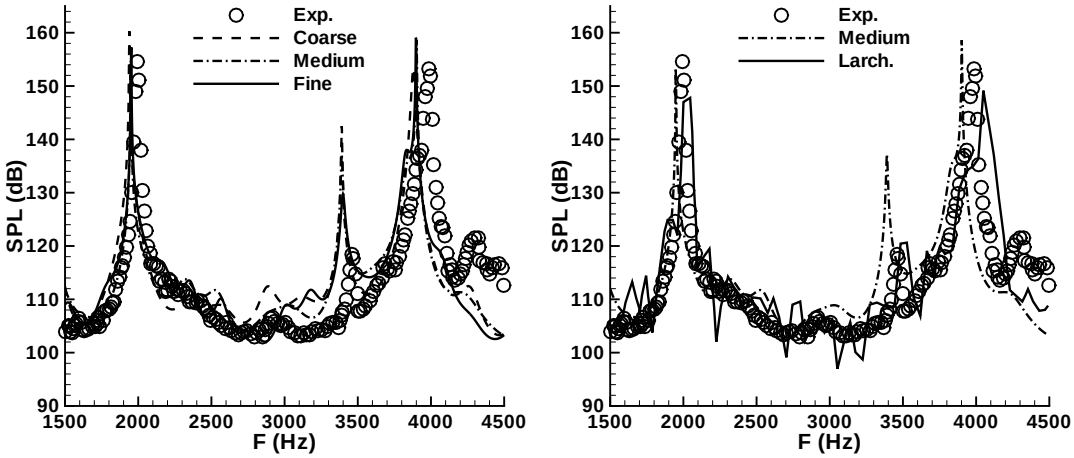

Figure 7.15: Pressure power spectrum highlighting the dominant acoustic modes for the ILES simulations (left) and comparison of the fine grid results with conventional LES results from [113]

reflected continuously within the cavity. This wave is stronger in the simulation than in experiment. A possible explanation is that in the experiment the acoustic wave is scattered by a series of interactions with turbulent vortices. The coarse resolution in the numerical simulation means that the vortices are not present, hence the acoustic waves are not scattered as effectively.

Figure 7.15 also shows a comparison of the medium grid simulation with the fine grid results of [113]. The prediction from the medium grid simulation of the current study is a better match to experimental data for the location and magnitude two strongest modes, however the conventional LES simulation captures the magnitude of the small peak better. It is possible that the combination of a two- and three-dimensional grid in the conventional LES simulation allowed better resolution of the flow within the cavity where the acoustic waves producing the small peak occur. It is expected that the shock capturing capability of the current method allows better resolution of strong acoustic waves (weak shocks), which appears to be confirmed here.

Comparing the full range, the fine grid level predicts the frequency of the harmonics up to approximately 20kHz (the first 11 modes), however the magnitude of the higher frequency peaks are overestimated compared to experiment. The medium grid performs better in terms of magnitude of the harmonics, however resolves up to about 15kHz (first 8 modes). The coarse mesh capture modes up to 12kHz, however there are several spurious peaks at high frequency which do not appear in the experimental results. In all, the agreement with experimental sound pressure spectra is excellent

7.1.4 Conclusions

This section has detailed the simulation of a deep, open cavity flow to validate the modified numerical method against quantitative experimental data. It has been shown that the mean flow and Reynolds stresses are in very good agreement with experiment, and convergence towards the experimental results with increasing resolution is apparent. The discrepancies with experimental data are largely due to an over-estimation of the boundary layer thickness at the inlet of the numerical domain. This meant that the initial thickness of the mixing layer was slightly too large, and the centre of the mixing layer is shifted by 1mm vertically compared to the experimentally measured position.

Pressure power spectra measured by Forestier *et al.* [59] have been compared to numerical data, where the frequency of the two dominant modes are predicted to within 2%, and the sound pressure level within 6dB for all grid resolutions. The finest grid level captures the frequency of harmonics up to 20kHz, however the magnitude of these peaks is overestimated. Results presented with the modified method without subgrid model compare excellently with conventional LES by Larcheveque *et al.* [113].

In summary, this section has validated the modified numerical scheme through simulations of a complex, wall bounded, compressible turbulent flow. The comparison shows excellent results for minimum modelling effort, and demonstrates that the key flow physics of the problem are captured accurately without the necessity of an explicit subgrid model.

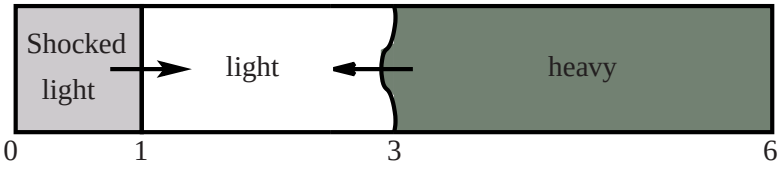

Figure 7.16: Schematic of the single mode Richtmyer-Meshkov initialisation .

7.2 Single Mode Richtmyer-Meshkov Instability

7.2.1 Introduction

This section investigates the influence of numerical method and grid resolution on the growth of a three dimensional single mode planar RM instability. The test case adopted is that of Li and Zhang [121]. Using these initial conditions the solution in the linear and non-linear regime is compared to numerical and theoretical solutions developed in Zhang and Sohn [201] and Richtmyer [155], and results employing a semi-Lagrangian finite difference code presented in [183].

Numerical codes for the simulation of such complex flows are typically calibrated against theoretical, experimental, or previous numerical studies. The solution gained when simulating flow instabilities depends greatly on the numerical schemes used, thus it is important to establish the independence of certain reference results from the choice of numerical scheme. In addition, by examining the grid convergence of the solution a single mode test case is a good measure of the resolution of a given numerical scheme.

7.2.2 Numerical Methods

Two numerical methods are employed in this section, the first being the well established second-order van Leer limiter, the second is the new low Mach limiting methodology with fifth-order accuracy, both employed in the MUSCL framework. The characteristics-based Riemann solver is used, along with third-order extended stability Runge-Kutta time stepping.

The initialisation for the single mode problem is identical to that used in Li and Zhang [121], and is illustrated in Figure 7.16. The size of the computational domain is $6\times1\times1$ and the boundary conditions are periodic in the y and z directions with an extended one dimensional domain in the x direction to reduce the effects of reflected waves. The incident shock Mach number is 1.5 and travels in the positive x direction. The initial interface perturbation is defined as $A = A_0(cos(ky) + cos(kz))$ where $k = 2\pi$ and $kA_0 = 0.238$. The fluids have a density ratio $\rho_1/\rho_2 = 1/5$, and $\gamma_1 = \gamma_2 = 1.4$. The computation takes advantage of the Galilean invariance of the governing equations in that an initial velocity of $u_0 = 151.1$m/s is given to the interface such that the mean position of the interface is stationary after the passage of the shock.

Several grid resolutions have been employed, $30\times5\times5$, $60\times10\times10$, $120\times20\times20$, $240\times$

40×40 and $480\times80\times80$. In presenting the results, all lengths are non-dimensionalised by the wavelength of the initial perturbation, and times by the wavelength and post-shock interface velocity. All theoretical results are computed using the post-shock Atwood number $At^+ = 0.65$, and the post-shock amplitude $A_0^+ = 0.43$. The spike height is the distance from the furthest point where the volume fraction $\alpha = 0.5$ to the centre of the mixing layer (defined by the position where an unperturbed interface would lie at). Similarly, the bubble position is the furthest point towards the heavy gas that a volume fraction of the 0.5 is found. The mixing layer width is the sum of the spike and bubble height.

Figure 7.17 shows the time development of the instability at the maximum grid resolution using van Leer and M5+LM limiting methods, through the linear and non-linear growth of the instability. It can be seen that the growth of the instability is dominated by the ring vortex structure as also seen in experimental studies [30]. There are additional fine scale features on the M5+LM simulation which are not present with van Leer due to the dissipative nature of the standard Godunov method.

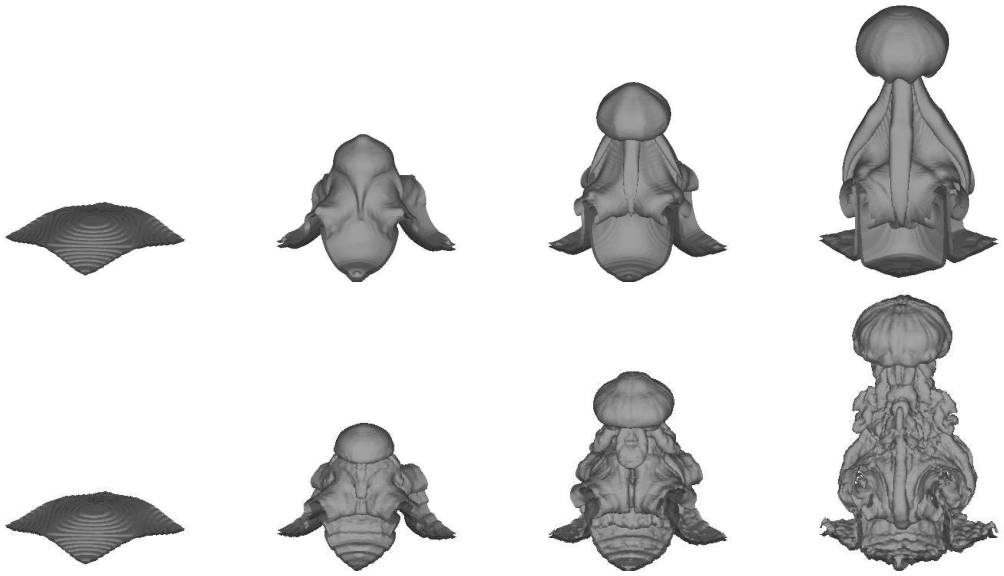

(a) $t = 0$ (b) $t = 3.0$ (c) $t = 6.3$ (d) $t = 12.9$

Figure 7.17: Isosurfaces of constant volume fraction 0.05 and 0.95 illustrating the development of the single mode RM instability using van Leer (top) compared to M5+LM (bottom) at the highest grid resolution

7.2.3 Results and Discussion

Figure 7.18 a) shows the grid converged mixing layer width compared to nonlinear theory by Zhang and Sohn [201], linear by Richtmyer [155] and simulations using a semi-Lagrangian finite difference code called 'TURMOIL' [183]. Figure 7.18 b) shows the converged bubble and spike size as a function of time. It is clear that there

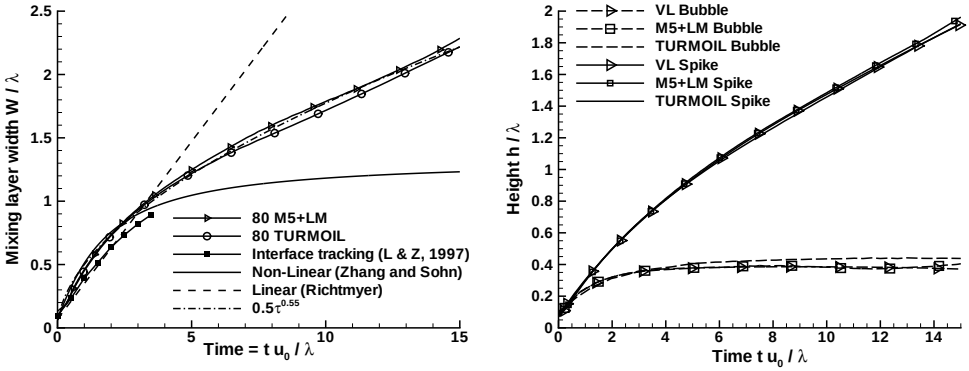

(a) Mixing layer width (b) Bubble and Spike height

Figure 7.18: Grid converged mixing layer widths

is excellent agreement between the Godunov and finite difference numerical methods at both early and late times. The results of Li and Zhang [121] appear to grow more slowly, however, comparing their images it appears that the numerical scheme is significantly more dissipative, thus removing kinetic energy from the system and slowing the growth of the mixing layer.

The mixing layer width grows more rapidly than predicted by linear theory, however it is an excellent match for the non-linear theory of Zhang and Sohn [201] up to a non-dimensional time of about 2.5. After this time the growth is dominated by the strong vortex ring which self-advects at a constant velocity. The dominance of this coherent structure causes the departure from non-linear theory, which depends on $1/t^2$ at late time. The behaviour over the time-scales considered within this study match a power law of $\approx \tau^{0.55}$, where τ is the non-dimensional time, but late time growth is linear.

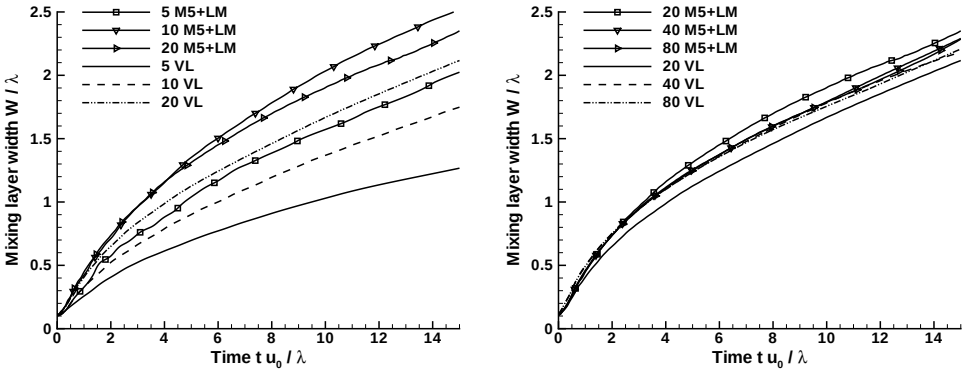

(a) Low Resolution (b) High Resolution

Figure 7.19: Development of the mixing layer widths as a function of grid resolution and numerical method

The bubble and spike widths are also in excellent agreement. Given these initial conditions the spike exhibits continued growth due to the vortex ring, however bubble growth stagnates very rapidly. At very late time the bubble begins to grow again due

to the expansion of the developing turbulent mixing layer. In addition to the plots shown, identical runs with several different limiting methods (van Albada, Minmod, and M3 limiter) have resulted in the same growth rates, as have simulations using a Roe scheme.

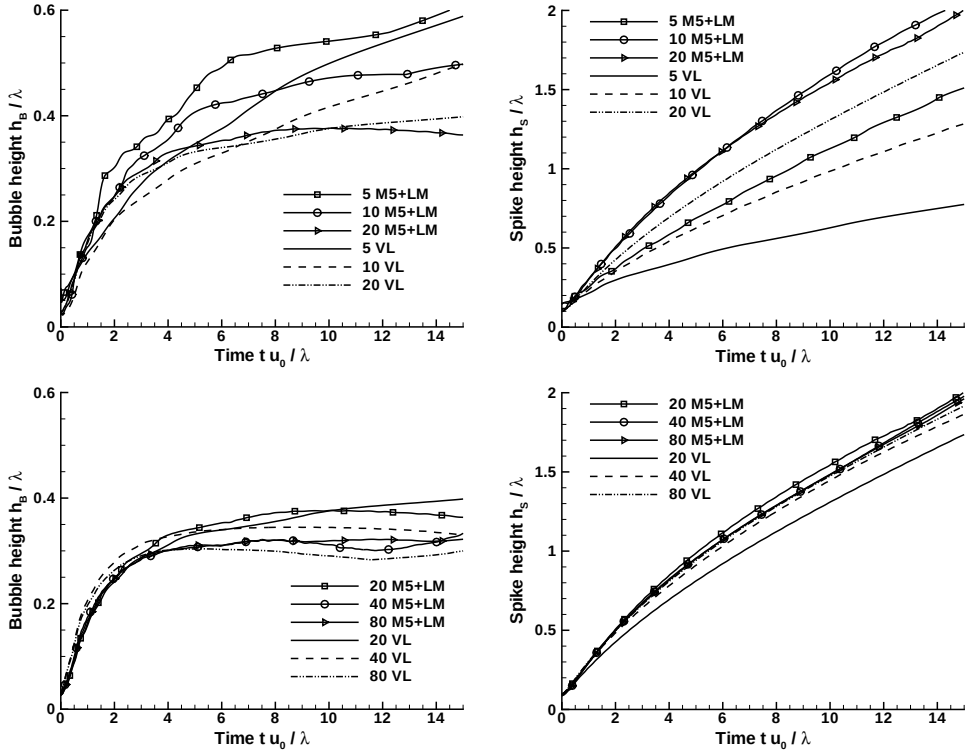

(a) Bubble (b) Spike

Figure 7.20: Development of the bubble and spike as a function of grid resolution and numerical method, low resolution (top) and high resolution (bottom)

Figures 7.19a) and b) show the development of the mixing width as a function of mesh resolution for both numerical methods. The total width of the mixing layer reaches an approximately converged solution for 20×20 cells for both methods. The difference in bubble heights is small compared to the overall mixing layer widths. At lower grid resolution (5 and 10 cross-section) the M5+LM method performs significantly better compared to the grid converged solution. At a cross-section of 10×10 the new method over predicts growth by about 6%. At the same resolution the van Leer limiter under predicts growth by 25%, and 10% at 20×20 cross-section.

The growth of the bubble and spike at the lower resolutions is shown in Figure 7.20 a) and b) for both numerical methods. The initial bubble growth is captured very well with the M5+LM method at all resolutions through the linear and early non-linear stage, which is not true of the van Leer limiter. Both methods are converged at 20×20 cross-section.

The growth of the spike shown in Figure 7.20 b) shows the large resolution improve-

ment when switching to the M5+LM method. The M5+LM limiter converges at a cross-section of 10×10 cells, however the van Leer limiter does not converge until a grid resolution four times greater in each direction.

An important point which has not been investigated is the influence of the order of accuracy of the representation of the initial perturbation. At present the initialisation is only second order accurate, meaning that at low grid resolution, the perturbation could be very inaccurate. It is expected that the higher order methods would perform much better given a higher-order accurate initial condition.

7.2.4 Conclusions

The converged growth rates of the single mode Richtmyer-Meshkov instability have been shown to be in good agreement with the theory of Zhang and Sohn [201] until the growth is dominated by the coherent ring vortex. Bubble growth stagnates very rapidly after the early non-linear stage, whereas the spike continues to grow due to self advection of the vortex ring.

It is demonstrated that the van Leer limiter removes kinetic energy more rapidly, leading to a weaker vortex at a given grid resolution. As the mean Mach number after passage of the shock wave is 0.1, and decreases with time, the Godunov scheme suffers heavily from excess dissipation as predicted in Chapter 5. This is only alleviated at higher grid resolution where the velocity jumps at the cell interface are reduced. This is not the case for the new scheme which converges at approximately half the grid resolution for the total mixing layer width, and a quarter the grid resolution for the spike height when compared to the van Leer limiter. This translates to a 16 or 64 times decrease in computational time.

7.3 Multimode Richtmyer-Meshkov

7.3.1 Introduction

This section investigates ILES of shock wave induced instabilities (Richtmyer-Meshkov) and turbulent mixing. Richtmyer Meshkov (RM) [155, 134] instability occurs when an incident shock wave passes through a perturbed interface between two gases, triggering growth of the interface width. These instabilities first grow linearly, and then transition to turbulence.

In the Section 2.3 the various approaches to the analysis of RM instability were discussed. It was shown that there are two main analytical approaches to the determination of the growth exponent of the mixing layer. The first is the growth of a fully turbulent slab (Section 2.3.1), where the initial perturbations have already saturated and there is no further significant growth of the long wavelengths. This is equivalent to the growth of a narrowband high wavenumber initial perturbation. The second is the assumption that the long wavelengths are still growing linearly during the time of interest to the observer (Section 2.3.2). Thus there is a continuous linear growth of largely irrotational long wavelengths, which overtake the nonlinearly saturated shorter wavelengths. It is a complex interaction involving the twofold process of nonlinear saturation followed by turbulent break down and dissipation of smaller modes, which are then supplied with energy from larger modes which subsequently saturate, break down, and begin to dissipate. This is equivalent to the growth of a perturbation from a broadband initial condition where the power in the initial perturbation spectrum is distributed over a wide range of wave numbers.

This section investigates the growth of a Richtmyer-Meshkov mixing layer using two different perturbations. The first is a narrowband combination of high frequency modes, which represents growth of a turbulent mixing layer purely via mode coupling of the high wave numbers. The second initial condition consists of a broadband linear combination of modes from one third the domain size to the high frequencies. If the initial conditions are forgotten then the asymptotic growth rate, and associated statistics of the mixing layer should be the same in both cases. However, as pointed out in Section 2.3.2, it is possible that the linear growth of the long wavelengths is faster than the growth of a turbulent slab, hence dictating the overall growth of the mixing zone.

7.3.2 Numerical Methods

This section is concerned with the simulation of the Euler equations, where viscosity is assumed negligible ($Re \rightarrow \infty$). The three-dimensional compressible Euler equations are solved using the direction split method. It is assumed that the fluid satisfies the ideal gas equation of state, where $\gamma = 5/3$ is the ratio of specific heats. In addition, a passive scalar is advected to track the two gas components, assumed to be miscible.

The numerical method is a standard finite volume solver employing the HLLC approx-

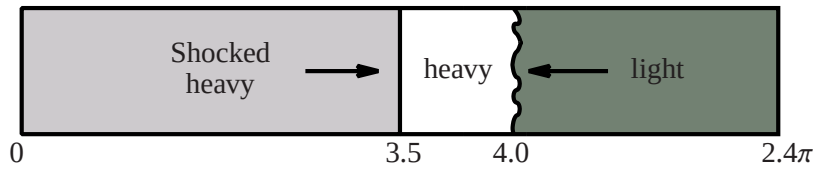

Figure 7.21: Schematic of the multi-mode Richtmyer-Meshkov initialisation .

imate Riemann solver [184], and using the ThCM multicomponent model to track the passive scalar. This section employs three different variable reconstruction methods: second-order van Leer limiting; ninth-order WENO [11]; and the modified low Mach corrected fifth-order method. For the details of these methods consult Chapter 3.

Initialisation

The test case uses the initial conditions derived by [198] (See Section 3.9.2) to examine the influence of initial conditions on the growth of the resultant mixing layer. The initial conditions are shown schematically in Figure 7.21. The flow field consists of a heavy and light gas separated by a perturbed interface where the perturbation satisfies a given power spectrum and mean amplitude. The incident shock wave is of Mach= 1.84, equivalent to a four-fold pressure increase across the shock wave. The initial conditions are

$$0.0 < x < 3.5 \quad (\rho, u, p) = (6.38, -61.5, 4 \times 10^5) \tag{7.3.1}$$

$$3.5 < x < 4.0 + \mathcal{S} \quad (\rho, u, p) = (3.0, -291.58, 10^5) \tag{7.3.2}$$

$$4.0 + \mathcal{S} < x < L_D \quad (\rho, u, p) = (1.0, -291.58, 10^5) \tag{7.3.3}$$

where an initial velocity is given to the gas interface such that the centre of the interface is stationary after passage of the shock wave. The ratio of specific heats, γ, is set to $5/3$. The post-shock Atwood number $At^+ = 0.48$.

For the broadband initialisation, the interface perturbation $\mathcal{S}$ is given as the sum of modes of random phase conforming to an initial power spectrum $P \propto c/k^2$ (See section 3.9.2). The modes excited are restricted between $\lambda_{min} = 32\pi/256$ and $\lambda_{max} = 2\pi/3$ and the standard deviation of the perturbation amplitude is $0.1\lambda_{min}$. The grid sizes used were $360\times256\times256$, $180\times128\times128$ and $90\times64\times64$, and the domain size is fixed at $2.4\pi \times 2\pi \times 2\pi$. This is essentially a convergence study with the same initial condition on all grids, only more poorly resolved on the coarsest grid. This problem was solved with the modified fifth-order limiter for all grids, and the WENO ninth-order and van Leer for the coarse and medium grids.

The narrowband perturbation has an initial power spectrum $P \propto c$, and excited modes lie between $\lambda_{min} = 16\Delta x$ and $\lambda_{max} = 32\Delta x$. The initial amplitude is $0.1\lambda_{min}$. In this case the initial perturbation has been chosen to lie at a high frequency, but where the numerical scheme resolves perturbations without dampening. This problem employs

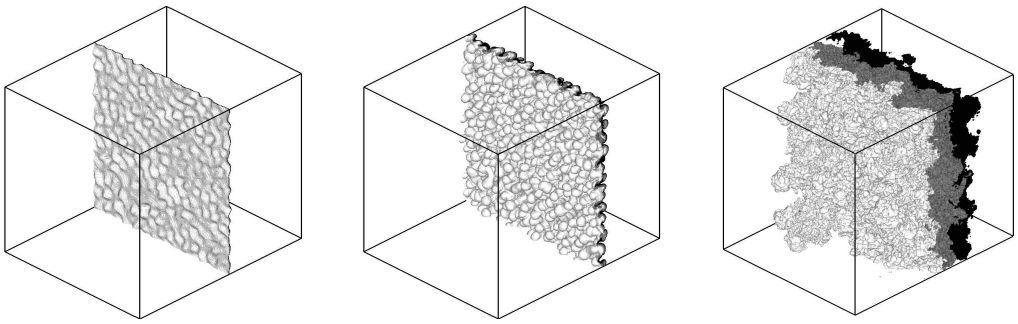

Figure 7.22: Evolution of mass fraction isosurfaces for the fine grid narrowband perturbations at $t\Delta u/\lambda_{min} = 0$, 7 and 250 using the modified fifth order scheme

grids of size $360 \times 300 \times 300$, $360 \times 150 \times 150$ and $360 \times 75 \times 75$. As the initial perturbation and amplitude is linked to the grid scale, the perturbations on the smaller grid grow faster, proportional to λ_{min}. To compensate for this the grid size in the x-direction is increased proportionally such that the cells remain square at all resolutions. In order of decreasing mesh size, the domain sizes are; $2.4\pi \times 2\pi \times 2\pi$, $4.8\pi \times 2\pi \times 2\pi$ and $9.6\pi \times 2\pi \times 2\pi$. This problem was solved using the modified fifth-order limiter.

Non-Dimensionalisations

Before discussing the results, it is important to set out the relevant scaling laws and non-dimensionalisations. Following Youngs [196] all length scales are normalised by the minimum wavelength λ_{min}, and wave numbers by $k_{min} = 1/\lambda_{min}$. The time is scaled via λ_{min} and Δu, which is the velocity impulse given to the interface. Finally, total kinetic energy, and the kinetic energy spectra are non-dimensionalised by $\lambda_{min}\Delta u^2\rho$, where $\rho = 1$. All subsequent results are non-dimensional.

Note that in all subsequent figures the standard numerical scheme is the modified fifth order method.

7.3.3 Results and Discussion

Flow Phenomenology

Figure 7.22 shows mass fraction isosurfaces illustrating the initial condition and evolution of the turbulent interface with time. It can be seen that for early time ($t\Delta u/\lambda_{min} = 7$) the flow field consists of a series of mushroom like structures generated by the deposition of vorticity at the gas interface. Kelvin-Helmoltz (KH) instabilities grow exponentially hence breaking the large coherent structures. At late time the flow field is turbulent, consisting of motion on many different scales. There are some 'coherent' structures remaining (mushrooms shedding KH vortices) at the gas front, but in between there is a well mixed zone.

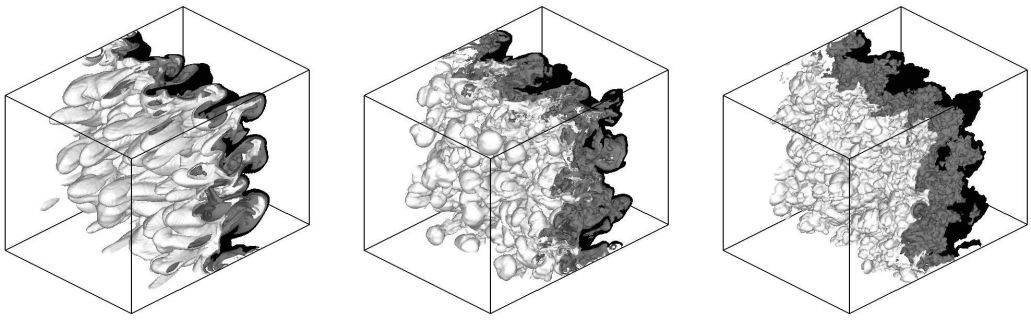

Figure 7.23: Comparison of the three numerical methods using broadband perturbations at $t\Delta u/\lambda_{min} = 250$ at 128 grid cross-section

Figure 7.23 shows the isosurfaces of mass fraction for each of the three numerical methods at late time for the 128 cross-section grid (broadband initial conditions). It is clear that the van Leer limiter is too dissipative to allow realistic growth of perturbations, hence, to economise on computational time, further results were not computed. Of WENO ninth order (W9) and the modified fifth order (M5+LM) the fifth-order has more fine scale structure, indicating less numerical dissipation. Comparing the flow structure in the broadband and narrowband simulations the narrowband simulation is much more regular, showing no large scale perturbations. The broadband initialisation shows a clear long wavelength perturbation, demonstrating that for the period of time under consideration, the initial conditions have a strong influence.

Growth Rates and Mixing Measures

In this section the following parameters are examined; Integral mixing layer width W; Molecular mixing fraction Θ; and the mixing parameter Ξ defined as

$$W = \int < \alpha_1 >< \alpha_2 > dx, \quad \Theta = \frac{\int < \alpha_1 \alpha_2 > dx}{\int < \alpha_1 >< \alpha_2 > dx}, \tag{7.3.4}$$

$$\Xi = \frac{\int < min(\alpha_1, \alpha_2) > dx}{\int min(< \alpha_1 >, < \alpha_2 >) dx}. \tag{7.3.5}$$

where $< \alpha_{1,2} >$ indicates the $y-z$ plane averaged volume fraction of species 1, 2 where species 1 is the heavy gas. It is generally accepted that the integral mixing layer width (considered less sensitive to fluctuations) grows at late time as t^θ. Θ gives a guide to the total reaction rate for a slow reaction, and Ξ is an equivalent measure for a fast reaction rate where one reactant is fully depleted. Figure 7.24 shows these quantities plotted for both sets of initial conditions, for all grid resolutions.

The mixing layer width exhibits good grid convergence, and is plotted on logarithmic axes to highlight the power-law behaviour of the amplitude. Assuming that amplitude is proportional to $C(t - t_0)^\theta$, and utilising a non-linear regression to gain the best fit

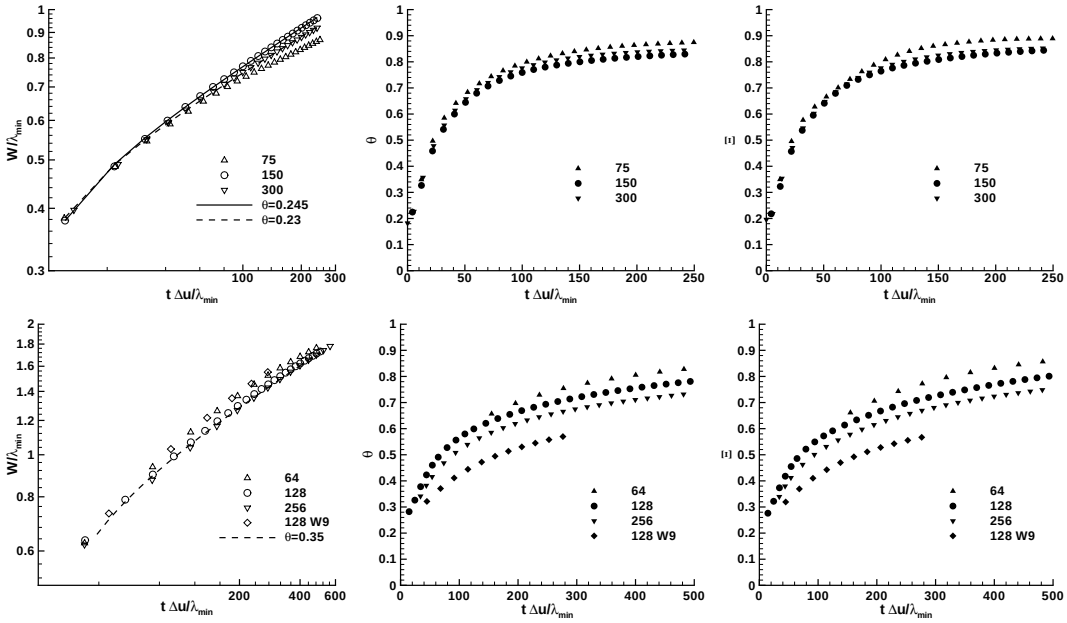

Figure 7.24: Integral mixing width, Molecular mixing fraction and mixing parameter for the narrowband perturbations (left) and broadband (right)

curve, $\theta = 0.24 \pm 0.015$ for the narrowband simulation. Comparison with previous simulations by Youngs [198] using a finite difference semi-Lagrangian method shows an almost exact match, lending weight to the fidelity of the numerical results. It is in is in good agreement with the experiments of Dimonte *et al.* [48] (see also Section 2.3.5) where the RM instability acts on a turbulent slab generated by RT instability (the initial turbulent slab can be interpreted as a form of narrow band initial perturbation). Compared to analytical theory detailed in Section 2.3 this result is consistent with the general consensus that $\theta = 2/3 - \mu$ [12], where the viscous correction $\mu \approx 5/12$ in this case. However, it is considerably lower than the lowest growth rate proposed by Zhou [202].

The broadband initial conditions give $\theta = 0.35 \pm 0.02$. This demonstrates that, for the duration of the simulation, the mixing layer width depends crucially on the form of the initial conditions. This is in good agreement with the theory of Inogamov [89], however it is likely that this theory is not valid with the power spectrum chosen, as it is narrow and the power spectrum is a relatively strong function of the wavenumber. However, it is lower than the predictions of Dimonte [46] and Youngs [198] based on the 'just saturated' mode (Section 2.3.2). The explanation for the low value of θ is that in the current simulations the ratio of maximum to minimum wavelength $\lambda_{max}/\lambda_{min} = 16/3 \approx 5.3$. This would mean that there is not a sufficiently wide range of modes which are simultaneously passing through linear and non-linear stages to determine the asymptotic value of θ for an infinite $1/k^2$ power spectrum.

The molecular mixing fraction Θ and mixing parameter Ξ both approach a constant state. This is achieved more rapidly with narrowband perturbations than with the

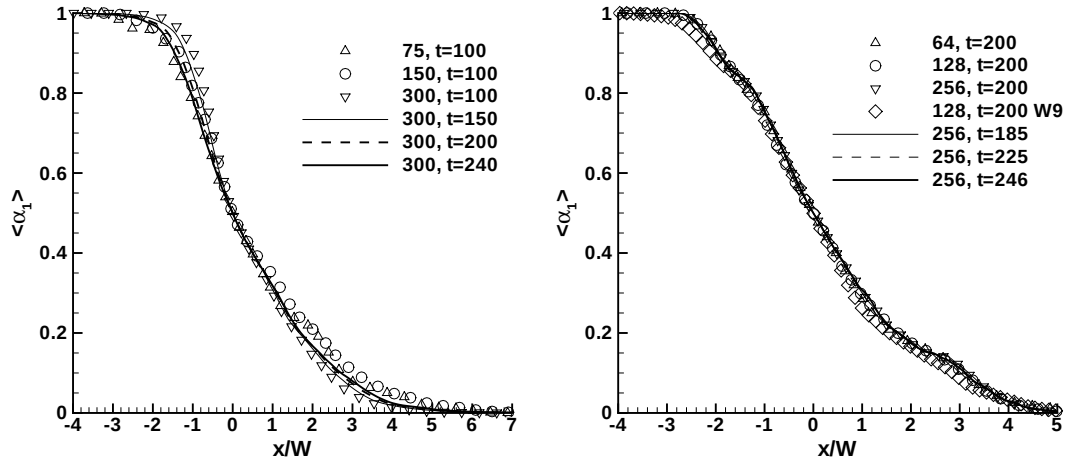

Figure 7.25: Plane averaged volume fraction for narrowband (left) and broadband (right) perturbations.

broadband initialisation. At the lower resolutions with M5+LM the level of molecular mixing is higher than with the WENO method, however as grid size increases both Θ and Ξ decrease. The asymptotic value of approximately 0.8 agrees well with previous mixing simulations of the related Rayleigh-Taylor instability by Youngs [197] and Cook and Zhou [42]. The slower convergence of the mixing statistics at high grid resolution indicates that a self-similar state has not yet been achieved for the broadband simulations.

For self-similarity the profiles of average volume fraction and mixing fractions should scale with a single characteristic length scale at all times, in this case the integral mixing layer width W. Figure 7.25 shows the plane averaged volume fraction. The scaled volume fraction profiles collapse excellently for all resolutions at all times for the narrowband and broadband perturbations, being almost identical at all times.

The narrowband perturbations lead to a smoother mean volume fraction profile, whereas the broad band perturbations give a smooth central region ($-1.5 < x/W < 1.5$) with outer regions on the bubble and spike side where the persisting large scale structures cause a break in the smooth profile. This change to the mean profile is most likely the late time growth of large scale perturbations which are not present in the narrowband simulation, and are at the head and tail of the mixing layer at late times.

Figure 7.26 the plane averaged mixing fraction $< \alpha_1\alpha_2 >$. The plane averaged mixing fractions are not as well converged. Interestingly, the level of mixing appears to be decreasing at higher resolution in both cases, indicating that the lower dissipation at higher resolution leads to less transport. The WENO limiter promotes greater mixing, having a profile which peaks at $< \alpha_1\alpha_2 >= 0.21$ as opposed to 0.16 for the M5+LM limiter at the same resolution. As time progresses the peak of $< \alpha_1\alpha_2 >$ increases, as expected.

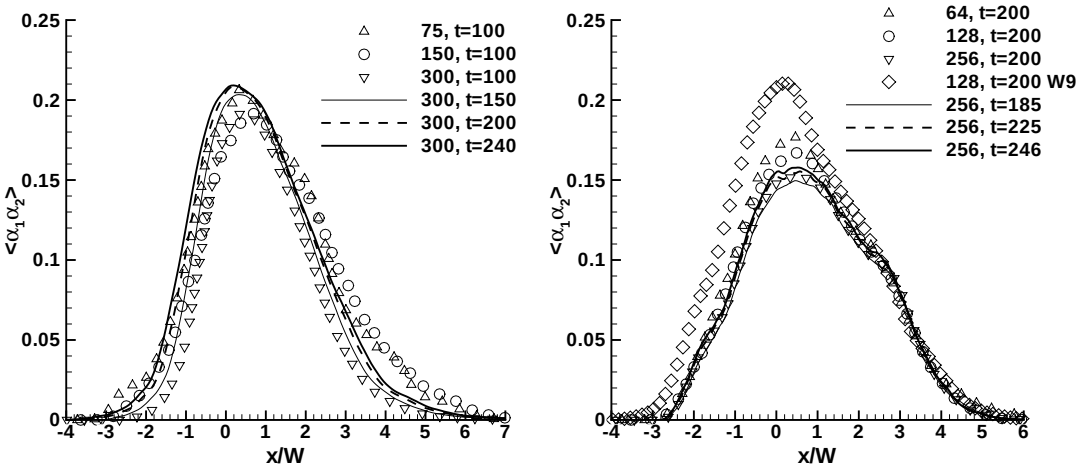

Figure 7.26: Plane averaged mixing fraction for narrowband (left) and broadband (right) perturbations.

Turbulent Kinetic Energy

Figure 7.27 shows the total fluctuating kinetic energy, computed from the fluctuating velocities. The fluctuating velocities are computed as the difference of the actual velocities minus the plane averaged velocity, summed over the entire mixing layer, i.e.

$$\tilde{u} = \frac{\sum_{yz} \rho u dV}{\sum_{yz} \rho dV}, \quad TKX = \sum_{xyz} \frac{1}{2}\rho(u - \tilde{u})^2 dV, \quad TKY = \sum_{xyz} \frac{1}{2}\rho v^2 dV \tag{7.3.6}$$

where $\tilde{(.)}$ is the Favre mass-weighted average, dV indicates the volume of the cell, $\sum_{yz}$ is the summation in the plane $x = const$, and $\sum_{xyz}$ is the summation over the whole volume. Note that the z direction turbulent kinetic energy is almost identical to the y direction, hence is omitted from the plots.

Both simulations demonstrate excellent grid convergence, the x direction turbulent kinetic energy decreasing throughout the simulations in a power law form. The y and z direction kinetic energy first increases as KH instability transfers energy from the x direction to the y and z.

In the narrowband simulation the turbulent kinetic energy in the x direction decreases at a rate proportional to $t^{-1.25}$, in the y and z proportional to $t^{-1.23}$, in good agreement with experimental results from grid generated homogeneous decaying turbulence [100]. The assumed power law line of best fit is shown in Figure 7.27, compared to the highest resolution simulation.

Assuming self-similar development of the mixing layer, the ratio of the x and y direction kinetic energies should be constant, i.e. θ should be the same for all directions. Given the difficulties in determining the virtual origin for the decay of turbulent kinetic energy (as discussed in Section 4.3.2), the difference in θ between the different

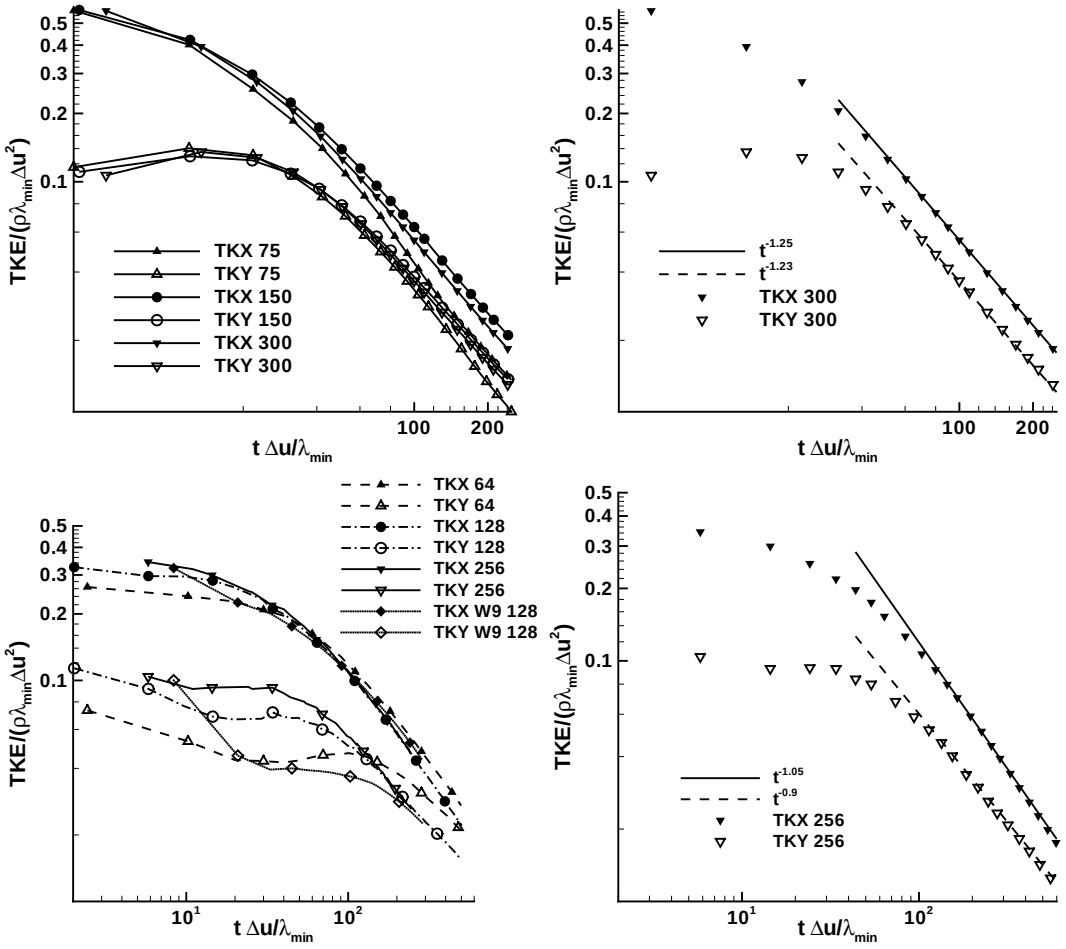

Figure 7.27: Resolved fluctuating kinetic energy and comparison with line of best fit for the narrowband (top) and broadband case (bottom)

kinetic energy components is not significant. The ratio of kinetic energies is plotted in Figure 7.28 for the narrowband initialisation, demonstrating that it asymptotes to approximately 1.5 at the finest grid resolution.

Given that the width of the mixing layer scales with t^θ, then the empirical relation $\epsilon \propto u^3/W$ (Equation 2.2.9) can be used to check the dissipation rate of kinetic energy. Hence $dq_K/dt \propto q_K^{3/2}/t^\theta$, with a solution of the form $q_K \propto t^{2\theta-2}$. This is the decay rate of mean kinetic energy across the mixing layer. The decay of total fluctuating kinetic energy computed in this section is proportional to the width of the mixing layer multiplied by the mean kinetic energy, i.e. $Wq_K \propto t^\theta t^{2\theta-2} \propto t^{3\theta-2}$. This result can also be gained by assuming that the mean velocity in the mixing layer is proportional to the growth of the mixing layer itself, giving $\sqrt{q_k} \propto dW/dt \propto t^{\theta-1}$. Computing this for the narrowband initial condition gives a decay of total fluctuating kinetic energy proportional to $t^{-1.28}$, in very good agreement with the directly measured values.

The decay rate in the broadband case is proportional to $t^{-1.05}$ for the x direction tur-

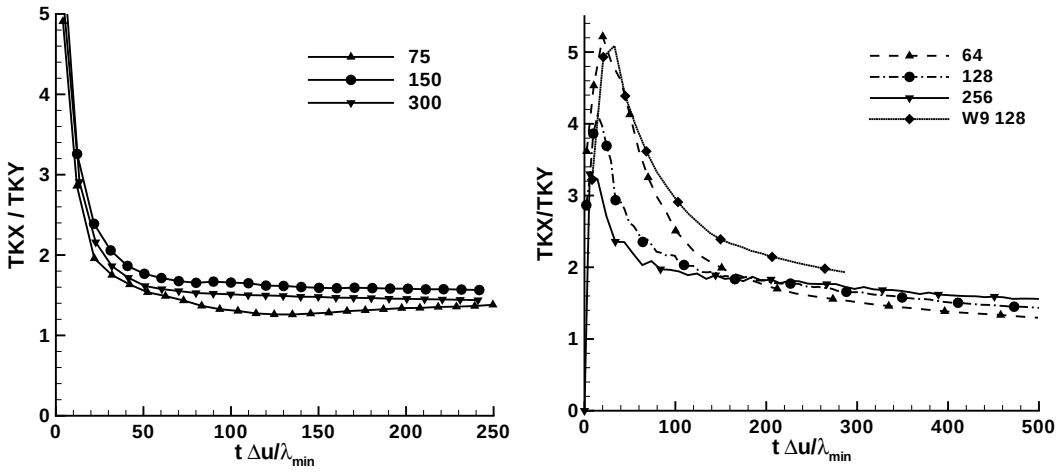

Figure 7.28: The ratio of the x and y direction fluctuating kinetic energy for the narrowband case (left) and the broadband case (right)

bulent kinetic energy, and $t^{-0.9}$ for the y and z directions (see Figure 7.27). As a large portion of the fluctuating kinetic energy is in the longer wavelengths, this leads to a lower kinetic energy dissipation rate than in the narrowband case. For the majority of the simulation the long wavelengths are irrotational (being in the linear stage of development), thus the transfer of fluctuating kinetic energy from the longitudinal to the lateral components is slower than in the narrowband simulation. This means that the dissipation of kinetic energy is not as efficient, giving a lower value of θ. Although it is not expected that the broadband simulation has lead to a fully developed turbulent mixing layer within the time scales simulated, computing the decay rate of total fluctuating kinetic energy (assuming it is proportional to $t^{3\theta-2}$) gives $d(KE)/dt \propto t^{0.98}$, again a very good estimate of the measured value. Examining the ratio of the turbulent kinetic energies in the longitudinal and lateral directions in Figure 7.28 implies that they are tending to a self-similar state where $TKX/TKY \approx 1.5$ as in the narrowband case. Again, this is consistent with the idea that the longest wavelengths are saturating, and that the flow physics is transitioning from growth due to the 'just-saturated' mode, to a fully developed anisotropic turbulent slab.

The instantaneous two dimensional kinetic energy spectra are compared to the theoretical results of Kolmogorov ($k^{-5/3}$) and the proposed solution for RM instability of $k^{-3/2}$ by Zhou [202] in Figure 7.29. This is computed in the midplane of the mixing layer, in the $y-z$ plane. Examining the narrowband results indicates excellent scaling of the kinetic energy spectra for the different grid resolutions under the non-dimensionalisations detailed in Section 7.3.2. The small scales are nearly identical, and the spectra appear to follow more closely the $k^{3/2}$ spectrum. The differences at large scales (low wavenumbers) reflect the limitations posed by grid size, which prevents further mode coupling in the low resolution simulations.

The broadband spectra also collapse well at different grid resolutions, and methods. Comparison between the different grids and methods show that the M5+LM method

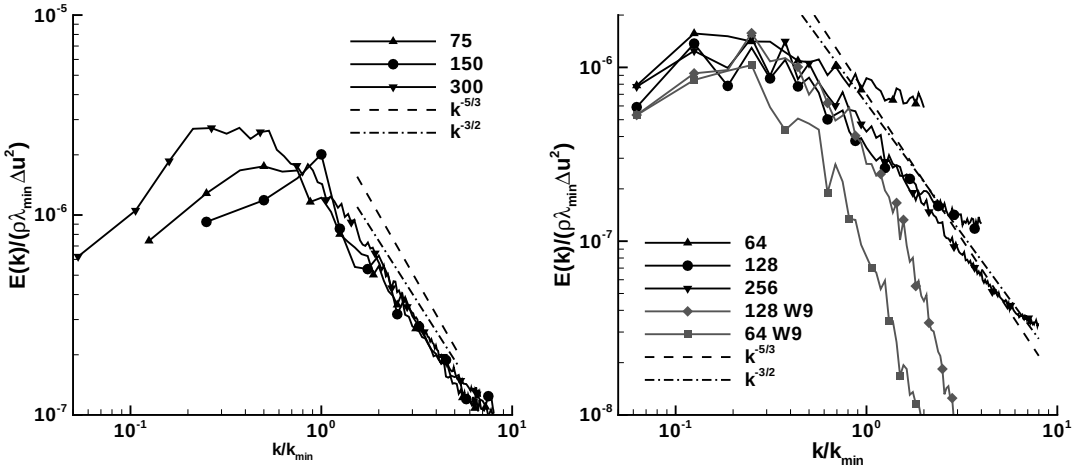

Figure 7.29: Fluctuating kinetic energy spectra for the narrowband (left) and broadband case (right)

is not sufficiently dissipative at low resolutions, and that the WENO method is too dissipative. This is consistent with the plane averaged mixing results presented in Figure 7.26, which demonstrate more mixing at the lower resolutions than at the higher resolutions. At the highest resolutions there is excellent agreement for the first 48 modes when comparing the 128 and 256 cross-section grids with the M5+LM method, and up to mode 28 with WENO. At moderate wavenumber the spectra appear to scale as $k^{-5/3}$, and at $k^{-3/2}$ at high wavenumber.

7.3.4 Conclusions

Simulations of shock induced turbulent mixing with two different initial conditions have been conducted. Two different high order methods have been used, and three different grid sizes. Excellent grid convergence is observed throughout.

The typical behaviour of a multimode Richtmyer-Meshkov simulation is seen, beginning with the growth of coherent 'mushroom' shaped structures which transition to a fully turbulent mixing zone. It is shown that the growth rate of the mixing zone depends on the initial perturbations, as the long wavelength perturbations promote a faster growth rate than short wavelength perturbations. This is most likely to be due to the slow but persistent growth of large scale perturbations which dominate over the short wavelengths at long times.

The growth rate for narrowband perturbations is in good agreement with experiments by Dimonte *et al.* [48], and within the bounds laid down by dimensional considerations of the expansion of a uniform slab of turbulence. The broadband perturbation leads to values of $\theta \approx 0.34$, which is lower than expected from the 'just saturated' mode analysis of Dimonte [46] and Youngs [198]. It is believed that this is due to the relatively small wavenumber range simulated, in that the longest wavelength is approximately

five times larger than the shortest. It is not believed that this is a sufficiently wide range, and that at late time the longest modes are close to saturation or have already saturated. This leads to a slower than theoretical growth rate.

Examining the mean volume fraction profiles and development of two mixing indicators implies that the development of the mixing zone has reached an approximate self-similar state. The asymptotic state is not reached as rapidly for the broadband perturbations as for the narrowband.

The turbulent kinetic energy decays most rapidly in the narrowband simulation ($\propto t^{-1.25}$), close to that expected from homogeneous decaying turbulence. The ratio of longitudinal to lateral turbulent kinetic energy is approximately constant at late times (≈ 1.5), indicating that there is a self-similar mixing layer. However, the broadband simulation demonstrates slower decay ($\propto t^{-1.05}$), as a larger proportion of the total fluctuating kinetic energy is in the irrotational (linear/early non-linear) flow field than in the narrowband initialisation.

Interestingly, predictions of the decay exponent of total fluctuating kinetic energy using the measured value of θ from the integral mixing width and the relation $dq_K/dt \propto q_K^{3/2}/W$ are close to those directly measured for both the narrowband and broadband perturbations. Turbulent kinetic energy spectra show a closer agreement to a $k^{-3/2}$ range at the high wavenumbers, with some $k^{-5/3}$ at intermediate scales.

7.4 Half-height Experiment

7.4.1 Introduction

Recent experimental results by Holder and Barton [83] permit validation of numerical methods for multi-component compressible turbulent mixing of two miscible gas species. The shock tube experiment consists of an incident shock wave of Mach 1.26 in air passing through a square block of Sulphur Hexafluoride (SF_6). As it passes through the block, initially small perturbations on the gas interface create both Richtmyer-Meshkov instabilities (vorticity deposition as the shock passes) [134, 155] and Kelvin-Helmholtz roll ups. These perturbations grow rapidly in size leading to turbulent transition of the flow, and inviscid mixing of the two gas components.

It is a great challenge to accurately simulate such a rich physical problem, and it is necessary to employ numerical methods which have sufficient dissipation to maintain monotonicity across shock waves, yet allow the growth of the initially small perturbations and capture contact surfaces with good accuracy. The Reynolds number based for this experiment is on the order of 5×10^6, thus given current computations power the simulations cannot be fully resolved. Due to this constraint ILES is employed with the new characteristics based Riemann solver for the ThCM model (derived in Chapter 3), and the new limiting methodology proposed in Chapter 6. These are validated against experimental data, and compared to existing numerical methods.

The layout of this section is as follows. Firstly the experiment is described in Section 7.4.2. The choice of governing equations is detailed in Section 7.4.3, along with the details of the initialisation, grid and boundary conditions. Next, the results obtained for second-, fifth-order and modified fifth-order are compared to experiment, and with each other.

7.4.2 Experimental Setup and Diagnostics

Figure 7.30 shows a schematic of the half-height experiment (See [83] for the full details). The shock tube contains air at atmospheric pressure and temperature. When the diaphragm is burst a shock of $M = 1.26$ propagates from left to right. At $x = 0$ there is a 'block' of SF_6 which is 5.5 times denser than air, and has $\gamma = 1.076$, which is initially held in place by microfilm membrane. The speed of sound is approximately three times slower in SF_6 than in air, thus inducing a strong Kelvin-Helmholtz instability on the upper surface of the block and rapid transition to turbulence. In addition to this, there is growth of Richtmyer-Meshkov type instabilities on the vertical interfaces. The shock wave reflects off the wall at the right side of the domain and passes back through the mixing region, injecting further energy into the turbulent mixing zone.

The output from the experiment was a series of images taken at specific times using a pulsed laser sheet. The SF_6 block was initially seeded with olive oil droplets, hence the intensity of the image represents the density of the SF_6 at a specific location.

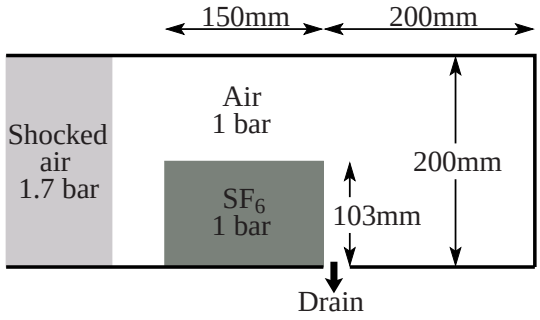

Figure 7.30: Schematic of the half-height experiment, note that the shock tube is 100mm deep .

7.4.3 Computational Approach

Given the presence of shock waves and compressible mixing, it is necessary to employ a compressible method. With a Reynolds number on the order of 10^6, the Kolmogorov length scale is significantly below the grid scale, and the effect of viscosity on the scales resolved by the grid is considered negligible. Thus the governing equations chosen are the Euler equations plus two additional equations for the multi-component model. At the pressures and temperatures considered, both SF_6 and air are approximated well by the ideal gas equation of state, and are miscible.

Grid and Initialisation

The co-ordinate system chosen has the x direction aligned with the initial direction of shock propagation, z in the vertical direction, and y in the homogeneous direction. The point $(0, 0, 0)$ is located at the bottom left hand interface between the SF_6 block and air. The numerical domain chosen extends from -0.45m to 0.35m in x, and takes the shock tube dimensions in the other two directions. This is longer than the test section shown in Figure 7.30 as it is necessary to capture the shock front reflected off the left face of the block of SF_6. The boundary conditions are taken as reflective (inviscid wall boundary condition) on the upper, lower and right-hand walls, and an extended one dimensional domain on the left hand interface in the x-direction. The y-direction boundary conditions are periodic.

There is special treatment required for the drain hole, which is modelled as an extended one dimensional domain. The incident shock wave can then diffract down the drain hole, entraining material in a similar manner to that seen in the experiment. At late times this holes acts as a nozzle where high speed air/SF_6 mixture exits the shock tube. The addition of the drain hole was demonstrated as being necessary in earlier studies [180, 16]. The extended one dimensional domain is initialised as pure air at atmospheric pressure and density.The drain hole is located between 0.153m$< x <$ 0.16m and 0.05m$< y <$ 0.95m.

The block of SF_6 is initially held in place with a microfilm membrane, which is destroyed by the incident shock wave. However, this membrane imparts a perturbation

onto the interface between the two gases which must be modelled, as this perturbation is the seed which triggers growth of the instabilities. Numerically, this perturbation is modelled as a summation of random modes with RMS amplitude of 0.1mm at wavelengths between 5mm to 50mm satisfying a power spectra proportional to the wavenumber of the mode. The upper interface is not held in place by a membrane and so in the experiment it is likely that this would be a diffuse interface, however it is modelled as a sharp interface numerically.

To facilitate comparison of the three numerical methods, simulations were run at two different grid resolutions for each method. The coarse grid was $300 \times 80 \times 160$, and the fine grid $600 \times 160 \times 320$. An additional grid of $750 \times 200 \times 400$ (double the number of mesh points in the fine grid) was run with fifth order limiting to test convergence of plane averaged statistics.

Finally, the density of SF_6 and air were 6.34kg/m^3 and 1.153kg/m^3, and the ratios of specific heats, γ, 1.076 and 1.4, respectively.

7.4.4 Results and Discussion

Comparison with Experiment

Figure 7.31 and 7.32 compare the experimental images with plane slices of SF_6 density taken from computational results. The vertical reference line on the experimental and computational images is at $x = 0.15$m. The white circle on the computational results indicates the position of the centre of the primary vortex in the experiment. This was determined approximately from the location of the darkest pixel in the experimental images in the region of the vortex core. For the first two time steps there is very little difference between the experimental and numerical images. There is slightly more roll-up of the primary vortex (developing at the upper left corner of the block) in the fifth-order methods as compared to the second-order method. At 0.37ms the shock wave is about a third of the way through the SF_6 block and has formed a Mach intersection. This links the plane shock transmitted through the SF_6 block with the shock which is propagating more rapidly through the air over the top of the block.

At 1ms the intersecting shock waves have converged at the lower right hand side of the block of SF_6, and reflect off the lower wall creating a region of very high pressure and density. The strong reflected shock induces a rapid post-shock velocity generating the bulge in the right interface of the block. Some differences between the numerical methods and the experiment can be seen. Initial instabilities in the primary vortex can be seen in both the experiment and the fifth-order method, which takes on an oval shape. This is not seen in the second-order method as the initial perturbations have been damped more heavily. However, there are signs of small Kelvin-Helmholtz instabilities on the upper interface of the SF_6 block in the fifth-order simulations which are not seen in the experiments. This is because in the experiments the upper interface was initially diffuse, which tends to inhibit the growth of such instabilities. An example of this behaviour can be seen by comparing simulations at high resolution with a

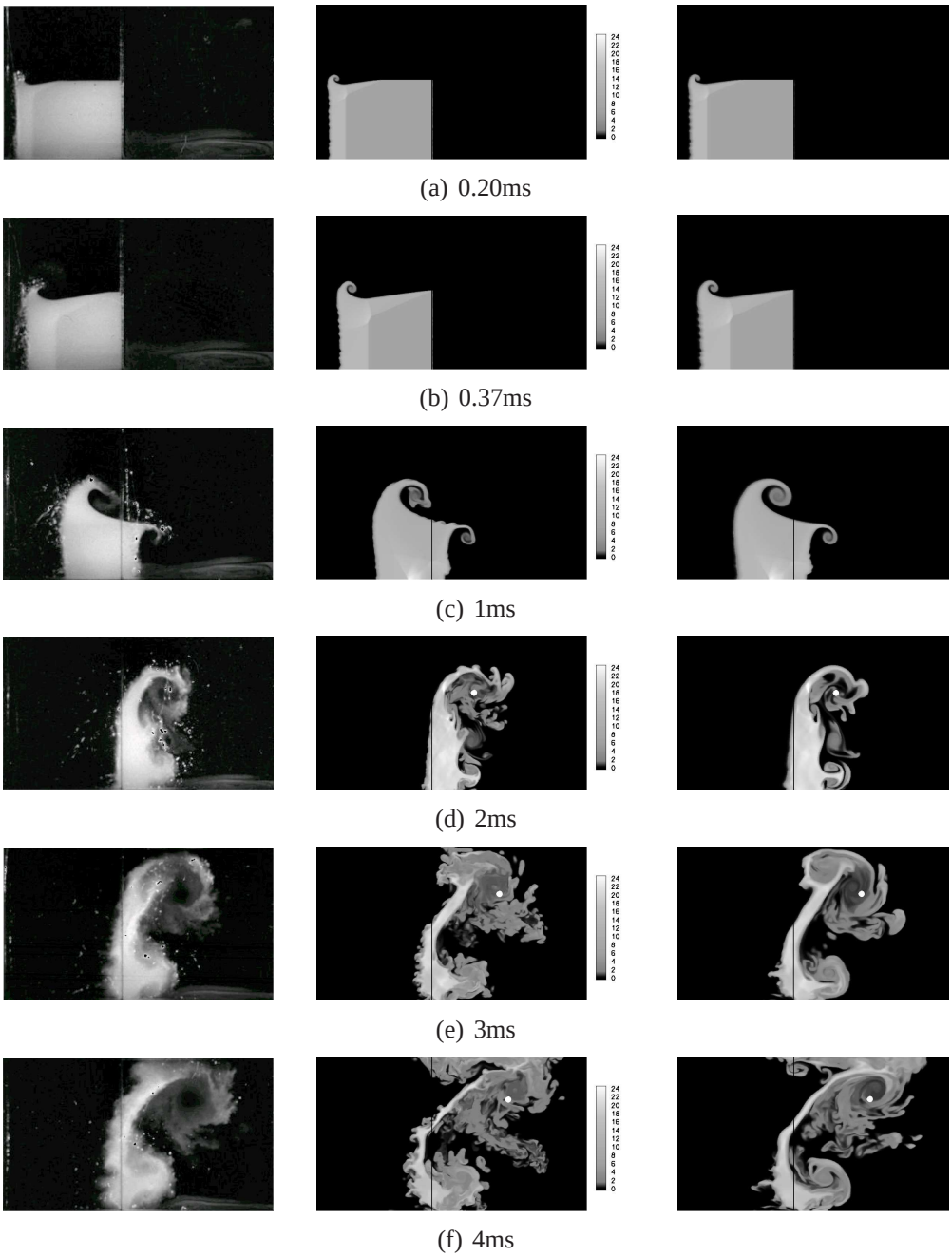

(a) 0.20ms

(b) 0.37ms

(c) 1ms

(d) 2ms

(e) 3ms

(f) 4ms

Figure 7.31: Comparison of experimental images (left, ©British Crown Copyright 2006/MOD) and SF_6 density (kg/m^3) for fifth-order (centre) and second-order (right) using the grid of cross-section of $600 \times 160 \times 320$. The white circle on the computational results indicates the location of the centre of the vortex in the experimental results, the vertical line is at $x = 0.25$

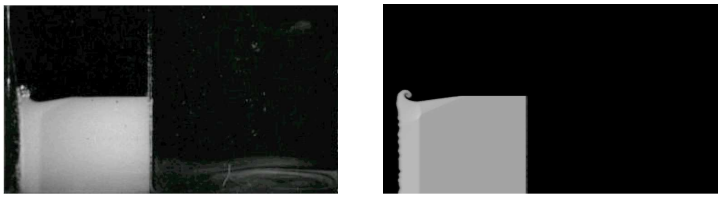

(a) 0.20ms

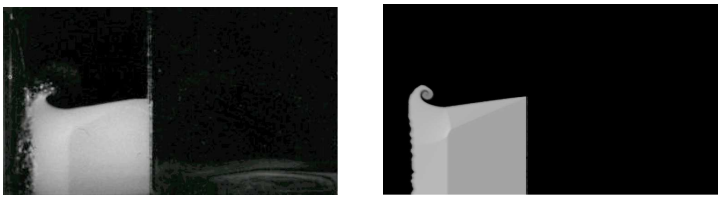

(b) 0.37ms

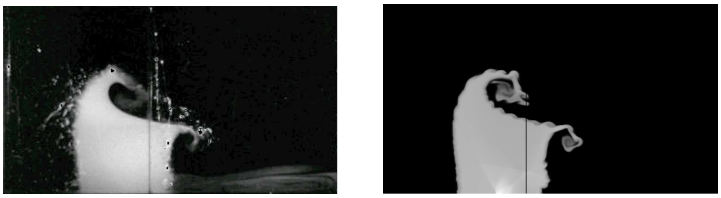

(c) 1ms

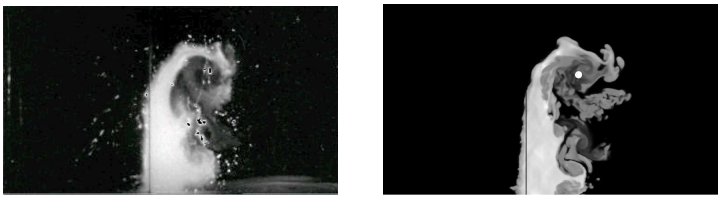

(d) 2ms

(e) 3ms

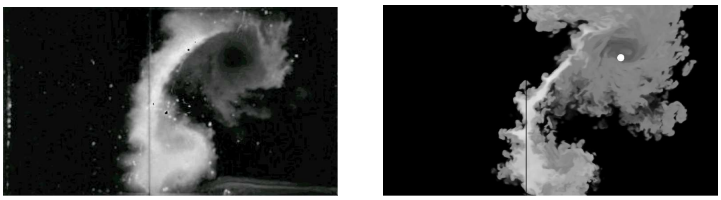

(f) 4ms

Figure 7.32: Comparison of experimental images (left, ©British Crown Copyright 2006/MOD) and SF_6 density (kg/m^3) for fifth-order with low Mach correction (right) using the grid of cross-section of $600 \times 160 \times 320$. The white circle on the computational results indicate the location of the centre of the vortex in the experimental results, the vertical line is at $x = 0.25$

sharp interfaces by Shi *et al* [163] which show Kelvin-Helmholtz instabilities along the interface compared with simulations by Latini *et al.* [115] with a diffuse initial interface which suppresses these features. The innate diffusivity within the second-order method also acts to suppress these features.

The shock reflects off the end of the shock wave, and passes through the developing mixing layer. By 2ms the shock wave has passed through the 'bulge' visible on the right-hand interface at 1ms producing a single mode 'mushroom' shaped vortex. At the same time the primary vortex has become unstable and a well mixed region is developing in the vortex core. The size and location of the main flow features are very similar in comparing experiments and simulation, however there is clearly more fine scale detail in the M5+LM simulation. The location of the vortex core is similar in all simulations. At 3ms the mixing continues to evolve, with additional mixing in the thin strip of material linking the 'mushroom' shaped feature with the primary vortex. This mixing is at a small scale relative to the grid resolution so it is not resolved at second-order accuracy, however at fifth-order some instability can be seen, and this is significantly improved in the low Mach corrected scheme. The primary vortex is slightly behind the location of the experimental vortex, and is captured much better with the fifth order methods.

The final images again agree very well, however there is a region of mixed fluid travelling along the top of the shock tube in the simulation which appears not to be present in the experiment. It is believed that this is due to the poor resolution of the experimental images as the laser sheet approaches the wall. An important point to note is that the final position of the SF_6 is slightly different in experiment and simulation. Referring to the position of the SF_6 relative to the reference line in Figures 7.31f) and 7.32f), it can be seen that the second- and fifth-order standard methods predict that the remains of the SF_6 block do not travel as far in the x-direction as in the experiment. The low Mach corrected scheme does a much better job at reproducing this detail, as it allows better resolution of the main flow features that influence the mean position of the SF_6.

An additional point to note is that the experimental images appear more diffuse as they do not represent a plane slice through the flow field. Although the laser sheet is extremely thin, the reflected light is subsequently scattered through additional interactions with oil droplets before reaching the imaging device. Figure 7.33 shows line-averaged SF_6 density which appears more diffuse as in the experimental images. It is clear that the fifth-order methods capture the small scale mixing at the thin strip much better than the second-order method, and predict the location of the vortex core closer to the actual location.

Measurements of the position of the SF_6 block and shock wave at early times have been taken. A comparison of experiment and the three numerical methods can be seen in Figure 7.34. The position of the block and the shock wave was identified using contours of 0.5 and 1.5 times the initial density of SF_6. There is a slight discrepancy in position of the diffracted shock in all numerical simulations. This is due to the initial diffuse interface in the experiment, which would lead to a larger vertical distance between the shock travelling in pure air and the shock travelling in pure SF_6.

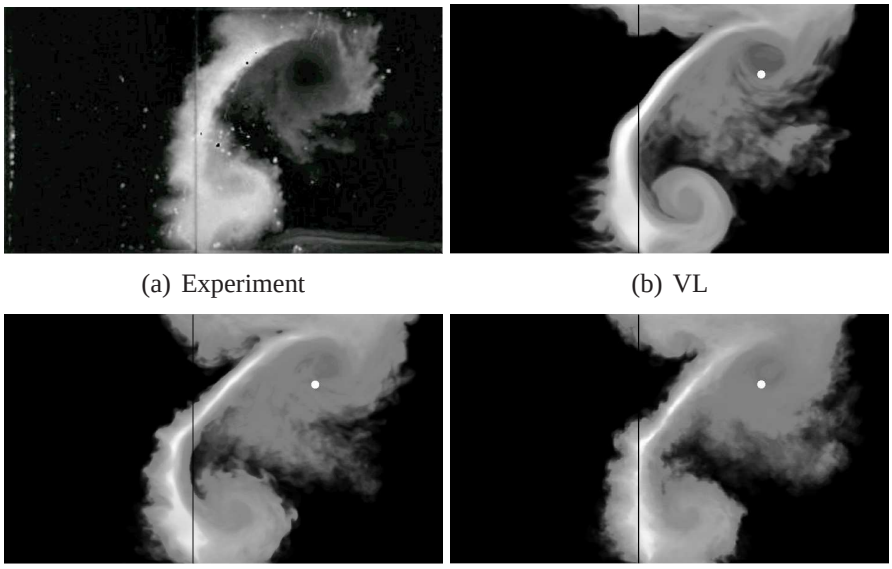

(a) Experiment (b) VL

(c) M5 (d) M5+LM

Figure 7.33: Line average SF_6 density at 4ms compared to the experimental images (©British Crown Copyright 2006/MOD), The white circle indicate the location of the experimental vortex centre

Examining the angle of the 'thin strip' which wraps around the primary vortex at late time (Figure 7.33), this is at a steeper angle than in the experiment. A possible explanation of this discrepancy is that the steeper shock angle in the simulations induces velocity which has a stronger vertical component than for the experimental shock.

Comparing the numerical methods, the material interface is captured significantly more sharply in the fifth-order methods than in the second-order method. Also, this validates the choice of governing equations as the shock wave is captured without oscillation, and the position of the material interfaces is captured well in comparison to the experiment.

Figure 7.35 shows volume fraction isosurfaces at 4ms, illustrating the highly turbulent nature of the flow, and the presence of fine scale features in the fifth-order simulation which are not present at second-order.

Turbulent Mixing and Kinetic Energy

As a means to compare and contrast the numerical methods, the turbulent kinetic energies and plane averaged mixing quantities have been computed for two different grid resolutions for each method. Figure 7.36 presents plane averaged mixing $< \alpha_1 >< \alpha_2 >$, and Figure 7.37 the quantity $< \alpha_1\alpha_2 >$, which is a measure of the amount of molecular mixing in the primary vortex. α_1 is the volume fraction of Air and α_2 that of SF_6.

The mixed region does not start until $x = 0.125m$ with the low Mach scheme as op-

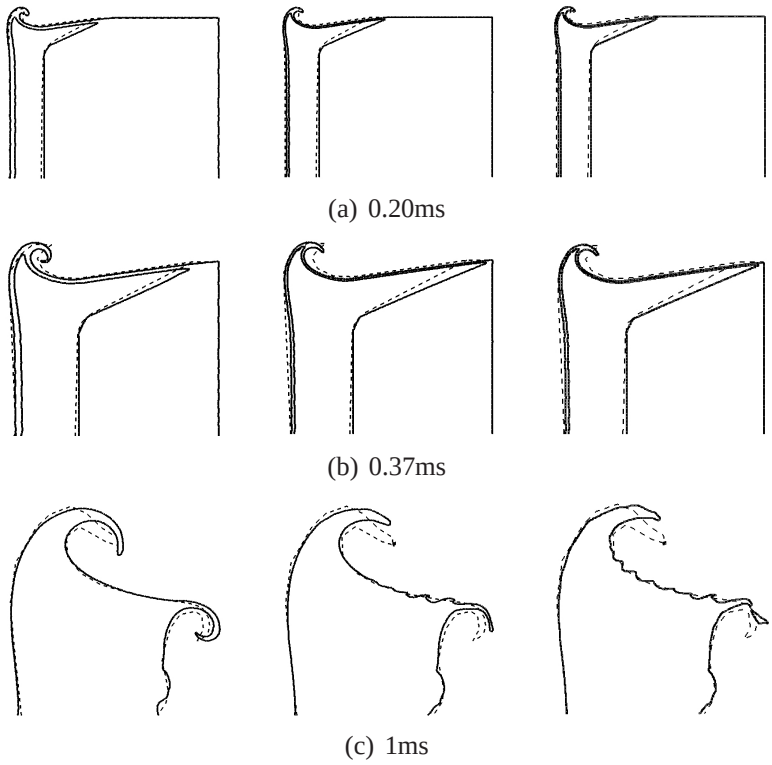

(a) 0.20ms

(b) 0.37ms

(c) 1ms

Figure 7.34: Comparison of experimental shock and SF_6 positions (dashed line) and numerical results (solid line) for second-order (left), fifth-order (centre) and modified fifth-order (right) using the grid of cross-section of 160×320

posed to $x = 0.115$ for the other two methods. As discussed in the previous section, the low Mach scheme is the better result in comparison with experimental images.

Apart from this difference, there is excellent agreement at all grid resolutions and between the numerical methods for the location and magnitude of the peaks of plane averaged mixing and molecular mixing. Slight differences appear at around $x = 0.16m$ in the plot of plane averaged mixing which is due to enhanced mixing at the right hand side of the thin strip of dense material. This is visible in Figure 7.33, and also appears in the level of molecular mixing in Figure 7.37, where molecular mixing is at a local minimum in the second-order method. There is a slight 'bump' at $x = 0.29m$ in the coarse resolution fifth-order simulations caused by the advection of a small region of dense fluid over the top of the primary vortex which does not occur in the finer resolution simulations, and is diffused in the coarse grid simulation at second-order.

The turbulent kinetic energy per metre is defined as

$$KE = \frac{1}{2}\int \rho K dy dz, \tag{7.4.1}$$

$$K = (u-\tilde{u})^2 + v^2 + (w-\tilde{w})^2, \tag{7.4.2}$$

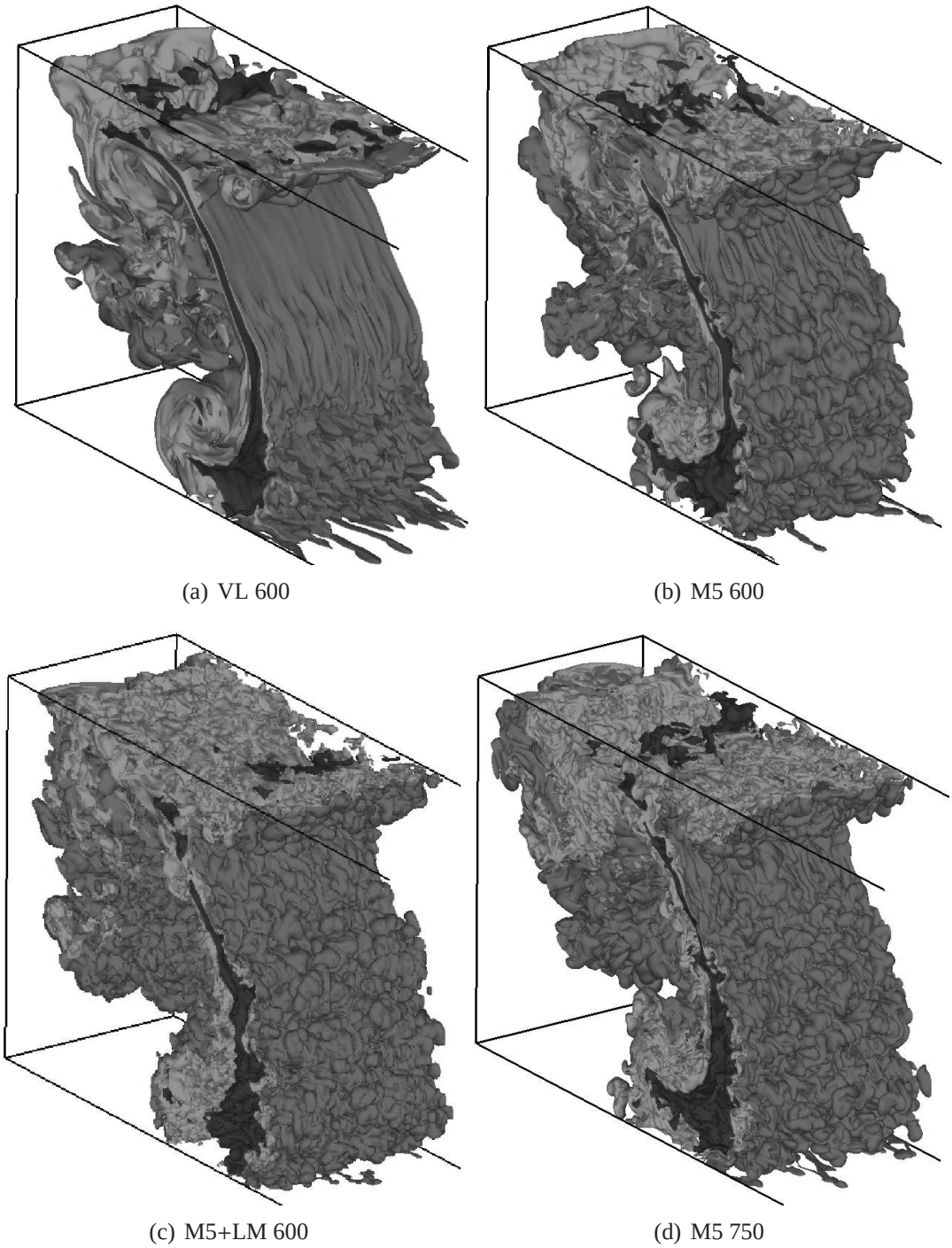

(a) VL 600 (b) M5 600

(c) M5+LM 600 (d) M5 750

Figure 7.35: Isosurfaces of 0.01, 0.5 and 0.99 volume fraction of air

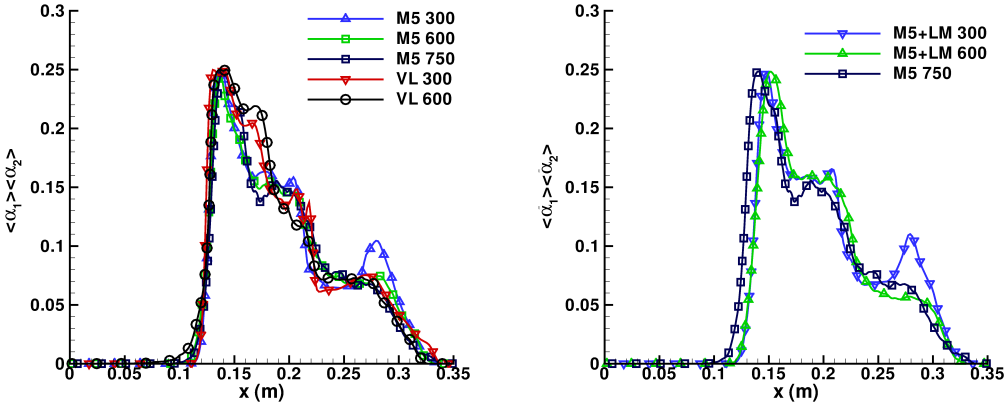

Figure 7.36: Comparison of $< \alpha_1 >< \alpha_2 >$ at 4ms

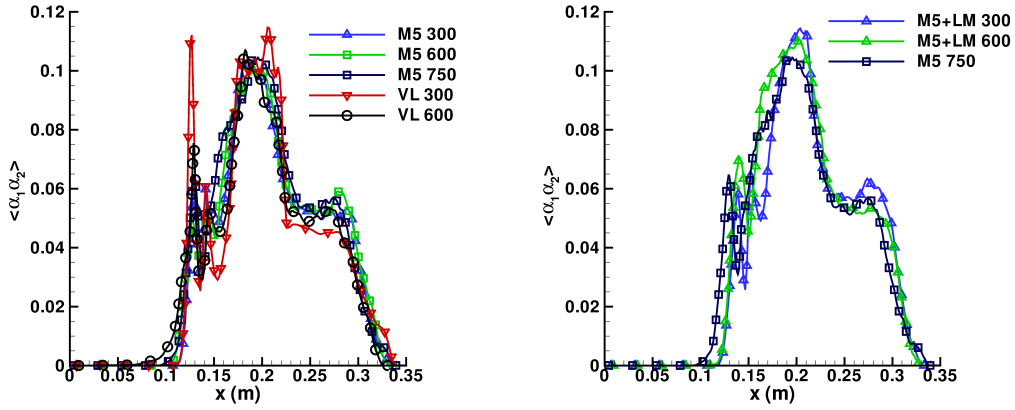

Figure 7.37: Comparison of $< \alpha_1 \alpha_2 >$ at 4ms

where the tilde quantities are Favre mass-weighted mean velocities in the homogeneous direction

$$\tilde{u} = \frac{\overline{\rho u}}{\overline{\rho}}, \qquad \tilde{w} = \frac{\overline{\rho w}}{\overline{\rho}}, \tag{7.4.3}$$

and $\overline{(.)}$ indicates a line averaged quantity in the periodic y direction. This is plotted in Figure 7.38 for t=4ms. There are two peaks in the line averaged kinetic energy corresponding to the location of the mushroom-shaped perturbation and the large primary vortex. There is a fairly large difference in resolved kinetic energy primarily due to the difference in grid scale. However, the fifth-order methods give higher peak plane averaged turbulent kinetic energy at a mesh resolution of $300 \times 80 \times 160$ than the second-order method at $600 \times 160 \times 320$. This indicates that the fifth-order methods are far superior in terms of resolution, especially considering that the fifth-order methods are only 18% slower in terms of total run time. The location of maximum kinetic energy is at $x = 0.26m$, and matches to within 5mm for all grid resolutions.

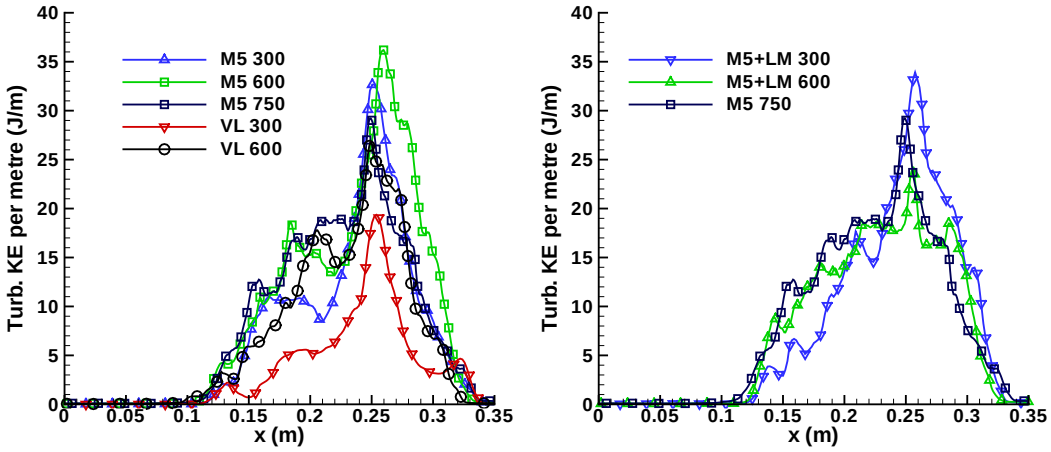

Figure 7.38: Comparison of turbulent kinetic energy per metre at 4ms

In comparing the two fifth-order methods it appears that the 600 resolution M5+LM agrees better with the highest resolution M5 simulation that the 600 resolution M5 method. The M5 method appears to slightly over-estimate fluctuating kinetic energy at this resolution, which the modified method corrects. At a grid resolution of 300 the fifth-order methods are fairly similar in plane averaged statistics, but the modified method resolves approximately 20% more kinetic energy.

Finally, the evolution of total resolved turbulent kinetic energy (TKE) as a function of time is shown in Figure 7.39. The initially small perturbations on the gas interfaces grow with time due to the combined action of Richtmyer-Meshkov and Kelvin-Helmholtz instabilities. This means that the kinetic energy increase begins earlier in the schemes which resolve the smaller perturbations, as is illustrated in Figure 7.39. As the turbulent perturbations become larger, then kinetic energy is resolved on the coarser grids. However, the injection of energy is in the form of an impulse as the incident shock and reshock pass through the mixing zone. Once the shock has left the domain, the TKE in the smallest scales resolved on the finest grid at fifth-order accuracy begin to dissipate. This does not occur using the other methods or grid sizes as they do not resolve these small vortices. Indeed, at the coarsest resolution with the second-order method, the TKE continues to grow up to the end of the simulation. An important point to note is that the variation and magnitude of the resolved TKE using the fifth-order limiter at the coarse resolution agrees very well with that captured by the second-order method on a grid twice the size in each direction. It should be noted that these results are also in excellent agreement with results presented using a semi-Lagrangian code in [180].

7.4.5 Conclusions

This section has validated the new multi-component scheme applied to a compressible, turbulent mixing experiment. In addition, comparison with standard numerical

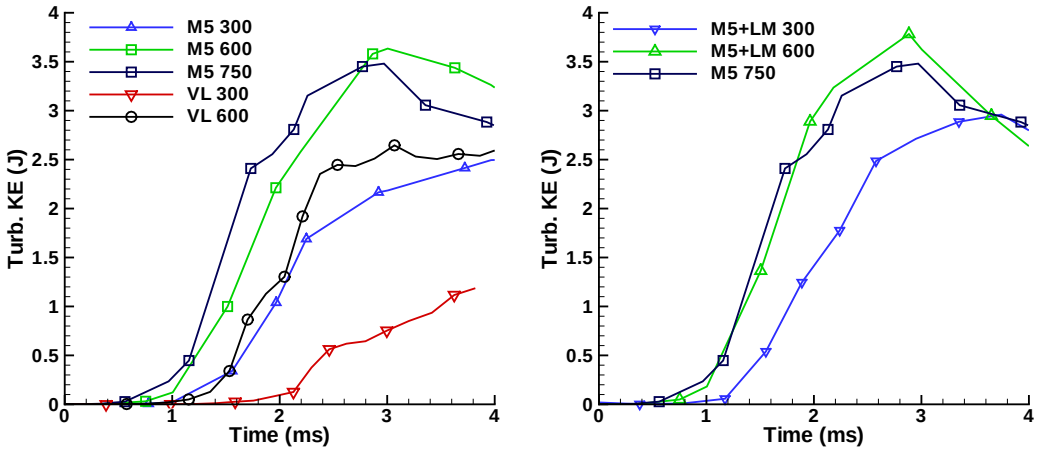

Figure 7.39: Comparison of total resolved turbulent kinetic energy variation with time, where time is measured from the passage of the shock through the first interface

schemes demonstrates the improved performance of the modified limiting method compared to the van Leer limiter, and the standard fifth-order limiter. This includes the mean position of the SF_6 block at late time, where the standard limiters at all resolutions give the left hand position of the block 1cm behind where it is in experimental images. There is a slight improvement in the prediction of the location of the centre of the primary vortex, and clear increase in fine scale structure at a given resolution.

Contrasting the three limiting methods, the mixing parameters are very similar at all grid resolutions (apart from the 1cm shift), however the levels of turbulent kinetic energy for both fifth-order methods are similar to the van Leer simulation at double the grid resolution in each direction. Furthermore, the behaviour of total turbulent kinetic energy with respect to time shows that the new modified fifth-order method gives results in very good agreement with the standard fifth-order method with double the number of grid points. This clearly demonstrates the advantage of accurately simulating low Mach features, even in an experiment where the primary flow features are well into the compressible regime (Mach> 0.5).

CHAPTER 8

Conclusions

8.1 Conclusions

The aim of this thesis was to implement, analyse and further develop numerical methods for the simulation of compressible, turbulent mixing. The investigation was motivated by the need for accurate simulation of the Richtmyer-Meshkov instability, which is of importance in the understanding the flow physics of phenomena such as supernovae to inertial confinement fusion.

The initial requirement was to implement a multi-component model capable of efficiently tracking two miscible gases. Given that the different fluids within a mixed cell can be assumed to have the same velocity and temperature, there are several possible models. Four modern gas mixture models were implemented into a compressible code, two quasi-conservative methods [4, 97], the mass fraction method and the Total Enthalpy Conservation of the Mixture (ThCM) [191] model. Several one-dimensional test cases were used to elucidate the differences between the mixture models. From numerical test cases it was clear that the mass fraction model was the worst, producing significant pressure oscillations in regions when a shock passes through a contact surface. It was shown theoretically that the ThCM model also does not maintain pressure equilibrium in mixed cells where the temperature varies across the cell, however these are not as severe as in those with the mass fraction model.

Both the Allaire *et al.* [4] quasi-conservative model and the Johnsen and Colonius [97] eliminate the problem of pressure oscillations, however in the presence of strong shock waves the Johnsen and Colonius approach breaks down, and variations in the ratio of specific heats occurs in the pure gas. The conclusion is that for simulations with strong (or convergent) shock waves the best model is the ThCM model, but for the majority of cases one of the quasi-conservative models should be employed.

Next, simulations of homogeneous decaying turbulence (HDT) in a periodic cube were used to examine in a detailed and quantitative manner the behaviour of state of the art high-resolution and high-order methods in implicit Large Eddy Simulation. Computations have been conducted at grid resolutions from 32^3 to 256^3 for seven different high-resolution methods ranging from second-order to ninth-order spatial accuracy.

The growth of the large scales, and dissipation of kinetic energy is captured well at resolutions greater than 32^3, or when using numerical methods of higher than third order accuracy. Velocity increment probability distribution functions (PDFs) match experimental results very well for MUSCL methods, whereas WENO methods have lower intermittency. All pressure PDFs are essentially Gaussian, indicating a partial decoupling of pressure and vorticity fields. The kinetic energy spectra and effective numerical filter show that all schemes are too dissipative at high wave number. Evaluating the numerical viscosity as a spectral eddy viscosity shows good qualitative agreement with theory, however if the effective cut-off wave number is chosen above $k_{max}/2$ then dissipation is higher than the theoretical solution. The fifth and higher order methods give results approximately equivalent to the lower order methods at double the grid resolution, making them computationally more efficient.

As a key conclusion of the study on homogeneous decaying turbulence was that the high wave number performance of the standard numerical schemes is rather poor, the source of this excess dissipation of turbulent kinetic energy was investigated. Firstly it is shown that the production of entropy exactly matches the irreversible change in kinetic energy of a compressible flow. Next, explicit formulae were derived for the rate of increase of entropy given arbitrary jumps in primitive variables at a cell interface. It was demonstrated that the inherent dissipation of the Godunov schemes is not proportional to the velocity jump cubed as is commonly assumed. The leading order dissipation rate of a Godunov method is proportional to the velocity jump squared multiplied by the speed of sound. The leading order dissipation rate associated with jumps in pressure, density and shear waves is detailed, however at low Mach numbers it is the dissipation due to the velocity jumps which dominates. All analytical results have been validated with simple numerical experiments and it is shown that the analysis applies to high order accurate methods in space and time. This means that dissipation of turbulent kinetic energy increases proportional to $1/M$, which is a significant restriction on accuracy of Godunov-type methods for shock-induced turbulent mixing.

As the leading order source of dissipation of kinetic energy is now identified, a simple modification of the extrapolation process was proposed to allow significantly improved resolution of low Mach perturbations for use in mixed compressible/incompressible flows. By scaling the velocity jump by Mach number, the dissipation rate is constant as the Mach number tends to zero, as opposed to the standard Godunov scheme where it becomes infinite. In addition, incompressible scaling of the pressure and density variations are recovered. The key feature of the numerical scheme is that the reconstruction is modified *locally*, hence the scheme can capture both shock waves and low Mach features in the same computational domain using the same formulation of the governing equations. The numerical modification adds negligible computational cost.

The modified limiting process was implemented in a fifth-order in space [107], third-order in time [173] finite volume Godunov method. Numerical tests demonstrate that the new scheme captures shocks well and significantly reduces high wave number dissipation in the case of homogeneous decaying turbulence and Richtmyer-Meshkov mixing. In the latter case the turbulent spectra match theoretical predictions excel-

lently.

As there is a lack of quantitative experimental data for compressible, shock-induced turbulent mixing, the method has been validated against a compressible cavity flow at Reynolds $860,000$ [59]. A comparison of the mean flow and Reynolds stresses at three different mesh resolutions demonstrates excellent convergence of the numerical results. There is a slight discrepancy in the location of the centre of the mixing layer over the cavity due to the simple initialisation method employed, and lack of a turbulent wall model. Comparing the results with conventional LES using an advanced selective mixed scale subgrid model [113] show that for mean flow properties the ILES results are slightly worse, however the LES results employ a turbulent wall model, and have adjusted the inlet boundary condition such that the mean velocity profile at the cavity matches the experimentally measured profile. LES results gained using the same inlet boundary conditions employed here are significantly worse. In comparing the sound pressure levels, the numerical simulations predict the fundamental frequencies to within 2% and amplitude to within 6dB at all grid levels. This is better than the agreement gained using LES with a selective mixed scale subgrid model.

The next test case involves the planar Richtmyer-Meshkov instability. Firstly, a single mode problem is investigated, using the new numerical method and the standard van Leer second-order method [187]. The converged results are compared to results using a semi-Lagrangian method [183], interface tracking [201], and two analytical theories [155, 201]. The converged growth rate for the Finite Volume and semi-Lagrangian methods are identical, and there is excellent agreement at early times with the analytical theory. At late times the analytical theory is not valid due to it's derivation based on a perturbation analysis. In addition, it is believed that the results gained using interface tracking were not fully converged at the given grid resolution. It is shown that the modified numerical method gives a converged mixing layer width at half the grid points in each direction over the van Leer scheme, and one quarter the grid points in each direction to capture the growth of the spike. This is a saving in computational time of sixteen and one hundred and twenty-eight times respectively. It is observed that the van Leer method suffers heavily from the increase of dissipation at low Mach as predicted from previous theoretical analysis in Chapter 5. However, it should be noted that at low grid resolutions (ten cells for a single mode), the modified numerical scheme predicts a growth more rapid than the converged growth, indicating that the new extrapolation method does not have sufficient dissipation at high wave numbers.

An important conclusion of the single mode study is that the non-linear theory of Zhang and Sohn [201] performs much better compared to the numerical results, indicating that this may be a better choice to use when developing analytical relationships for multimode simulations. Nearly all models based on the 'just saturated' mode, bubble growth and merger detailed in Section 2.3 use linear theory during the derivation.

Multimode Richtmyer-Meshkov instability has been simulated using two initial conditions. The first is a narrowband perturbation consisting only of high wavenumber modes. The purpose of this is to compute the growth rate of a mixing layer which expands only through mode coupling. The second initial condition is a broadband

frequency spectrum from long to short wavelengths. This was to test the growth rate of the resultant mixing layer when there is the combination of mode coupling, and linear/non-linear growth of large scale perturbations occurring simultaneously. To test grid convergence, each case was run at three different grid levels, each subsequent grid having twice the number of points in each direction. Three numerical methods were employed, the van Leer second-order extrapolation, Weighted Essentially Non-Oscillatory (WENO) ninth-order, and the new modified fifth-order method. The van Leer method was tested at moderate resolution, but the results were poor due to excessive numerical dissipation.

The results gained for the fifth order modified method confirmed that the growth exponent of the RM mixing layer is dependent on the initial conditions, being equal to 0.24 ± 0.015 for the mode coupling case, and 0.35 ± 0.01 for the broadband initial conditions. The narrowband perturbations are in good agreement with experimental results by Dimonte *et al* [48], and the general consensus for expansion of a turbulent slab ($\theta \approx 2/3-\mu$). This is almost identical to the previous results of Youngs [198] using a completely different numerical approach. However, the broadband results are lower than expected according to analytical models by Dimonte [46] and Youngs [198], the difference attributed to the relatively low ratio of maximum to minimum wavelength of the initial perturbation. The molecular mix fraction tends towards 0.8 at late time in good agreement with previous results [197, 42], and a good level of self-similarity of the volume fraction profiles is demonstrated throughout the duration of the simulation.

The total fluctuating turbulent kinetic energy in the narrowband case decays at a rate proportional to $t^{-1.25}$ for the longitudinal direction, in close agreement with that expected from homogeneous turbulence, but lower than that suggested by Llor [123] for a slab of decaying turbulence. The ratio of the longitudinal and lateral turbulent kinetic energies approaches a constant ≈ 1.5 at late times, again reinforcing that the layer is developing in an approximately self-similar manner. Dimensional estimates predict that the decay rate of total fluctuating kinetic energy is proportional to $t^{3\theta-2}$, leading to an estimate of $t^{-1.28}$ using the θ determined from the integral mixing width, in excellent agreement with direct measurements.

The decay of turbulent kinetic energy is significantly lower for the broadband initialisation, proportional to $t^{-1.05}$ in the longitudinal direction, which is to be expected as a large portion of the initial kinetic energy is in the low wavenumber region of the spectrum. The flow at the long wavelengths is largely irrotational, and thus does not dissipate as effectively as the fully developed turbulent slab in the narrowband simulation. Interestingly, although it is not expected that the mixing layer is fully developed, the empirical relation $dq_K/dt \propto q_k^{3/2}/W$ also gives a good estimate of the decay rate of turbulent kinetic energy based on the growth exponent of the integral mixing width.

In addition, two dimensional spectra have been computed in the centre of the mixing layer at several different times. Excellent grid convergences is seen, however at the lowest grid resolution ($90 \times 64 \times 64$) the modified numerical method is not dissipative enough. This is in agreement with results from the single mode simulations. There is an extensive power-law region in the spectra which is closer to the $k^{-3/2}$ spectra pro-

posed by Zhou [202], than the Kolmogorov spectrum, although the difference between the two power laws is not large enough to make a definitive statement. The WENO results match excellently at low wave numbers, however they are too dissipative at high wavenumber, as although they have a much higher formal order of accuracy, they suffer from the same increase of dissipation at low Mach discussed in Chapter 5.

Finally, the modified fifth-order method was compared to the standard fifth-order and second-order van Leer method in the simulation of the half-height shock tube experiment [83]. The half-height experiment is a rich physical problem with strong Kelvin-Helmholtz and Richtmyer-Meshkov instabilities, and mixing of two gases with different ratios of specific heats. The three methods were compared against qualitative experimental data, and it was shown that the new modified scheme gave improved agreement in terms of position of the SF_6 block, and position of the main flow features. In addition, there is a significant increase in fine scale features when using the modified scheme. There are slight discrepancies with the experimental results, the main being that there is a difference in the angle of the refracted shock wave which passes through the block of SF_6. The source of this error is in the modelling of the problem where it was assumed that the upper surface of the block is sharp, whereas in reality there would be a diffuse layer between the air and SF_6. In comparing the numerical schemes, the two fifth-order methods give turbulent kinetic energy levels comparable to the van Leer method at half the grid size in each direction. The time dependent behaviour of turbulent kinetic energy for the modified fifth-order method agrees very well with the standard method with double the number of grid points. This is a significant saving in computational time for equivalent results.

8.2 Summary of Contributions

This thesis has

- Proposed, implemented and validated comprehensively a simple reconstruction procedure which significantly improves the ability of Godunov methods to capture simultaneously both low Mach features and shock waves without modifying the formulation of the governing equations, at negligible computational expense
- Detailed a numerically validated theoretical analysis of the dissipation of kinetic energy in low Mach flows when using a Godunov-type numerical scheme.
- Investigated in a comprehensive and quantitative manner the ability of state of the art Finite Volume methods to represent homogeneous decaying turbulence
- Validation of the new extrapolation method against experimental results for a deep, open cavity at high Reynolds number $(860,000)$, additionally showing that an explicit subgrid model is not necessary when using this method

- Investigated the flow physics of RM single and multimode perturbations for perfect gases, confirming earlier results by Youngs [198] that the growth rate is strongly dependent on initial conditions. Demonstrated excellent grid convergence of the new method, allowing detailed discussion of the turbulent flow physics
- Gained excellent qualitative agreement with the shock tube mixing experiments of Holder and Barton [83] using the new methodology, and demonstrated that the new approach allows a significant saving in terms of computational time
- Assessed the ability of modern, state of the art multicomponent gas mixture models compared to classical approaches, demonstrating their relative strengths and weaknesses
- Demonstrated analytically the link between increase of entropy and dissipation of kinetic energy, and showing how this can be used to analyse the performance of numerical schemes at low Mach
- Showed analytically that the leading order increase in entropy in Godunov-type schemes is not due to the identification of shock waves in the solution of the Riemann problem at the cell interface
- Derived several new multicomponent approximate Riemann solvers based on the characteristics approach, and on the Roe method
- Showed theoretically that the Total Enthalpy Conservation of the Mixture model does not maintain pressure equilibrium at a contact discontinuity, contrary to the analysis presented by Wang *et al.* [191]

8.3 Future Research

8.3.1 Numerics

The research detailed in this thesis has opened up several areas for future work. The theoretical analysis of Godunov-type schemes can be extended to higher order schemes relatively easily, as the first order analysis will still apply at the cell interface. It is only necessary to take into consideration the variation of the kinetic energy and entropy within the cell itself due to the higher order reconstruction. This analysis could be coupled with formulating criteria for sufficient dissipation with regard to consistent convergence of the numerical scheme, as it has been demonstrated that the current implementation is not sufficiently dissipative at low grid resolutions. This is manifested through a relatively flat spectrum at high wavenumber.

A key difficulty is the extension of the theoretical analysis to look at Galilean invariance. This has been attempted using the linearised Riemann solver approximation

employed in Chapter 3, however, for regimes where the dissipation rate is not dominated by the dissipation proportional to the speed of sound, the linearised solver is a poor approximation of the exact solution (or more accurate approximate solvers, e.g. HLLC).

Experiments with different forms of the low Mach modification to the base extrapolation scheme yield surprisingly similar result. This implies that the dissipation due to velocity jumps is no longer the prime source of dissipation, as was the aim of the modification. However, this means that dissipation due to pressure and density jumps now contribute significantly to the total dissipation. This does not fit with Kolmogorov's analysis of the dissipation rate of turbulence which only depends on the velocity differences.

A key addition to the current work would be to conduct a stability analysis of the modified numerical scheme. Numerical tests have shown a stability envelope similar to that of the original numerical scheme, however the modified method is slightly less stable. A formal stability analysis should bring out this difference.

A major restriction to the efficient simulation of near-incompressible flows is the CFL condition. One method used by semi-Lagrangian schemes is to split the time step into two components, one related to the signals travelling at the speed of sound, the other to the convective quantities. By splitting the flux computation in this manner a significant time saving can be made, as several relatively fast computations of flux due to the $u+a$ and $u-a$ characteristics can be made for each u characteristic. A potentially worthwhile direction for research would be an equivalent form of this for Godunov-type methods, potentially employing a flux splitting approach to separate the fluxes along the $u+a$ and $u-a$ characteristics from those along the u characteristic.

Finally, in most of the simulations the interface perturbation was initialised at only second-order accuracy in space. It is possible that this is a serious issue at low grid resolution (i.e. 10-20 cells per wavelength) when using a higher order method. This should be investigated for single mode, and then multimode configurations.

8.3.2 Flow Physics

The current numerical method is extremely well suited to the simulation of flows with both compressible and incompressible features. It is intended that the simulation of multimode RM instability should be used to verify current theory on the growth of the mixing layer, and in particular validate the assumptions inherent in each of the models for the growth rate of the RM layer. This has been highlighted in the literature survey where it was shown that several of the models are only applicable for a specific set of initial perturbations.

In the determination of growth of a turbulent slab, it would be interesting to investigate in more depth the model parameters The most important parameter would be the determination of the constant of proportionality in the relation $dq_K/dt \propto q_k^{3/2}/W$ for narrowband initial conditions, which plays a key part in determining θ.

In the case of broadband initial perturbations, the logical direction for future work is to increase the ratio of maximum to minimum wavelength. Simulations with both constant and $1/k^2$ power spectra could be used to examine the 'just saturated' mode analysis of Inogamov [89], Dimonte [46] and Youngs [198] respectively. On the theoretical side, it is possible that these theories could be improved by substituting the Zhang and Sohn non-linear single mode growth rate [201] for the linear Richtmyer equation in all derivations. This is based on the observation in Section 7.2 that the non-linear theory is a much better match to single mode growth rate than Richtmyer's analysis.

Finally, obvious further parameters to investigate are the influence of Atwood number, and the effect of incident shock strength on the growth exponent.

The test cases employed in this thesis have evolved considerably from the first iterations, however there are several improvements which can be made. Firstly, future simulations of cavity flows should include a turbulent wall model to verify the conjecture that the remaining discrepancy is due to poor representation of the boundary layer at the upstream corner of the cavity. For the simulation of the half-height shock tube experiment it is necessary to include a diffuse upper surface to gain the correct angle of the diffracted shock wave.

A key issue which spans both numerics and flow physics is the determination of the stability of structures within the developing flow. The current implementation allows rapid growth of secondary instabilities (i.e. Kelvin-Helmholtz instabilities along the RM bubble and spike, or at non-diffuse contact surfaces), however it is not clear whether the seed for these perturbations is physical. The receptivity of numerical schemes to round-off error perturbations is an important area to clarify.

Bibliography

[1] R. Abgrall. Generalisation of the Roe scheme for the computation of a mixture of perfect gases. *Rech. Aerosp. 6*, 6:31–44, 1988.

[2] R. Abgrall. How to prevent pressure oscillations in multi-component flow calculations: A quasi conservative approach. *J. Comput. Phys.*, 125:150–160, 1996.

[3] R. Abgrall and S. Karni. Computations of compressible multifluids. *J. Comput. Phys.*, 169:594–623, 2000.

[4] G. Allaire, S. Clerc, and S. Kokh. A five-equation model for the simulation of interfaces between compressible fluids. *J. Comput. Phys.*, 181:577–616, 2002.

[5] A.S. Almgren, J.B. Bell, C.A. Rendleman, and M. Zingale. Low Mach number modeling of type Ia supernovae. I Hydrodynamics. *Astrophys. J.*, 637:922–936, 2006.

[6] U. Alon, J. Hecht, D. Ofer, and D. Shvarts. Power laws and similarity of Rayleigh-Taylor and Richtmyer-Meshkov mixing fronts at all density ratios. *Phys. Rev. Lett.*, 74(4):534–537, 1995.

[7] P. Amendt, J.D. Colvin, R.E. Tipton, D.E. Hinkel, M.J. Edwards, O.L. Landen, J.D. Ramshaw, L.J. Suter, W.S. Varnum, and R.G. Watt. Indirect-drive noncryogenic double-shell ignition targets for the National Ignition Facility: Design and analysis. *Phys. Plasmas*, 9(5):2221–2233, 2002.

[8] J.R. Anderson. *Fundamentals of Aerodynamics*. McGraw Hill, 2001.

[9] R. Anderson and C. Meneveau. Effects of the similarity model in finite-difference LES of isotropic turbulence using a Lagrangian dynamic mixed model. *Flow Turbul. Combust.*, 62:201–225, 1999.

[10] R.A. Antonia and P. Burattini. Approach to the 4/5 law in homogeneous isotropic turbulence. *J. Fluid Mech.*, 550:175–184, 2006.

[11] D.S. Balsara and C.-W. Shu. Monotonicity preserving weighted essentially non-oscillatory schemes with increasingly high order of accuracy. *J. Comput. Phys.*, 160:405–452, 2000.

[12] G.I. Barenblatt, G. Looss, and D.D. Joseph. *Nonlinear Dynamics and Turbulence*. Pitman Publishing, 1983.

[13] T.J. Barth. Numerical methods for gasdynamic systems on unstructured meshes. In *Introduction to Recent Developments in Theory and Numerics for Conservation Laws*. Springer-Verlag, 1999.

[14] G.K. Batchelor. *The theory of homogeneous turbulence*. Cambridge University Press, 1970.

[15] G.K. Batchelor, I. Proudman, and W.H. Reid. The large scale structure of homogeneous turbulence. *Phil. Trans. Roy. Soc. London A*, 248:369–406, 1956.

[16] K. Bates, N. Nikiforakis, and D. Holder. Richtmyer-Meshkov instability induced by the interaction of a shock wave with a block of SF_6. *Phys. Fluids*, 19:036101, 2007.

[17] A. Bejan. *Entropy Generation Minimization: The Method of Thermodynamic Optimization of Finite-Time Systems and Finite-Time Processes*. CRC Press, 1996.

[18] D.J. Benson. Computational methods in Lagrangian and Eulerian hydrocodes. *Comput. Meth. Appl. Mech. Eng.*, pages 235–394, 1992.

[19] H.A. Bethe. On the theory of shock waves for an arbitrary equation of state. Technical report, Office of Scientific Research and Development, May 1942.

[20] P. Birken and A. Meister. Stability of preconditioned finite volume schemes at low Mach numbers. *BIT*, 45:463–480, 2005.

[21] G. Birkhoff. Fourier synthesis of homogeneous turbulence. *Commun. Pure Appl. Math.*, 7:19–44, 1954.

[22] G.A. Blaisdell, N.N. Mansour, and W.C. Reynolds. Compressibility effects on the growth and structure of homogeneous turbulent shear flow. *J. Fluid Mech.*, 256:443–485, 1993.

[23] J.M. Blondin, R.A. Chevalier, and D.M. Frierson. Pulsar wind nebulae in evolved supernova remnants. *Astrophys. J.*, 563:806–815, 2001.

[24] J.P. Boris, F.F. Grinstein, E.S. Oran, and R.L. Kolbe. New insights into large eddy simulation. *Fluid. Dyn. Res.*, 10:199–228, 1992.

[25] M.E. Brachet. Direct simulation of three-dimensional turbulence in the Taylor-Green vortex. *Fluid. Dyn. Res.*, 8:1–8, 1991.

[26] M. Brouillette. The Richtmyer-Meshkov instability. *Annu. Rev. Fluid Mech.*, 34:445–468, 2002.

[27] D. Carati, S. Ghosal, and P. Moin. On the representation of backscatter in dynamic localization models. *Phys. Fluids*, 7(3):606–616, 1995.

[28] D. Carati, G.S. Winckelmans, and H. Jeanmart. Exact expansions for filtered-scales modelling with a wide class of LES filters. In *Direct and Large Eddy Simulation III*, pages 213–224. Kluwer, 1999.

[29] S. Cerutti and C. Meneveau. Statistics of filtered velocity in grid and wake turbulence. *Phys. Fluids*, 12(5):1143–1165, 2000.

[30] P.R. Chapman and J.W. Jacobs. Experiments on the three-dimensional incompressible Richtmyer-Meshkov instability. *Phys. Fluids*, 18:074101–, 2006.

[31] D. Chargy, R. Abgrall, L. Fezoui, and B. Larrouturou. Comparisons of several upwind schemes for multi-component one-dimensional inviscid flows. *INRIA Rapports de Recherche No 1253*, 1990.

[32] S. Chen, G.D. Doolen, R.H. Kraichnan, and Z-S. She. On statistical correlations between velocity increments and locally averaged dissipation in homogeneous turbulence. *Phys. Fluids A*, 5(2):458–463, 1992.

[33] J.P. Chollet. Two-point closures as a subgrid-scale modelling tool for large eddy simulations. In *Turbulent Shear Flows IV*. Springer-Verlag, 1984.

[34] R.B. Christensen. Godunov methods on a staggered mesh - an improved artificial viscosity. Technical report, Lawrence Livermore National Laboratory, 1990.

[35] S.G. Chumakov and C.J. Rutland. Dynamic structure subgrid-scale models for large eddy simulation. *Int. J. Numer. Meth. Fl.*, 47:911–923, 2005.

[36] M. Ciardi, P. Sagaut, M. Klein, and W.N. Dawes. A dynamic finite volume scheme for large-eddy simulation on unstructured grids. *J. Comput. Phys.*, 210:632–655, 2005.

[37] T.T. Clark and Y. Zhou. Growth rate exponents of Richtmyer-Meshkov mixing layers. *J. Appl. Mech.*, 73:461–268, 2006.

[38] J.F. Clarke, S. Karni, J.J. Quirk, P.L. Roe, L.G. Simmonds, and E.F. Toro. Numerical computation of two dimensional unsteady detonation waves in high-energy solids. *J. Comput. Phys.*, 106:215–233, 1993.

[39] R.H. Cohen, W.P. Dannevik, A.M. Dimits, D.E. Eliason, Y. Mirin, A.A.and Zhou, D.H. Porter, and P.R. Woodward. Three-dimensional simulation of a Richtmyer-Meshkov instability with a two-scale initial perturbation. *Phys. Fluids*, 14(10):3692–3709, 2002.

[40] B.D. Collins and J.W. Jacobs. PLIF flow visualization and measurements of the Richtmyer-Meshkov instability of an air/SF_6 interface. *J. Fluid. Mech.*, 464:113–136, 2002.

[41] G. Comte-Bellot and S. Corrsin. The use of a contraction to improve the isotropy of grid generated turbulence. *J. Fluid Mech.*, 25:657–682, 1966.

[42] A.W. Cook and Y. Zhou. Energy transfer in Rayleigh-Taylor instability. *Phys. Rev. E*, 66:026312, 2002.

[43] R. Courant and D. Hilbert. *Methoden der mathematischen Physik*. Springer, 1968.

[44] P.A. Davidson. *Turbulence - An Introduction for Scientists and Engineers*. Oxford University Press, 2004.

[45] G. Dimonte. Spanwise homogeneous buoyancy-drag model for Rayleigh-Taylor mixing and experimental evaluation. *Phys. Plasmas*, 7(6):2255–2269, 2000.

[46] G. Dimonte, C.E. Frerking, and M. Schneider. Richtmyer-Meshkov instability in the turbulent regime. *Phys. Rev. Lett.*, 74:4855–4858, 1995.

[47] G. Dimonte and M. Schneider. Turbulent Richtmyer-Meshkov instability experiments with strong radiatively driven shocks. *Phys. Plasmas*, 4(12):4347–4357, 1997.

[48] G. Dimonte and M. Schneider. Density ratio dependence of Rayleigh-Taylor mixing for sustained and impulsive acceleration histories. *Phys. Fluids*, 12:304–321, 2000.

[49] J.A. Domaradzki, Z. Xiao, and P.K. Smolarkiewicz. Effective eddy viscosities in implicit large eddy simulations of turbulent flows. *Phys. Fluids*, 15(12):3890–3893, 2003.

[50] P.G. Drazin and W.H. Reid. *Hydrodynamic Stability*. Cambridge University Press, 2004.

[51] D. Drikakis. Advances in turbulent flow computations using high-resolution methods. *Prog. Aerosp. Sci.*, 39:405–424, 2003.

[52] D. Drikakis, C. Fureby, F. Grinstein, M. Hahn, and D. Youngs. MILES of transition to turbulence in the Taylor-Green vortex system. In *ERCOFTAC Workshop on Direct and Large Eddy Simulation-6*, page 133, 2006.

[53] D. Drikakis and W. Rider. *High-Resolution Methods for Incompressible and Low-Speed Flows*. Springer Verlag, 2004.

[54] D. Drikakis and S. Tsangaris. An implicit characteristic-flux-averaging method for the Euler equations for real gases. *Int. J. Numer. Fl.*, 12:711–726, 1991.

[55] A. Eberle. Characteristic flux averaging approach to the solution of Euler's equations. Technical report, VKI Lecture Series, 1987.

[56] G. Erlebacher, M.Y. Hussaini, H.O. Kreiss, and S. Sarkar. The analysis and simulation of compressible turbulence. *Theor. Comp. Fluid Dyn.*, 2:73–95, 1990.

[57] ESA/NASA. http://www.esa.int/esaSC/SEMVCHVLWFE_index_0.html, Aug. 2007.

[58] B. Fishbine. Code validation experiments. *Los Alamos Research Quaterly*, Fall 2002.

[59] N. Forestier, L. Jacquin, and P. Geffroy. The mixing layer over a deep cavity at high-subsonic speed. *J. Fluid Mech.*, 475:101–144, 2003.

[60] C. Fureby and F.F. Grinstein. Large eddy simulation of high-Reynolds-number free and wall-bounded flows. *J. Comput. Phys.*, 181:68–97, 2002.

[61] C. Fureby, F. Tabor, H.G. Weller, and A.D. Gosman. A comparative study of subgrid scale models in homogeneous isotropic turbulence. *Phys. Fluids*, 9(5):1416–1429, 1997.

[62] E. Garnier, M. Mossi, P. Sagaut, P. Comte, and M. Deville. On the use of shock-capturing schemes for large-eddy simulation. *J. Comput. Phys.*, 153:273–311, 1999.

[63] S. Gauthier and M. Bonnet. A $k - \epsilon$ model for turbulent mixing in shock-tube flows induced by Rayleigh-Taylor instability. *Phys. Fluids A*, 2(9):1685–1694, 1990.

[64] B.J. Geurts. *Elements of Direct and Large-Eddy Simulation*. R.T. Edwards, 2003.

[65] S.K. Godunov. A finite-difference method for the computation of discontinuous solutions of the equations of fluid dynamics. *Mat. Sb.*, 47:271–295, 1959.

[66] V.N. Goncharov. Analytical model of nonlinear, single-mode, classical Rayleigh Taylor instability at arbitrary Atwood numbers. *Phys. Rev. Lett.*, 88(13):134502, 2002.

[67] R.E. Gordnier and M.R. Visbal. Compact different scheme applied to simulation of low-sweep delta wing flow. *AIAA J.*, 43(8):1744–1752, 2005.

[68] T. Gotoh, D. Fukayama, and T. Nakano. Velocity field statistics in homogeneous steady turbulence obtained using a high resolution direct numerical simulation. *Phys. Fluids*, 14(3):1065–1081, 2002.

[69] S. Gottlieb and C-W Shu. Total Variation Diminishing Runge-Kutta schemes. *Math. Comput.*, 67(221):73–85, 1998.

[70] F.F. Grinstein and C. Fureby. Recent progress on MILES for high Reynolds number flows. *J. Fluid Eng.- T. ASME*, 848:848–861, 2002.

[71] F.F. Grinstein, L.G. Margolin, and W.J. Rider, editors. *Implicit Large Eddy Simulation: Computing Turbulent Fluid Dynamics*. Cambridge University Press, 2007.

[72] H. Guillard. Recent developments in the computation of compressible low Mach number flows. *Flow Turbul Combust*, 76:363–369, 2006.

[73] H. Guillard and A. Murrone. On the behaviour of upwind schemes in the low Mach number limit:II. Godunov type schemes. *Comput. Fluids*, 33:655–675, 2004.

[74] H. Guillard and C. Viozat. On the behaviour of upwind schemes in the low Mach number limit. *Comput. Fluids*, 28:63–86, 1999.

[75] M. Hahn and D. Drikakis. Large eddy simulation of compressible turbulence using high-resolution methods. *Int. J. Numer. Meth. Fl.*, 49:971–977, 2005.

[76] A. Harten, B. Engquist, S. Osher, and S.R. Chakravarthy. Uniformly high order accurate essentially non-oscillatory schemes, iii. *J. Comput. Phys.*, 71(2):231–303, 1987.

[77] A. Harten and J.M. Hyman. Self adjusting grid methods for one-dimensional hyperbolic conservation laws. *J. Comput. Phys.*, 50:235–269, 1983.

[78] N.E.L. Haughen and A. Brandenburg. Inertial range scaling in numerical turbulence with hyperviscosity. *Phys. Rev. E*, 70:026405, 2004.

[79] J. Hecht, U. Alon, and D. Shvarts. Potential flow models of Rayleigh-Taylor and Richtmyer-Meshkov bubble fronts. *Phys. Fluids*, 12:4019–4029, 1994.

[80] J.R. Herring and R.M. Kerr. Development of enstrophy and spectra in numerical turbulence. *Phys. Fluids A*, 5(11):2792–2798, 1993.

[81] S. Hickel, N.A. Adams, and J.A. Domaradzki. An adaptive local deconvolution method for implict LES. *J. Comput. Phys.*, 213:413–436, 2006.

[82] J.O. Hinze. *Turbulence*. McGraw-Hill, 2 edition, 1975.

[83] D.A. Holder and C.J. Barton. Shock tube Richtmyer-Meshkov experiments: inverse chevron and half height. In *Proceedings of the 9th IWPCTM*, 2004.

[84] R.L. Holmes, G. Dimonte, B. Fryxell, M.L. Gittings, J.W. Grove, M.S. Schneider, D.H. Sharp, A.L. Velikovich, R.P. Weaver, and Q. Zhang. Richtmyer-Meshkov instability growth: experiment, simulation and theory. *J. Fluid Mech.*, 389:55–79, 1999.

[85] T.Y. Hou and P.G. Le Floch. Why non-conservative schemes converge to wrong solutions - error analysis. *Math. Comput.*, 62:497–530, 1994.

[86] M-J Huang and A. Leonard. Power-law decay of homogeneous turbulence at low Reynolds numbers. *Phys. Fluids*, 6(11):3765–3775, 1994.

[87] T.J.R. Hughes, L. Mazzei, and A.A. Oberai. The multiscale formation of large eddy simulation: Decay of homogeneous isotropic turbulence. *Phys. Fluids*, 13(2):505–512, 2001.

[88] H. Hugonoit. On the propagation of motion in bodies and in perfect gases in particular - II. *Journal de l'Ecole Polytechnique*, 58:1–125, 1889.

[89] N. Inogamov. Richtmyer-meshkov turbulence. In *IWPCTM 10*, 2006.

[90] T. Ishida, P.A. Davidson, and Y. Kaneda. On the decay of isotropic turbulence. *J. Fluid Mech.*, 564:455–475, 2006.

[91] J.W. Jacobs, D.G. Jenkins, D.L. Klein, and R.F. Benjamin. Nonlinear growth of the shock-accelerated instability of a thin fluid layer. *J. Fluid Mech.*, 295:23–42, 1995.

[92] A. Jameson. Time dependent calculations using multigrid, with applications to unsteady flows past airfoils and wings. *AIAA 91-1596*, 1991.

[93] P. Jenny, B. Muller, and H. Thomann. Correction of conservative Euler solvers for gas mixtures. *J. Comput. Phys.*, 132:91–107, 1997.

[94] J. Jeong and F. Hussain. On the identification of a vortex. *J. Fluid. Mech.*, 285:69–94, 1995.

[95] G.-S. Jiang and C.-W. Shu. Efficient implementation of weighted ENO schemes. *J. Comput. Phys.*, 126:202–228, 1996.

[96] J. Jimenez, A.A. Wray, P.G. Saffman, and R.S. Rogallo. The structure of intense vorticity in isotropic turbulence. *J. Fluid Mech.*, 255:65–90, 1993.

[97] E. Johnsen and T. Colonius. Implementation of WENO schemes in compressible multicomponent flow problems. *J. Comput. Phys.*, 219(2):715–732, 2006.

[98] J.N. Johnson and R. Cheret, editors. *Classic Papers in Shock Compression Science*. Springer-Verlag, 1998.

[99] Y. Kaneda, T. Ishihara, M. Yokokawa, K. Itakura, and A. Uno. Energy dissipation rate and energy spectrum in high resolution direct numerical simulations of turbulence in a periodic box. *Phys. Fluids*, 15(2):L21–L24, 2003.

[100] H.S. Kang, S. Chester, and C. Meneveau. Decaying turbulence in an active-grid-generated flow and comparisons with large-eddy simulation. *J. Fluid Mech.*, 480:129–160, 2003.

[101] T. von Karman and L. Howarth. On the statistical theory of isotropic turbulence. *Proc. Roy. Soc. London A*, 164:192–215, 1938.

[102] S. Karni. Viscous shock profiles and primitive formulations. *SIAM J. Num. Anal.*, 29:1592–1609, 1992.

[103] S. Karni. Multicomponent flow calculations by a consistent primitive algorithm. *J. Comput. Phys.*, 112:31–43, 1994.

[104] S. Karni. Hybrid multifluid algorithms. *SIAM J.Sci.Comp.*, 17:1019–1039, 1996.

[105] R.M. Kelvin. Hydrokinetic solutions and observations. *Phil. Mag.*, 42:362–377, 1871.

[106] R.M. Kerr. Higher order derivative correlations and the alignment of small scale structures in isotropic turbulence. *J. Fluid Mech.*, 153:31–58, 1985.

[107] K.H. Kim and C. Kim. Accurate, efficient and monotonic numerical methods for multi-dimensional compressible flows part II: Multi-dimensional limiting process. *J. Comput. Phys.*, 208:570–615, 2005.

[108] S. Klainerman and A. Madja. Compressible and incompressible fluids. *Comm. Pure Appl. Math.*, 33:399–440, 1982.

[109] R. Klein. Semi-implicit extension of a Godunov-type scheme based on low Mach number asymptotics I:One-dimensional flow. *J. Comput. Phys.*, 121:213–237, 1995.

[110] A.N. Kolmogorov. The local structure of turbulence in an incompressible fluid at very high Reynolds numbers. *Dokl. Akad. Nauk. SSSR*, 30:299, 1941.

[111] A.N. Kolmogorov. A refinement of previous hypotheses concerning the local structure of turbulence in a viscous incompressible fluid at high Reynolds number. *J. Fluid Mech.*, 13:82–85, 1962.

[112] L.S.G. Kovasznay. Turbulence in supersonic flow. *J. Aero. Sci.*, 1953.

[113] L. Larcheveque, P. Sagaut, I. Mary, and O. Labbe. Large-eddy simulation of a compressible flow past a deep cavity. *Phys. Fluids*, 15(1):193–209, 2003.

[114] B. Larrouturou. How to preserve the mass fractions positivity when computing compressible multi-component flows. *INRIA Rapports de Recherche No. 1080*, 1989.

[115] M. Latini, O. Schilling, and W.S. Don. Effects of WENO flux reconstruction order and spatial resolutoin on reshocked two-dimensional Richtmyer-Meshkov instability. *J. Comput. Phys.*, 221:805–836, 2007.

[116] D. Layzer. On the instability of superposed fluids in a gravitational field. *Astrophys. J.*, 122(1):1–12, 1955.

[117] S-H Lee. Convergence characteristics of preconditioned Euler equations. *J. Comput. Phys.*, 208:266–288, 2005.

[118] E. Lenormand, P. Sagaut, L.T. Phuoc, and P. Comte. Subgrid-scale models for large-eddy simulation of compressible wall bounded flows. *AIAA J.*, 38(8):1340–1350, 2000.

[119] M. Lesieur. *Turbulence in Fluids*. Kluwer Academic Publishers, 1987.

[120] M. Lesieur and O. Metais. New trends in large-eddy simulations of turbulence. *Annu. Rev. Fluid Mech.*, 28:45–82, 1996.

[121] X.L. Li and Q. Zhang. A comparative numerical study of the Richtmyer-Meshkov instability with nonlinear analysis in two and three dimensions. *Phys. Fluids*, 9(10):3069–3077, 1997.

[122] R. Liska and B. Wendroff. Comparison of several difference schemes on 1D and 2D test problems for the Euler equations. *SIAM J. Sci. Comput.*, 25(3):995–1017, 2003.

[123] A. Llor. Invariants of free turbulent decay. *submitted to Nat, Phys.*, 2006.

[124] L.G. Loitsyanskii. *Mechanics of Liquids and Gases*. Pergamon Press, 1966.

[125] G. Mackley. http://www.emergency.co.nz/archive/etna07.html, Aug. 2007.

[126] L.G. Margolin and W.J. Rider. A rationale for implicit turbulence modelling. *Int. J. Numer. Meth. Fl.*, 39:821–841, 2002.

[127] L.G. Margolin and W.J. Rider. The design and construction of implicit LES modes. *Int. J. Numer. Meth. Fl.*, 47:1173–1179, 2005.

[128] L.G. Margolin, W.J. Rider, and F.F. Grinstein. Modeling turbulent flow with implicit LES. *J. Turbul.*, 7(15):1–27, 2006.

[129] L.G. Margolin, P.K. Smolarkiewicz, and Z. Sorbjan. Large-eddy simulations of convective boundary layers using nonoscillatory differencing. *Physica D*, 133:390–397, 1999.

[130] L.G. Margolin, P.K. Smolarkiewicz, and A.A. Wyszogrodzki. Implicit turbulence modelling for high Reynolds number flows. *J. Fluids Eng.*, 124:862–867, 2002.

[131] R. Menikoff. Numerical anomalies mimicking physical effects. Technical report, Los Alamos, 1995.

[132] R. Menikoff and B.J. Plohr. The Riemann problem for fluid flow of real materials. *Rev Mod Phys*, 61(1):75–130, 1989.

[133] M.L. Merriam. Smoothing and the second law. *Comput Method Appl M*, 64:177–193, 1987.

[134] E.E. Meshkov. Instability of the interface of two gases accelerated by a shock wave. *Fluid Dyn.*, 43(5):101–104, 1969.

[135] O. Metais and M. Lesieur. Spectral large-eddy simulation of isotropic and stably stratified turbulence. *J. Fluid Mech.*, 239:157–194, 1992.

[136] K.O. Mikaelian. Turbulent mixing generated by Rayleigh-Taylor and Richtmyer-Meshkov instabilities. *Physica D*, 36:343–357, 1989.

[137] G.H. Miller and E.G. Puckett. A high-order Godunov method for multiple condensed phases. *J. Comput. Phys.*, 128:134–164, 1996.

[138] M.S. Mohammed and J.C. LaRue. The decay power law in grid-generated turbulence. *J. Fluid Mech.*, 219:195–215, 1990.

[139] F. Moisy, P. Tabeling, and H. Willaime. Kolmogorov equation in a fully developed turbulence experiment. *Phys. Rev. Lett.*, 82(20):3994–3997, 1999.

[140] Z. Mydlarski, L.and Warhaft. On the onset of high-Reynolds grid-generated wind tunnel turbulence. *J. Fluid Mech.*, 320:331–368, 1996.

[141] NASA/JPL-Caltech/STScI/CXC/SAO. http://www.nasa.gov/multimedia/imagegallery/image_feature_532.html, Aug. 2007.

[142] G.F. Naterer. *Heat Transfer in Single and Multiphase Systems*. CRC Press, 2003.

[143] W.F. Noh. Errors for calculations of strong shocks using and artificial viscosity and an artificial heat flux. *J. Comput. Phys.*, 72:78–120, 1987.

[144] M. Oberlack. On the decay exponent of isotropic turbulence. *Proc. Appl. Math. Mech.*, 1:294–297, 2002.

[145] D. Oron, L. Arazi, D. Kartoon, A. Rikanati, U. Alon, and D. Shvarts. Dimensionality dependence of the Rayleigh-Taylor and Richtmyer-Meshkov instability late time scaling laws. *Phys. Plasmas*, 8(6):2883–2889, 2001.

[146] S.A. Orzag and G.S. Patterson. Numerical simulation of three-dimensional homogeneous isotropic turbulence. *Phys. Rev. Lett.*, 28:76–79, 1972.

[147] R. Panda, V. Sonnad, and E. Clementi. Turbulence in a randomly stirred fluid. *Phys. Fluids A*, 1(6):1045–1053, 1989.

[148] S.B. Pope. *Turbulent Flows*. Cambridge University Press, 2000.

[149] D.H. Porter, P.R. Woodward, and A. Pouquet. Inertial range structures in decaying compressible turbulent flows. *Phys. Fluids*, 10(1):237–245, 1998.

[150] J.K. Prasad, A. Rasheed, S. Kumar, and B. Sturtevant. The late-time development of the Richtmyer-Meshkov instability. *Phys. Fluids*, 12(8):2108–2115, 2000.

[151] WH. Press, S.A. Teukolsky, W.T. Vetterling, and B.P. Flannery. *Numerical Recipes in Fortran 90: the art of scientific computing*. Cambridge University Press, 1996.

[152] I. Proudman and W.H. Reid. On the decay of a normally distributed and homogeneous turbulent velocity field. *Philos. Trans. R. Soc. London*, 247A:163–189, 1954.

[153] J.J. Quirk and S. Karni. On the dynamics of a shock-bubble interaction. *NASA ICASE Report No. 94-75*, 1994.

[154] J.D. Ramshaw. Simple model for linear and nonlinear mixing at unstable fluid interfaces with variable acceleration. *Phys. Rev. E*, 58(5):5834–5840, 1998.

[155] R.D. Richtmyer. Taylor instability in shock acceleration of compressible fluids. *Comm. Pure Appl. Math.*, 13:297–319, 1960.

[156] P.M. Rightley, P. Vorobieff, R. Martin, and R.F. Benjamin. Experimental observations of the mixing transition in a shock accelerated gas curtain. *Phys. Fluids*, 11(1):186–200, 1999.

[157] J.E. Rossiter. Wind-tunnel experiments on the flow over rectangular cavities at subsonic and transonic speeds. Technical report, Aero. Res. Counc. R & M, No. 3438, 1964.

[158] S.G. Saddoughi and S.V. Veeravalli. Local isotropy in turbulent boundary layers at high Reynolds number. *J. Fluid Mech.*, 268:333–372, 1994.

[159] P. Sagaut. *Large Eddy Simulation for Incompressible Flows*. Springer Verlag, 2001.

[160] R. Samtaney, D.I. Pullin, and B. Kosovic. Direct numerical simulation of decaying compressible turbulence and shocklet statistics. *Phys. Fluids*, 13(5):1415–1430, 2001.

[161] J. Sesterhenn, B. Muller, and H. Thomann. On the cancellation problem in calculating compressible low Mach number flows. *J. Comput. Phys.*, 151:597–615, 1999.

[162] B. Shannon. http://www.siskiyous.edu/shasta/env/clouds/, Aug. 2007.

[163] J. Shi, Y-T Zhang, and C-W Shu. Resolution of high order WENO schemes for complicated flow structures. *J. Comput. Phys.*, 186:690–696, 2003.

[164] C.-W. Shu. Total-variation-diminishing time discretizations. *SIAM J. Sci. Stat. Comp.*, 9:1073–1084, 1988.

[165] C.-W. Shu and S. Osher. Efficient implementation of essentially non-oscillating shock-capturing schemes. *J. Comput. Phys.*, 77:439–471, 1988.

[166] C.-W. Shu and S. Osher. Efficient implementation of essentially non-oscillating shock-capturing schemes II. *J. Comput. Phys.*, 83:32–78, 1989.

[167] K.M. Shyue. An efficient shock-capturing algorithm for compressible multi-component problems. *J. Comput. Phys.*, 142:208–242, 1998.

[168] A. Simone, G.N. Coleman, and C. Cambon. The effect of compressibility on turbulent shear flow: a rapid distortion theory and direct numerical simulation study. *J. Fluid Mech.*, 330:307–338, 1997.

[169] L. Skrbek and S.R. Stalp. On the decay of homogeneous isotropic turbulence. *Phys. Fluids*, 12(8):1997–2019, 2000.

[170] P.K. Smolarkiewicz and L.G. Margolin. MPDATA: a finite difference solver for geophysical flows. *J. Comput. Phys.*, 140(2):459–480, 1998.

[171] G.A Sod. A survey of several finite difference methods for systems of nonlinear hyperbolic conservation laws. *J. Comput. Phys.*, 27:1–31, 1997.

[172] S-I Sohn. Simple potential-flow model of Rayleigh-Taylor and Richtmyer-Meshkov instabilities for all density ratios. *Phys. Rev. E*, 67:026301, 2003.

[173] R.J. Spiteri and S.J. Ruuth. A class of optimal high-order strong-stability preserving time discretization methods. *SIAM J. Sci. Comput.*, 40(2):469–491, 2002.

[174] K.R. Sreenivasan. On the scaling of the turbulence energy dissipation rate. *Phys. Fluids*, 27(5):1048–1051, 1984.

[175] K.R. Sreenivasan. On the universality of the Kolmogorov constant. *Phys. Fluids*, 7(11):2778–2784, 1995.

[176] K.R. Sreenivasan and R.A. Antonia. The phenomenology of small-scale turbulence. *Annu. Rev. Fluid Mech.*, 29:435–472, 1997.

[177] G.I. Taylor. Statistical theory of turbulence. *Proc. Roy. Soc. A*, 151:421–478, 1935.

[178] H. Tennekes and J.L. Lumley. *A First Course in Turbulence*. MIT Press, 1972.

[179] M. Terracol and P. Sagaut. A multilevel-based dynamic approach for subgrid-scale modeling in large-eddy simulation. *Phys. Fluids*, 15(12):3671–3682, 2003.

[180] B. Thornber and D. Drikakis. Large-eddy simulation of multi-component compressible turbulent flows using high resolution methods. *accepted, Comput. Fluids*, 2007.

[181] B. Thornber and D. Drikakis. Numerical dissipation of upwind schemes in low Mach flow. *Int. J. Numer. Meth. Fluids*, 2007.

[182] B. Thornber, A. Mosedale, and D. Drikakis. On the Implicit Large Eddy Simulation of homogeneous decaying turbulence. *J. Comput. Phys.*, 226:1902–1929, 2007.

[183] B. Thornber, D. Youngs, and D. Drikakis. High resolution methods for planar 3D Richtmyer-Meshkov instabilities. In *IWPCTM 10*, 2006.

[184] E.F. Toro. *Riemann Solvers and Numerical Methods for Fluid Dynamics*. Springer-Verlag, 1997.

[185] E. Turkel, A. Fiterman, and B. van Leer. *Preconditioning and the limit of the compressible to the incompressible flow equations for finite difference schemes*. John Wiley and Sons, 1994.

[186] M. van Dyke, editor. *An Album of Fluid Motion*. Parabolic Press, 1982.

[187] B. van Leer. Towards the ultimate conservative difference scheme.IV. A new approach to numerical convection. *J. Comput. Phys.*, 23:276–299, 1977.

[188] A. Vincent and M. Meneguzzi. The spatial structure and statistical properties of homogeneous turbulence. *J. Fluid Mech.*, 225:1–20, 1991.

[189] G. Volpe. Performance of compressible flow codes at low Mach number. *AIAA J.*, 31:49–56, 1993.

[190] L. Wang, S. Chen, J.G. Brasseur, and J.C. Wyngaard. Examination of hypotheses in the Kolmogorov refined turbulence theory through high-resolution simulations. Part 1. Velocity field. *J. Fluid Mech.*, 309:113–156, 1996.

[191] S.P. Wang, M.H. Anderson, J.G. Oakley, and R. Corradini, M.L.and Bonazza. A thermodynamically consistent and fully conservative treatment of contact discontinuities for compressible multi-component flows. *J. Comput. Phys.*, 195:528–559, 2004.

[192] V. Yakhot. Decay of three-dimensional turbulence at high Reynolds numbers. *J. Fluid Mech.*, 505:87–91, 2004.

[193] V. Yakhot and S.A. Orszag. Renormalization group analysis of turbulence. *Phys. Rev. Lett.*, 57:1722–1725, 1986.

[194] D.L. Youngs. Numerical simulation of turbulent mixing by Rayleigh-Taylor instability. *Physica D*, 12:32–44, 1984.

[195] D.L. Youngs. Three-dimensional numerical simulation of turbulent mixing by Rayleigh-Taylor instability. *Phys. Fluids A*, 3(5):1312–1320, 1991.

[196] D.L. Youngs. Numerical simulation of mixing by Rayleigh-Taylor and Richtmyer-Meshkov instabilities. *Laser Part. Beams*, 12:725–750, 1994.

[197] D.L. Youngs. Application of MILES to Rayleigh-Taylor and Richtmyer-Meshkov mixing. *AIAA-2003-4102*, 2003.

[198] D.L. Youngs. Effect of initial conditions on self-similar turbulent mixing. In *IWPCTM 9*, 2004.

[199] D.L. Youngs. ILES of Rayleigh-Taylor and Richtmyer-Meshkov mixing. In *ECCOMAS 2006*, 2006.

[200] D.L. Youngs and R.J.R. Williams. Turbulent mixing in spherical implosions. *accepted, Int. J. Numer. Meth. Fl.*, 2007.

[201] Q. Zhang and S-I. Sohn. Nonlinear theory of unstable fluid mixing driven by shock wave. *Phys. Fluids*, 9(4):1106–1124, 1997.

[202] Y. Zhou. A scaling analysis of turbulent flows driven by Rayleigh-Taylor and Richtmyer-Meshkov instabilities. *Phys. Fluids*, 13(2):538–543, 2001.

[203] J. Zoltak and D. Drikakis. Hybrid upwind methods for the simulation of unsteady shock-wave diffraction over a cylinder. *Comput. Method. Appl. M.*, 162:165–185, 1998.

APPENDIX **A**

Symmetric Limiters

The MUSCL (Monotone Upstream-Centred Schemes for Conservation Laws) method is used to determine the cell interface variables by extrapolating the cell averaged variables. Examining Equation (3.4.2) it is clear that if

$$\phi\left(r^{lim,L}\right)(U_i - U_{i-1}) = \phi\left(\frac{1}{r^{lim,L}}\right)(U_{i+1} - U_i), \tag{A.0.1}$$

$$\phi\left(r^{lim,R}\right)(U_i - U_{i-1}) = \phi\left(\frac{1}{r^{lim,R}}\right)(U_{i+1} - U_i), \tag{A.0.2}$$

then the resultant interpolated quantity is independent of c. This is the case for the van Albada, van Leer and Minmod limiters which are always of second-order accuracy in the standard MUSCL format. As an example this can be shown to be true of the van Leer limiter. Setting the differences $(U_i - U_{i-1}) = \Delta_{i-1/2}$ and $(U_{i+1} - U_i) = \Delta_{i+1/2}$, then the left hand interpolated values are independent of c as

$$\begin{aligned}
\phi\left(r^{lim,L}\right)(U_i - U_{i-1}) &= \frac{2r^{lim,L}}{1 + r^{lim,L}}(U_i - U_{i-1}), \\
&= \frac{2\Delta_{i+1/2}\Delta_{i-1/2}}{\Delta_{i-1/2}(1 + \Delta_{i+1/2}/\Delta_{i-1/2})}, \\
&= \frac{2\Delta_{i+1/2}\Delta_{i-1/2}}{\Delta_{i-1/2} + \Delta_{i+1/2}},
\end{aligned} \tag{A.0.3}$$

also,

$$\begin{aligned}
\phi\left(\frac{1}{r^{lim,L}}\right)(U_{i+1} - U_i) &= \frac{2/r^{lim,L}}{1 + 1/r^{lim,L}}(U_{i+1} - U_i), \\
&= \frac{2\Delta_{i-1/2}\Delta_{i+1/2}}{\Delta_{i+1/2}(1 + \Delta_{i-1/2}/\Delta_{i+1/2})}, \\
&= \frac{2\Delta_{i+1/2}\Delta_{i-1/2}}{\Delta_{i-1/2} + \Delta_{i+1/2}}.
\end{aligned} \tag{A.0.4}$$

thus demonstrating that this limiter satisfies the criteria in Equation (A.0.2) meaning that it is at most second-order accurate. Equivalent results can be shown for the Min-mod, van Albada and other second order limiters.

APPENDIX **B**

Entropy Analysis

B.1 Entropy Increase for an Isolated Velocity Discontinuity

Beginning with the one-dimensional Euler equations

$$\frac{\partial \mathbf{U}}{\partial t} + \frac{\partial \mathbf{E}}{\partial x} = 0, \tag{B.1.1}$$

where,

$$\mathbf{U} = [\rho,\ \ \rho u, e]^T, \tag{B.1.2}$$

$$\mathbf{E} = \left[\rho u,\ \ \rho u^2 + p,\ \ (e + p)u\right]^T, \tag{B.1.3}$$

$$e = \rho i + 0.5\rho\left(u^2\right), \tag{B.1.4}$$

$$p = \rho i\,(\gamma - 1), \tag{B.1.5}$$

and ρ, i, u are the density, specific internal energy per unit volume and x-direction velocity component, respectively. Throughout this appendix it is assumed that the fluid satisfies the ideal gas equation of state. The Euler equations are discretised using a first order accurate method in time and space

$$\mathbf{U}_j^{n+1} = \mathbf{U}_j^n - \nu\left(\mathbf{E}_{i+1/2}^n - \mathbf{E}_{i-1/2}^n\right) \tag{B.1.6}$$

$$\nu = \frac{\Delta t}{\Delta x}, \tag{B.1.7}$$

Given initial conditions

$$p_L = p_R = p, \qquad \rho_L = \rho_R = \rho, \qquad u_L = \Delta u, \qquad u_R = 0, \tag{B.1.8}$$

where the cells j and $j-1$ are in the left state, cell $j+1$ is the right state. The interface flux $\mathbf{E}^n_{i-1/2}$ is computed directly from the left hand quantities. The values of the primitive variables required to compute $\mathbf{E}^n_{i+1/2}$ are determined by solving the Riemann problem at the interface with the left and right quantities. This can be estimated with reasonable accuracy using a linearised approximation ([184], p.279)

$$p^* = p + \frac{\Delta u \rho a}{2} \tag{B.1.9}$$

$$u^* = \frac{\Delta u}{2} \tag{B.1.10}$$

$$\rho^* = \rho + \frac{\Delta u \rho}{2a}. \tag{B.1.11}$$

Thus, the conserved variables at the next time step are

$$\mathbf{U}^{n+1}_j = \begin{bmatrix} \rho \\ \rho\Delta u \\ \frac{p}{\gamma-1} + \frac{1}{2}\rho\Delta u^2 \end{bmatrix} + \nu \begin{bmatrix} \rho\Delta u - \left(\rho + \frac{\Delta u\rho}{2a}\right)\frac{\Delta u}{2} \\ \rho\Delta u^2 + p - \left(\rho + \frac{\Delta u\rho}{2a}\right)\frac{\Delta u^2}{4} - p - \frac{\Delta u\rho a}{2} \\ \left(\frac{p\gamma\Delta u}{\gamma-1} + \frac{1}{2}\rho\Delta u^3\right) - \left(\frac{\left(p+\frac{\Delta u\rho a}{2}\right)\gamma\Delta u}{2(\gamma-1)} + \left(\rho + \frac{\Delta u\rho}{2a}\right)\frac{\Delta u^3}{16}\right) \end{bmatrix}, \tag{B.1.12}$$

simplifying,

$$\rho^{n+1} = \rho\left(1 + \frac{\nu\Delta u}{4}\left(2 - \frac{\Delta u}{a}\right)\right), \tag{B.1.13}$$

$$u^{n+1} = \Delta u \frac{1 + \frac{\nu\Delta u}{8}\left(6 - \frac{\Delta u}{a} - \frac{4a}{\Delta u}\right)}{\left(1 + \frac{\nu\Delta u}{4}\left(2 - \frac{\Delta u}{a}\right)\right)}, \tag{B.1.14}$$

$$E^{n+1} = \frac{p}{\gamma-1}\left(1 + \frac{\nu\gamma\Delta u}{2}\right) + \frac{1}{2}\rho\Delta u^2\left[1 + \frac{\nu\Delta u}{16}\left(14 - \frac{\Delta u}{a} - \frac{8\gamma a}{\Delta u(\gamma-1)}\right)\right]. \tag{B.1.15}$$

Next the pressure can be computed from $\left(E - 1/2\rho u^2\right)^{n+1}(\gamma-1)$

$$p^{n+1} = \left[\frac{p}{\gamma-1}\left(1 + \frac{\nu\gamma\Delta u}{2}\right) + \frac{1}{2}\rho\Delta u^2\left[1 + \frac{\nu\Delta u}{16}\left(14 - \frac{\Delta u}{a} - \frac{8\gamma a}{\Delta u(\gamma-1)}\right)\right] - \frac{1}{2}\rho\Delta u^2 \frac{\left[1 + \frac{\nu\Delta u}{8}\left(6 - \frac{\Delta u}{a} - \frac{4a}{\Delta u}\right)\right]^2}{\left(1 + \frac{\nu\Delta u}{4}\left(2 - \frac{\Delta u}{a}\right)\right)}\right](\gamma-1). \tag{B.1.16}$$

At this point the pressure at time level $n+1$ is simplified by expanding the last term in the above equation in a binomial series, $(1+x)^{-1} \approx 1 - x + x^2 - ...$, where terms up to order Δu^2 are kept. Starting with the denominator

$$\frac{1}{1+\frac{\nu\Delta u}{2}-\frac{\nu\Delta u^2}{4a}} \approx 1 - \frac{\nu\Delta u}{2} + \frac{\nu\Delta u^2}{4a} + \frac{\nu^2\Delta u^2}{4} + O\left(\frac{\Delta u}{a}\right)^3 \approx 1, \tag{B.1.17}$$

multiplying out the numerator

$$\left[1 + \frac{\nu\Delta u}{8}\left(6 - \frac{\Delta u}{a} - \frac{4a}{\Delta u}\right)\right]^2 \approx 1 - \nu a + \frac{\nu^2 a^2}{4}, \tag{B.1.18}$$

the pressure can now be written as

$$p^{n+1} \approx p\left[1 + \frac{\nu\gamma\Delta u}{2} + \frac{\gamma\nu\Delta u^2}{8a}\left(2\gamma - 4 - \nu a\left(\gamma - 1\right)\right)\right]. \tag{B.1.19}$$

For u^{n+1} and ρ^{n+1}:

$$\rho^{n+1} = \rho\left(1 + \frac{\nu\Delta u}{2} - \frac{\nu\Delta u^2}{4a}\right), \tag{B.1.20}$$

$$u^{n+1} \approx \Delta u\left(1 - \frac{\nu a}{2}\right). \tag{B.1.21}$$

Setting $\nu = C/a$ and $M = 0$ clearly gives $lim_{M\to 0}\Delta S = 0$. In practise this limit is not reached for flows of typical interest (i.e. moving flows). The change in entropy is

$$\begin{aligned}
\Delta S &= \frac{R}{\gamma-1} ln\left(\frac{p}{\rho^\gamma}\right)^{n+1} - \frac{R}{\gamma-1} ln\left(\frac{p}{\rho^\gamma}\right)^{n} \\
&\approx \frac{R}{\gamma-1} ln\left(\frac{p\left[1+\frac{\nu\gamma\Delta u}{2}+\frac{\gamma\nu\Delta u^2}{8a}\left(2\gamma-4-\nu a\left(\gamma-1\right)\right)\right]}{\left(\rho\left(1+\frac{\nu\Delta u}{2}-\frac{\nu\Delta u^2}{4a}\right)\right)^\gamma}\right) - \frac{R}{\gamma-1} ln\left(\frac{p}{\rho^\gamma}\right) \\
&\approx \frac{R}{\gamma-1} ln\left(\frac{1+\frac{\nu\gamma\Delta u}{2}+\frac{\gamma\nu\Delta u^2}{8a}\left(2\gamma-4-\nu a\left(\gamma-1\right)\right)}{\left(1+\frac{\nu\Delta u}{2}-\frac{\nu\Delta u^2}{4a}\right)^\gamma}\right).
\end{aligned} \tag{B.1.22}$$

Expanding the denominator in a series where

$$\frac{1}{(1+z)^m} = 1 - mz + \frac{m\left(m+1\right)}{2!}z^2 - \frac{m\left(m+1\right)\left(m+2\right)}{3!}z^3 + ... \tag{B.1.23}$$

$$\frac{1}{\left(1+\frac{\nu\Delta u}{2}-\frac{\nu\Delta u^2}{4a}\right)^\gamma} = 1 - \frac{\gamma\nu\Delta u}{2} + \frac{\gamma\nu\Delta u^2}{4a} + \gamma\left(\gamma+1\right)\frac{\nu^2\Delta u^2}{8} + O\left(\Delta u^3\right). \tag{B.1.24}$$

Multiplying this by the numerator gives

$$\begin{aligned}\frac{1+\frac{\gamma\nu\Delta u}{2}+\frac{\gamma\nu\Delta u^2}{8a}\left(2\gamma-4-\nu a\left(\gamma-1\right)\right)}{\left(1+\frac{\nu\Delta u}{2}-\frac{\nu\Delta u^2}{4a}\right)^{\gamma}} &\approx \left(1+\frac{\gamma\nu\Delta u}{2}+\frac{\gamma\nu\Delta u^2}{8a}\left(2\gamma-4-\nu a\left(\gamma-1\right)\right)\right)\\ &\quad\left(1-\frac{\gamma\nu\Delta u}{2}+\frac{\gamma\nu\Delta u^2}{4a}+\gamma\left(\gamma+1\right)\frac{\nu^2\Delta u^2}{8}\right)\\ &\approx 1+\frac{\gamma\nu\Delta u^2}{8a}\left[2\gamma-2+2\nu a\left(1-\gamma\right)\right]. \quad \text{(B.1.25)}\end{aligned}$$

Additionally, for $\left|\frac{\gamma\nu\Delta u^2}{8a}\left[2\gamma-2+2\nu a\left(1-\gamma\right)\right]\right| < 1$ the series expansion of the natural logarithm can be employed:

$$ln\left(1+x\right)=x-\frac{x^2}{2}+\frac{x^3}{3}. \quad \text{(B.1.26)}$$

to give Equation (5.5.8).

B.2 Mathematica Script to Derive Leading Order Dissipation Terms

The leading order dissipation rate at an interface where there is a jump in all primitive variables can be computed using the following script in the symbolic manipulation software Mathematica.

```
(*Initial Conditions*)
pr = p - dp/2;
pl = p + dp/2;
ur = u - du/2;
ul = u + du/2;
rr = r - dr/2;
rl = r + dr/2;

(*Star Quantities*)
ps = (pr + pl)/2 + (ul - ur)r a/2;
us = (ur + ul)/2 + (pl - pr)/(2 r a);
rs = rl + (ul - us) r/a;

(*Compute conservative variables at the next time step*)
u1 = rl + v (rl ul - rs us)
u2 = rl ul + v (rl ul^2 + pl - rs us^2 - ps)
u3 = pl/(g - 1) + rl ul^2/2 +
    v ((pl g/(g - 1) + rl ul^2/2) ul - (ps g/(g - 1) + rs us^2/2)us)

{*Calculate primitive variables at the next times step*)
r1 = Simplify[Expand[u1]]
u1 = Simplify[Expand[u2/u1]]
e1 = Simplify[Expand[u3]]
p1 = (g - 1)(e1 - 1/2 r1 u1^2)
```

```
(*Calculate the entropy change and multiply by temperature*)
ln = p1/r1^g ((rl)^g/(pl));
ds = C/(g - 1)(ln - 1);
Tds = ds a^2/(g C);

(*Expand each variable in terms of the jump size to gain the leading order terms*)
TdsExp = Expand[Normal[Series[Normal[Series[Normal[Series[Tds, {dp, 0, 2}]],
{du, 0, 2}]], {dr, 0, 2}]]]

(*Substitute speed of sound instead of pressure p*)
TdsExp2 = TdsExp1 /. p -> r a^2/g
```

All that remains is to simplify the resulting expression to gain several leading order terms.

APPENDIX C

Modified Roe Scheme for Low Mach Flows

C.1 Introduction

It is quite common to use Godunov type upwind methods for simulation of flows with both compressible and incompressible nature, or where the monotonicity of certain properties are required. An example of this is the Richtmyer-Meshkov instability, where a shock wave passes through a perturbed interface, generating a turbulent mixing layer. Once the shock wave has passed, the mixing layer develops in a largely incompressible manner. It is well known that upwind schemes are excessively dissipative at low Mach number, however the mechanism for this is not widely understood. The analysis detailed in Chapter 5 shows that the increase in entropy is approximately equal to the irreversible dissipation of kinetic energy at low Mach. It also shows that the leading order increase of entropy in Godunov type methods is due to numerical dissipation within the momentum equations, which can be written as

$$T\Delta S = \epsilon_{num} = \frac{(1-C)}{4\Delta x} a \Delta u^2 + ... \tag{C.1.1}$$

where T, u and a are the temperature, velocity normal to the cell interface and speed of sound respectively. Δx is the length of the computational cell, C the Courant-Friedrich-Levy (CFL) number, ΔS the change in entropy. ϵ_{num} is the numerical dissipation rate of kinetic energy. It can be seen that the dissipation rate becomes infinite as $M \to 0$ (equivalently as $a \to \infty$). This appendix derives a new Roe scheme for the multicomponent equation set of Wang *et al.* [191] and proposes a modification of the numerical dissipation in the momentum equations which corrects the Mach number dependence of the numerical dissipation. The performance of this scheme is illustrated via a simple single mode Kelvin-Helmholtz test case.

C.2 Governing Equations and Numerical Scheme

This section concerns the low Mach performance of compressible, multi-component schemes. The governing equations chosen are the Euler equations plus two additional

equations for the multi-component model. The three dimensional compressible Euler equations for a Cartesian co-ordinate system can be written in conservative variables as:

$$\frac{\partial \mathbf{U}}{\partial t} + \frac{\partial \mathbf{E}}{\partial x} + \frac{\partial \mathbf{F}}{\partial y} + \frac{\partial \mathbf{G}}{\partial z} = 0, \tag{C.2.1}$$

where,

$$\mathbf{U} = [\rho,\ \rho u,\ \rho v,\ \rho w,\ e]^T, \quad \mathbf{E} = \left[\rho u,\ \rho u^2 + p,\ \rho uv,\ \rho uw,\ (e+p)u\right]^T,$$

$$\mathbf{F} = \left[\rho v,\ \rho uv,\ \rho v^2 + p,\ \rho vw,\ (e+p)v\right]^T, \quad \mathbf{G} = \left[\rho w,\ \rho uw,\ \rho vw,\ \rho w^2 + p,\ (e+p)w\right]^T,$$

$$e = \rho i + 0.5\rho q^2,$$

and ρ, i, u, v, w are the density, internal energy and Cartesian velocity components respectively. The system of equations is completed with the specification of an ideal gas equation of state, $p = \rho i\,(\gamma - 1)$. The multi-component model employed is that proposed by Wang *et al.* [191], which is based on the conservation of total enthalpy within the fluid mixture and consists of tracking two additional equations

$$\frac{\partial}{\partial t}\left(\frac{\rho\chi}{\mathcal{M}}\right) + \frac{\partial}{\partial x}\left(\frac{\rho u\chi}{\mathcal{M}}\right) + \frac{\partial}{\partial y}\left(\frac{\rho v\chi}{\mathcal{M}}\right) + \frac{\partial}{\partial z}\left(\frac{\rho w\chi}{\mathcal{M}}\right) = 0, \tag{C.2.2}$$

$$\frac{\partial}{\partial t}\left(\frac{\rho}{\mathcal{M}}\right) + \frac{\partial}{\partial x}\left(\frac{\rho u}{\mathcal{M}}\right) + \frac{\partial}{\partial y}\left(\frac{\rho v}{\mathcal{M}}\right) + \frac{\partial}{\partial z}\left(\frac{\rho w}{\mathcal{M}}\right) = 0, \tag{C.2.3}$$

where $\mathcal{M}$ is the molecular mass of the mixture, and the variable $\chi = \gamma/(\gamma - 1)$ for a perfect gas. A new Roe scheme has been derived for this set of governing equations, solved in a direction-split form. The flux for the Roe scheme can be written as

$$\mathbf{F_{i+1/2}} = \frac{1}{2}\left(\mathbf{F_L} + \mathbf{F_R}\right) - \frac{1}{2}\sum_{i=1,7} \delta_i \left|\lambda_i^{eig}\right| \mathbf{K}^i, \tag{C.2.4}$$

where the eigenvalues are

$$\lambda_1^{eig} = \lambda_2^{eig} = \lambda_3^{eig} = \lambda_4^{eig} = \lambda_5^{eig} = u, \quad \lambda_6^{eig} = u - a, \quad \lambda_7^{eig} = u + a \tag{C.2.5}$$

and the speed of sound $a^2 = (H - q)\,/\,(\chi - 1)$. With some algebraic manipulation the eigenvectors can be cast into the following form

$$K^1 = \begin{bmatrix} 0 \\ 0 \\ 0 \\ 0 \\ 0 \\ \chi \\ 1 \end{bmatrix}, \; K^2 = \begin{bmatrix} 0 \\ 0 \\ 0 \\ 0 \\ -a^2(\chi-1)\mathcal{M}/\chi \\ -1 \\ 0 \end{bmatrix}, \; K^3 = \begin{bmatrix} 1 \\ u \\ v \\ w \\ q \\ 0 \\ 0 \end{bmatrix}, \; K^4 = \begin{bmatrix} 0 \\ 0 \\ 1 \\ 0 \\ v \\ 0 \\ 0 \end{bmatrix}, \tag{C.2.6}$$

$$K^5 = \begin{bmatrix} 0 \\ 0 \\ 0 \\ 1 \\ w \\ 0 \\ 0 \end{bmatrix}, \; K^6 = \begin{bmatrix} 1 \\ u-a \\ v \\ w \\ a^2(\chi-1) - au + q \\ \chi/\mathcal{M} \\ 1/\mathcal{M} \end{bmatrix}, \; K^7 = \begin{bmatrix} 1 \\ u+a \\ v \\ w \\ a^2(\chi-1) + au + q \\ \chi/\mathcal{M} \\ 1/\mathcal{M} \end{bmatrix}. \tag{C.2.7}$$

The wave strengths, δ_i, required for the Roe scheme are given by

$$\delta_1 = \Delta u_6/\chi - 2\overline{\Delta A}/\mathcal{M}, \quad \delta_2 = \chi\overline{\Delta u_7}, \quad \delta_3 = -\mathcal{M}\overline{\Delta u_7} + \Delta u_1 - 2\overline{\Delta A},$$
$$\delta_4 = \Delta u_3 - v\Delta u_1, \quad \delta_5 = \Delta u_4 - w\Delta u_1, \quad \delta_6 = \mathcal{M}\overline{\Delta u_7}/2 - (\Delta u_2 - u\Delta u_1)/2a + \overline{\Delta A},$$
$$\delta_7 = \delta_6 + (\Delta u_2 - u\Delta u_1)/a,$$

$$\overline{\Delta A} = \frac{\Delta u_5 - u\Delta u_2 - v\Delta u_3 - w\Delta u_4 + q\Delta u_1}{2a^2(\chi-1)}, \qquad \overline{\Delta u_7} = \Delta u_7 - \frac{1}{\chi}\Delta u_6. \tag{C.2.8}$$

Following the analysis by Guillard and Viozat [74] the asymptotic behaviour of the dissipation in the Roe flux can be determined. This is achieved by substituting

$$\begin{aligned} \rho &= \rho_{ref}\left(\rho_0 + M^2\rho_2 + ...\right) & u &= a_{ref}(0 + Mu_1 + ...) \\ v &= a_{ref}(0 + Mv_1 + ...) & w &= a_{ref}(0 + Mw_1 + ...) \\ p &= \rho_{ref}a_{ref}^2\left(p_0 + M^2p_2 + ...\right), \end{aligned} \tag{C.2.9}$$

into Equation (C.2.4), where M is the reference Mach number. Next all terms (for all equations) in the computation of the Roe flux are expanded to leading order in Mach. There is only one leading order term at low Mach, giving

$$(\rho u^2 + p)_{i+1/2} \approx \frac{1}{2}\left((\rho u^2 + p)_L + (\rho u^2 + p)_R\right) + \frac{1}{4}M\rho_{ref}a_{ref}^2a_0\left(\Delta(\rho_0 u_1) - u_1\Delta(\rho_0)\right). \tag{C.2.10}$$

This single term is the only term of order Mach, and arises because $\delta_6 = -\delta_7$ and, $K_2^6 = -K_2^7$, where $(.)_2$ indicates the second row of the eigenvector. As expected, this

result is identical to that given in the analysis of the Euler equations under Godunov form [73] (noting that $\Delta(\rho_0 u_1) - u_1\Delta(\rho_0) = \rho_0\Delta(u_1)$). The next terms in the expansion are constant with Mach, hence these are not the source of increased dissipation in incompressible flows and are neglected here. Computing the dissipation of kinetic energy due to this term gives the leading order term shown in Equation C.1.1. As $M \to 0$ ($a_{ref} \to \infty$) then the Roe scheme gives infinite dissipation. To rectify this, one can modify the second row of the eigenvectors K_2^6 and K_2^7 by a factor of Mach in low Mach regions. In this appendix the sixth and seventh eigenvectors are modified as

$$K_2^6 = u - a \to u - \beta a, \qquad K_2^7 = u + a \to u + \beta a \tag{C.2.11}$$

Here, $\beta = \min(10M, 1)$, such that the original Roe scheme is recovered for interfaces where $M > 0.1$. This makes the leading order dissipation tend to a constant value as Mach number tends to zero. If the new flux Jacobian is computed using the new set of eigenvectors it is seen that this modification changes only the u-momentum flux from $\rho u^2 + p$ to $\rho u^2 + \beta p$. The modification could be viewed as a change in the governing equations which are being solved, which is not desirable. However, the standard fluxes are dominated by unphysical viscous dissipation at low Mach, and are hence also not solving the Euler equations - but the Euler equations plus a large viscous term. The contribution from the Roe scheme can be understood as an additional term required only to stabilise the central difference flux. Hence the form of this stabilisation does not necessarily require a physical basis, but it must not dominate the flow physics (as happens with the standard flux at low Mach). This modification also allows good stability according to the standard CFL condition, as opposed to standard preconditioned methods where stability in explicit time-stepping is prohibitive [20], thus can be used where the time stepping is not constrained by the low Mach portion of the flow. In addition, it preserves exactly a stationary material interface.

C.3 Numerical Test Case

The effective resolution of the modified Roe scheme is now tested in the simulation of a single mode Kelvin-Helmholtz (KH) instability. The above method is implemented in conjuction with third-order accurate Runge-Kutta time-stepping [173], and with fifth-order (in one dimension) MUSCL reconstruction [107]. The computational domain is square and spans $[-0.5, -0.5]$ to $[0.5, 0.5]$ and is discretised with 16 cells in each direction. The initial conditions consist of a perturbed shear layer, where the flow is initially parallel, but for a small perturbation velocity which triggers the development of a KH vortex. The initial perturbation is written in the form of the divergence of a vector potential A_z so that the flow field is approximately solenoidal [199]. In summary,

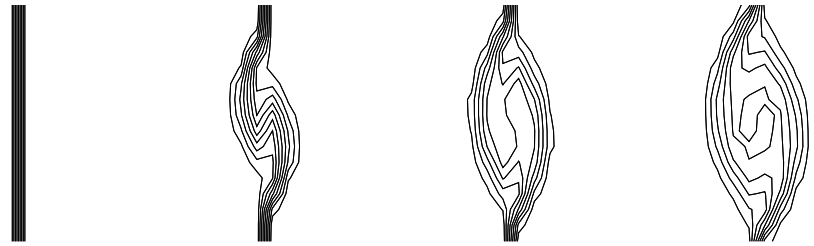

(a) t=0, $M = 0.2$ (b) t=1, $M = 0.2$ (c) t=2, $M = 0.2$ (d) t=3, $M = 0.2$

Figure C.1: Time development of the single mode KH instability using the standard Roe scheme. Nine contours of volume fraction from 0.1 to 0.9

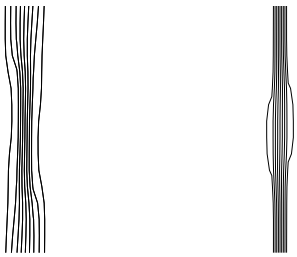

(a) t=3, $M = 0.02$ (b) t=3, $M = 0.002$

Figure C.2: Simulations of the KH instability at M=0.02 and M=0.002 using the standard Roe scheme

$$
\begin{aligned}
v &= -\Delta U/2 - \tfrac{\partial A_z}{\partial x} & u &= \frac{\partial A_z}{\partial y}, & &\text{for } x < 0 \\
v &= \Delta U/2 + \tfrac{\partial A_z}{\partial x} & u &= \frac{\partial A_z}{\partial y}, & &\text{for } x > 0 \\
A_z &= \tfrac{U_0}{k}\cos(ky)\exp^{-k|x|} & U_0 &= 0.1\Delta U, & \Delta U &= 1
\end{aligned}
\tag{C.3.1}
$$

where ΔU is the difference in mean flow velocity U across the mixing layer. The Mach number, defined by $\Delta U/a$, is adjusted by changing the pressure. Density is fixed at $\rho = 1$, and $\gamma = 5/3$. The coarse resolution is deliberately chosen to highlight the scheme's ability to capture what would be a high wavenumber perturbation on a larger grid. It also allows easy demonstration of the low Mach behaviour of the dissipation of kinetic energy.

The development of the instability when using the standard Roe scheme at $M = 0.2$ is illustrated in Figure C.1. The initially small perturbation is absolutely unstable and forms the characteristic KH vortex. Contours of volume fraction are also shown in Figure C.2 for $M = 0.02$ and $M = 0.002$, where excessive dissipation prevents growth of the instability. Figure C.3 shows volume fraction contours for the modified scheme at the final time step, where the modified dissipation allows the development of a near Mach independent structure.

An additional issue with low Mach Godunov type simulations is that the numerical

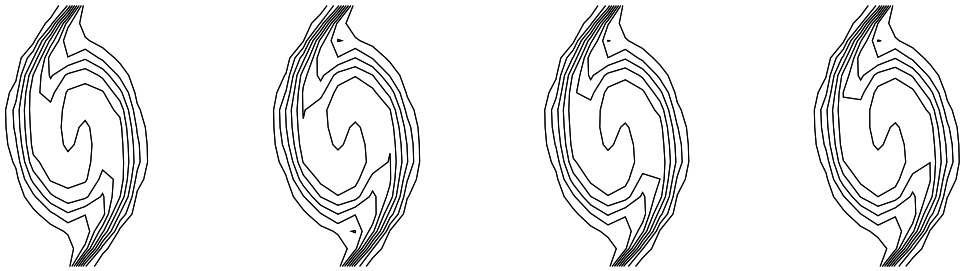

(a) $M = 0.2$ (b) $M = 0.02$ (c) $M = 0.002$ (d) $M = 0.0002$

Figure C.3: Nine contours of volume fraction from 0.1 to 0.9 at $t = 3$ for the modified scheme

Table C.1: Scaling of the maximum pressure and density fluctuations with Mach at $t = 3$

Mach	$\Delta p_{max}/(pM^2)$	$\Delta\rho_{max}/(\rho M^2)$
$M = 0.2$	0.683	0.525
$M = 0.02$	0.633	0.575
$M = 0.002$	0.650	0.35
$M = 0.0002$	0.633	12.5

dissipation causes anomalous scaling of the pressure with Mach number [74]. Table C.1 shows the variation of pressure and density differences with respect to Mach. The pressure variations follow the correct M^2 scaling, however the density variations follow that scaling only to $M \approx 0.002$, below which there is a departure from the expected behaviour. It is believed that this is due to the problem of 'cancellation' errors. Sesterhenn *et al* [161] demonstrated that this is a potential issue even at $M \approx 0.02$.

C.4 Conclusions

This appendix has presented a new Roe scheme to solve the multicomponent equations of Wang *et al.* [191] and proposed a modification to this scheme for low Mach flows. This removes the leading order Mach dependent dissipation and is demonstrated to provide consistent result at Mach numbers as low as 10^{-4}. It also shows correct M^2 scaling of pressure fluctuations, however, the density fluctuations deviate from this below $M \approx 0.002$. This is believed to be due to cancellation errors.